

Search for low-spin states above the $5-\alpha$
break-up threshold in ^{20}Ne

by

Jacobus Andreas Swartz

*Dissertation presented for the degree of Doctor of Natural Philosophy
in the Faculty of Science at Stellenbosch University*



Department of Physics,
University of Stellenbosch,
Private Bag X1, Matieland 7602,
South Africa

Promoters:

Prof. Paul Papka

Dept. of Physics

Dr. Frederick David Smit

Dept. of Nuclear Physics, iThemba LABS

April 2014

Declaration

By submitting this thesis electronically, I declare that the entirety of the work contained therein is my own, original work, that I am the sole author thereof (save to the extent explicitly otherwise stated), that reproduction and publication thereof by Stellenbosch University will not infringe any third party rights and that I have not previously in its entirety or in part submitted it for obtaining any qualification.

.....

Signature

.....

Date

Acknowledgement

The financial assistance of the National Research Foundation (NRF) towards this research is hereby acknowledged. Opinions expressed and conclusions arrived at, are those of the author and are not necessarily to be attributed to the NRF.

ABSTRACT

The study of α clustering is a well-established topic of research in nuclear physics. Recent experimental evidence has revealed the first 2^+ excitation of the Hoyle state in ^{12}C , which is known to have a strong α cluster structure. The idea of multi-particle α cluster structures in light nuclear matter has received much attention from theoretical investigations of late. This research has profound implications in the fields of both nuclear structure and nuclear astrophysics.

The ^{20}Ne nucleus is a good example for α clustering, since many of its states are known to have α clustering structures. Few low spin states are known at high excitation energies of this nucleus. It is predicted that this nucleus contains a 0^+ 5- α cluster state, a so-called ‘Hoyle analogue state’, above its 5- α break-up threshold at $E_x = 19.17$ MeV.

This thesis presents a study of the ^{20}Ne nucleus with the $^{22}\text{Ne}(p,t)^{20}\text{Ne}$ reaction at laboratory angles $\theta_{lab} = (0^\circ, 7^\circ, 16^\circ, 27^\circ)$. The iThemba LABS $K600$ magnetic spectrometer was employed with a beam of energy $E_{lab} = 60$ MeV, incident upon a ^{22}Ne gas target held intact by Aramid foils. The aim was to search for low spin states in ^{20}Ne at excitation energies above $E_x = 15$ MeV, and, possibly, to find an indication of the 5- α cluster state.

Three narrow states were discovered at energies of $E_x = 20.59$ MeV, $E_x = 21.16$ MeV and $E_x = 21.80$ MeV. Calculations performed with the isobaric multiplet mass equation indicate that these states may be $T = 2$ isobaric analogue states of three known states in ^{20}O . However, shell-model calculations indicate that these states may also have $T = 0$ or $T = 1$ isospin values. There is also evidence of a new state at $E_x = 17.67$ MeV and, possibly, of a collection of new states which could not be resolved at $E_x = 18.84$ MeV.

A tentative candidate for the desired 5- α cluster state was observed, but this will require another measurement with cleaner background to be confirmed.

OPSOMMING

Alfa bondelvorming is 'n gevestigde navorsingsonderwerp in kernfisika. Daar is onlangse bewyse vir die ontdekking van die 2^+ opwekking van die Hoyle toestand in ^{12}C , wat 'n erkende alfa bondelstruktuur het. Die idee van multi-alfa bondelstrukture in ligte kerne het onlangs baie aandag geniet in teoretiese ondersoeke. Hierdie navorsing het besondere implikasies vir kernstruktuur, sowel as vir kernastrofisika.

Die ^{20}Ne kern bied 'n ideale voorbeeld vir alfa bondelvorming aangesien dit bekend is dat baie van die kern se toestande alfa bondelstrukture het. Min lae-spin toestande is by hoë opwekenergieë bekend in hierdie kern. Daar word voorspel dat 'n 0^+ 5-alfa bondeltoestand, 'n sogenaamde 'Hoyle analogoostoestand', bo die drumpel vir 5-alfa verval by $E_x = 19.17$ MeV bestaan.

Hierdie tesis beskryf 'n studie van die ^{20}Ne kern met die $^{22}\text{Ne}(p,t)^{20}\text{Ne}$ reaksie by laboratorium hoeke van $\theta_{lab} = (0^\circ, 7^\circ, 16^\circ, 27^\circ)$. Die K600 magnetiese spektrometer van iThemba LABS is gebruik met 'n proton bundel, by 'n energie van $E_{lab} = 60$ MeV, wat op 'n ^{22}Ne gas teiken omhul met aramid foelies gerig is. Die doel was om lae-spin toestande in ^{20}Ne by opwekenergieë bo $E_x = 15$ MeV op te spoor, en om moontlik ook 'n aanduiding van die 5-alfa bondeltoestand te vind.

Drie smal toestande is by energieë van $E_x = 20.59$ MeV, $E_x = 21.16$ MeV en $E_x = 21.80$ MeV opgespoor. Berekeninge wat met die isobariese multiplet massa vergelyking uitgevoer is, dui daarop dat hierdie toestande $T = 2$ isobariese analogoostoestande van drie bekende toestande in ^{20}O kan wees, hoewel skilmodel berekeninge ook $T = 0$ en $T = 1$ kandidate aandui. Daar is ook bewyse van 'n nuwe toestand by $E_x = 17.67$ MeV, en moontlik van 'n versameling nuwe toestande rondom $E_x = 18.84$ MeV wat nie uitmekaar geken kon word nie.

'n Tentatiewe kandidaat vir die gesogte 5-alfa bondel toestand is waargeneem, maar nog 'n meting met 'n skoner agtergrond word vir bevestiging benodig.

Acknowledgements

I would like to thank the following people who helped me get this far:

- My head supervisor, Prof Paul Papka, who is like a well of energy and ideas. His perpetual excitedness about experimental physics just has to rub off on anyone who works with him. Thank you for making physics fun, and for getting me into this and so many other interesting projects.
- My co-supervisor, Dr Ricky Smit, whose wisdom and years of knowledge about magnetic spectrometers should be considered a national treasure. Thank you for guiding me through these last three years, and for making me wiser and more knowledgeable about many topics, from space-weather to spectrometers.
- The captain of the *K600*, Dr Retief Neveling, who is more organised than any physicist of which I know. Thank you for teaching me how the spectrometer works, mentoring me through my post-graduate career and keeping the *K600* ship afloat at all times.
- My fellow local *K600* student, Fhumulani Nemulodi, for valuable discussions on DWBA, FRESCO etc. and help with many night-shifts.
- The people who helped during the experimental times (the ones not yet mentioned above): Dr Deon Steyn, Dr Zinhle Buthelezi, Dr Siegie Förtsch, Prof Martin Freer, Dr Tzany Kokalova, Dr Nico Orce and Joele Mira. Your time and input to this project is sincerely appreciated.
- Prof Atsushi Tamii for being so kind as to give us those aramid foils.
- Prof Carlos Pineda-Vargas and Dr Christopher Mtshali for helping me with the microPIXE and RBS measurements, and for analysing these data, despite some setbacks caused by the MRD fire. That information was very valuable to this thesis. I also thank the Van de Graaff accelerator team for providing a good beam for these measurements.
- The iThemba LABS Proposal Advisory Committee for allocating beam time to this project, and the guys in the SSC accelerator team for providing a stable beam over four weekends.

- Our mechanical engineer, Franz Gonglach, for his help with the cryogenic gas target development.
- Rob Mcalister and the rest of the vacuum lab guys for leak-testing all our equipment.
- Prof Werner Richter for performing the IMME calculations and proof-reading my chapters on the theory and the interpretation of the new states, and Prof Alex Brown for performing the NuShellX and FRESCO calculations. Your theoretical inputs are much appreciated.
- I must also acknowledge a few people, all of whom I haven't seen for quite some time, who inspired me to pursue science in general, and eventually nuclear physics specifically: Barry Lane (St. George's Preparatory), Hela Roux (Pearson High School), Prof Japie Engelbrecht (Nelson Mandela Metropolitan University - NMMU), Dr Pearl Berndt-Lewis (NMMU) and Prof Gregory Hillhouse (Stellenbosch University).

Laastens, maar nie die minste nie, dankie:

- Estée, vir al jou liefde en geduld deur my langdurige studenteloopbaan.
- My ouers en grootouers vir ondersteuning en inspirasie waarsonder ek nie so ver sou gekom het nie.

Hierdie tesis word opgedra aan my oupa, Jacobus Andreas Nel.

CONTENTS

ABSTRACT	4
LIST OF TABLES	v
LIST OF FIGURES	vii
1. Introduction	1
1.1 Background of study	2
1.2 On experimental methods	5
2. Theoretical formalisms	12
2.1 DWBA calculation	13
2.2 Coupled reaction channels	17
2.3 Shell-model calculations	18
2.4 Isobaric multiplet mass equation	20
2.4.1 On isospin	20
2.4.2 The IMME calculations	22
2.4.2.1 Basic equations	22
2.4.2.2 With IMME code	23
3. Experimental setup and method	28
3.1 The <i>K</i> 600 magnetic spectrometer	29
3.2 The focal plane detector package	31
3.2.1 The VDCs	32
3.2.2 The Scintillation detectors	33
3.3 The beam stops	38
3.3.1 The finite angle beam stop	38
3.3.2 The zero degree beam stop	39
3.4 Dispersion Matching	40
3.5 The ^{22}Ne uncooled gas cell target	41
3.5.1 Resolution	41
3.5.1.1 Energy resolution	41
3.5.1.2 Angular resolution	43
3.5.1.3 Resolution of previous gas cell measurements	43
3.5.2 The gas cell	46

3.5.3	The aramid foils	47
3.5.4	Gas contaminants	51
3.5.5	The target ladder	53
3.6	Cryogenic gas target development	55
3.6.1	Choice of foils	55
3.6.2	The new gas target ladder	55
3.6.3	Gas flow and thermal conductivity	58
3.6.4	Conclusion	61
3.7	Electronics	62
3.8	Experimental procedure	65
4.	Analysis of $^{22}\text{Ne}(p,t)^{20}\text{Ne}$ data	67
4.1	VDC operation	67
4.2	Analysis of the 52 MeV (p,t) data set	72
4.2.1	Background clean-up with particle identification gates	72
4.2.2	Kinematic corrections	75
4.2.3	Background targets	77
4.2.4	The calibration procedure	79
4.3	Analysis of the 46 MeV and 48 MeV (p,t) data sets	83
4.4	Analysis of the 41 MeV and 42 MeV (p,t) data sets	85
4.5	Analysis of the 36 MeV and 37 MeV (p,t) data sets	87
4.6	Analysis of the 33.5 MeV (p,t) data set	91
4.6.1	Mapping of background	93
4.6.2	Calibration with oxygen peaks	96
4.6.3	Spectra from possible contaminants	97
4.7	Summary of all data sets	102
4.8	Cross sections	106
4.8.1	Method of extraction	106
4.8.2	Background subtraction	108
4.8.3	Errors	118
4.8.3.1	Angular uncertainty	118
4.8.3.2	Variables which influence cross section	118
4.8.3.3	Uncertainty in excitation energy	119
4.9	Observed energy resolution values	119
4.10	Results	123

5. Interpretation of the new states	128
5.1 IMME calculations	129
5.2 NuShellX and FRESCO calculations	134
5.3 The $5\text{-}\alpha$ cluster candidate	138
6. Conclusion and future prospects	140
6.1 Conclusion	140
6.2 Future prospects	141
A. The IMME.C code	148
B. Data sets over full energy range	150
C. Absolute cross sections of known states	154
D. Results from NuShellX and FRESCO at non-zero angles	160
. Bibliography	167

LIST OF TABLES

1.1	Known states in the region of the 0^+ state of interest	8
1.2	The beam energies which were recorded during each weekend	11
2.1	The optical model parameters for the DWBA calculation.	17
2.2	The centre-of-mass angles corresponding to the non-zero laboratory angles which were investigated	17
2.3	Calculated values from IMME.C code for excitation energies of known $T = 2$ IAS states in self-conjugate α -nuclei, compared to known experimental values	27
3.1	A summary of the materials seen in the focal plane by the particles after exiting the <i>K</i> 600 vacuum chamber	35
3.2	A summary of the calculated energy loss values of ejectile particles through the paddles	35
3.3	Calculated TOF ranges of deuterons and tritons	37
3.4	The stoichiometries of elements on the foils inside and outside the irradiated regions	48
3.5	Compositions of trace contaminants on the aramid foils	50
3.6	Resolution values obtained with the (p,p') reaction	65
4.1	The values of the parameters with which the 52 MeV (p,t) field setting was investigated	79
4.2	The discrete experimental peaks used for the calibration of the 52 MeV field setting at $\theta_{lab} = 0.5^\circ$	79
4.3	The values of parameters with which the 46/48 MeV (p,t) field setting was investigated	83
4.4	The values of parameters for the background measurement of the 46/48 MeV (p,t) field setting	83
4.5	Values of parameters with which the 41/42 MeV (p,t) field setting was inves- tigated	85
4.6	Values of parameters for the background data of the 41/42 MeV (p,t) field setting	85
4.7	Values of parameters with which the 36/37 MeV (p,t) field setting was inves- tigated.	87

4.8	Values of parameters for the background measurement with the 36/37 MeV (p,t) field setting	87
4.9	Values of parameters with which the target and background material were investigated with the 33.5 MeV field setting.	92
4.10	Calculated triton ejectile energies from different possible reactions	94
4.11	The discrete experimental peaks used for the calibration of the 33.5 MeV field setting at $\theta_{lab} = -1^\circ$	96
4.12	Measured widths of known states in ^{20}Ne	124
4.13	Measured and calculated widths of candidate new states in ^{20}Ne	125
4.14	Absolute cross sections extracted for newly observed states in ^{20}Ne	125
5.1	Excitation energy values in ^{20}O obtained with an IMME calculation on the new ^{20}Ne states	129
5.2	Excitation energy values in ^{20}Ne obtained with an IMME code	133
6.1	Calculated and experimental relative cross sections $\frac{d\sigma(p,t)/d\Omega}{d\sigma(p,^3\text{He})/d\Omega}$ for states with $T_f = T_i + 1$	143
6.2	Known states in the region of interest in ^{20}F	145
C.1	Absolute cross sections extracted for known negative parity states in ^{20}Ne . .	154
C.2	Absolute cross sections extracted for known positive parity states in ^{20}Ne . .	155

LIST OF FIGURES

1.1	The Ikeda diagram	3
1.2	Energy spectra from a previous measurement to investigate the $^{22}\text{Ne}(p,t)^{20}\text{Ne}$ and $^{22}\text{Ne}(p,^3\text{He})^{20}\text{F}$ reactions	7
1.3	Schematic representation of the masses of the $T = 1$ and $T = 2$ states in ^{20}Ne and its isobaric nuclei ^{20}F and ^{20}O	9
1.4	Data from RNCP for the $^{24}\text{Mg}(p,t)^{22}\text{Mg}$ reaction	10
2.1	Angular distribution plots for states from the $^{22}\text{Ne}(p,t)^{20}\text{Ne}$ reaction from a DWBA calculation	15
2.2	Data from a previous measurement of the $^{22}\text{Ne}(p,t)^{20}\text{Ne}$ reaction with CCBA and DWBA calculations	16
2.3	Shell model diagram filled up to $N = Z = 8$	20
2.4	Isobar diagram for $A = 20$ nuclei	22
2.5	Deviations from experimentally known values for calculations of the mass excesses of even nuclei with the IMME.C code	26
2.6	Procedure used to calculate energies of isobaric analogue states with the IMME.C code.	27
3.1	Floor plan of the iThemba LABS cyclotron facility	28
3.2	Schematic layout of the $K600$ magnetic spectrometer	30
3.3	The focal plane detector package	31
3.4	A cross-section through a VDC	32
3.5	The 1/4"-thick paddle scintillator cut open	36
3.6	The first paddle in position in the focal plane	36
3.7	Calculated energy loss and TOF ranges for Paddle 1	38
3.8	The scattering chamber beam stop	39
3.9	The L-shaped zero degree (p,t) beam stop	40
3.10	The gas target frame with aramid windows	44
3.11	A $^{20}\text{Ne}(p,t)^{18}\text{Ne}$ spectrum obtained in a previous measurement with the $K600$ spectrometer	45

3.12	The body of the 10 mm thick gas target cell	46
3.13	MicroPIXE maps of chlorine composition of the aramid foils	49
3.14	Rutherford backscattering (RBS) spectra measured on the aramid foils	49
3.15	MicroPIXE spectra displaying chlorine and all the trace contaminants on the aramid foils	50
3.16	Residual gas analyser data for the ^{22}Ne gas	52
3.17	The uncooled target ladder	53
3.18	Diagram of the gas handling system	54
3.19	The cryogenic gas target ladder	57
3.20	Aluminium side plates used for clamping on both sides of the gas cells	58
3.21	The target gas cells with aramid foils	58
3.22	A test gas target cell with glue grooves cut around its inner ring	58
3.23	The Dewar flask on top of the spectrometer scattering chamber being filled with liquid nitrogen	59
3.24	The cryogenic gas target ladder with copper frame and aluminium plates attached	60
3.25	Copper braids connected by a continuous body of copper, mostly hidden underneath aluminised mylar foil, to a body of copper connected to the Dewar flask	61
3.26	The steel pipes which connect the pipes from the gas cells to the gas handling system in the cryogenic target system	62
3.27	Diagram of the trigger electronics	64
3.28	The pepperpot collimator	65
4.1	Drift times recorded for individual signal wires	68
4.2	The spectrum of all drift times which were measured in the first X-wire chamber	69
4.3	Drift distances corresponding to the drift time spectrum in Fig. 4.2	69
4.4	Lookup table for drift times and drift distances	70
4.5	A wire hits per channel spectrum for VDC X1	70
4.6	Signal wire hits per event for VDC X1	71

4.7	A focal plane position spectrum for VDC X1	72
4.8	Paddle 1 vs Time-of-flight (TOF) spectrum for the 52 MeV field setting at $\theta_{lab} = 0.5^\circ$	73
4.9	Y2 position vs X1 position spectrum for the 52 MeV (p,t) field setting at $\theta_{lab} = 0.5^\circ$	74
4.10	Shape correction of θ_{lab} vs X focal plane position spectrum for the 52 MeV (p,t) field setting centred at $\theta_{lab} = 7^\circ$	76
4.11	Background data from different background targets	78
4.12	The particle momenta and focal plane positions of calibration data points of the $\theta_{lab} = 0.5^\circ$ and $E_t = 52$ MeV setting	80
4.13	An excitation energy spectrum for the 52 MeV $^{22}\text{Ne}(p,t)^{20}\text{Ne}$ field setting at $\theta_{lab} = 0.5^\circ$	81
4.14	The differences between the known values and the measured mean values from the energy calibration in the present experiment for the states observed with the 52 MeV $^{22}\text{Ne}(p,t)^{20}\text{Ne}$ field setting at $\theta_{lab} = 0.5^\circ$	82
4.15	Excitation energy spectra from the 46 MeV and 48 MeV field settings	84
4.16	Excitation energy spectra from the 41 MeV and 42 MeV field settings.	86
4.17	Paddle 1 vs TOF spectrum for the 36 MeV field setting at $\theta_{lab} = -1^\circ$	88
4.18	Excitation energy spectra from the 36 MeV and 37 MeV field settings.	89
4.19	The ground state of ^{10}C measured with two 6- μm -thick aramid foils with gas in the target, and with only one 6- μm -thick aramid foil	90
4.20	Drawing of the paths of ejectile triton particles coming from either of the two aramid foils	91
4.21	Paddle 1 vs TOF spectrum for the 33.5 MeV field setting at $\theta_{lab} = -1^\circ$	92
4.22	Carbon foil and oxygen gas calibration data.	95
4.23	Triton momenta and focal plane position for calibration data points of the $\theta_{lab} = -1^\circ$ and $E_t = 33.5$ MeV setting.	96
4.24	Aramid background data and ^{22}Ne gas-filled target data compared to calibration data measured with oxygen, nitrogen, argon and natural neon gases.	98
4.25	Excitation energy spectra for the two highest excitation energy fields measured with $\theta_{lab} = -1^\circ$ and $\theta_{lab} = 7^\circ$	100

4.26	Excitation energy spectra from the 33.5 MeV field setting at $\theta_{lab} = 16^\circ$ and $\theta_{lab} = 27^\circ$	101
4.27	The quadratic, linear and constant terms in the calibration equations for each energy setting at $\theta_{lab} = 0^\circ$	103
4.28	The excitation energy spectrum for all field settings on the aramid foil close to or at $\theta_{lab} = 0^\circ$	104
4.29	The excitation energy spectrum for all field settings on the ^{22}Ne gas-filled target close to or at $\theta_{lab} = 0^\circ$	105
4.30	Background-subtracted spectrum for the 33.5 MeV field setting at $\theta_{lab} = -1^\circ$	110
4.31	Fit of the 5- α cluster candidate state	111
4.32	Background-subtracted spectrum for the 33.5 MeV field setting at $\theta_{lab} = 7^\circ$	112
4.33	Background-subtracted spectrum for the 31 MeV field setting at $\theta_{lab} = 7^\circ$	113
4.34	Background-subtracted spectrum for the 33.5 MeV field setting at $\theta_{lab} = 16^\circ$	116
4.35	Background-subtracted spectrum for the 33.5 MeV field setting at $\theta_{lab} = 27^\circ$	117
4.36	Observed energy resolution values with (p,t) reaction at $\theta_{lab} = 0^\circ$	121
4.37	Observed energy resolution values with (p,t) reaction at $\theta_{lab} = 7^\circ$	122
4.38	Observed energy resolution values with (p,t) reaction at $\theta_{lab} = 16^\circ$	122
4.39	Observed energy resolution values with (p,t) reaction at $\theta_{lab} = 27^\circ$	123
4.40	Angular distribution plots for states measured between $E_x = 0$ and $E_x = 7$ MeV	126
4.41	Angular distribution plots for states measured above $E_x = 16$ MeV	127
5.1	Measured and calculated angular distribution plots of known states in ^{20}Ne	130
5.2	Angular distribution plots of experimentally observed $T = 2$ candidate and calculated $T = 2$ states	131
5.3	Calculated and experimental states in ^{20}O	132
5.4	Cross section values from NuShellX and FRESCO at $\theta_{lab} = 0^\circ$	136
5.5	Cross section values extracted from the $\theta_{lab} = 0^\circ$ data.	137
5.6	Comparison of calculated and observed states in ^{20}Ne	139
6.1	The <i>Hagar</i> NaI detector for large-volume γ -ray detection	142
6.2	Energy spectra measured with the (p,t) and $(p,^3\text{He})$ reactions using the same ^{22}Ne gas target, beam and angle	144

6.3	Energy spectra measured with the (p,t) and $(p,^3\text{He})$ reactions on a ^{14}C target	147
B.1	The excitation energy spectrum for all field settings on the ^{22}Ne gas-filled target at $\theta_{lab} = 7^\circ$	151
B.2	The excitation energy spectrum for all field settings on the ^{22}Ne gas-filled target at $\theta_{lab} = 16^\circ$	152
B.3	The excitation energy spectrum for all field settings on the ^{22}Ne gas-filled target at $\theta_{lab} = 27^\circ$	153
C.1	Angular distribution plots for states measured between $E_x = 7$ and $E_x = 10.3$ MeV	156
C.2	Angular distribution plots for states measured between $E_x = 10.3$ and $E_x = 12$ MeV	157
C.3	Angular distribution plots for states measured between $E_x = 12$ and $E_x = 13.8$ MeV	158
C.4	Angular distribution plots for states measured between $E_x = 13.8$ and $E_x = 18$ MeV	159
D.1	Cross section values from NuShellX and Fresco at $\theta_{lab} = 7^\circ$	161
D.2	Cross section values from NuShellX and Fresco at $\theta_{lab} = 16^\circ$	162
D.3	Cross section values from NuShellX and Fresco at $\theta_{lab} = 27^\circ$	163
D.4	Cross section values extracted from the $\theta_{lab} = 7^\circ$ data	164
D.5	Cross section values extracted from the $\theta_{lab} = 16^\circ$ data	165
D.6	Cross section values extracted from the $\theta_{lab} = 27^\circ$ data	166

CHAPTER 1

Introduction

Ever since the nuclear model of the atom was established by Ernest Rutherford in 1911, α particles have been known to be electron-free helium nuclei. Rutherford also coined the terms α -decay and β -decay when he differentiated between these two modes of radioactive decay [1]. The discovery of α -decay from heavy elements like Radium, Thorium and Uranium led to speculation that α particles might be preformed in atomic nuclei. In the 1930s, Hafstad and Teller proposed that self-conjugate α nuclei may be described as systems composed of $A = 4n-\alpha$ cluster structures [2]. Thus was born the field of α clustering in nuclear physics.

Nucleons may exist as protons or neutrons in either spin-up or spin-down states. It is therefore not surprising that the α particle completely fills the first $0s$ nuclear shell with its constituent two protons and two neutrons in spin-up and spin-down states. It has a remarkably high binding energy, and its first decay level is found at an excitation energy of beyond $E_x = 20$ MeV [3]. This makes the idea of the α cluster as a fundamental subunit of nuclei, especially self-conjugate α nuclei, very plausible.

Recently, there has been a great deal of interest in $n-\alpha$ clusters in light self-conjugate α nuclei. The most famous example of such a state exists in ^{12}C at an excitation energy of $E_x = 7.65$ MeV. This state is a necessary condition for the generation of carbon during helium fusion in α -particle rich stellar matter. Fred Hoyle first predicted the existence of this state early in the 1950s [4], and soon afterwards it was measured within a few keV of the predicted energy value [5]. Today, the Hoyle state is known to have a dilute gas-like α -particle cluster structure through a number of theoretical studies [6, 7, 8, 9, 10, 11, 12, 13, 14], and a measurement of its radius [15]. The first ab-initio calculation of this state indicates an obtuse triangular configuration of α clusters [16, 17].

A state which is analogous to the Hoyle state is expected in ^{20}Ne above the $5-\alpha$ break-up threshold at $E_x = 19.17$ MeV, as indicated on the Ikeda diagram in Fig. 1.1 [18]. This follows from the so-called ‘threshold rule’ for α clustering in light α -nuclei, which predicts an $n-\alpha$ state near to the $n-\alpha$ break-up threshold of any self-conjugate $n-\alpha$ nucleus. The nature and characteristics of these states are of fundamental importance to nuclear struc-

1. Introduction

ture and to the nucleosynthesis of the elements [19, 20, 21]. The ^{20}Ne nucleus specifically is an ideal nucleus for studying α clustering since a number of its most prominent bands may be described in terms of an α particle existing outside of a core of ^{16}O , which is a closed shell nucleus.

This thesis describes an experimental investigation of ^{20}Ne , populated by means of the $^{22}\text{Ne}(p,t)^{20}\text{Ne}$ reaction. The aim was to map out the low-spin states of this nucleus, which may include the proposed 5- α cluster state and possibly isobaric analogue states, in a high excitation energy region ($E_x = 15 - 25$ MeV). Chapter 2 describes the different theoretical models which were employed to choose the experimental angles and interpret the data, while Chapter 3 describes the experimental setup, and Chapter 4 expounds on the data analysis. Chapter 5 provides a discussion of the analysed data in terms of different models from Chapter 2 and Chapter 6 presents a conclusion to the work.

This chapter proceeds with Section 1.1, which gives a historical overview of the study of α clustering for light α nuclei in general and for the ^{20}Ne nucleus specifically. Section 1.2 concludes this chapter with an overview of the experimental problems and the solutions which were put forth.

1.1 Background of study

It has been found that α clustering is a phenomenon that is observed at certain excitation energies in nuclei, but normally not in their ground states. A notorious exception to this rule would be ^8Be , which is unique among known self-conjugate α nuclei because of the 2- α cluster structure of its ground state [22]. The cluster structure of the ^8Be ground state is vitally important to the nucleosynthesis of ^{12}C in stars. The ^8Be 2- α cluster may pick up another α particle and, provided that the necessary energy is present in the system, it may form the Hoyle state in ^{12}C [4, 5].

The Hoyle state has a narrow width (i.e. a significant lifetime), of which a large contribution is from α decay, maintained by a large Coulomb barrier. These properties, and its excitation energy value, do not fit into the framework of the nuclear shell model picture [23].

Recently, theoretical investigations have indicated that the Hoyle state may be a state of α condensate nature [24]. This has triggered a series of theoretical investigations into the occurrence of α condensate states in light self-conjugate α nuclei i.e. ^{16}O , ^{20}Ne , ^{24}Mg ,

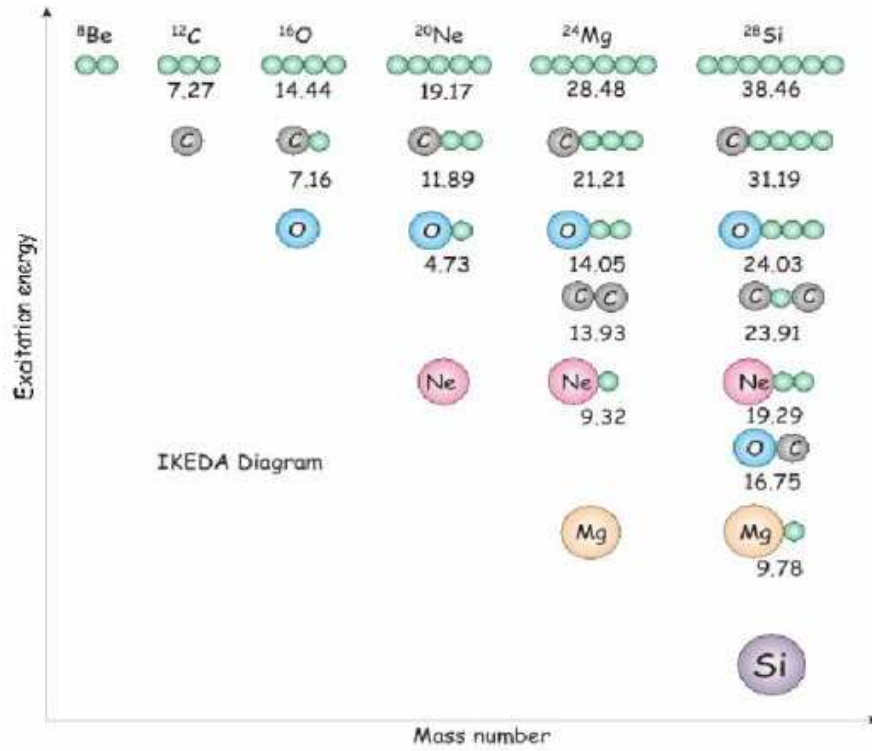


FIG. 1.1: The Ikeda diagram, which indicates the threshold energies in MeV of the different α -decay modes in the six lightest self-conjugate α -nuclei. According to Ikeda's theory, a corresponding α -cluster state may be expected above each threshold. This figure was taken from Ref. [18].

etc. [25, 26, 27, 28, 29, 30, 31]. The idea of α condensation in light α nuclei is analogous to Bose-Einstein condensation from atomic physics, which has been observed through the magneto-optical trapping of Rb and Na atoms. It is a topic of much controversy in nuclear physics, and it will require further theoretical investigation as well as experimental evidence [32, 33].

No threshold energy is indicated for ^8Be in Fig. 1.1, since it already α decays in its ground state. The ^{12}C nucleus has its 3α threshold at $E_x = 7.27$ MeV, which is 0.38 MeV below the Hoyle state. A candidate for the 4α cluster with the anticipated 0^+ spin-parity has also been identified at $E_x = 15.10$ MeV in ^{16}O [34], 0.66 MeV above the 4α threshold. Such a state, like the 5α cluster state in ^{20}Ne , would be analogous to the Hoyle state in ^{12}C .

It is known that the ^{12}C that is formed in the three- α process, which is allowed by the Hoyle state, may continue the element synthesis during stellar helium-burning by forming

1. Introduction

^{16}O through the α capture reaction $^{12}\text{C}(\alpha,\gamma)^{16}\text{O}$. This reaction proceeds mainly through the bound 7.116 MeV state in ^{16}O , which is not a Hoyle-analogue state. Likewise, the ^{20}Ne nucleus may be formed by the $^{16}\text{O}(\alpha,\gamma)^{20}\text{Ne}$ α -capture reaction through states with an $\alpha + ^{16}\text{O}$ cluster structure [35]. Nevertheless, Hoyle-analogue states would provide additional gateways for the stellar nucleosynthesis of ^{16}O and ^{20}Ne through 4- or 5- α capture reactions. The ^{20}Ne nucleus plays a pivotal role in the production of the α -nuclei ^{24}Mg , ^{28}Si , ^{32}S , ^{36}Ar and ^{40}Ca through the α process, for instance [35]. Elucidating its nucleosynthesis is key to our understanding of nuclear abundances.

Since it is one of the most abundant nuclei in the universe, it is not surprising that ^{20}Ne has been studied extensively with shell models [36], Hartree Fock calculations [37], and cluster models [38]. Alpha cluster models in particular have had much success in describing this nucleus [39]. Prominent α clustering bands in ^{20}Ne include the $K^\pi = 0^-$ and $K^\pi = 0_4^+$ rotational bands which have experimentally verified $\alpha + ^{16}\text{O}$ cluster structures [40, 41].

The $K^\pi = 0^+$ ground state band and the $K^\pi = 0^-$ band with its band head at $E_x = 5.79$ MeV were once proposed to be inversion doublet bands with a parity violating $\alpha + ^{16}\text{O}$ cluster structure [42]. It was soon discovered, however, that the $K^\pi = 0^+$ band does not have as good a cluster structure as the $K^\pi = 0^-$ band. It is also not well described as having a mean-field-like structure. Today it is described as having a ‘transitional character between mean-field like structure and cluster structure’ [38]. The $\alpha + ^{16}\text{O}$ cluster model space is not large enough to reproduce the $K^\pi = 0_2^+$, $K^\pi = 0_3^+$ and $K^\pi = 2^-$ bands. To reproduce these bands, Fujiwara *et al.* used a model which includes $^8\text{Be} + ^{12}\text{C}$ cluster states coupled to $\alpha + ^{16}\text{O}$ cluster states [43].

Experimentally, ^{20}Ne has been thoroughly investigated with a range of reactions and to date 233 states in ^{20}Ne are known at excitation energies between the ground state and $E_x = 28.2$ MeV [3]. Yet there remains a gap in our knowledge in the excitation energy region beyond the 2^+ state at $E_x = 18.43$ MeV. Above this energy there are 49 known states which mostly have relatively broad widths (generally between 100 keV and 500 keV, but sometimes even wider).

The existence of narrow states in this region might signify the existence of isobaric analogue states (IAS) of known states in ^{20}Ne isobars [44]. The highest known isospin $T = 2$ state in ^{20}Ne is the 18.43 MeV 2^+ state, which is related to the 1.673 MeV 2^+ state in ^{20}O [45]. Its γ -decay is known to proceed through the second 2^+ , $T = 1$ state at

1. Introduction

$E_x = 12.221$ MeV [46]. The ground state of ^{20}O also has a ^{20}Ne analogue, in the form of the strong 16.73 MeV 0^+ state [45]. These two lowest $T = 2$ states of ^{20}Ne were both measured with the (p,t) reaction on ^{22}Ne . This is a reaction of the form

$$[(Z, N + 2)T = 1, T_z = 1] + p \longrightarrow [(Z, N)T = 2, T_z = 0] + t, \quad (1.1)$$

which has been proven to be effective at populating $T = 2$ states in $T_z = 0$ residual nuclei such as ^{20}Ne [45, 47]. Coulomb shift calculations predict isospin $T = 2$ states with the following energies and spin-parities: 20.17 MeV 4^+ , 20.522 MeV 2^+ and 20.845 MeV 0^+ . These states would respectively be related to the following known states in ^{20}O : 3.570 MeV 4^+ , 4.072 MeV 2^+ and 4.456 MeV 0^+ [48].

The discovery of the 0^+ $5-\alpha$ cluster state in ^{20}Ne would be an even more exciting find than the discovery of heretofore unknown IAS states. This requires an effective reaction for measuring 0^+ states.

1.2 On experimental methods

The present experiment was performed mainly to search for the 0^+ $5-\alpha$ cluster state, which is expected above the $5-\alpha$ break-up threshold at $E_x = 19.17$ MeV, and to pinpoint its position by performing high-resolution measurements of the (p,t) 2 neutron pick-up reaction on ^{22}Ne utilising the *K600* magnetic spectrometer at small angles, which include zero degrees as well as larger angles. The experiment was also performed to map out other low-spin states in the same energy region.

Around the region of the $5-\alpha$ break-up threshold in ^{20}Ne , only high spin $J^\pi \geq 4^+$ states are known, most probably because of the types of reactions used to populate these states. These broad, high spin states are very dense in the energy region $E_x = 17$ to $E_x = 25$ MeV [3]. Hence, one might expect a fair amount of overlapping between the higher spin states and the 0^+ $5-\alpha$ state of interest. The high density of states in this energy region, which is partly displayed in Table 1.1, is the chief obstacle to measuring the $5-\alpha$ cluster state. This problem should be mitigated by the high selectivity of the (p,t) reaction to 0^+ states at forward angles.

The initial plan was to investigate this energy region with the $^{20}\text{Ne}(\alpha,\alpha')^{20}\text{Ne}$ reaction since this reaction would provide the optimal cross section values to populate the 0^+ α

1. Introduction

cluster state of interest. This plan was abandoned, however, after energy loss calculations indicated that the resolution might be insufficient with an α beam using the gas target cell described in Section 3.5.

The (p,t) reaction around 0° and at finite angles can also provide a selective probe to search for the 0^+ states in ^{20}Ne . Various publications from recent years claim to have measured a number of new 0^+ and 2^+ (i.e. low-spin) states in nuclei by means of the (p,t) reaction at various angles from $\theta_{cm} = 0^\circ$ to $\theta_{cm} = 50^\circ$ [49, 50, 51, 52, 53]. At forward angles, the $L = 0$ transitions which populate 0^+ states are enhanced most, relative to the interfering higher spin states. This may not be the most selective reaction for populating α cluster states, but it is suitable for mapping out the low-spin states in the energy region above the $5\text{-}\alpha$ break-up threshold in ^{20}Ne .

The (p,t) reaction is also a selective probe to investigate $T = T_z + 2$ states [54]. Consider the following reaction in terms of conservation of isospin: $A(N,Z)[a,b]B(N',Z')$, where A represents the target nucleus, B is the residual nucleus, a is the incident particle and b is the ejectile particle. States will be populated in nucleus B with the following isospins:

$$\vec{T}^B = \vec{T}^A + \vec{T}^a + \vec{T}^b. \quad (1.2)$$

For a (p,t) reaction with $T^A \geq 1$, levels in nucleus B with $T^B = T^A + 1$, T^A , and $T^A - 1$ may be populated [54]. It follows that $T = 2$, $T = 1$ and $T = 0$ states may be populated in the residual nucleus when the (p,t) reaction is performed on a $T = 1$ target nucleus such as ^{22}Ne . The $T = 2$ states in $T_z = 0$ nuclei such as ^{20}Ne are normally located at energies where the level densities are highly dense, therefore a selective reaction is required to enhance $T = 2$ states with respect to nearby $T = 1$ and $T = 0$ states. Shell model calculations and experimental evidence indicate that this is the case with the (p,t) reaction on $T_z = 1$ target nuclei [54].

As mentioned before, the two lowest $T = 2$ states in ^{20}Ne were reportedly measured with the $^{22}\text{Ne}(p,t)^{20}\text{Ne}$ reaction in Ref. [45]. These data were recorded with a beam energy of $E_p = 43.7$ MeV and at an angle of $\theta_{lab} = 25^\circ$ for the ejectile tritons. A resolution of 150 keV FWHM (full-width-at-half-maximum) was obtained. This was improved by a factor of close to 3 in the present measurement by using a thin gas target and the high-resolution drift-chamber detectors of the $K600$ magnetic spectrometer. Also, the ^{22}Ne gas

in Ref. [45] was merely 91.3% pure, which is much less than what was made available for this measurement.

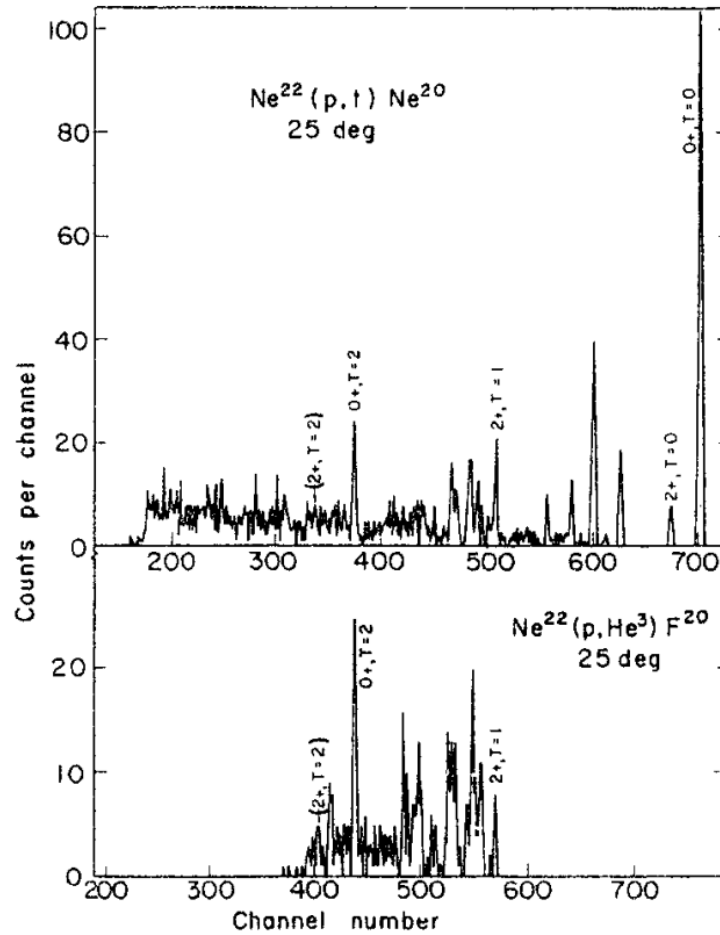


FIG. 1.2: The triton energy spectrum from the $^{22}\text{Ne}(p,t)^{20}\text{Ne}$ measurement is shown at the top, and the ^3He energy spectrum from the $^{22}\text{Ne}(p,^3\text{He})^{20}\text{F}$ measurement at the bottom. Both were measured at an angle of $\theta_{lab} = 25^\circ$ with $E_p = 43.7$ MeV [45].

The $L = 0$ transition to the first 0^+ , $T = 2$ state in ^{20}Ne , as observed in Ref. [45], was strongly populated with a width defined by the experimental resolution, as shown in Fig. 1.2. The $L = 2$ transition to the first 2^+ , $T = 2$ state is also observed, though it is not as prominent. Fig. 1.2 also shows $^{22}\text{Ne}(p,^3\text{He})^{20}\text{F}$ data from the same experiment where all the $T = 1$ and $T = 2$ states in ^{20}F are populated. These states are aligned with their analogues in ^{20}Ne in the figure.

E_x [MeV]	Reaction	J^π	Γ [keV]
19.051	A	5^-	90
19.150	A	6^+	200
19.284	A	6^+	140
19.298	A	7^-	430
19.443	A	6^+	130
19.536	A	6^+	250
19.655	A	6^+	140
19.731	A	8^+	330
19.845	A	6^+	360
19.859	A	5^-	170
19.884	AB	7^-	120
19.991	A	4^+	130
20.027	A	6^+	80
20.106	A	7^-	190
20.150			?
20.168	A	6^+	290
20.296	A	7^-	255
20.341	A	5^-	190
20.344	A	7^-	135
20.419	A	6^+	215
20.445	A	6^+	370
20.468	A	5^-	280
20.686	CAD	9^-	78
20.760	AB	7^-	240
20.800	A	5^-	170
20.950	CA	7^-	300
21.062	CADE	9^-	60
21.300	AB	7^-	300
21.800	CAB	7^-	300
22.300	CAB	7^-	500

TABLE 1.1: Known states in the region of the 0^+ state of interest. A denotes the reactions $^{16}\text{O}(\alpha, \alpha')$ and $^{16}\text{O}(\alpha, 2\alpha')$, B denotes $^{16}\text{O}({}^6\text{Li}, d)$, C denotes $^{12}\text{C}({}^{12}\text{C}, \alpha)$, D denotes $^{16}\text{O}({}^7\text{Li}, t)$, and E denotes $^{16}\text{O}({}^{12}\text{C}, {}^8\text{Be})$ [3].

Fig. 1.3 represents the masses of the analogue states in the neutron-rich isobaric neighbouring nuclei of ^{20}Ne which are reported in Ref. [45]. Prior to the present measurement, only two $T = 2$ states in ^{20}Ne were known, although several more $T = 1$ states were identified since Ref. [45]. These two states, and possibly also other $T = 2$ states at higher excitation energies ($E_x \geq 20$ MeV), should be strongly populated by the present measurement.

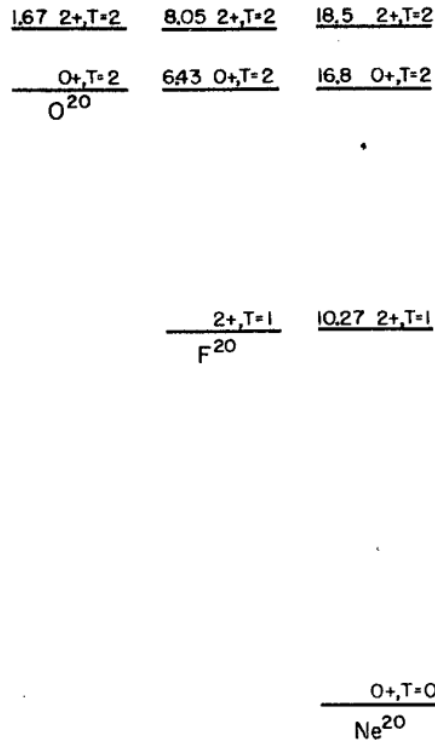


FIG. 1.3: A schematic representation of the masses of the $T = 1$ and $T = 2$ analogue states of ^{20}Ne in the isobaric neighbouring nuclei ^{20}F and ^{20}O , shown relative to the position of the ground state of ^{20}Ne , from Ref. [45].

Measurements for the present study were also performed at a set of larger angles $\theta_{lab} = (7^\circ, 16^\circ, 27^\circ)$ in order to characterise the spins and parities of the states populated. These angles were chosen after distorted-wave Born-approximation (DWBA) calculations were performed with the DWUCK4 code, which is described in Chapter 2.

Fig. 1.4 shows cross section data from a (p,t) experiment which was recently conducted at the Research Centre for Nuclear Physics (RCNP) with a ^{24}Mg target [53]. The 0^+ states are clearly enhanced at angles near to 0° for the $^{24}\text{Mg}(p,t)^{22}\text{Mg}$ reaction which was investigated, and they drop off very quickly as the angle increases. A similar effect is observed in other cases with the (p,t) reaction on nuclei with similar or much heavier masses [49, 50, 52, 53].

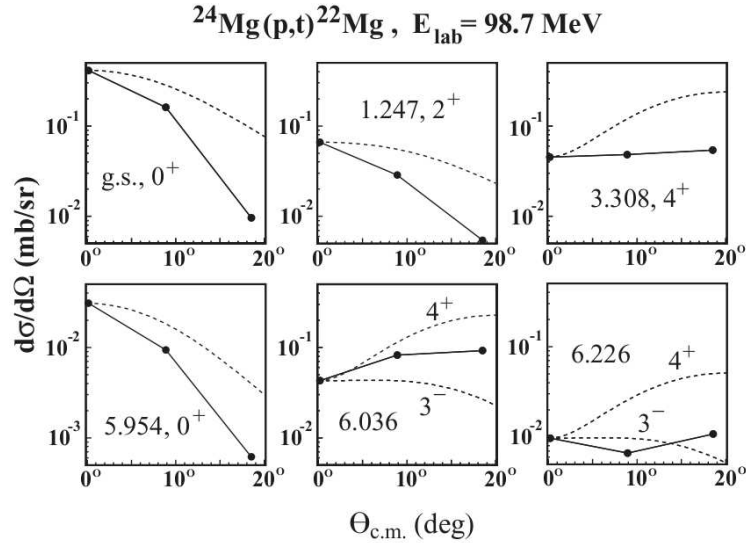


FIG. 1.4: Measured angular distribution plots from RCNP for six different states measured with the $^{24}\text{Mg}(p,t)^{22}\text{Mg}$ reaction. Note how the 0^+ and 2^+ states in ^{22}Mg are enhanced close to $\theta_{cm} = 0^\circ$, and drop off as the angle increases. The dotted curves were generated by DWBA calculations. This figure is from Ref. [53].

A ^{22}Ne gas target, which is described in detail in Section 3.5, was used for this experiment. For measurements at larger angles, the length of the gas target could adversely affect the resolution. Calculations shown in Section 3.5.1 indicated that this would not be a problem for the envisaged angles and reaction. Nevertheless, a cryogenic gas target system, which is described in Section 3.6, was developed as a back-up, in case there were problems during the measurement.

To determine the optimal beam energy, a calculation based on the following equation for determining the most favoured orbital angular momentum L of a (p,t) reaction was

1. Introduction

performed [55]:

$$L = \sqrt{\frac{2 \cdot m_p}{\hbar^2}} \cdot R \cdot [\sqrt{3 \cdot (E_p - E_C + Q)} - \sqrt{E_p - E_C}]. \quad (1.3)$$

In Eq. 1.3, the variables m_p , E_p , E_C , Q and R represent proton mass, beam particle kinetic energy, Coulomb energy, reaction Q -value and interaction radius respectively. It was found that the optimum energy is $E_p = 34.9$ MeV for a state located at $E_x = 20$ MeV, which is roughly in the middle of the region of interest. For the $^{22}\text{Ne}(p,t)^{20}\text{Ne}$ reaction, which has a Q -value of $Q = -8.6$ MeV [56], this would imply an ejectile energy of $E_t = 6.3$ MeV. This is far too low for a particle to reach the plastic scintillation detectors. Therefore, the beam energy of $E_p = 60$ MeV was eventually selected as a compromise to allow particles to reach the first plastic scintillation detector with sufficient energy to form the event trigger signal (see Section 3.2.2). Table 1.2 shows the beam energies which were recorded during the measurement.

Weekend #	Beam energy [MeV]
1	60.0
2	60.5
3	60.32
4	60.01

TABLE 1.2: The beam energies which were recorded for each weekend

CHAPTER 2

Theoretical formalisms

Direct transfer reactions may be loosely described as the class of nuclear transfer reactions where the wave functions of the initial and the final states have a good overlap, and where little rearrangement of the target nucleus occurs. Typically, a direct reaction may affect only one or two nucleons in the target nucleus, thus making it sensitive to single- or two-particle excitations in the nucleus. Unlike compound nuclear reactions, such reactions do not involve an intermediate phase where a compound nucleus is formed, hence the timescale of such a reaction is typically comparable to the time required for the incident particle to transit the nucleus. In a direct reaction, the nature of the excitation of the residual nucleus depends on how it was formed, whereas in a compound reaction all the information about the initial wave function is lost in the intermediate phase, apart from the total angular momentum and parity. This makes direct reactions a very powerful spectroscopic tool. Direct reaction theory is useful in testing shell-model predictions since it provides information about few-nucleon excitations, or transfers, across or from shell-model nuclear orbitals [57].

The distorted-wave Born-approximation (DWBA) theory may be used to predict the strength with which a specific state will be populated by a one- or two-step direct nuclear reaction, for a particular angle and beam particle energy. DWUCK4 [58], which is a code for DWBA calculations, was employed prior to the experiment to select the experimental angles. The coupled reaction channels (CRC) method may be used to describe multi-step direct reactions. FRESCO [59], which is a CRC code, may be used together with NuShellX [60], which is a shell-model based code, to calculate the strengths with which possible new states with specific characteristics (isospins, spins, parities etc.) should be populated at certain beam particle energies and detection angles. These codes were used to understand newly observed states after the experiment. The isobaric multiplet mass equation (IMME) may be used to calculate the energy of any member of an isobaric multiplet of isobaric analogue states (IAS states) [61]. This equation was employed after the experiment to determine whether some of the newly observed states may be members of such an isobaric multiplet. The purpose of this chapter is to describe the theoretical formalisms behind

these techniques.

2.1 DWBA calculation

DWBA theory treats the projectile and ejectile ions in a transfer reaction as moving under the influence of long-range Coulomb and short-range nuclear forces. It assumes elastic scattering to be the predominant component of a transfer reaction, and treats the inelastic component as a perturbation. The elastic scattering is described by the phenomenological optical model potential U . DWBA has traditionally been used to describe one-step reaction processes between one nucleus and another [62]. Calculations with the DWUCK4 code for DWBA are performed using a zero-range interaction, which is an approximation, especially for particle transfer reactions such as the (p,t) reaction [58]. In DWBA, the cross section of any reaction with the form $A(a,b)B$ may be written as

$$\frac{d\sigma}{d\Omega} = \frac{\mu}{2\pi\hbar^2} \frac{v_b}{v_a} \frac{1}{(2J_A + 1)(2s_a - 1)} \sum_{M_A M_B m_a m_b} |T^{M_A M_B m_a m_b}|^2, \quad (2.1)$$

where μ is the reduced mass of the whole system, v_a and v_b are the projectile and ejectile speeds, J_A is the orbital angular momentum of the target nucleus, s_a is the spin of the projectile, and M_A , M_B , m_a and m_b are the masses of the target nucleus, residual nucleus, projectile and ejectile respectively. The DWUCK4 code computes a transition amplitude T for a reaction of the form $A(a,b)B$ with the formula:

$$T = \vartheta \int d^3r_b \int d^3r_a \chi^-(\vec{k}_f, \vec{r}_b)^* \langle bB | U | aA \rangle \chi^+(\vec{k}_i, \vec{r}_a), \quad (2.2)$$

where χ^- and χ^+ represent the distorted waves, and \vec{r}_a and \vec{r}_b are the relative coordinates for the respective systems (a,A) and (b,B) . The variables \vec{k}_i and \vec{k}_f represent the momenta of the incoming and outgoing spherical plane waves. The variable ϑ is the Jacobian for the transformation of coordinates from the lab to the centre-of-mass frame for the (a,A) and (b,B) systems, while $\langle bB | U | aA \rangle$ is the form factor for the reaction and must contain a δ function between the coordinates \vec{r}_a and \vec{r}_b [58], in order to satisfy the zero-range approximation. The optical model potential represents scattering in terms of a complex potential $U(r)$ [63]:

$$U(r) = V(r) + iW(r). \quad (2.3)$$

The real part of the potential $V(r)$ is related to elastic scattering, while the imaginary part $W(r)$ accounts for absorption, and r represents the radius. The optical model potential which was used for the present case is a combination of a Woods-Saxon volume and surface derivative, with the real part [64]:

$$V(r) = V_c(r) + V_s(r) + V_{rC}(r) + V_{RC}(r) , \quad (2.4)$$

where

- $V_c = -V_R f(r, R_R, a_R)$ is the central real part with radius R_R and diffuseness a_R ,
- $V_s = V_{so} \sigma \cdot l \bar{\lambda}_\pi^2 (1/r) (d/dr) [f(r, R_{so}, a_{so})]$ accounts for the spin-orbit contribution,
- $V_{rC} = (Zze^2/2R_c) [3 - (r^2)/R_c^2]$ is the Coulomb contribution at $r \leq R_C$ (R_C is the Coulomb radius), and
- $V_{RC} = Zze^2/r$ is the Coulomb contribution at $r \geq R_C$.

The imaginary part of the potential may be written as:

$$W(r) = W_V(r) + W_S(r) , \quad (2.5)$$

where

- $W_V = -W_v f(r, R'_W, a'_W)$ is from the imaginary volume, and
- $W_S = W_{SF} 4a_W (d/dr) [f(r, R_W, a_W)]$ is the imaginary surface term.

The function $f(r, R, a)$ in $V(r)$ and $W(r)$ has the Woods-Saxon form:

$$f(r, R, a) = [1 + e^{(r-A/a)}]^{-1} . \quad (2.6)$$

The remaining variables mentioned above are defined as follows:

- $\sigma \cdot l$ is the scalar product of the intrinsic and orbital angular momentum operators.
- j and l are the total and orbital angular momentum quantum numbers of the projectile.

- $\bar{\lambda}_\pi$ is the pion Compton wavelength.
- Z and z are the charges of the target and projectile respectively.

All radii in these equations were calculated with $R = rA^{1/3}$. The accuracy of the present DWBA calculations depend on the values chosen for the optical model parameters V_R , r_R , a_R , W_V , W_{SF} , r_W , a_W and r_c .

Calculations were performed with this code for the first three states from the $^{22}\text{Ne}(p,t)^{20}\text{Ne}$ reaction, with a proton beam energy of $E_p = 60$ MeV. These calculations used the zero-range force constant from Ref. [65] ($D_0^2 = 26.2 \times 10^4$ MeV²fm³) to generate the absolute cross section values which are shown in the angular distribution plot in Fig. 2.1. The results indicate an absolute maximum for 0^+ states at $\theta_{cm} = 0^\circ$, a minimum at $\theta_{cm} = 20^\circ$, and a second maximum at $\theta_{cm} = 29^\circ$. This is in good agreement with the measurement, coupled-channels Born approximation (CCBA) and DWBA calculations for $^{22}\text{Ne}(p,t)^{20}\text{Ne}$ at a proton beam energy of $E_p = 40$ MeV from Ref. [66] shown in Fig. 2.2. The angles which were chosen for the current experiment are indicated on Fig. 2.1. The centre-of-mass angle of $\theta_{cm} = 17.5^\circ$ was selected since the spectrometer scattering chamber experienced vacuum problems related to its sliding seal at $\theta_{cm} = 20^\circ$.

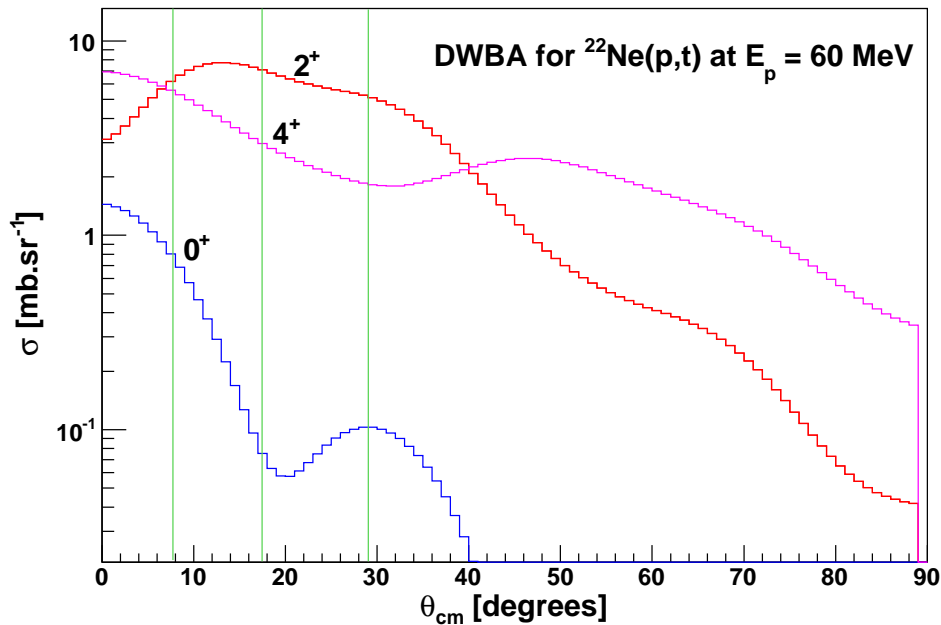


FIG. 2.1: Angular distribution predictions for states from the $^{22}\text{Ne}(p,t)^{20}\text{Ne}$ reaction with $E_p = 60$ MeV from DWUCK4 calculation. The green lines indicate the centre-of-mass angles which were selected for the experiment.

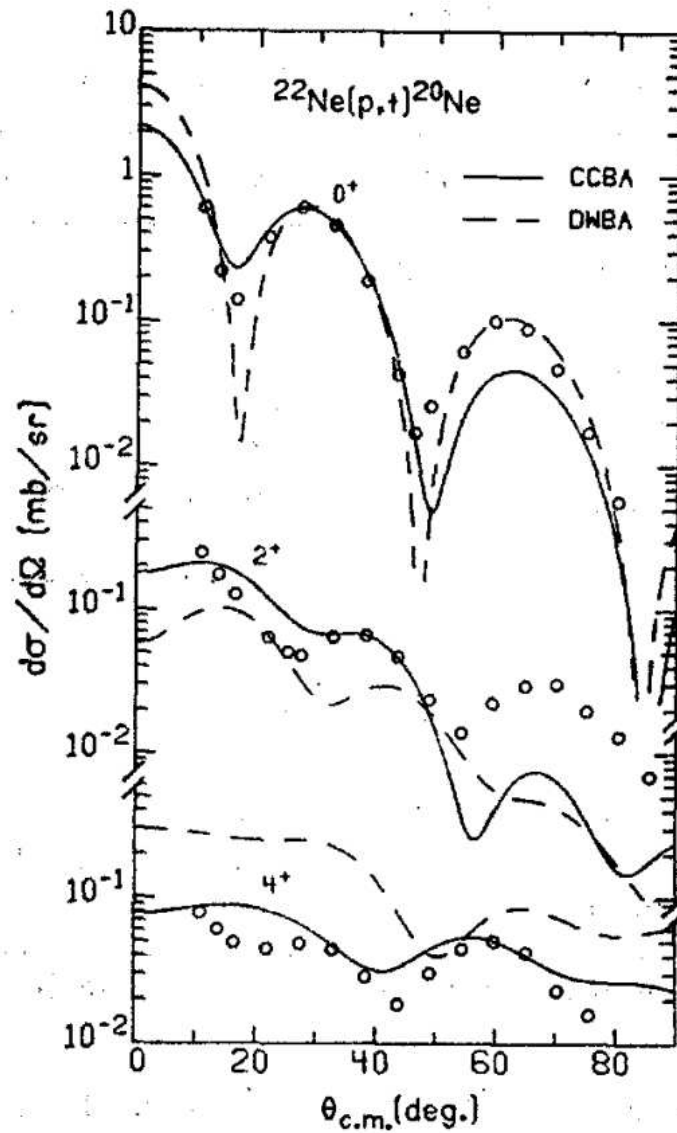


FIG. 2.2: Data measured at $E_p = 40$ MeV (round circles) from Ref. [65] are compared to CCBA (solid lines) and DWBA (dashed lines) calculations for the 0^+ , 2^+ and 4^+ ground band states of ^{20}Ne [66].

A list of the optical model parameters which were used are shown here in Table 2.1. The centre-of-mass angles chosen for the non-zero angle measurements translate into the laboratory angles for the $^{22}\text{Ne}(p,t)^{20}\text{Ne}$ reaction that are indicated in Table 2.2.

Channel	V_R [MeV]	r_R [fm]	a_R [fm]	W_V [MeV]	W_{SF} [MeV]	r_W [fm]	a_W [fm]	r_c [fm]
$p+^{22}\text{Ne}$	52.2	1.11	0.57	6.2	1.11	1.11	0.50	1.11
$t+^{20}\text{Ne}$	160.4	1.20	0.72	25.0	1.40	1.40	0.84	1.30

TABLE 2.1: The optical model parameters for the DWUCK4 calculation. These values were taken from the calculations in Ref. [65].

θ_{cm} [degrees]	θ_{lab} [degrees]
7.7	7.0
17.5	16.0
29.0	27.0

TABLE 2.2: The centre-of-mass angles corresponding to the non-zero laboratory angles which were investigated

2.2 Coupled reaction channels

DWBA theory is most successful in describing reactions where the interactions between particles are comparatively weak i.e. for low beam energies or light ions. For reactions which involve a larger inelastic component, related to phenomena such as nucleon transfer, nuclear deformations and single particle excitations [62, 67], DWBA becomes inadequate. In such cases it is reasonable to use coupled-channels (CC) calculations. In these calculations, a finite number of reaction channels are considered, and the interactions are described to any or all orders for these channels [67]. The effects of couplings to channels outside of this chosen finite number are described by a complex optical potential. With CC calculations, the effects of multi-step processes may be described, where with DWBA this is possible only for one- or two-step processes. When rearrangement processes are considered, this method becomes known as the coupled reaction channels (CRC) method [57].

With the CRC method, a two-step process such as $(p,d;d,t)$ may contribute to the (p,t) transfer reaction [57]. The FRESKO code for CRC calculations can simulate finite-range

transfer interactions for a number of mass partitions and any number of nuclear excitations in each partition [59]. A mass partition in this context may refer to the two nuclei $a + A$ before, or to $b + B$ after, a transfer reaction of the form $A(a,b)B$ [57]. FRESKO is based on the CRC model for direct reactions, in which a model is constructed for the system wave function, and Schrödinger's equation is then solved as accurately as possible within this model space. The model used for FRESKO projects the complete wave function $\bar{\Psi}$ onto a state which is a product $\phi_i = \phi_{ip} \times \phi_{it}$ of projectile and target states with a wave function $\psi_i(R_i)$ which describes their relative motion [62]:

$$P\bar{\Psi} = \Psi = \sum_i^N \phi_i \psi_i(R_i). \quad (2.7)$$

The symbol P represents the projection operator in Eq. 2.7. The basis states may be either bound states of their respective nuclei, or discrete representations of continuum levels. The states ϕ_i may be in different mass partitions, or they may be excited states of the projectile or target in any one of the mass partitions. By projecting Schrödinger's equation separately on each basis state ϕ_i , one may derive the set of equations:

$$[E_i - H_i]\psi_i(R_i) = \sum_{j \neq i} \langle \phi_i | H - E | \phi_j \rangle \psi_j(R_j), \quad (2.8)$$

where E_i is the asymptotic kinetic energy in the i^{th} channel, and H is the model Hamiltonian for the CRC system. Eq. 2.8 couples together all the unknown wave functions $\Psi_i(R_i)$ [62].

2.3 Shell-model calculations

Nuclear physicists developed the nuclear shell model after witnessing the success of the atomic shell model in describing atomic structure. The discovery of the so-called 'magic number' nuclei, which are nuclei with remarkably high binding energies at certain numbers for Z and N , supported the idea of shell closures in nuclei. The nuclear shell model assumes that the motion of each individual nucleon is determined by a potential which is created by all the other nucleons in a nucleus. This treatment allows individual nucleons to occupy the energy levels of a series of subshells [63].

The time-dependent Schrödinger equation $H\Psi = E\Psi$ cannot be solved exactly for most nuclear systems due to the many-body nature of such calculations. To mitigate

this problem, the Configuration Interaction (CI) Method, which includes the nuclear shell model [68], was developed. In the CI method, the nuclear Hamiltonian is written as:

$$H = T + V = [T + V_{mf}] + [V - V_{mf}] , \quad (2.9)$$

where T is the kinetic energy operator and V is the potential energy operator. The mean field potential V_{mf} is chosen as a single particle interaction (i.e. n -nucleus interaction) such that

$$V_{mf} = \sum_{i=1}^A v(r_i), \quad (2.10)$$

where $v(r_i)$ is the potential related to the i^{th} individual nucleon in the mean field at position r_i in the nucleus. The mean field Hamiltonian $H_0 = T + V_{mf}$ is selected to be a reasonable approximation to the exact solution to the many-body Schrödinger equation, making $H_1 = V - V_{mf}$ relatively small and solvable by perturbation theory. The CI method is used to solve nuclear problems by selecting an inert core of mass A_c occupied by single particle levels in a nucleus of mass A , thus reducing the problem to one with A_{val} valence nucleons, with mass $A_{val} = A - A_c$, which may be configured in any possible way in the valence orbital space. This space is usually chosen according to Harmonic Oscillator (HO) shells, i.e. the $N = 0, 1, 2, 3$ shells corresponding to the s, p, sd and pf model spaces [68]. For the present case, an inert core consisting of doubly magic ^{16}O was chosen, which implies calculations involving 2 valence protons and 2 valence neutrons in the sd model space from $A = 17$ to $A = 40$. To solve the eigenvalue problem, the NuShellX code for nuclear shell-model calculations was employed. The calculations were carried out in the sd model space with the USDB Hamiltonian [69] using the code NuShellX@MSU [70]. These calculations involved two-body matrix elements for the valence protons and neutrons. A total of 63 matrix elements and 3 single-particle energies were used [60, 69].

Only states with positive parity values π could be calculated, since $\pi = (-1)^l$ for states in HO shells ($l = 0$ for s -orbital or $l = 2$ for d -orbitals in sd -shell). Intruder states, resulting from particle-hole p - h excitations across the p - sd shell gap for example, were not calculated since they were not included in the model space. The shell-model diagram in Fig. 2.3 represents the ^{16}O nucleus for either protons or neutrons, with an empty sd -shell. The states in ^{20}Ne generated by NuShellX were used to perform the coupled reaction channels calculations for the $^{22}\text{Ne}(p,t)^{20}\text{Ne}$ reaction with the FRESCO code. All

calculations using FRESKO and NuShellX were performed by Alex Brown [71].

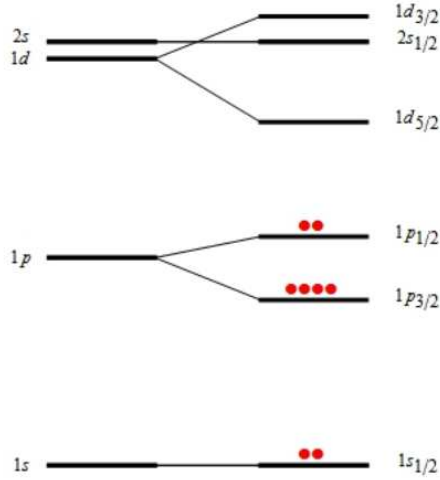


FIG. 2.3: The first three nuclear shells (left) and their nuclear orbitals (right) filled up to $N = Z = 8$, which corresponds to ^{16}O . The red balls may represent either protons or neutrons. This diagram is taken from Ref. [72].

2.4 Isobaric multiplet mass equation

2.4.1 On isospin

The charge-independence of nucleon-nucleon interactions, which is embodied in the concept of isospin, is the reason for remarkable symmetries in nuclei which are most apparent near the $N = Z$ line [73]. The isospin quantum number T , which was first applied to nuclei by Werner Heisenberg in 1932 [74], describes protons and neutrons, which have the same spins ($S = \frac{1}{2}$) and nearly the same masses, as two different states of the same particle. In the isospin approach, all nucleons are assigned the same isospin of $t = \frac{1}{2}$, but different isospin projections of $t_z = +\frac{1}{2}$ and $t_z = -\frac{1}{2}$ for neutrons and protons, respectively. Therefore, the isospin projection T_z of a nucleus with N neutrons and Z protons is calculated with $T_z = (N - Z)/2$. The minimum allowed isospin in a nucleus is $T = |T_z|$.

A nucleus in an isobaric multiplet is characterised by its T_z . In even nuclei (i.e. nuclei with an equal number of protons and neutrons), such as ^{20}Ne , $T_z = 0$ and most states in such a nucleus will have $T = 0$. This means that a nuclear state with an identical configuration of nucleons cannot be constructed in the isobaric neighbour of this nucleus. If it were possible to construct a corresponding state with the same configuration of nucleons

in an isobaric neighbour nucleus with $Z+1$ protons and $N-1$ neutrons, but not in the nucleus with $Z+2$ and $N-2$, then these two states would constitute isobaric analogue states (IAS states) of each other with isospin $T = 1$. A corresponding state, which would be another IAS state of the two aforementioned states, could then also be constructed in the nucleus with $Z-1$ and $N-1$. In the same way $T = 2$ states could be constructed in five isobaric nuclei, $T = 3$ states in seven isobaric nuclei and so forth [73].

The decay of high isospin states is governed by the following isospin selection rules [75]: A transition from an initial state with isospin T_i to a final state with isospin T_f , through an isospin tensor operator of degree l , is allowed if

$$|T_i - l| \leq T_f \leq (T_i + l) . \quad (2.11)$$

For a single-particle process, such as β - or γ -decay, l can only be 0 or 1, thus simplifying the rule to $T_f = T_i, T_i \pm 1$. Therefore, a nuclear state with $T > T_z$ may undergo γ -decay to states with $T = T, T \pm 1$ in the same nucleus, or β -decay to states in neighbouring nuclei with $T = T, T \pm 1$. There are small energy differences between IAS states which may be attributed to a charge-dependence in the forces between nucleons. Charge symmetry of the attractive nucleon-nucleon force V requires that

$$V_{nn} = V_{pp} , \quad (2.12)$$

while charge-independence requires the former condition as well as

$$V_{np} = V_{nn} = V_{pp} \quad (2.13)$$

to be met. These two conditions are generally broken in nuclei, but with only slight deviations in both cases [73]. This is observed by investigating the energy levels of mirror nuclei i.e. pairs of nuclei with identical A -numbers, but with Z -numbers $Z_1 = A + x$ and $Z_2 = A - x$ where x is an integer. The energy levels of such nuclei are nearly identical proving that the nucleon-nucleon force is nearly, but not entirely, charge-independent. The charge-dependence originates not only from the Coulomb interaction between protons, but also from charge-dependent forces of nuclear origin. Today, the latter are understood to result from the mass difference between u and d quarks and the electromagnetic forces

between these fundamental particles [76]. This isospin symmetry breaking is the reason that isospin is considered to be an approximate, but not an exact quantum number [77]. Fig. 2.4 illustrates this phenomenon for the case of $A = 20$ isobars. The pairs of mirror nuclei, (^{20}Mg , ^{20}O) and (^{20}Na , ^{20}F), have almost identical energy levels, but with a small shift in energy which raises the proton-rich nuclei to higher energies.

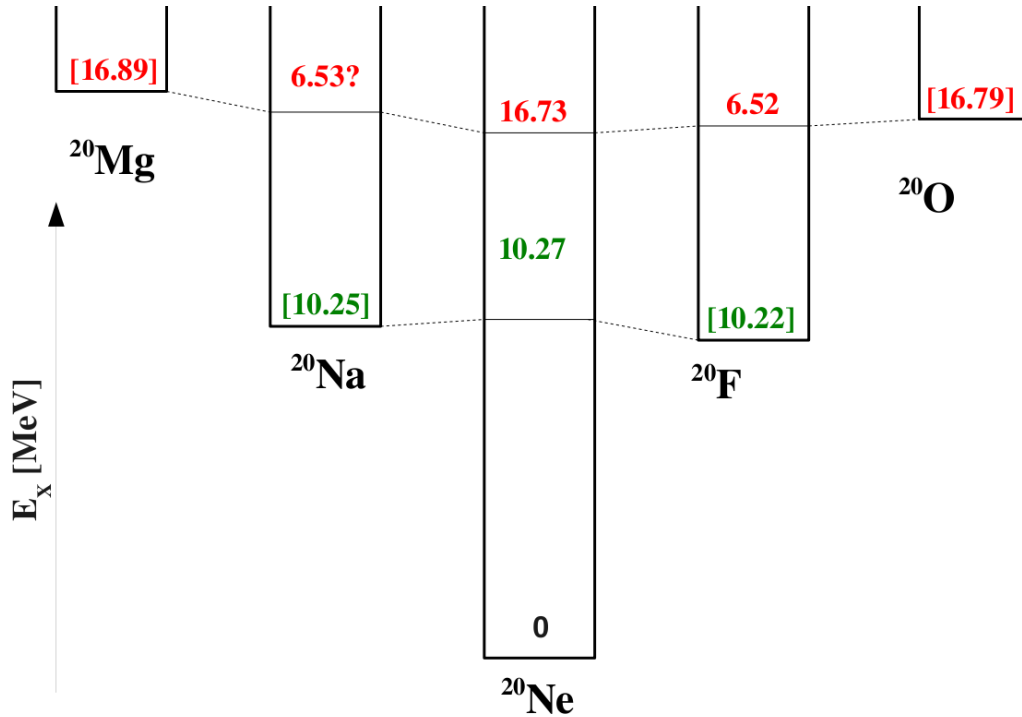


FIG. 2.4: An isobar diagram of $A = 20$ nuclei, showing the nuclear energies of states in the first $T = 1, J^\pi = 2^+$ triplet, in ^{20}Na , ^{20}Ne and ^{20}F , and the first $T = 2, J^\pi = 0^+$ quintet which appears in all five nuclei on the diagram. The ground state energies of the isobars of ^{20}Ne are indicated with respect to the ground state energy of ^{20}Ne , in square brackets [78].

2.4.2 The IMME calculations

2.4.2.1 Basic equations

It has been found that, assuming that the wave functions of the $2T + 1$ members of an isobaric multiplet are considered identical apart from T_z , and that only two-body forces are responsible for the perturbing charge-dependent effects, the masses of the members of such a multiplet may be calculated with the isobaric multiplet mass equation (IMME)

[79]. The IMME

$$M(A, T, T_z) = a(A, T) + b(A, T)T_z + c(A, T)T_z^2 \quad (2.14)$$

may also be used to calculate the mass energy M of any state with isospin T in a nucleus with isospin projection T_z and mass number A [61, 80, 81]. The first term a , the isoscalar term, is related to the strong interaction and is responsible for most of the nuclear binding energy [77]. The coefficient b is related to the Coulomb interaction [77], and in the case of ^{20}Ne it may be calculated as

$$b = \frac{B(^{20}\text{F}) - B(^{20}\text{Ne})}{2}, \quad (2.15)$$

where B denotes the binding energies of these isobaric neighbours of ^{20}Ne . The coefficient c is related to the charge asymmetric parts of the nucleon-nucleon interaction [77], and for this case is

$$c = \frac{B(^{20}\text{F}) + B(^{20}\text{Na})}{2} - B(^{20}\text{Ne}) . \quad (2.16)$$

After these coefficients were determined, the following relationship between the binding energy of a nucleus with two extra neutrons B_{2n} and that of its isobaric partner nucleus with no extra neutrons B_0 was invoked:

$$B_{2n} = B_0 + 2b + 4c . \quad (2.17)$$

For the present case, where states observed in ^{20}Ne are compared to possible analogues in ^{20}O , Eq. 2.17 becomes

$$B_{2n}(^{20}\text{O}) = B_0(^{20}\text{Ne}) + 2b + 4c . \quad (2.18)$$

The IMME methodology described here was employed by Werner Richter [82], using the experimental energy values which were extracted for the new states in Chapter 4.

2.4.2.2 With IMME code

Calculations were also attempted with the code IMME.C [81], which is a mass prediction code written with C++ programming language in ROOT version 5 [83]. This code, which is displayed in Appendix A, uses the formalism of Ref. [84], which is briefly described here.

The Coulomb energy expectation value is:

$$E_c(A, T, T_z) = E_c^{(0)}(A, T) - T_z E_c^{(1)}(A, T) + [3T_z^2 - T(T + 1)]E_c^{(2)}(A, T) , \quad (2.19)$$

where $E_c^{(0)}$, $E_c^{(1)}$ and $E_c^{(2)}$ represent the scalar, vector and tensor Coulomb energies. The mass of any member of an isobaric multiplet may be written as:

$$M(A, T, T_z) = M_0(A, T) + E_c(A, T, T_z) + \Delta_{nh}T_z , \quad (2.20)$$

where M_0 represents the charge-free nuclear mass and $\Delta_{nh} = 782.354$ keV is the neutron-hydrogen mass difference. The Coulomb energy term from Eq. 2.19 is substituted into Eq. 2.20, to obtain the coefficients of the IMME equation:

$$a = M_0 + E_c^{(0)} - T(T + 1)E_c^{(2)} , \quad (2.21)$$

$$b = \Delta_{nh} - E_c^{(1)} , \quad (2.22)$$

$$c = 3E_c^{(2)} . \quad (2.23)$$

If the nucleus is considered as a homogeneously charged sphere with radius $R = r_0A^{1/3}$, one may write [61]:

$$E_c^{(1)} = \frac{3e^2A^{2/3}}{5r_0} , \quad (2.24)$$

$$E_c^{(2)} = \frac{e^2}{5r_0A^{1/3}} , \quad (2.25)$$

for the vector and tensor Coulomb energies. The values of b and c may be calculated by solving Eqs. 2.22 and 2.23. The a coefficient depends upon the scalar Coulomb energy $E_c^{(0)}$, which cannot be separated from the charge-free nuclear mass M_0 .

The IMME.C code proceeds by calculating $E_c^{(0)}$ for members of an isobaric multiplet with Eq. 2.14 (the IMME equation) and Eq. 2.21. The known masses of experimentally observed nuclei are used for M and M_0 where M is the proton-rich nucleus of interest and M_0 is the nucleus such that $M_0 = M(N + 1, Z - 1)$. This calculation is performed successively, from the neutron-rich to the neutron-deficient side of a series of isobars, until the nucleus of interest is reached. The values of $E_c^{(0)}$, obtained from these calculations,

are plotted against Z , and the value of $E_c^{(0)}$ is extrapolated for the nucleus of interest. This way, the Coulomb effect is incorporated by the $E_c^{(0)}$ term in the a -coefficient of the IMME, by the change in mass energy which was induced every time a proton was added and a neutron was removed. After calculating the a -coefficient, the IMME may be solved for the final nucleus of interest [81].

In the calculations for IAS states of ^{20}Ne , this code was employed to find the mass excess of the ^{20}Ne nucleus, by using the masses of all known nuclei with $Z < 10$ and $A = 20$. It was also used to calculate the masses of all $(N - 2, Z + 2)$ nuclei of the near-lying self-conjugate α nuclei ^8Be , ^{12}C and ^{16}O . These calculated values are consistently higher than the known experimental values, as was also observed with the calculations in Ref. [81]. The opposite was observed for odd-odd nuclei, as shown in Fig. 2.5 from Ref. [81], with the calculations consistently predicting lower-than-measured values. It was presumed that this may be attributed to the pairing energy, which lowers the energy of an even-even nucleus, and increases the energy of an odd-odd nucleus.

Hence, it was necessary to obtain an estimate of the pairing energy correction for $A = 20$ nuclei to produce reliable mass predictions in this isobaric region. To do this, a linear fit through the calculated mass excess values (from the IMME.C code) of ^8C , ^{12}O and ^{16}Ne was used to obtain a mass excess value for ^{20}Mg . The difference between this value and the known experimental mass excess of ^{20}Mg was used as an estimate of the pairing energy. The following equation was employed to calculate the energies of IAS states in the final nucleus of interest:

$$E'_x(N, Z) = ME(N + 2, Z - 2) + E_x(N + 2, Z - 2) - ME(N, Z) - \Delta E_{pair}(N - 2, Z + 2) - I(N, Z), \quad (2.26)$$

where $ME(N, Z)$ refers to the known experimental mass excess of the self-conjugate α nucleus of interest, ^{20}Ne in the present case, $\Delta E_{pair}(N - 2, Z + 2)$ refers to the pairing energy as calculated for the nucleus with two more protons in the same isobaric multiplet, which would be ^{20}Mg in the present case, and $I(N, Z)$ is the calculation, with the IMME.C code, of the mass excess of the nucleus of interest. This whole procedure is illustrated in terms of the chart of nuclides in Fig. 2.6. The first three terms of Eq. 2.26 may be reduced to the mass excess of the state chosen in the nucleus with $(N + 2, Z - 2)$, ^{20}O in this case, with respect to the mass excess of the nucleus of interest with (N, Z) . The fourth term

provides an estimate of the pairing energy present in $A = 20$ nuclei, estimated with the IMME.C code for the case of proton-rich nuclei calculated from the known values of their neutron-rich isobars, and the fifth term gives a value of the ground state mass excess of the ^{20}Ne nucleus, calculated with neutron-rich isobars. The results shown in Table 2.3 were obtained by applying this procedure to known $T = 2$ states in light self-conjugate α nuclei. The calculations are mostly within 1 MeV of the known experimental values. The lowest two $T = 2$ states in ^{20}Ne are predicted at about 600 keV below the known experimental values, therefore this method may be trusted to give some indication of where IAS states may be expected in the ^{20}Ne excitation energy spectrum, based on known energy levels in ^{20}O . This method has some level of success specifically for light self-conjugate α nuclei. The discrepancies between predicted and experimental values may possibly be attributed to the uncertainty related to the calculation of the pairing energy.

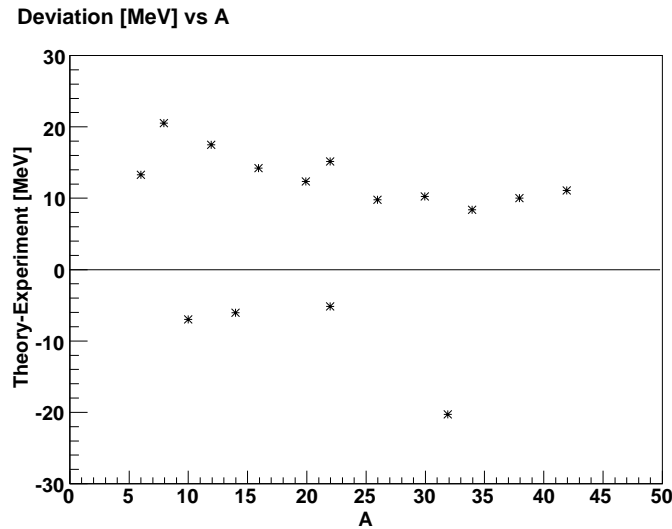


FIG. 2.5: Deviations from experimentally known values for calculations of the mass excesses of even nuclei with the IMME.C code, taken from Ref. [81]. In even-even nuclei, the mass excess is always over-predicted by the code, owing to a higher binding energy which results from the pairing effect. In odd-odd nuclei, the opposite occurs.

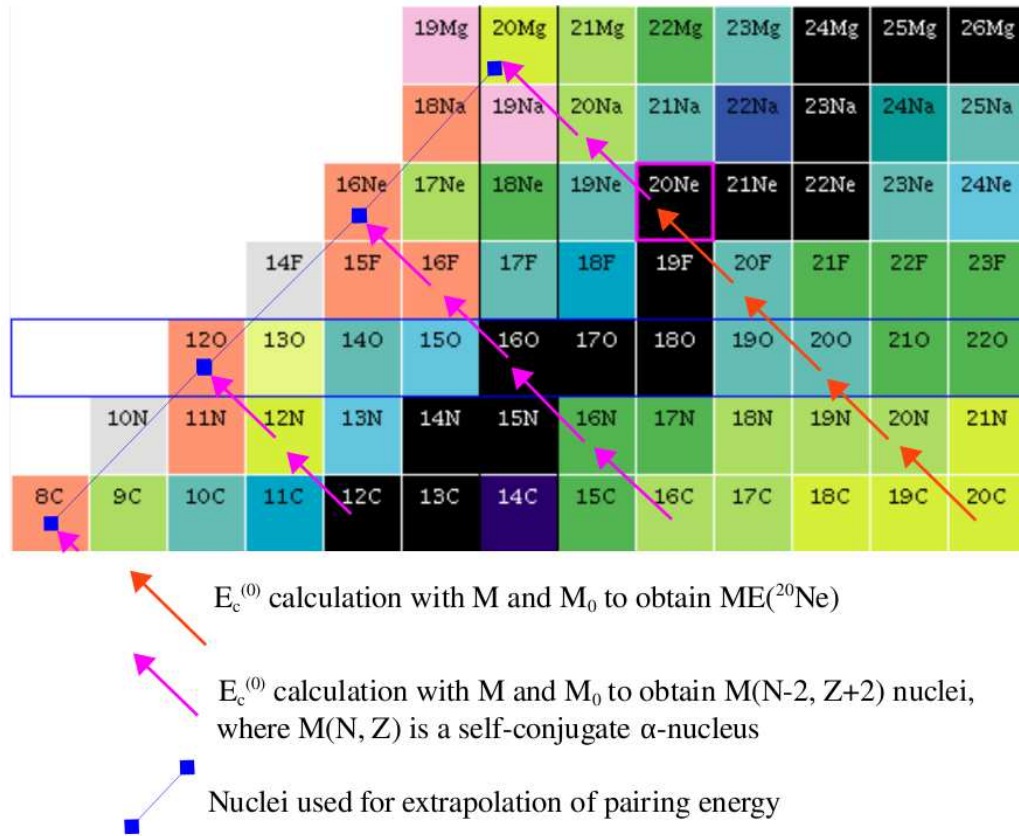


FIG. 2.6: Illustration of the procedure used to calculate IAS states with the IMME.C code, in terms of the chart of nuclides (for the case of ^{20}Ne). The nuclide chart is taken from Ref. [3].

Nucleus	Experimental $E_x(N+2, Z-2)$ [3] [MeV]	Calculated $E_x(N, Z)$ [MeV]	Experimental $E_x(N, Z)$ [3] [MeV]
^{12}C	0	28.54	27.595
^{16}O	0	23.323	22.721
	1.77	25.089	24.522
^{20}Ne	0	16.133	16.73
	1.674	17.807	18.43

TABLE 2.3: Calculated values from IMME.C code for excitation energies of known $T = 2$ IAS states in self-conjugate α -nuclei, compared to known experimental values

CHAPTER 3

Experimental setup and method

For this work, a proton beam with an energy close to $E_p = 60$ MeV (see Table 1.2) was provided for four weekends by the Separated Sector Cyclotron (SSC) facility at iThemba LABS Western Cape [85]. This facility is shown diagrammatically in Fig. 3.1.

Protons were delivered to the SSC from the Solid Pole Injector Cyclotron 1 (SPC1), which has an internal Penning Ion Gauge (PIG) ion source. From here, they were steered through the X, P1, P2 and S lines before being delivered to the K600 magnetic spectrometer vault, which is where the measurement of the (p,t) reaction on a ^{22}Ne gas target took place.

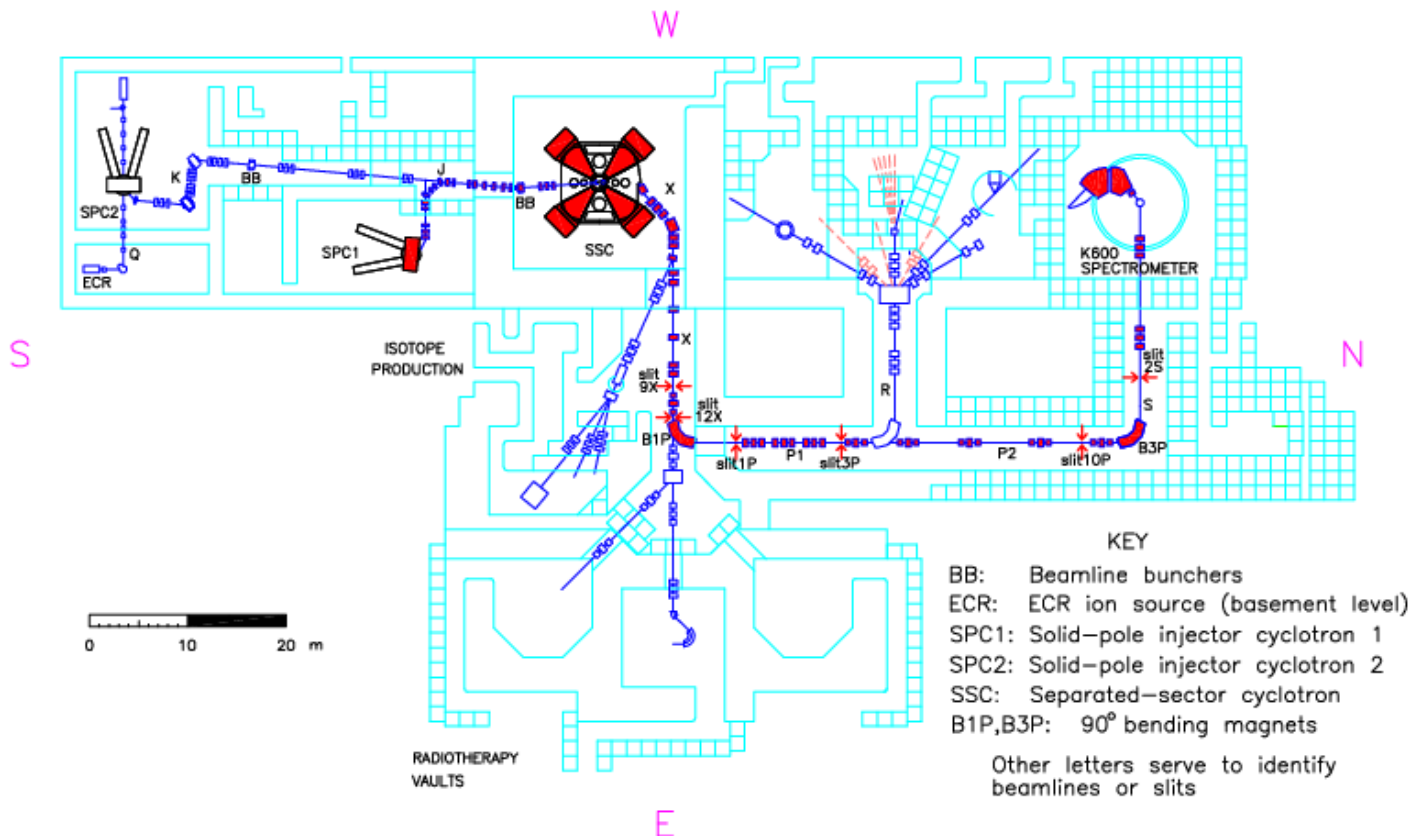


FIG. 3.1: Floor plan of the iThemba LABS cyclotron facility

3.1 The *K600* magnetic spectrometer

The iThemba LABS *K600* magnetic spectrometer [86] is based on the *K600* spectrometer of the Indiana University Cyclotron Facility (IUCF), which was decommissioned in 1999. Today, the IUCF *K600* forms part of the beamline of the Grand Raiden magnetic spectrometer [87] at the Research Centre for Nuclear Physics (RCNP) in Osaka, Japan. The Grand Raiden spectrometer is the only other magnetic spectrometer in the world which can perform high energy resolution measurements ($\text{FWHM} \leq 50 \text{ keV}$) at $\theta_{lab} = 0^\circ$ with medium energy beams in the range of $E_{beam} = 50 - 400 \text{ MeV}$.

The *K600* light ion spectrometer is illustrated in Fig. 3.2. It derives its name from its *K*-value of $K = 600$, which is the maximum magnetic rigidity of charged particles for which it is designed. K is calculated with the equation

$$K = \frac{mE}{q^2}, \quad (3.1)$$

where m is the atomic mass number of the particle, q is its charge state, and E is its kinetic energy in MeV [81]. The spectrometer can therefore measure scattered protons or α particles with energies up to $E_p = 600 \text{ MeV}$, and tritons up to $E_t = 200 \text{ MeV}$.

The spectrometer may be operated in the zero degree mode or at a range of larger angles. It can measure triton spectra from the (p,t) reaction with typical resolutions of 32 keV at $E_p = 100 \text{ MeV}$ and 48 keV at $E_p = 200 \text{ MeV}$ [86]. When its magnetic fields are set to the appropriate values to measure the (p,t) reaction in its focal plane, most contaminant particles (such as protons, deuterons and α -particles) will not have sufficient rigidity to also reach the focal plane. Contaminant particles that do reach the focal plane may be separated from the triton particles using the energy loss and time-of-flight information. (see Section 3.2.2).

Hence, the *K600* spectrometer can measure high resolution (p,t) spectra devoid of major particle background. It was also found that, at $E_p = 60 \text{ MeV}$, its energy resolution would not be excessively hampered by the use of the gas targets described in Sections 3.5 and 3.6. This makes the *K600* an ideal experimental tool for investigating ^{20}Ne with the (p,t) reaction on a ^{22}Ne gas target.

After passing through the last S-line magnets in the *K600* vault, the proton particles reach the scattering chamber, which is located at the turning axis of the spectrometer (see

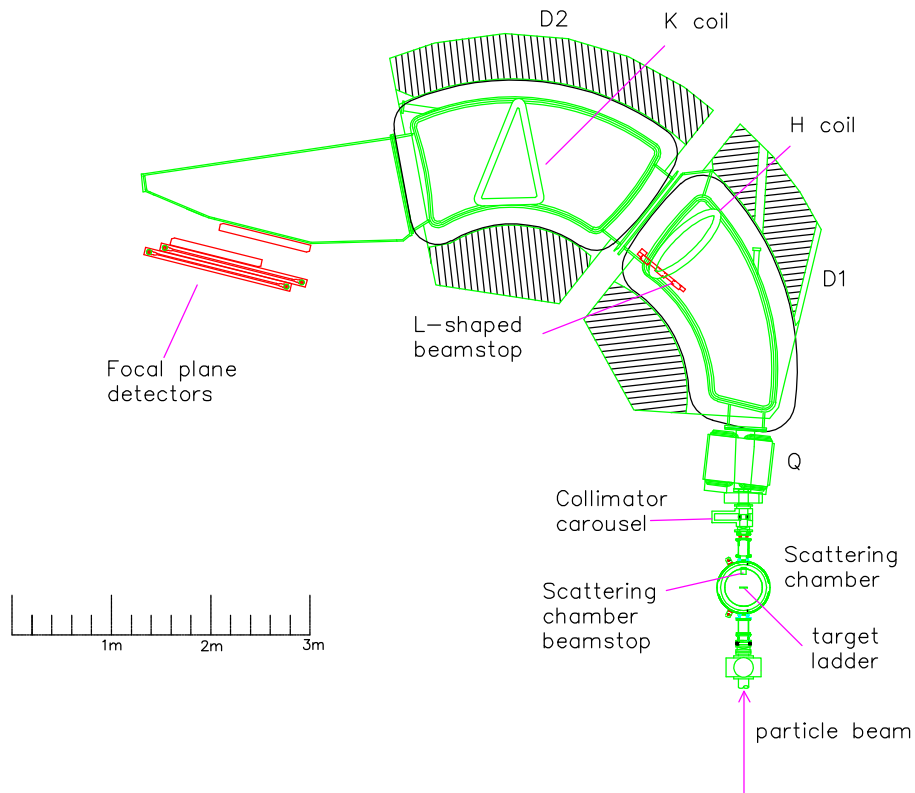


FIG. 3.2: Schematic layout of the *K600* magnetic spectrometer for zero degree and finite angle measurements with detectors in the medium dispersion focal plane

Fig. 3.2). This chamber has a diameter of 524 mm and houses the target ladder. The different ladders that were employed are described in Sections 3.5.5 and 3.6.2.

A round brass collimator with a diameter of 49 mm and a thickness of 51 mm at a distance of 735 mm from the target centre was used during data taking. This implies an angular acceptance of $\Delta\theta_{lab} = \pm 1.91^\circ$ from the central laboratory angle.

The *K600* spectrometer consists of five active elements, namely the two dipoles (D1 and D2), a quadrupole Q in front of D1, and two trim coils (K and H). The K-coil is used to correct for first-order aberrations, while the H-coil is used to correct for the effect of second-order aberrations on the excited state line shapes and to optimise the resolution.

Different beam stops are required for zero degree and finite angle measurements with the *K600* spectrometer. These are described in Section 3.3. This experiment employed the medium dispersion focal plane of the spectrometer, mainly at $\theta_{lab} = 0^\circ$ during Weekends 2 and 3, and at finite angles during Weekends 1 and 4.

3.2 The focal plane detector package

The focal plane detector package for any *K600* experiment consists of vertical drift chambers (VDCs) and plastic scintillation detectors (plastic scintillators/paddles) situated downstream from the VDCs. The paddles provide the event trigger for the VDCs to begin collecting drift time information. The detectors are placed on steel support rails as shown in Fig. 3.3. The present experiment employed two VDCs and one plastic scintillation detector during data taking.



FIG. 3.3: The focal plane detector package: two plastic scintillation detectors, which have photomultiplier tubes at both ends, are positioned to the left on the steel support rails. Two VDCs are positioned to their right on the same rails. The pre-amp cards of the VDCs are connected to the VDC PC board at the top of the two drift chambers. The ribbon cables connect the pre-amp cards to the electronics. High voltage cables are connected to the sides of the VDCs.

3.2.1 The VDCs

A VDC is a type of multi-wire drift chamber (MWDC). It relies on the ionization of gas molecules to cause electron drift towards the signal wires under a uniform electric field, where electron avalanching takes place to induce the electrical signal [88]. It has the capability of measuring the arrival times of the pulses precisely from its wires. Therefore, with the drift velocity of electrons within the chamber known, the path of an incident particle through the chamber may be determined [81, 88]. This is required to have the position sensitivity to achieve the necessary resolution through track reconstruction.

A cross-sectional drawing illustrating the main components of the drift chambers used in this study is shown in Fig. 3.4 [89]. It was filled with a mixture of 90% Ar and 10% CO₂ gas. This gas fills the distance of 8 mm between the wires and the aluminium HV (high voltage) planes to either side of the signal wire plane. The HV planes induce the uniform electric field when high voltage is applied to them. They are stretched equally in all directions to become almost perfectly flat [81]. Two 25- μm -thick mylar planes isolate the interior of the drift chamber from the atmosphere [90].

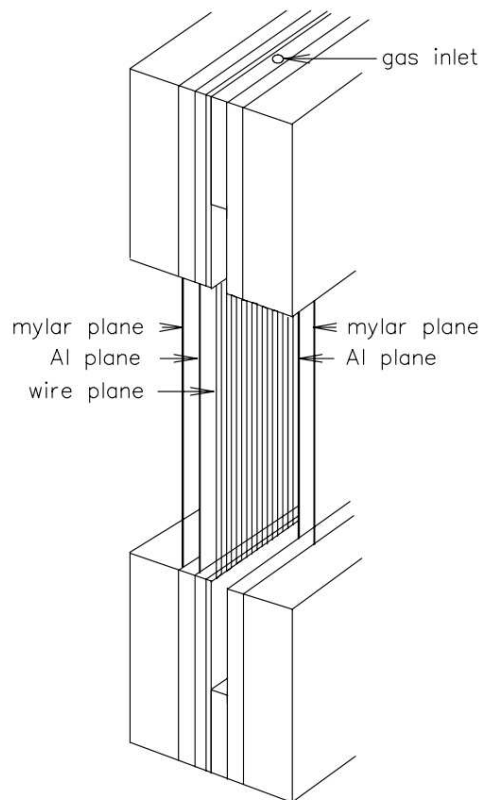


FIG. 3.4: A cross-section through a VDC illustrating the main components

The wire plane consists of 50- μm -diameter gold-plated tungsten guard wires and 20- μm -diameter gold-plated tungsten signal wires interspersed between them [90]. The signal wires record the data, while the guard wires define drift cells to each individual signal wire with a width of 4 mm and a length of 8 mm to the HV planes on both sides of the wire plane.

Two different models of VDC were used during this experiment:

1. An X-only VDC, which consists of 199 guard wires and 198 signal wires, all vertical [90]. This model has 2 HV planes on either side of the wire plane.
2. A newer X-U VDC, which may be rotated to be used as a U-X chamber as well. It contains an X plane with 201 guard wires and 198 signal wires, all vertical, followed by a U plane with 146 guard wires and 143 signal wires slanted at 50° with respect to the horizontal. This chamber provides the additional ability of measuring vertical position information. The X- and U-wire planes are interspersed between 3 HV planes [81].

For the first two weekends of data taking, one X-only VDC was employed, followed by an X-U VDC. After the second weekend, it was found during offline analysis that not much is gained from the vertical position information, in terms of eliminating background data. Hence, for the third and fourth weekends, two X-only VDCs were employed, in order to give triton ejectile particles less material to penetrate en route to the first plastic scintillation detector. The X-wire planes provide horizontal position information almost over the entire length of the 800 mm \times 100 mm medium dispersion focal plane. Incident scattered and reaction particles traverse the wire planes at angles from 28° to 42° , which means crossing 5 or 6 X-wires and 3 or 4 U-wires while in the chamber. With accurate particle track reconstruction, followed by a correct focal plane position-to-energy calibration, the VDC becomes a powerful tool to generate excitation energy spectra in atomic nuclei.

3.2.2 The Scintillation detectors

The plastic scintillators provide the trigger signals for data collection in the focal plane, and also generate particle identification (PID) spectra through the energy loss (ΔE) and time-of-flight (TOF) information it provides. The scintillators are made of BC-408 plastic

scintillator material [91] and they are wrapped in aluminised mylar to make them light-tight. The area dimensions of the paddles are 122 cm \times 10.2 cm on the side facing towards the beam. They are connected by adiabatic light guides to photomultiplier tubes at both ends, from which the signals go to the electronics [90]. The paddles and their photomultiplier tubes are covered by a thin layer of paper to shield the photomultiplier tubes and light guides from light within the vault. This experiment employed one 1/4"-thick paddle P1, followed by a 1/2"-thick paddle P2.

Energy loss calculations were performed, based on the specifications of materials, shown in Table 3.1, that the tritons would traverse. For the case of tritons with an energy of $E_t = 32$ MeV, which is very close to the region of interest, the ejectile particles enter P1 with very little energy (see the first row of Table 3.2). Therefore, the particles are stopped within a short distance and produce a weak signal in the photomultiplier tubes of P1. To strengthen this signal, and to ensure that triton particles with energies down to $E_t = 30$ MeV reach this paddle, the paper layer of P1 was cut open on the upstream side of the detector as in Fig. 3.5. With this layer of paper removed, a triton which started at $E_t = 32$ MeV before exiting the *K600* vacuum could now reach P1 with an energy of $E'_t = 13.7$ MeV, as shown in Table 3.2. Since these particles would not have the energy to pass through P1 and reach P2, the paddles were operated in P1 only logic mode during (p,t) data taking. Certain lights within the vault cannot be switched off during experiments, e.g. the magnet safety lights. To prevent such light from causing unnecessary scintillations within the opened paddle, the interior of the paddle was screened off. Fig. 3.6 shows the paddle in position for the experiment, next to the second VDC.

Magnetic rigidity calculations indicate that, for tritons in the main energy region of interest for this experiment, i.e. from $E_t = 28$ MeV to $E_t = 34$ MeV, deuterons are the only other particle species which will also reach the focal plane in significant numbers. The anticipated energy loss of deuterons in the paddles is shown in the third row of Table 3.2, since this would be one method of separating the tritons from the deuterons.

Early in each weekend, the (p,p') mode was utilised for beam tuning at a field setting suitable for $E_p = 55 - 60$ MeV protons. In this case, it was calculated that the ejectile particles should deposit a large amount of energy in both paddles, as shown in the fourth row of Table 3.2. Therefore, P1 and P2 were used in coincidence during (p,p') beam tuning.

Material	Thickness [mm]	Effective thickness [mm]
Kapton	0.075	0.128
Air	620.0	1054
Mylar	0.050	0.085
Ar-CO ₂ gas	48.0	81.6
Al	0.12	0.20
W	0.10	0.17
Paper	0.40	0.68
Paddle 1	6.35	10.80
Air	100.0	170.0
Paper	0.40	0.68
Al	0.058	0.10
Paddle 2	12.70	21.6

TABLE 3.1: A summary of the materials seen in the focal plane by the particles after exiting the *K600* vacuum chamber, for the case of one X-U VDC, followed by a 1/4"-thick scintillator and a 1/2"-thick scintillator. The 2nd column lists the real material thickness, and the 3rd column lists the effective thickness traversed by particles at an incident angle of 35°.

Particle	E into P1 [MeV]	$\Delta EP1$ [MeV]	Range in P1 [mm]	$\Delta EP2$ [MeV]	Range in P2 [mm]
t - (paper included)	1.87	1.87	0.0032	0	0
t - (paper removed)	13.7	13.7	0.87	0	0
d - (paper removed)	35.1	35.1	6.43	0	0
p - (paper included)	49.5	16.2	10.80	31.1	9.03

TABLE 3.2: A summary of the calculated energy loss values of ejectile particles through the paddles. The calculations were performed for an initial triton energy of $E_t = 32$ MeV, a deuteron energy of $E_d = 48$ MeV, and a proton energy of $E_p = 55$ MeV.



FIG. 3.5: The 1/4"-thick paddle scintillator cut open to present less material to low energy tritons



FIG. 3.6: The paddle in position for the experiment, next to the second VDC

TOF information is generated by the time difference between paddle signals and the beam RF signal. Therefore, calculations were performed to obtain approximate values of the TOF regions which the tritons and deuterons might inhabit for the highest and lowest triton energy ranges to be investigated. The TOF is calculated relativistically with

$$\text{TOF} = \frac{d}{v}, \quad (3.2)$$

where the velocity v is calculated by

$$v = c \cdot \sqrt{1 - \left(\frac{M}{E_{total}}\right)^2}. \quad (3.3)$$

The distance d is varied between minimum and maximum flight path values of $d = 7.78$ m and $d = 8.87$ m for a particle travelling from the target to the medium dispersion focal plane. The mass and total energy of the particle is represented by M and E_{total} respectively, and c denotes the speed of light in Eq. 3.3. The results of these calculations, shown in Table 3.3, indicate that it is possible to differentiate the tritons from the deuterons using TOF selection.

Particle	Triton E -range [MeV]	TOF-range [ns]
d	52.9 - 43.8	n/a
t	52.9 - 43.8	142 - 156
d	34.2 - 28.5	118 - 129
t	34.2 - 28.5	176 - 192

TABLE 3.3: The TOF ranges of deuterons and tritons at two different triton energy settings. It is kinematically impossible to observe deuterons in the 52.9 - 43.8 MeV triton range since their energies would then be 65.7 MeV and higher.

At a beam energy of $E_{beam} = 60$ MeV, a time interval between beam packets from the cyclotron is merely 41 ns, which is more than a factor of 4 smaller than some of the values in Table 3.3. This means that there will be wrap-around of TOF regions, which could result in two particles from two consecutive beam pulses with different real TOFs being measured in the same 41 ns region. The TOF information in Fig. 3.7 was generated by a code which takes this wrap-around into account. The result of Fig. 3.7 indicates that the TOF ranges of the tritons and the deuterons should not overlap.

As a safeguard against possible time overlap from deuterons, pulse selection of one in every five beam packets was employed. By this means, the full TOF information of both particles is exploited as a beam packet arrives once every 205 ns. Hence, different particles can be separated more easily. Thus any possible interference with the triton locus from deuterons which deposit little energy to P1 is eliminated.

As soon as the triton locus from the (p,t) reaction was identified, its signal strength in

the Pad1 vs TOF spectrum was adjusted by optimising the paddle voltages, in order to keep the tritons out of the low-energy background.

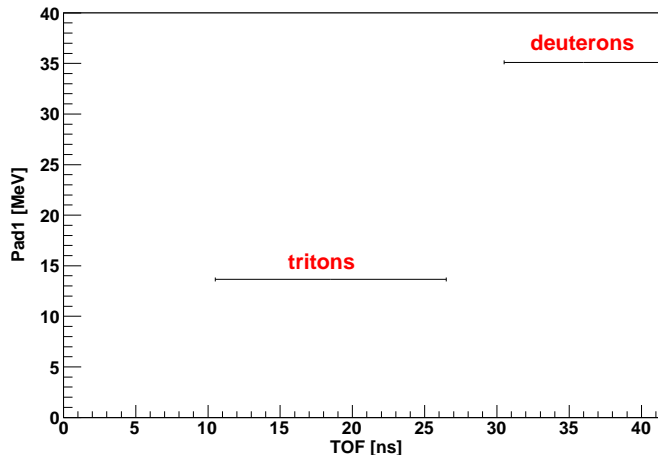


FIG. 3.7: The anticipated energy loss values in Paddle 1, plotted against the TOF ranges expected to be measured in the 41 ns TOF window (without pulse selection) for the tritons and the deuterons at the triton energy range $E_t = 34.2 - 28.5$ MeV.

The measured TOF spectra were compared to these predicted values and the energy loss spectra were interpreted according to the relationship:

$$-\frac{dE}{dx} \propto \frac{(Ze)^2}{v^2}, \quad (3.4)$$

which holds as a corollary of the Bethe-Bloch equation [92]. Particles which reach the paddles with different velocities (and therefore energies) will, for that reason, have different energy loss characteristics. These were used to set software gates on the regions of interest in PID spectra.

3.3 The beam stops

3.3.1 The finite angle beam stop

The scattering chamber beam stop shown in Fig. 3.8 was used for the non-zero or finite angle measurements. This beam stop makes it possible to collect data at spectrometer angles between $\theta_{lab} = 5^\circ$ and $\theta_{lab} = 21^\circ$ degrees, which implies a minimum central $K600$ angle of $\theta_{lab} = 7^\circ$ and a $\pm 1.91^\circ$ angular range. At smaller spectrometer angles, the background from this beam stop becomes unacceptable for effective data taking [90].

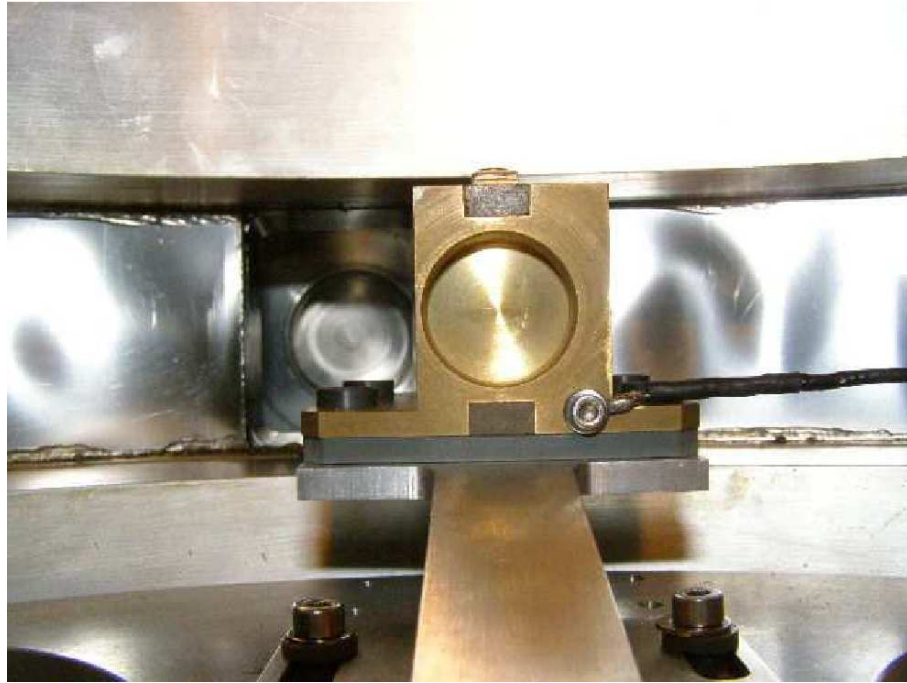


FIG. 3.8: The scattering chamber beam stop seen from the target ladder

3.3.2 The zero degree beam stop

The alternative L-shaped beam stop shown in Fig. 3.9 was inserted between D1 and D2 during the $\theta_{lab} = 0^\circ$ measurements. This is a composite beam stop made of three separate brass blocks which each have their own connection to the current integrator box in the K600 vault [90]. The position of the beam in the spectrometer can therefore be traced during an experiment by looking at the beam current measured on each component. The same model beam stop was used successfully in the past for (p,t) measurements at $\theta_{lab} = 0^\circ$ [93].

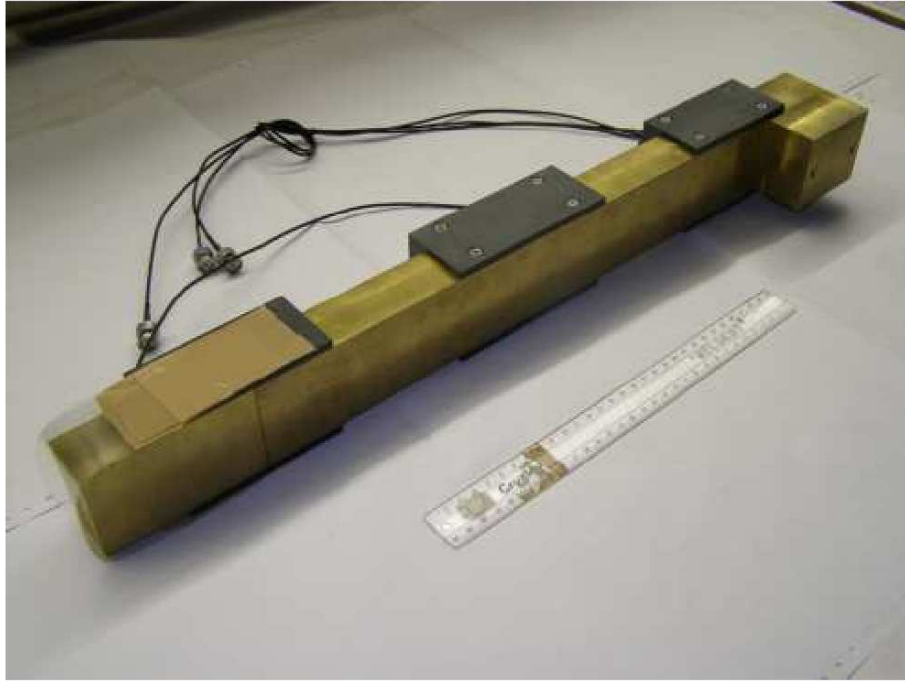


FIG. 3.9: The L-shaped zero degree (p,t) beam stop

3.4 Dispersion Matching

With a non-dispersion matched or achromatic beam, the positions and angles of particles which reach the target are independent of their kinematics. This means that the spatial and angular resolution in the spectrometer focal plane is limited by the momentum and angle spread of the beam particles [90]. The $K600$ spectrometer provides lateral, but not angular, dispersion matching. In lateral dispersion matching, the beamline magnets are adjusted so that the particles with higher momenta have to travel a longer distance to the focal plane than the particles with lower momenta. The beam is adjusted in this way until the effect of the initial momentum spread of the beam on the resolution is minimized. Eventually, resolution values down to the limit of the spectrometer's measurement capability may in principle be achieved by employing this technique [90]. This experiment utilised a dispersion matched beam from the SSC, which means that, at the target, the dispersion of the beamline was matched to the dispersion of the spectrometer so that a resolution that is superior to the energy variation in the beam could be achieved at the focal plane [94, 95]. For a detailed description of dispersion matching, refer to Ref. [96].

3.5 The ^{22}Ne uncooled gas cell target

Most of the data for this experiment were obtained using an uncooled gas cell target with a thickness of 10 mm. There were initial concerns about this target for measurements at angles of $\theta_{lab} = 20^\circ$ and beyond, where the length of the target poses a potential problem. Particles scattered from the front of such targets have different scattering angles to particles scattered from the back. This is detrimental to the resolution and accuracy of both the focal plane position and the scattering angle determination. The calculations based on Ref. [97], in Section 3.5.1, indicate that the 10-mm-thick target could still be sufficiently thin up to an angle as large as $\theta_{lab} = 30^\circ$. Nevertheless, the gas cell development work in Section 3.6 was performed to address potential resolution issues associated with using such a thick gas cell. The gas cell described in Section 3.6 could also provide the advantage of a higher areal density of material for the same absolute thickness of the gas cell.

3.5.1 Resolution

This section describes calculations and a previous measurement, which were used to estimate the resolution of the uncooled gas target cell.

3.5.1.1 Energy resolution

These calculations were performed for a gas cell thickness of $T = 10$ mm and an ejectile triton energy of $E_0 = 33.0$ MeV: The relativistic relationship between energy and momentum is as follows:

$$\frac{\Delta p_T}{p_0} = \alpha \frac{\Delta E_T}{E_0} \quad (3.5)$$

where Δp_T is the momentum uncertainty due to the cell thickness, ΔE_T is the energy uncertainty due to the cell thickness, p_0 is the averaged momentum and E_0 the averaged kinetic energy of the scattered particles. The factor

$$\alpha = \frac{(E_0 + M)}{(E_0 + 2M)}, \quad (3.6)$$

where M is the mass of the ejectile particles, therefore

$$\alpha = \frac{(33.0 + 2809.0) \text{ MeV}}{(33.0 + 2 \times 2809.0) \text{ MeV}} = 0.503 . \quad (3.7)$$

In terms of the ion optics of the spectrometer, it is also known that

$$\frac{\Delta p_T}{p_0} = \frac{\Delta x_T}{D} , \quad (3.8)$$

where Δx_T is the distance at the focal plane between particles scattered at the front and at the back of the gas cell, and $D = (x|\frac{\Delta p}{p})$ is the momentum dispersion of the spectrometer. For the $K600$ magnetic spectrometer:

$$D = 0.084 \text{ m/\%} \quad (3.9)$$

and

$$(x|x) = 0.52 , \quad (3.10)$$

where $(x|x)$ is the horizontal magnification of the spectrometer [90]. The distance Δx_T in the focal plane between particles can therefore be written as

$$\Delta x_T = (x|x) \times T \cdot \sin \theta_{lab} = 0.0052 \times \sin \theta_{lab} \text{ m}, \quad (3.11)$$

where θ_{lab} is the scattering angle. Inserting Eq. 3.8 into Eq. 3.5 yields:

$$\frac{\Delta x_T}{D} = \alpha \frac{\Delta E_T}{E_0}. \quad (3.12)$$

Inserting the known values from above, this becomes:

$$\Delta E_T = \frac{E_0 \cdot \Delta x_T}{D \cdot \alpha} = 21 \text{ keV} \quad (3.13)$$

for a scattering angle of $\theta_{lab} = 30^\circ$. The total energy resolution E_{TOT} is a quadratic sum of the resolution when the cell thickness equals zero $\Delta E_{T=0}$, and the energy uncertainty owing to the cell thickness ΔE_T .

$$\Delta E_{TOT} = \sqrt{\Delta E_{T=0}^2 + \Delta E_T^2}. \quad (3.14)$$

$$\implies \Delta E_{TOT} = \sqrt{(50 \text{ keV})^2 + (21 \text{ keV})^2} = 54 \text{ keV}. \quad (3.15)$$

From these calculations it is clear that energy resolution values below 60 keV could be achieved with the 10-mm-thick gas cell target even at an angle of $\theta_{lab} = 30^\circ$. This is acceptable for the present measurement, since it provides the means to measure the widths of states that are much narrower than what has previously been observed in the energy region of interest in the ^{20}Ne nucleus. Furthermore, the $5\text{-}\alpha$ cluster state may be expected to have a width of at least a few hundred keV, therefore its width could be accurately determined with an energy resolution below 60 keV.

3.5.1.2 Angular resolution

The uncertainty of the scattering angle ($\theta = \theta_{lab}$) on account of the gas cell target thickness is expressed as $\theta_{T,tgt}$. It may be calculated with the following equation:

$$\theta_{T,tgt} = \frac{(\theta|x)}{(\theta|\theta)} \times T \sin\theta \quad (3.16)$$

where $(\theta|x)$ and $(\theta|\theta)$ are matrix elements of the $K600$ with the following known values [90]:

$$(\theta|\theta) = -1.90 \quad (3.17)$$

$$(\theta|x) = -8 \text{ m}\tan.\text{cm}^{-1} = -0.8 \text{ rad.m}^{-1}. \quad (3.18)$$

Therefore:

$$\theta_{T,tgt}(\theta) = 0.0042.\sin\theta \text{ rad} \quad (3.19)$$

$$\implies \theta_{T,tgt}(30^\circ) = 0.0021 \text{ rad} = 0.12^\circ. \quad (3.20)$$

This additional spread in angular range is also acceptable. According to the calculations for both energy and angular resolution, a thinner target is not indispensable for performing the measurement, even at the largest considered angle of $\theta_{cm} = 30^\circ$.

3.5.1.3 Resolution of previous gas cell measurements

The 10-mm-thick gas cell target was successfully used previously for the experiment “Resonance States in ^{30}S , ^{34}Ar and ^{38}Ca Nuclei using the (p,t) Reaction and Reaction Rates in the Rp-Process”, hereafter referred to as experiment PR137b [98, 99]. During that exper-

iment, ^{20}Ne gas was used to investigate the $^{20}\text{Ne}(p,t)^{18}\text{Ne}$ reaction. Fig. 3.10 illustrates the setup which was used for experiment PR137b. It basically consists of a cell with two aramid windows of $6\ \mu\text{m}$ thickness which contains the gaseous material.

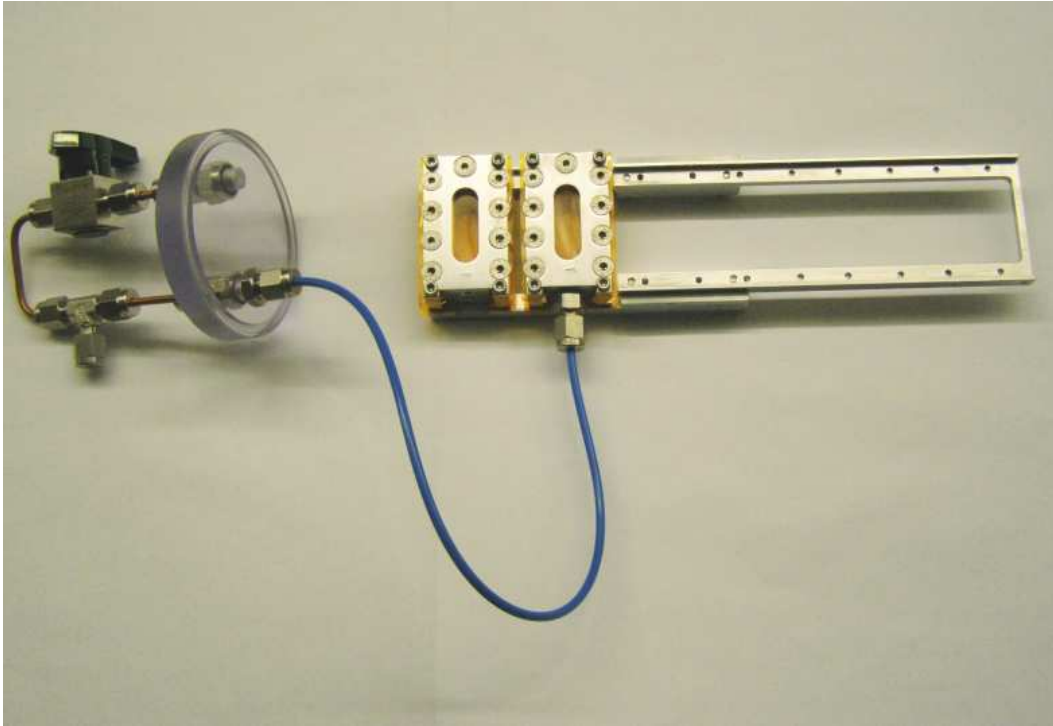


FIG. 3.10: The gas target frame with aramid windows from experiment PR137b [100]

Fig. 3.11 shows data that were acquired with the ^{20}Ne gas target at $\theta_{lab} = -1.2^\circ$ during experiment PR137b [98]. The K600 magnets were set to measure states in the excitation energy range of $E_x = 0$ to $E_x = 9.5$ MeV in ^{18}Ne . At a beam energy of $E_p = 100$ MeV, resolution values as low as $\text{FWHM} = 30$ keV could be obtained with a ^{20}Ne gas pressure of $P = P_{atm}$. This proves that sufficient resolution values may be achieved, despite the energy loss through the aramid windows and target material. Similar resolution values could be expected with the ^{22}Ne gas target at forward angles. The desired beam energy of $E_p = 60$ MeV provides a smaller spread in incident beam energy, although straggling and multiple scattering will introduce a larger energy spread at lower beam and ejectile energies.

Based on the experience gained during experiment PR137b, as well as the calculations in Sections 3.5.1.1 and 3.5.1.2, it was decided that the uncooled gas cell could be used for the $\theta_{lab} = 0^\circ$ and larger angle measurements of this experiment. Resolution values

achieved during the current experiment are displayed in Figs. 4.36 to 4.39 in Chapter 4.

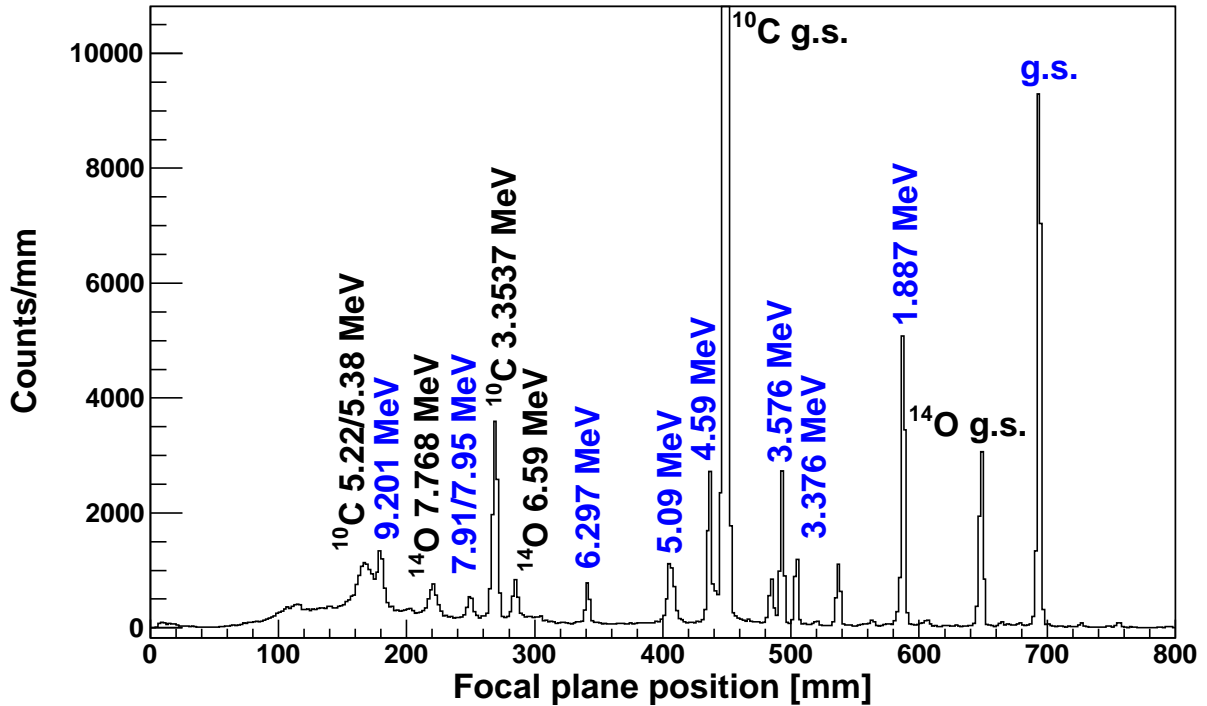


FIG. 3.11: This $^{20}\text{Ne}(p,t)^{18}\text{Ne}$ spectrum at $\theta_{lab} = -1.2^\circ$ and $E_p = 100$ MeV was obtained by S. O'Brien *et al.* in experiment PR137b. Peaks from the $^{20}\text{Ne}(p,t)^{18}\text{Ne}$ reaction have blue labels, while peaks from the aramid foil have black labels. A resolution of 30 keV was obtained on the ground state with a gas pressure of $P = P_{atm}$ and the peak positions could be determined to within 10 keV [98].

3.5.2 The gas cell

The gas cell consists of a body of aluminium with two foils on either side clamped down onto the body by two aluminium end plates. Fig. 3.12 presents a drawing of the 10-mm-thick body of the gas cell. The dimensions of its stadium-shaped entrance area are 1×3 cm². The edges of this entrance area and the end plates are smoothed to prevent foil-damage upon application of differential gas pressure to the foils. The single hole on the one side of the cell is an opening for a gas pipe fitting. This hole contains a groove for a rubber O-ring which provides sealing. The top face of the cell body contains a stadium-shaped groove which runs around the central opening of the cell. This groove is for another rubber O-ring. There are also two parallel rows of six holes each, and one more hole on the side opposite the gas pipe opening.

The tapped holes (excluding those on the four corners), are for screws to fasten a plate to the top of the gas cell. The four smaller holes that remain, which are situated at each of the corners, are for thinner screws to secure the entire gas cell system (body and two plates) to the target ladder. Holes are punched through the two 6 μ m thick aramid foils, one for each side, for fitting screws. The foil is inserted between the plate on one side and the cell and O-ring on the other. By fastening the screws, the plate is clamped tight against the cell, so that the O-ring is compressed and thus provides good sealing.



FIG. 3.12: The body of the 10 mm thick gas target cell

3.5.3 The aramid foils

The aramid material was obtained from RCNP in Japan, who purchased it from the Toray company [101]. Its chemical composition is $C_{14}O_2N_2Cl_2H_8$ and the weight ratios are (C, O, N, Cl, H) = 54.74, 10.42, 9.12, 23.09, 2.63. Its density is reported as 1.5 mg.cm^{-3} and its thickness has been calculated at $t = 5.5 \text{ }\mu\text{m}$, assuming the aforementioned density. Its areal density was measured to be $\rho = 0.8273 \text{ mg.cm}^{-2}$ [101, 102].

After the fourth weekend of data taking, a dark brown and a light brown spot were visible on each of the aramid foils. These spots were presumed to correspond to regions irradiated with the beam with target angles of $\theta_{tgt} = 0^\circ$ and $\theta_{tgt} = 27^\circ$ respectively. An ion beam analysis test was performed at the Materials Research Department of iThemba LABS to verify the purity of this foil and to investigate the change in its composition due to the beam after the experiment, using the foils which were employed during Weekend 4. A microfocused proton beam with energy $E_p = 3 \text{ MeV}$ and intensity $I_p = 100 \text{ pA}$ was delivered from the Van de Graaff accelerator to the nuclear microprobe that was used to investigate this foil with Rutherford backscattering spectrometry (RBS) and a microPIXE (Proton Induced X-ray emission) analysis [103]. For the microPIXE measurement, a proton beam induces characteristic X-ray emission from the heavier elements in the foil, which may be used to interpret the composition of trace elements on the foil with relative accuracy of 10% to 20% [104].

The RBS technique is used to determine the thickness of the foil by looking at the yield and energy distribution of backscattered ions. This information is used to correct the microPIXE data for the self-absorption of X-rays in the foil, hence, by using RBS in conjunction with microPIXE, the relative compositions of trace elements could be determined very accurately [104].

The elemental map of chlorine within and around the region irradiated by the 60 MeV protons was obtained with the technique of Dynamic Analysis using the software package GeoPIXE [105, 106]. These maps, shown in Fig. 3.13, display a dramatic change in the chlorine composition of the foil in the pair of regions, corresponding to the front and back foils, that were irradiated at $\theta_{tgt} = 0^\circ$ during Weekend 4. These regions were irradiated with beam currents of about $I_p = 15 \text{ nA}$ on average for a period of roughly 40 hours during Weekend 4. On the front foil, the average chlorine composition of the foil decreases from 15.16% outside of the irradiated regions to 6.55% within the region that was irradiated at

$\theta_{tgt} = 0^\circ$. Chlorine atoms appear to have been sputtered off the aramid foil in this region.

For the last 16 hours of Weekend 4, the target angle was changed to $\theta_{tgt} = 27^\circ$ for the measurements at $\theta_{lab} = 27^\circ$, thus causing the foils to be irradiated at different regions of both foils. A similar beam current was applied and the effect seen in Fig. 3.13 was observed again, but to a lesser extent corresponding to the difference in beam time spent on the two target angles.

The sputtering of chlorine that is observed in Fig. 3.13 raises the question whether the same occurred with the carbon, oxygen and nitrogen atoms. In the RBS spectrum in Fig. 3.14, the carbon peak is clearly seen to be thinner in the spectrum measured inside the irradiated region. However, Table 3.4 indicates no significant change in the relative stoichiometries of carbon, oxygen or nitrogen inside and outside this spot. Since carbon, oxygen and nitrogen constitute more than 80% of the total mass of the foil, it must be assumed that all 3 these elements were sputtered off the foil to some degree to bring about the observed difference in thickness inside and outside of the irradiated region. The dramatic change in the thickness of the chlorine peak in Fig. 3.14 serves as further evidence that this element was sputtered off the foil.

This result makes the normalisation of the foil-related background with the gas-filled target data problematic for Weekend 4. This normalisation is necessary to perform accurate background subtraction at $\theta_{lab} = 16^\circ$ and $\theta_{lab} = 27^\circ$. The same problem was presumed not to occur at $\theta_{lab} = 0^\circ$ and $\theta_{lab} = 7^\circ$, since the normalisation of the background measured at these angles did not require any compensation for a change in the foil thickness during beam time. This is probably because these angles experienced either far smaller beam currents ($I_p = 1$ nA) or shorter counting times.

Foil	Thickness [μm]	C	O	N	Cl
Front (outside spot)	6.0 ± 0.30	830	90	70	10
Front (inside spot)	5.0 ± 0.25	823	100	70	7
Back (outside spot)	6.0 ± 0.30	821	90	80	9
Back (inside spot)	5.7 ± 0.29	823	90	80	7

TABLE 3.4: The stoichiometries of elements on the foils inside and outside of the regions that were irradiated at $\theta_{tgt} = 0^\circ$, deduced from RBS data. The numbers should add up to 1000 in each row.

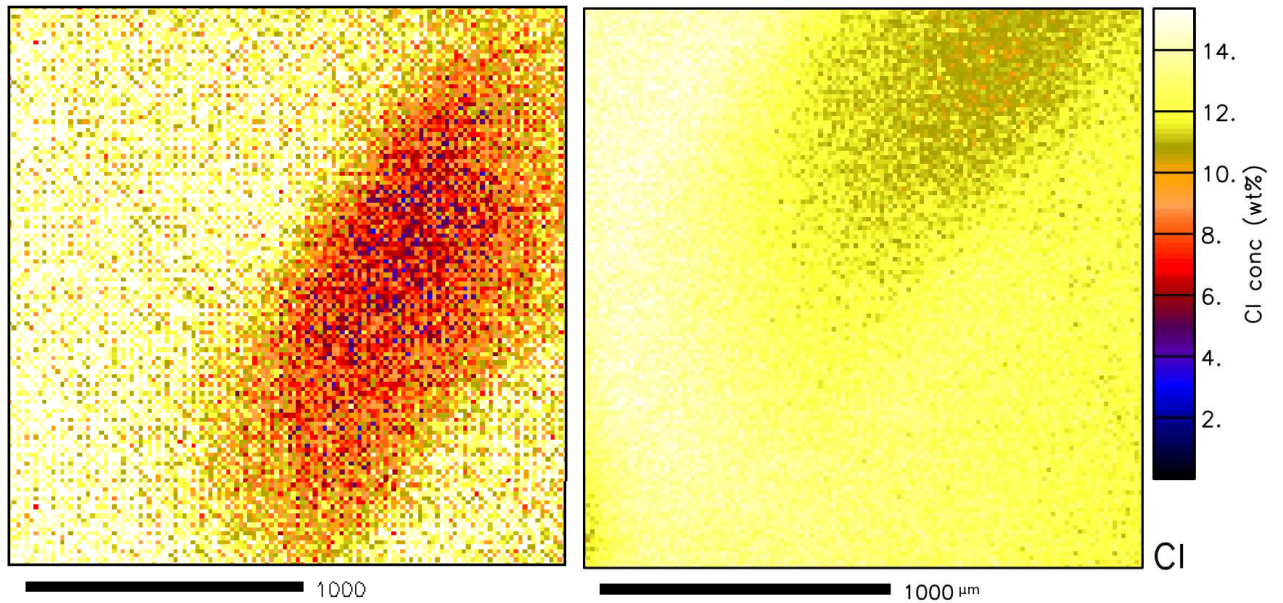


FIG. 3.13: MicroPIXE maps of the chlorine composition (in %) of the aramid foils are shown for the front and back foils at left and right respectively. The darker regions are where the foils were irradiated at $\theta_{tgt} = 0^\circ$.

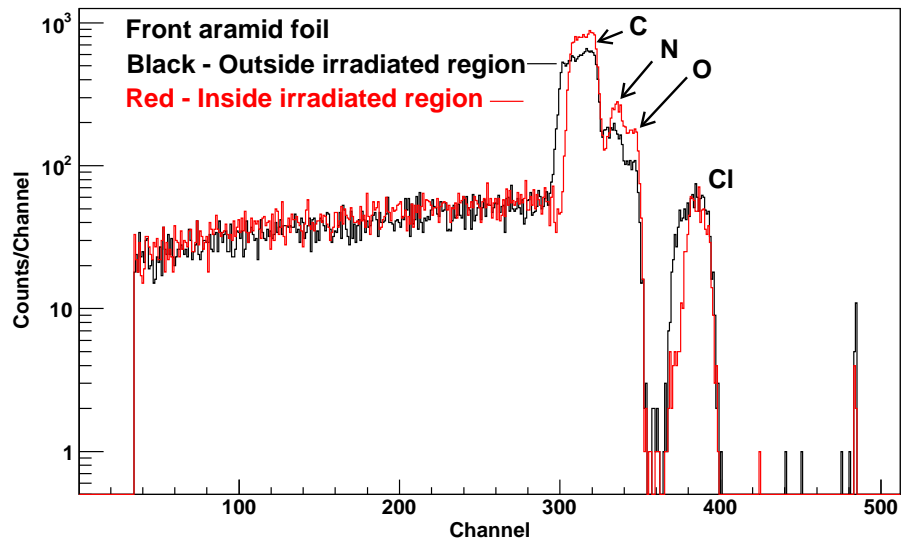


FIG. 3.14: The RBS spectra measured outside (black spectrum) and inside (red spectrum) the irradiated region

Fig. 3.15 shows X-ray spectra from trace contaminants on the foil generated by a microPIXE analysis. The largest trace contamination was from Si on the front foil, outside the irradiated region, at a relative composition of 0.0035%. It is noticeable that traces of potassium, calcium, iron, copper and zinc were found in the irradiated region on the back foil, but not on the front (see Table 3.5). The reasons for this are unclear, but it does not affect the $^{22}\text{Ne}(p,t)^{20}\text{Ne}$ data.

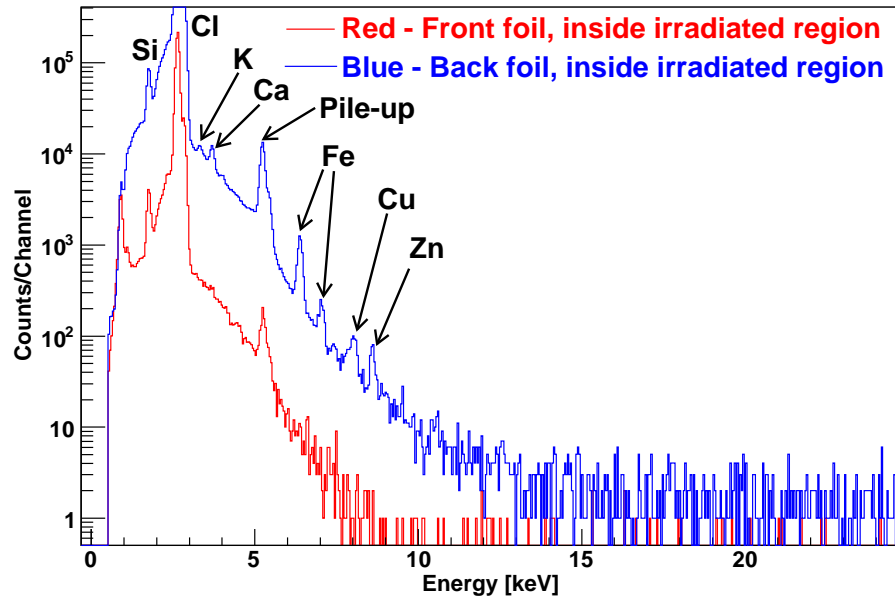


FIG. 3.15: MicroPIXE spectra displaying chlorine and all the trace contaminants inside the region irradiated at $\theta_{tgt} = 0^\circ$ on the front foil are shown by the red spectrum and those on the back foil are shown by the blue spectrum.

Element	Front foil (inside spot)	Back foil (inside spot)
Cl	65487 ± 569 (24)	111619 ± 122 (6.9)
Si	3297 ± 135 (74)	3108 ± 122 (21)
P	418 ± 116 (39)	645 ± 186 (12)
S	1189 ± 145 (32)	1344 ± 209 (9.4)
K		47 ± 2 (3.1)
Ca		99 ± 3 (2.5)
Fe		56 ± 5 (1.2)
Cu		6.3 ± 0.8 (1.9)
Zn		7 ± 2 (1.8)

TABLE 3.5: Compositions of trace contaminant elements on the foils in ppm (parts-per-million), inside the region irradiated at $\theta_{tgt} = 0^\circ$. The detection limits are shown in brackets.

3.5.4 Gas contaminants

Peaks from gas contaminants in the energy region of interest pose potential problems, therefore measurements were performed with an Extorr residual gas analyser (RGA) to estimate the positions and strengths which could be expected from such peaks in the $^{22}\text{Ne}(p,t)^{20}\text{Ne}$ energy spectra. The RGA is a quadrupole mass spectrometer with a built-in Pirani gauge and an ion gauge which constantly monitor the total pressure. With these gauges, the RGA can measure the total gas pressure from atmospheric pressure $P = P_{atm}$ to high vacuum $P = 10^{-9}$ mbar, and partial pressures at below $P = 10^{-12}$ mbar. At these low pressures the RGA uses a filament composed of thoria coated iridium to perform mass measurements [107].

The ^{22}Ne gas was obtained from Chemgas in Boulogne, France, who reported it to be 99.97% isotopically pure [108]. The RGA spectrum in Fig. 3.16 a) indicates the singly-charged $^{22}\text{Ne}^+$ gas ions at a partial pressure close to $P = 2 \times 10^{-4}$ mbar, about 30 times higher than singly-charged $^1\text{H}^+$, which is the next most prominent ion in the spectrum. Doubly charged ^{22}Ne is also noticeable at a pressure of $P = 1 \times 10^{-6}$ mbar. The majority of contaminants in the ^{22}Ne spectrum (e.g. N_2 , O_2 , H_2O , CO_2 , the hydrocarbon chains, etc.) correspond to ions that are also visible in the vacuum spectrum in Fig. 3.16 (bottom). Most of these ions, excepting ^{20}Ne and the argon isotopes, for instance, are also present in the aramid foils, which means that they must make minor contributions to the aramid peaks in the (p,t) spectra measured with the spectrometer. Seven isotopes of xenon are observed at masses from $A = 128$ to $A = 136$. The isotopes ^{129}Xe , ^{131}Xe and ^{132}Xe have the highest partial pressure values, all of which are close to $P = 3 \times 10^{-9}$ mbar. This is 5 orders of magnitude lower than the ^{22}Ne gas. Furthermore, the $^{129}\text{Xe}(p,t)^{127}\text{Xe}$ reaction has the largest combination of Q -value for the (p,t) reaction ($Q = -8.0$ MeV) and highest known excitation energy value in the residual nucleus ($E_x = 9.52$ MeV), giving it an effective Q -value Q_f :

$$Q_f = |Q| + E_x = 17.52 \text{ MeV} . \quad (3.21)$$

The $^{22}\text{Ne}(p,t)^{20}\text{Ne}$ reaction has a Q -value of $Q = -8.64$ MeV. The most important excitation energy region for this experiment lies beyond $E_x = 15$ MeV, which requires a minimum effective Q -value $Q_f = 23.64$ MeV. Hence, these xenon isotopes do not present a problem for the measurement [56].

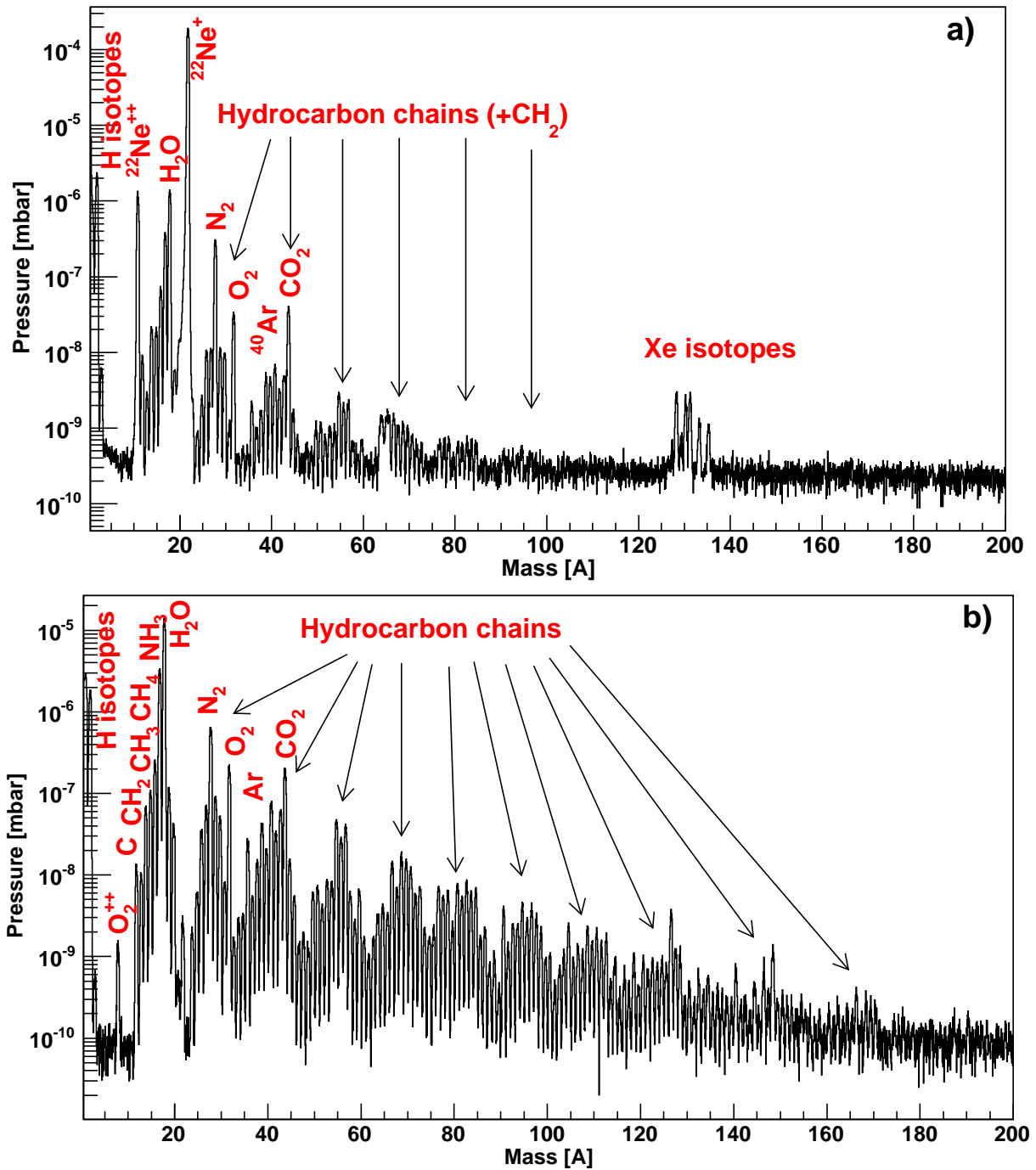


FIG. 3.16: The RGA data in a) were obtained with ^{22}Ne gas at $P = 1 \times 10^{-5}$ mbar, and in b) the vacuum data were measured at $P = 1.3 \times 10^{-7}$ mbar.

3.5.5 The target ladder

The target ladder used in this experiment is shown in Fig. 3.17. It contains, from the top:

- a gas cell filled with ^{22}Ne gas at the beginning of the weekend,
- a spare gas cell kept empty until required,
- a ZnS scintillating viewer for focusing the beamspot,
- a single aramid foil for background measurements (thickness = $12.5\ \mu\text{m}$ for Weekends 1 to 3, thickness = $6\ \mu\text{m}$ for Weekend 4),
- a $2\ \text{mg}\cdot\text{cm}^{-2}\ ^{12}\text{C}$ target for calibration, and
- an empty background target for halo measurements.



FIG. 3.17: The target ladder used during the second weekend of data taking. Apart from minor adjustments, the target ladders used for the other weekends were the same as this one.

Both of the top two slots contain a target cell with 6- μm -thick aramid foils spaced 1 cm apart. The fourth and fifth slots from the top contain round frames of diameter $D = 25$ mm. The gas pipes from the two gas cells both lead through a valve to a mutual gas pipe which leads through another valve to the gas bottle, as shown in Fig. 3.18. There is also a mutual venting valve, indicated in Fig. 3.18. Thus, by opening the valve to one cell and closing the valve to the other, one could vent a gas cell, or fill it from the bottle, without affecting the other cell. Pipes with a diameter of 1/8" were used throughout to minimise gas loss.

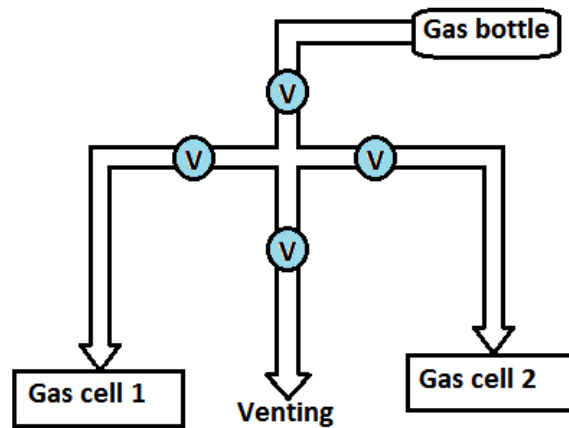


FIG. 3.18: The gas handling system operating between the gas bottle and the gas cells. Each valve is indicated by a blue circle with a 'V' written inside it.

3.6 Cryogenic gas target development

A target was designed to operate at temperatures of around $T = 100$ K, compressing the material by a factor of 3, according to the ideal gas law $PV = nRT$. This makes it possible for a target with a thickness of 3 mm to have the same effective thickness of material as an uncooled target with a thickness of 9 mm. It was designed as a safety measure, in case the desired resolution values were not achieved with the 10-mm-thick target discussed in Section 3.5, and it was used for the first weekend of data taking.

3.6.1 Choice of foils

Tests were performed on aramid foils thinner than $6 \mu\text{m}$ and on mylar, which would have been particularly useful since it contains carbon and oxygen, but not nitrogen or chlorine. These foils were found to be too unstable for experiments with the beam. Another option that was considered was to use aluminised mylar, which would have been far more durable than pure mylar. However, calculations showed that the $^{27}\text{Al}(p,t)^{25}\text{Al}$ reaction would produce an intrusive continuum of ^{25}Al states in the ^{20}Ne excitation energy region around $E_x = 20$ MeV. Hence it was decided to resume using the $6\text{-}\mu\text{m}$ -thick aramid foils described in Section 3.5.3.

3.6.2 The new gas target ladder

At $T = 100$ K, rubber O-rings become rigid and shrink, and thus they can no longer provide effective sealing of the gas cell against a leak into vacuum. A mixture of Araldite Standard slow-setting epoxy adhesive was therefore considered as an alternative to seal the gas inside the target.

The aramid foils were glued directly to the body of the gas cell. To accommodate the glue, the groove for the O-ring was removed and all the holes for screws were removed, apart from the four in the corners required for attaching the cell to the target frame. The edges of the inner ring of the cells and cover plates, which were still used for sealing to some degree, were rounded to protect the aramid foil. The gas cell surfaces were sand-blasted to provide some grip for the glue.

The gas target ladder was redesigned as shown in Fig. 3.19. This design provides thermal conductivity (see Section 3.6.3) and makes the glueing process effective by providing ample space and few holes to avoid when applying glue. The bottom two gas target po-

sitions in this design have steel gas pipes connected to them. The middle one, which has no gas pipe fitting, was used for background measurements with two 6- μm -thick aramid windows. The top two slots were left open for the viewer and a calibration target (in this case a 12.5- μm -thick aramid foil was used).

The Araldite mixture was homogeneously applied to the top of the gas cell before the aramid foil was applied to the gas cell. Then a kapton foil, followed by several sheets of paper and a lead block were put on top of this. The kapton was used to prevent glue from sticking to the paper. The paper was used to prevent any of the surface irregularities of the lead block from harming the foil. The weight of the lead block was used to ‘seal’ the area where the aramid foil came into contact with the gas cell, while the glue was left to set for at least 90 minutes.

At the end of the 90 minutes, the lead block, paper and kapton were removed and any paper sticking to the gas cell was removed with a blade. At this stage, the gas target frame was turned around and the same procedure was repeated on its other side. Aluminium side plates were then fastened on both sides of the gas cells and clamped tight for extra sealing. The plates that were used in this last step were identical to the ones used with the original gas target, except for the fact that they had only four holes, one in each corner as shown in Fig. 3.20.

Initially, the gas cells were glued up to the edges of their inner rings. This method was not very successful since gas leaks usually occurred somewhere along the edge of the inner ring. It is possible that the Araldite glue, upon drying, may form sharp edges on the foil inside the gas cell opening, which could, with the application of differential pressure to the gas foil, create regions of increased tension in the foil, which could cause the foil to tear. To prevent this, the areas immediately around the outer edges were kept clean of any glue in the tests that followed, as well as in the final product. This is illustrated in Fig. 3.21. Some glue could still run to the inner edge of the cell, but the distance around the edge where foil damage could occur due to the glue would be smaller, leading to a smaller probability of damage.

The next step was to cut a glue groove with a depth of about 1 mm into the inner ring of the gas cell target. Any glue which could accidentally run off to the inner edge would then drop into this groove where it could not touch the aramid foil and form sharp edges on the foil inside the gas cell opening. This would make the glueing process more



FIG. 3.19: The cryogenic gas target ladder. The bottom two target positions are for gas targets and hence are connected to two steel gas pipes. The middle target position is for aramid background measurements and the empty top two positions are for the viewer and a calibration target. The three copper blocks form a copper frame for thermal conductivity. The gas pipes are connected to the gas handling system.

reproducible. It would also increase the area of contact between foil, glue and cell, which would make it less probable for air to tunnel through this area. The prototype shown in Fig. 3.22 was built, but this plan unfortunately was abandoned due to lack of time



FIG. 3.20: Aluminium side plates used for clamping on both sides of the gas cells



FIG. 3.21: The target gas cells with aramid foils. The Araldite glue was not applied around the edges of the openings in these cells.

for proper testing. In the future, this technique may be explored for similar gas target experiments.



FIG. 3.22: A test gas target cell with glue grooves cut around its inner ring

3.6.3 Gas flow and thermal conductivity

This gas target needed to make thermal contact with the liquid nitrogen in the Dewar flask on top of the spectrometer scattering chamber shown in Fig. 3.23. At the same time, it was a requirement that the target ladder was able to move between all five target ladder

positions. The usual plastic gas pipes supplying gas to the gas cells cannot operate at the liquid nitrogen temperatures, therefore an alternative system with metal pipes which could fit into the chamber at any of the five ladder positions had to be found.



FIG. 3.23: The Dewar flask on top of the spectrometer scattering chamber, being filled with liquid nitrogen. The ^{22}Ne gas bottle can be seen below and to the right of the Dewar flask.

To solve the first problem, the following was done: A copper frame consisting of three copper blocks shown in Figs. 3.19 and 3.24 was built to fit around the edges of the target ladder. A heat-conducting compound was applied inside the grooves of these blocks to provide a thermal bond with the stainless steel body of the target ladder. Two braids of copper were used to join this to the body of copper shown in Fig. 3.25. This body of copper was connected to the body of the Dewar flask that was filled with liquid nitrogen. With the flexibility of the braided wires, the target ladder could be driven up and down while maintaining thermal contact between itself and the Dewar flask.



FIG. 3.24: The cryogenic gas target ladder with copper frame and aluminium plates attached

To solve the second problem, the steel pipes shown in Figs. 3.19 and 3.24 were built to form part of the gas cell targets. These steel pipes were connected, via plastic pipes to maintain the mobility of the ladder, to the pipes in Fig. 3.26 which lead to the gas handling system illustrated in Fig. 3.18. Copper braids were wrapped around all these pipes for thermal conduction.

A PT100 probe was attached to a corner of the bottom gas cell, to measure the temperature at the bottom of the gas target ladder. The first test was performed in the target chamber under vacuum and with nitrogen gas at $P = 1$ bar in one of the gas cells. This test was performed with no thermal shielding, and yielded temperatures of only $T = 220$ K. For the second test, an aluminised mylar foil was wrapped around the body of the target ladder and the copper in Fig. 3.25 to act as an infrared shield. The lowest temperature recorded during this test was $T = 123$ K, therefore it was presumed that infrared radiation kept the temperature from dropping further in the first test. This temperature would already be enough to increase the gas density by a factor of almost three.

This target leaked at a rate of $\Delta P/\Delta t = 0.1$ bar / hour with its total pressure above $P = 1$ bar, and then at $\Delta P/\Delta t = 0.1$ bar / 24 hours after its total pressure had dropped below $P = 1$ bar. This kind of leakage was typical for half of the newest versions of the



FIG. 3.25: The copper braids at the bottom of this picture are connected by a continuous body of copper, mostly hidden underneath the aluminised mylar foil, to the piece of copper at the top of the picture. This piece of copper was connected to the Dewar flask that was filled with liquid nitrogen during the experiment.

gas cell. The others would leak much faster and drop down from $P = 1$ bar to $P = 0.5$ bar in less than 5 hours.

3.6.4 Conclusion

At the end of these tests, a cryogenic gas cell target ladder was prepared for which the thermal conductivity was close to the level envisaged, but which was still had relatively large leak rates in the vacuum of the scattering chamber. However, by the start of the experiment, this cryogenic target was already at a stage where it could be used if sufficiently low resolution values could not be attained for the large angle measurements ($\theta_{lab} = 16^\circ$, $\theta_{lab} = 27^\circ$) with the 10-mm-thick uncooled gas target. With a few more tests and fine tuning of the target assembly technique, a cryogenic gas target with lower leak rates could soon be available for future spectrometer experiments. This would be very useful in improving the positional and angular resolution of gas target experiments.

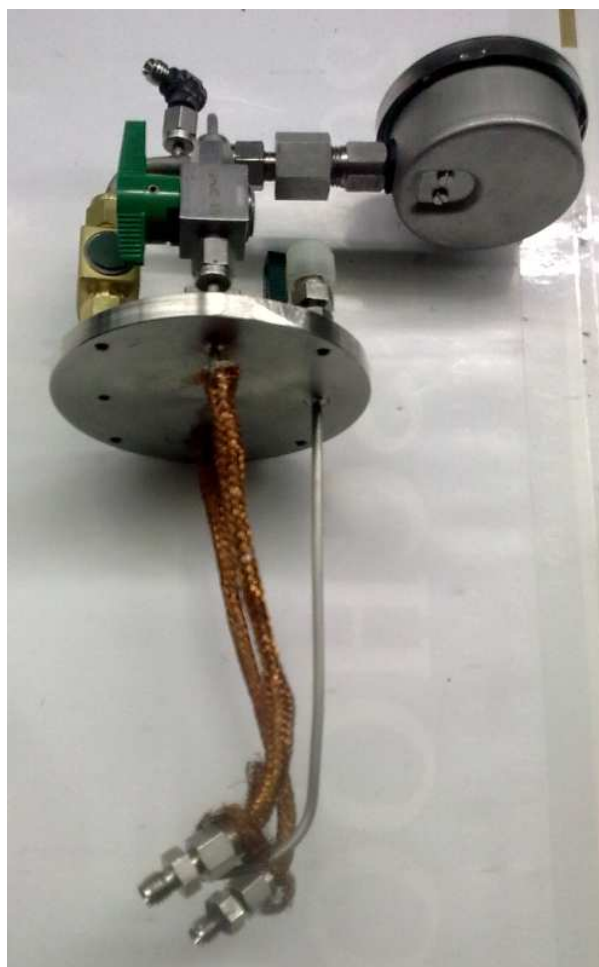


FIG. 3.26: The steel gas pipes, covered by copper meshes, were used to connect the plastic pipes from the gas cells to the gas handling system.

3.7 Electronics

The events detected by the focal plane detectors were transmitted to electronic modules adhering to Nuclear Instrumentation Module (NIM) and Versa Modula Europe (VME) standards which converted these events into digital data that could be interpreted by the Maximum Integration Data Acquisition System (MIDAS) software [109].

A block diagram representing the trigger electronic modules which were employed is shown in Fig. 3.27. This section describes the operation of these modules during the measurement, starting with the paddles. Data measured by each of the paddles is sent to a linear fan-out (Lin Fan), where a delay of 150 ns was applied before it was sent through to the QDC to produce the pulse height information. The timing signal was sent from the Lin Fan to the constant fraction discriminator (CFD), from where it was sent to the

TDCs (time digitizer channels) and a mean timer between the signals from both sides of the paddle. The mean timer makes the signal to the discriminator independent of the position where the ejectile particle traversed the paddle. In this experiment, the second paddle was used only during beam optimisation in the (p,p') mode, though the delay of 20.5 ns on its mean timer controlled the timing of the paddle signals.

For the (p,t) mode which was used for data taking, the cable from the Paddle 2 mean timer was disconnected, thereby taking Paddle 2 out of the circuit. It was then reconnected to the discriminator of Paddle 1 as indicated by the red arrow in Fig. 3.27, thus maintaining the same timing for a measurement with only Paddle 1.

From the discriminator, the signal was fed through to the four-fold logic unit (4FLU) where paddle coincidence events were selected with the logic requirements:

- $(P1 \cdot P2)$ for beam optimisation in the (p,p') mode, and
- P1 only for recording data in the (p,t) mode.

This 4FLU unit sent an output via a discriminator to another 4FLU unit, which received the RF signal via a discriminator. Whenever this second 4FLU unit registered a paddle coincidence along with the RF signal, it would send an output signal to the TDCs associated with TOF information. The first 4FLU also sends the trigger signal for TDC counting, which opens a time gate of width $t = 1.9 \mu\text{s}$ during which the TDCs may register TOF and wire chamber events. Its last output goes via two discriminators and a gate-and-delay generator (GDG), which applies a delay of 515 ns to this signal, to the TDCs associated with VDC counting.

The system dead time was measured with a pulser and two scaler modules, namely the inhibited and the uninhibited. The pulser signal was sent to one scaler module to generate the uninhibited signal. The same pulser signal was inhibited by the system *busy* signal from the QDC to generate the inhibited signal which was sent to an identical scaler module. The system dead time D could be calculated by comparing the number of pulses measured by these two modules. The current measured at the beam stop was fed to a current integrator (CI), which generates output pulses at a frequency of 1 kHz at full-scale current setting. Hence, a current of I nA at a CI range setting of R nA generates an event rate of I/R kHz. The total charge collected during data taking may be used to infer the number of protons incident at the beam stop.

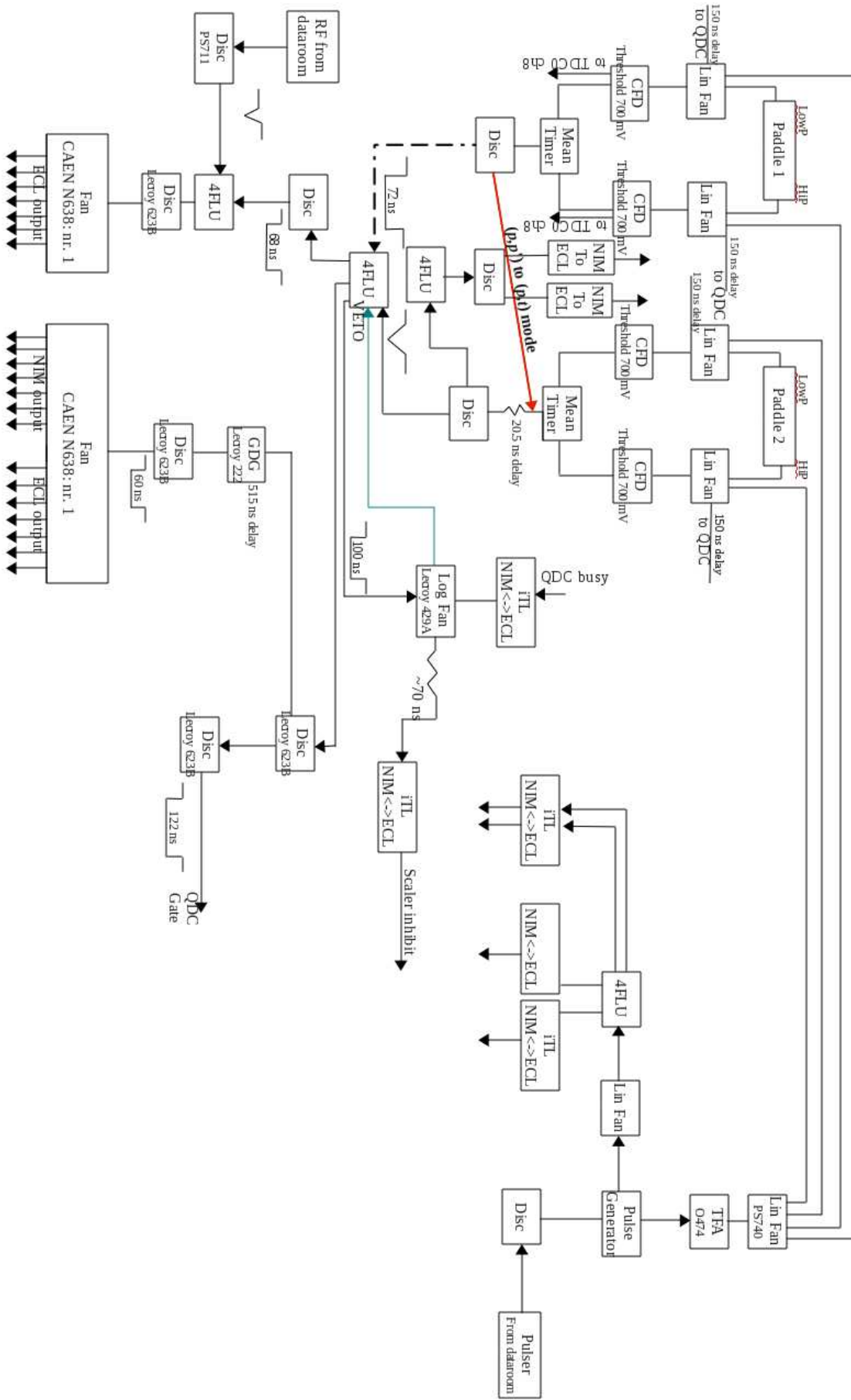


FIG. 3.27: Diagram of the trigger electronics

3.8 Experimental procedure

Prior to the arrival of the beam from the SSC, the scattering chamber and spectrometer vacuum was pumped down to below $P = 1 \times 10^{-5}$ mbar with the target ladder in the chamber. The magnets were switched on and set to the appropriate field setting for the beginning of the weekend ((p,p') at $E_p = 55$ MeV). The (p,p') reaction delivers a far higher count rate than the (p,t) reaction, making it more suitable for beam optimisation.

The viewer and another ZnS mesh-shaped scintillator situated upstream from the target, just after the last quadrupole in the S-line, were used for focusing the beam. Thereafter the resolution of the already dispersion matched beam was further optimised using the last three beamline quadrupoles within the K600 vault and the two trim coils in the spectrometer. The best resolutions obtained with the (p,p') reaction are shown in Table 3.6.

Weekend	FWHM [keV]	Nucleus and state	Target
1	22	^{12}C 4.439 MeV	12.5 μm aramid
2	22	^{12}C g.s.	Natural carbon foil
3	23	^{12}C g.s.	12.5 μm aramid
4	27	^{12}C g.s.	Natural carbon foil

TABLE 3.6: The best resolutions obtained with the (p,p') reaction for the different weekends

Next, the pepperpot collimator, shown in Fig. 3.28, was used together with an aramid target. From the positions of the slots on this collimator, one may deduce the exact scattering angles of the particles which travelled through them. This makes the pepperpot collimator a very powerful tool for making angular calibrations during off-line analysis.



FIG. 3.28: Front view of the pepperpot collimator [90]

With these tasks completed, the spectrometer could be set to the (p,t) mode. When changing from the (p,p') to the (p,t) setting, the magnets were adjusted according to the difference in magnetic rigidity between a proton and a triton. After being magnetised once, and having the magnetic field brought back down to zero, the ferromagnetic material of the spectrometer magnets will still retain considerable residual magnetisation. In order to get rid of this hysteresis, the spectrometer magnets are cycled to their minimum and maximum values every time the magnetic fields are changed. Through this procedure, considerable magnetisation is induced in the direction opposite to where the magnets were magnetised, so that at the end of this procedure, zero residual magnetisation will be left in the magnets [90].

The ^{22}Ne gas was inserted into the target cell up to a pressure of $P = 1.5$ bar for data collection, and was refilled whenever the pressure dropped below $P = 1.2$ bar. Background measurements were performed, typically for an hour for each three hours of ^{22}Ne data. However, at angles of $\theta_{lab} = -1^\circ$ and $\theta_{lab} = 7^\circ$, with the 33.5 MeV (p,t) field setting, the background and ^{22}Ne counting times were kept approximately equal to aid background subtraction during offline data analysis.

CHAPTER 4

Analysis of $^{22}\text{Ne}(p,t)^{20}\text{Ne}$ data

Measurements were made at a selected range of laboratory angles (0° , 7° , 16° , 27°) and magnetic field settings with the following corresponding triton ejectile energies: 31 MeV, 33.5 MeV, 36/37 MeV, 41/42 MeV, 46/48 MeV and 52 MeV. The excitation energy of the 5- α break-up threshold in ^{20}Ne ($E_x = 19.2$ MeV) corresponds to a triton ejectile energy of $E_t = 32.0$ MeV for a proton beam energy of $E_{lab} = 60.0$ MeV at $\theta_{lab} = 0^\circ$. Therefore the field settings for ejectile energies of 33.5 MeV would be appropriate for exploring the region above the 5- α break-up threshold in ^{20}Ne , and also for investigating the high excitation energy region in this nucleus at $E_x = 17 - 25$ MeV. The other field settings were necessary for energy calibration and to understand the ^{20}Ne excitation energy spectra. The ground state of ^{20}Ne was found in the 52 MeV field setting.

This chapter begins with Section 4.1 which explains how the raw data from the scintillators and VDCs are converted into meaningful spectra. The calibration data sets are discussed thereafter in Sections 4.2 to 4.5, followed by the 33.5 MeV (p,t) setting, where new ^{20}Ne states were observed, in Section 4.6. Section 4.7 provides a summary of all the data sets which were obtained, while Section 4.8 describes the extraction of the experimental cross sections and Section 4.9 the experimental resolution values. Section 4.10 concludes this chapter by displaying and discussing the final angular distribution plots.

4.1 VDC operation

The operation of the VDC is explained in more detail in Ref. [81], but a brief account follows here: Fig. 4.1 shows the drift times which were recorded at each individual wire channel from the first X-only drift chamber for a period of approximately one hour. The time axis should be read from right to left, because the detector is operated in common stop mode. The ionization of the Ar-CO₂ gas in the drift chamber, due to ejectile particles passing through the chamber, occurs from a maximum distance of 8 mm from the wire plane, which generates the maximum drift times approximately corresponding to the left-edges of the V-shapes in Fig. 4.1. The rest of the V-shapes are generated by gas ionization from particles passing over the the wire plane and eventually out of the chamber on the

opposite side of the wire plane. In each drift cell, which is associated with a specific signal wire, the number of events per time bin dN/dt is described by [110]:

$$\frac{dN}{dt} = \frac{dN}{ds} \cdot \frac{ds}{dt}, \quad (4.1)$$

where ds represents an element of distance along an electric field line, dN/ds is the linear density of time tracks along ds , and ds/dt is the drift velocity in the chamber. In the region radially near to the signal wire, dN/ds reaches a maximum due to geometrical effects and ds/dt rises dramatically, especially in the region very near to the signal wire, due to a much higher electric field. Hence, there appears a locus in drift times at time = 800 ns, which represents the minimum possible drift times of charged particles in the drift chamber. This is a relative time caused by delays in the electronics. The fact that this locus for minimum drift times is lined up as it is in Fig. 4.1 shows that the offset times due to different cable lengths etc. for the different TDC channels of this chamber have been corrected for, and the drift times recorded are therefore valid. This locus is related to the peak around the same time in the spectrum for all drift times in Fig. 4.2.

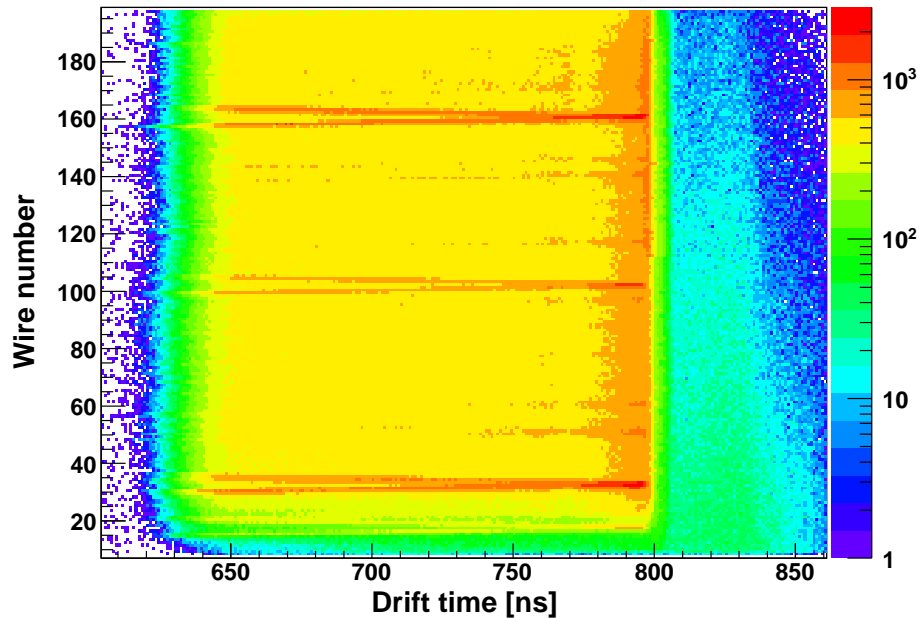


FIG. 4.1: The drift times on the x-axis were recorded for each individual signal wire of the first drift chamber on the y-axis in the $\theta_{lab} = 0^\circ$ and 33.5 MeV triton field setting, after a correction for the cable length offset times was implemented.

The drift times in Fig. 4.2 are converted to the drift distances in Fig. 4.3 with the aid

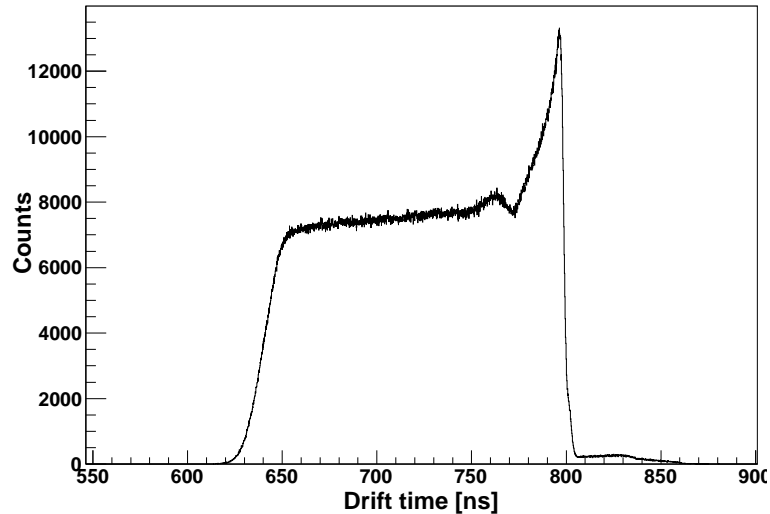


FIG. 4.2: The spectrum of all drift times which were measured in the first X-wire chamber

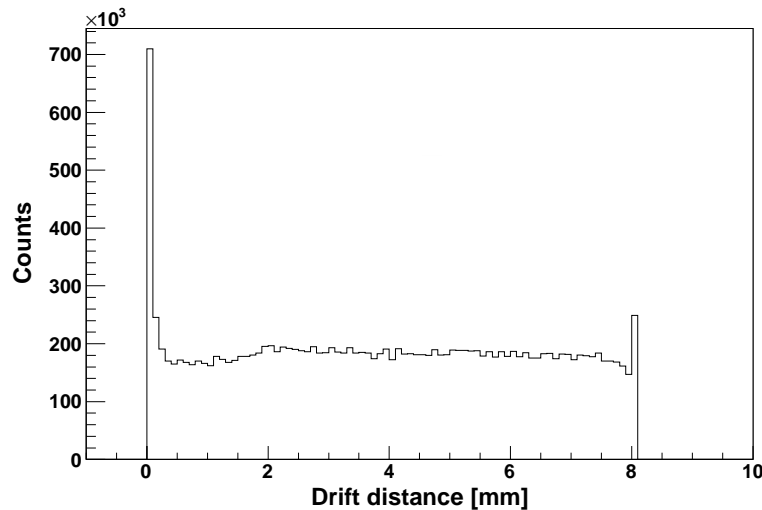


FIG. 4.3: The spectrum of drift distances corresponding to the drift time spectrum in Fig. 4.2

of the lookup table (LUT) in Fig. 4.4. The raw wire hits per channel, or ‘hit pattern’, spectrum is shown in Fig. 4.5. ‘Good’ VDC events are chosen from all these wire hits. The spectrum for signal wire hits per event in Fig. 4.6 shows a clear maximum around 5 to 6 wires per event. This may be anticipated for particles crossing the signal wire plane at angles between $\theta = 28^\circ$ and $\theta = 42^\circ$, with a mean value close to $\theta = 35^\circ$ [81]. Events corresponding to particles entering the signal wire plane from outside of this angular range should be rejected since they are not valid events. Therefore, ‘good’ events, which consist of sets of successive signal wire hits conforming to the following requirements are selected:

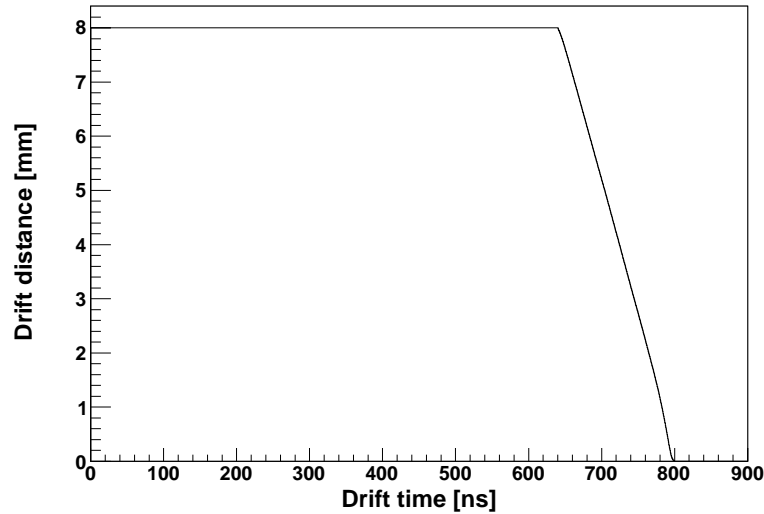


FIG. 4.4: This lookup table is used to convert the drift times (x-axis) in spectra such as in Fig. 4.2 to drift distances (y-axis) in spectra such as in Fig. 4.3.

- A minimum of three and a maximum of nine signal wire hits;
- The signal wire hits must be adjoining, unless a maximum of one signal wire is missing in a set of adjoining signal wire hits;
- The drift times should fall within a range corresponding to approximately 650 ns to 800 ns in Fig. 4.2.

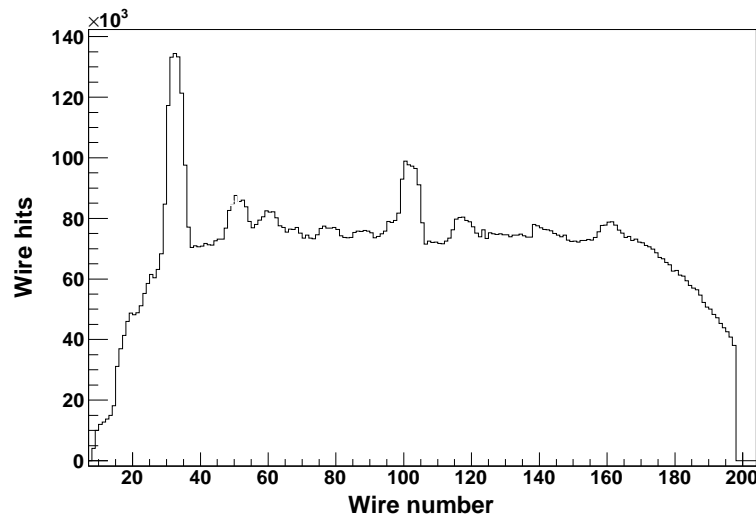


FIG. 4.5: A wire hits per channel spectrum for VDC X1

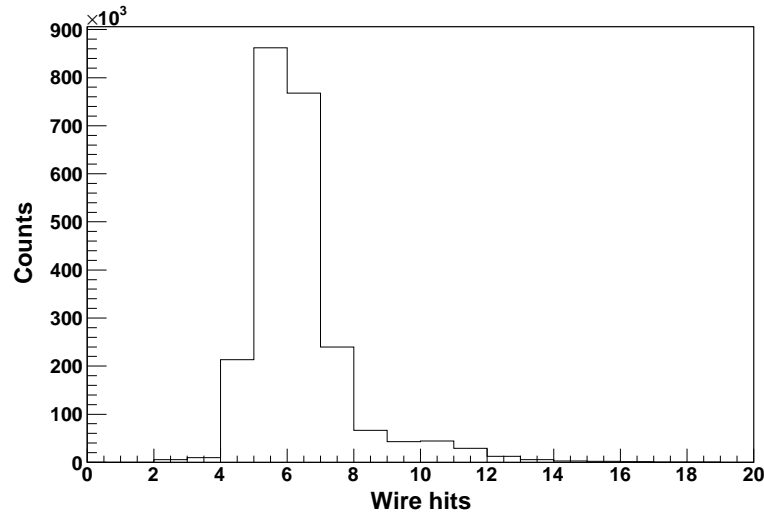


FIG. 4.6: Signal wire hits per event for VDC X1

The efficiency of data collection of a wire chamber is found by calculating the ratio between the good events and all PID selected events recorded by the chamber. Following this, the efficiency, ϵ , of the measurement may be calculated with the formulas: $\epsilon_{X1X2} = X1_{eff} \cdot X2_{eff}$ for the measurements made with two drift chambers with only X-wire planes, and $\epsilon_{X1X2U2} = X1_{eff} \cdot X2_{eff} \cdot U2_{eff}$ for the measurements which included a U-wire plane, where Xi_{eff} and Ui_{eff} denote the efficiencies of individual wire planes ($i = 1, 2$). The efficiency is always calculated for events which fall within a certain subset of events (e.g. all triton events) selected with a particle identification (PID) spectrum such as in Fig. 4.8.

At this stage, with the correct drift distances found for valid drift chamber events, focal plane position spectra such as the one in Fig. 4.7 may be generated. The full range of scattering angles, from $\theta_{K600} = -1.91^\circ$ to $\theta_{K600} = 1.91^\circ$ with respect to the central spectrometer angle, is covered for most of the 800-mm range of focal plane position which is represented by this spectrum.

The focal plane position spectrum may be converted to excitation energy, and the conversion is approximately linear, although a small quadratic term is necessary to obtain an accurate energy calibration. This procedure is discussed in Section 4.2.4. Triton energy increases from left to right and excitation energy from right to left in Fig. 4.7.

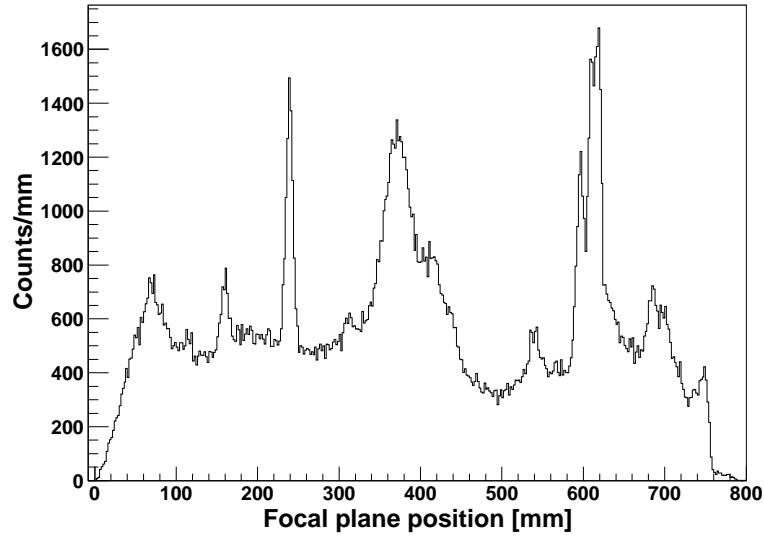


FIG. 4.7: A focal plane position spectrum measured at $\theta_{lab} = 0^\circ$ and the magnetic field setting for tritons at $E_t = 33.5$ MeV

4.2 Analysis of the 52 MeV (p,t) data set

The method of analysis for data acquired at the various field settings described in Sections 4.2 to 4.6 are very similar. Therefore, a detailed description of the analysis methods, which were also employed for the succeeding data sets, is given in this section.

The 52 MeV (p,t) field setting data were taken with the paddle trigger logic of P1 only, as was the case for all (p,t) data during this experiment. Currents were applied to the K600 magnets to induce the appropriate magnetic fields to measure tritons with energies close to 52 MeV in the focal plane of the spectrometer. Data at $\theta_{lab} = 0^\circ$ and $\theta_{lab} = 7^\circ$ were taken during Weekend 2, while data at $\theta_{lab} = 16^\circ$ and $\theta_{lab} = 27^\circ$ were taken during Weekend 4 with respective beam energies of $E_p = 60.5$ MeV and $E_p = 60.01$ MeV as shown in Table 1.2 in Chapter 1. The $^{22}\text{Ne}(p,t)^{20}\text{Ne}$ reaction has a Q -value of $Q = -8.64$ MeV [56], so with a 60.0 MeV beam one could expect to measure the ground state of ^{20}Ne at a triton energy of $E_t = 51.36$ MeV. This makes the 52 MeV field setting appropriate for investigating the lowest excitation energy states of ^{20}Ne .

4.2.1 Background clean-up with particle identification gates

By performing magnetic rigidity calculations, considering that $Q = -8.14$ MeV for the $^{22}\text{Ne}(p,d)^{21}\text{Ne}$ reaction [56], it was found that no other particles with significant cross sections could be expected to reach the focal plane of the spectrometer at this field setting.

In Fig. 4.8, the triton locus is in the black rectangle within which the PID gates were set. The strong locus at TOF = 220 ns to TOF = 265 ns is from beam-related background, which is prevalent with the (p,t) reaction close to $\theta_{lab} = 0^\circ$ and predominantly related to the L-shaped beam stop. The line at 3300 in Paddle 1 light output is related to the pulser, and the background below 500 in light output is related to radiation from within the vault. These data were acquired with a beam current of $I_p = 5$ nA for a duration of 62 minutes on a ^{22}Ne gas cell target with a pressure of $P = 1.45$ bar. The central angle of the spectrometer was set at $\theta_{lab} = 0.5^\circ$. This shift from the $\theta_{lab} = 0^\circ$ setting was chosen because the L-shaped beam stop obstructed the triton ejectiles from $\theta_{lab} = -2^\circ$ to $\theta_{lab} = -1.5^\circ$ in this energy region. The same problem was experienced with some of the $\theta_{lab} = 7^\circ$ data, resulting in smaller angular ranges and different central angles for the measurements of certain experimental peaks. Any shifts from central angles of $\theta_{lab} = 0^\circ$ or $\theta_{lab} = 7^\circ$ in data sets which were intended for these angles were necessitated by particle obstruction by the beam stop.

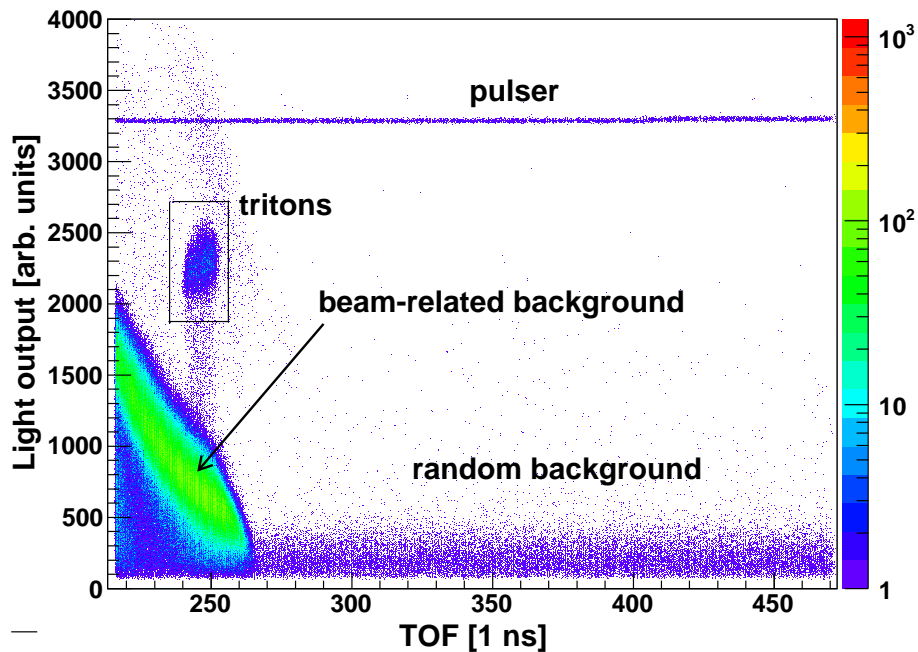


FIG. 4.8: The measured Paddle 1 vs TOF spectrum for the 52 MeV (p,t) field setting at $\theta_{lab} = 0.5^\circ$. The PID gates were set as indicated by the black rectangle which contains the locus that represents the tritons from the $^{22}\text{Ne}(p,t)^{20}\text{Ne}$ reaction.

For the measurement at the $E_t = 52$ MeV and $\theta_{lab} = 0.5^\circ$ setting, the X-U wire chamber configuration was used for the second drift chamber, which means that Y- (vertical) position information was gathered in addition to X- (horizontal) position information. The Y-position information was used as an additional tool to remove background data because it may be used to identify events from particles which do not have proper vertical focusing, e.g. particles scattered off the beam stop, cosmic particles, etc. Fig. 4.9 illustrates the software gates for Y which were used for this setting.

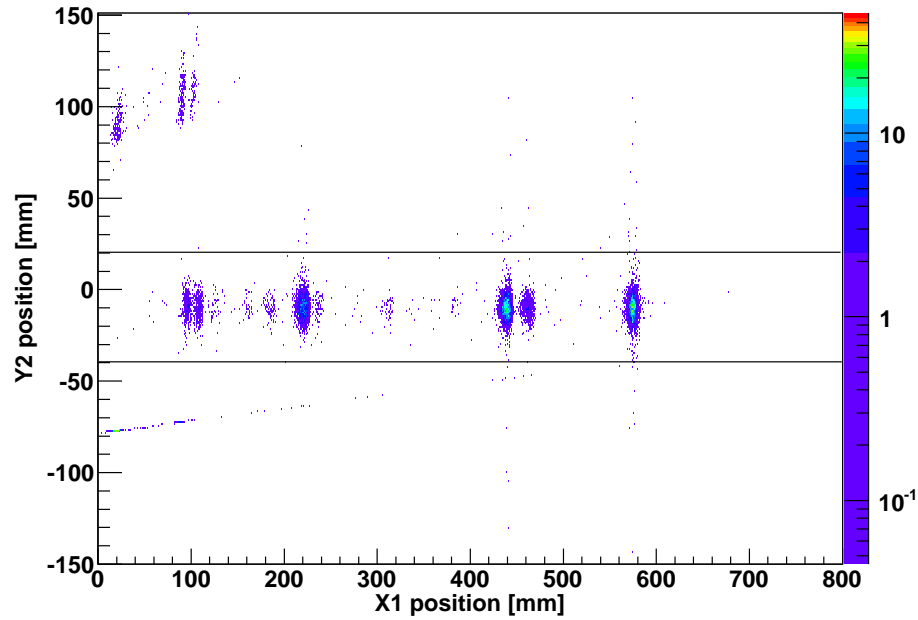


FIG. 4.9: The measured Y2 position vs X1 position spectrum for the 52 MeV (p,t) field setting at $\theta_{lab} = 0.5^\circ$. The gates for data with acceptable vertical focusing were set within the two black lines.

4.2.2 Kinematic corrections

Particles were measured at the focal plane over a range of scattering angles of $\Delta\theta_{lab} = \pm 1.91^\circ$. The spectra in Fig. 4.10 a) and b), which were measured at $\theta_{lab} = 7^\circ$, illustrate this by showing the angular spread of events captured over a 100 mm range in the focal plane position. In Fig. 4.10 a) the positions of the states display an angular dependency which will have a detrimental effect on the position resolution. This was reduced during offline analysis by straightening the ^{20}Ne locii and thereby generating the spectrum in Fig. 4.10 b). Fig. 4.10 c) is a projection onto the x-axis of Fig. 4.10 b).

Due to the difference in kinematics, tritons produced in the $^{22}\text{Ne}(p,t)^{20}\text{Ne}$ reaction will produce loci in the scattering angle vs position spectrum which have slopes that are different from tritons produced from other target nuclei. This can be seen in Fig. 4.10 b) where the peak to the right of the 2^+ 1.633 MeV peak in ^{20}Ne has a slightly different slope from the peaks related to the $^{22}\text{Ne}(p,t)^{20}\text{Ne}$ reaction. Kinematic calculations indicate that the ground state of ^{35}Cl may be expected at about 270 keV above the first 2^+ state of ^{20}Ne in triton energy. It was presumed that the peak to the right of the 1.633 MeV peak may be associated with the aforementioned state, which would be populated by the $^{37}\text{Cl}(p,t)^{35}\text{Cl}$ reaction from chlorine in the aramid foil. This was later confirmed by a calibration in triton energy.

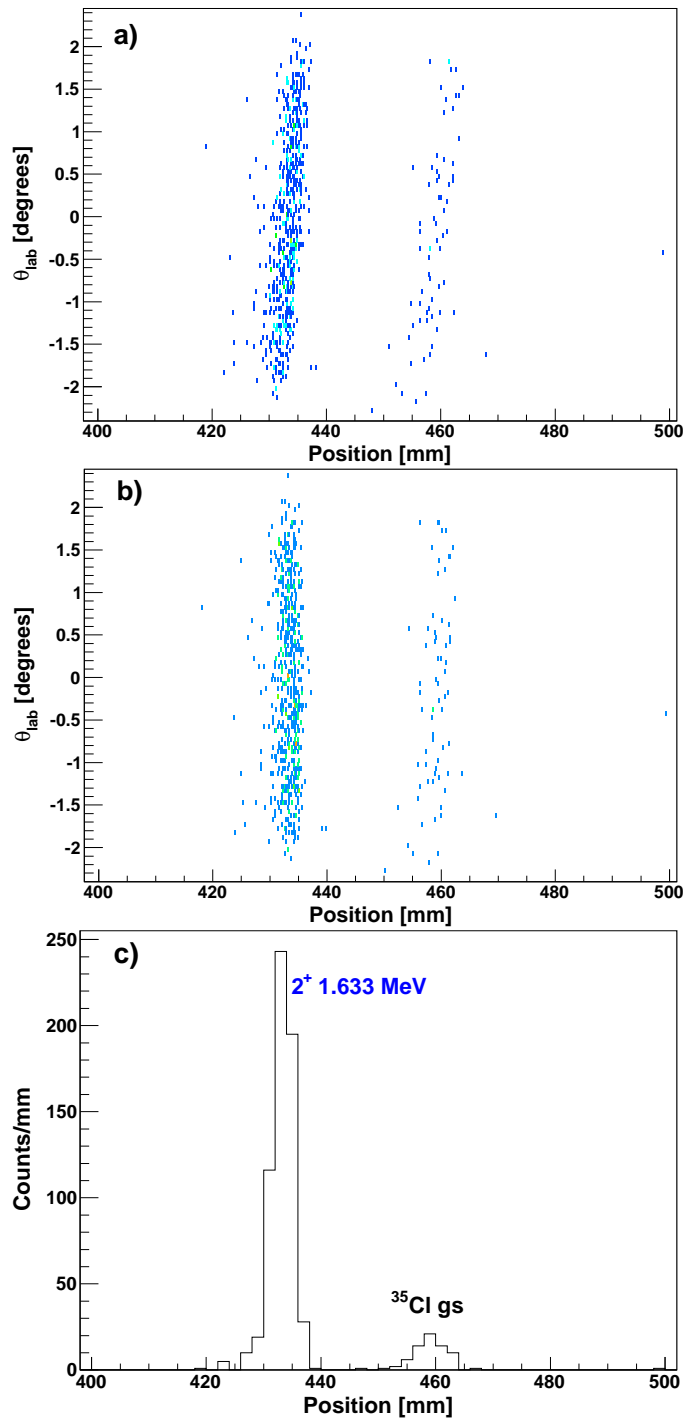


FIG. 4.10: A section of the measured spectrum of θ_{lab} vs X focal plane position for the 52 MeV (p,t) field setting centred at $\theta_{lab} = 7^\circ$ is shown without any shape correction in a), and with a correction in b). A projection of the spectrum in b) on the focal plane position is shown in c).

4.2.3 Background targets

Two different targets were used to investigate the aramid-related background in the $^{22}\text{Ne}(p,t)^{20}\text{Ne}$ data spectra:

1. The first consisted of an empty gas cell target, therefore one 6- μm layer of aramid material followed by another 6 μm of aramid 1 cm apart (see Section 3.5.2). Data were taken with this target for about 20 minutes, with a beam current of $I_p = 5.3$ nA and a count rate of about 600 Hz.
2. The second consisted of a single strip of aramid with a thickness of 12.5 μm (6 μm in Weekend 4). This target was placed in a beam current of $I_p = 5.3$ nA for about 30 minutes, during which time data were collected at a rate of 680 Hz.

Essentially, the two targets should have given approximately the same results since there should not have been any gas between the two layers of aramid in the first background target, and the second target had nearly the same thickness as the first. In practice, however, there was a gas leakage from the ^{22}Ne gas cell into the empty background cell. In Fig. 4.11 one observes that there are some weak states in b), with the empty gas cell target, which do not appear in a) when the single aramid foil is the target. These weak states in b) correspond to strong states in c), which is the ^{22}Ne gas-filled target spectrum, thus indicating that the weak states in b) could be associated with neon.

If the gas cell is kept below atmospheric pressure, in-gassing might occur through a valve outside of the scattering chamber in the gas line to the ^{22}Ne bottle. This puts the purity of the ^{22}Ne gas target at risk.

With out-gassing one risks the reliability of the empty gas cell target, but this may be substituted for the single layer of aramid. Hence, it was decided to keep the pressure high above standard atmospheric pressure at $P = 1.5$ bar. This provides the advantage that the areal density of material, and hence the statistics, is increased. This is advantageous up to some limit where the resolution is adversely affected by the density of material.

According to kinematic calculations, the positions of the neon peaks in Fig. 4.11 c) are consistent with the lowest excitation energy states of ^{20}Ne with the strong peak furthest to the right being the ground state.

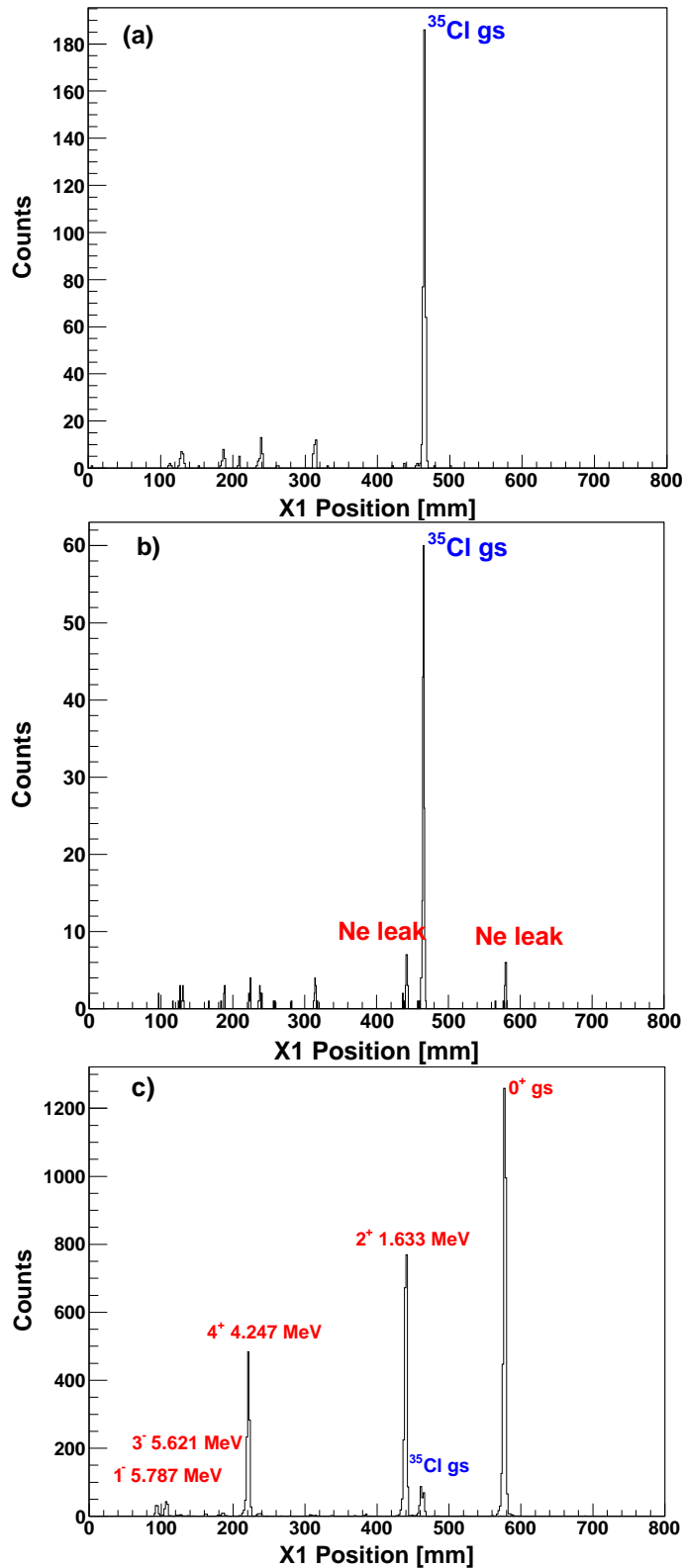


FIG. 4.11: Background data measured with the single $12.5\text{-}\mu\text{m}$ aramid layer and the empty gas cell at $\theta_{lab} = 0.5^\circ$ are shown in a) and b) respectively, while c) shows data which were taken at the same angle with a gas cell filled with ^{22}Ne gas. The energy values of the known states were obtained from the EXFOR database [3].

As mentioned before, the 52 MeV field setting was investigated at four different angles. This was done with the approximate parameter-values indicated in Table 4.1.

θ_{lab}	Beam energy	I_p	Count rate	Time	Pressure
[degrees]	[MeV]	[nA]	[Hz]	[minutes]	[bar]
0.5	60.50	5	600	62	1.45
7	60.50	9	100	11	1.4
16	60.01	21	1060	32	1.4
27	60.01	14	700	27	1.5

TABLE 4.1: Parameter-values with which the 52 MeV (p,t) field setting was investigated

4.2.4 The calibration procedure

The first three states of ^{20}Ne could be quickly identified in spectra such as in Fig. 4.11 c), by looking at the distances between these peaks and the line shapes of these peaks in θ_{lab} vs X focal plane position spectra such as is shown in Fig. 4.10 b). A preliminary quadratic calibration with these three peaks revealed the two weak peaks at around Xpos = 100 mm in Fig. 4.11 c) to be the excited states of ^{20}Ne at $E_x = 5.621$ MeV and $E_x = 5.788$ MeV. Hence, five peaks in the $^{22}\text{Ne}(p,t)^{20}\text{Ne}$ spectrum in Fig. 4.11 c) were assigned to the known states mentioned in Table 4.2. Based on these assumptions and the measured focal plane positions of these states, quadratic calibrations of both triton energy and excitation energy to focal plane position were obtained.

Known experimental value [keV]	J^π	Position [mm]	Position w.r.t. ground state [mm]	Triton momentum [MeV/c]
0	0^+	577.4	0	536.8
1634	2^+	439.5	137.9	528.5
4248	4^+	221.0	356.4	514.9
5621	3^-	107.3	470.1	507.6
5788	1^-	94.3	483.1	506.7

TABLE 4.2: The measured excitation energy values of the ^{20}Ne energy levels, adopted in the literature, in the 1st column [3] are matched to the positions of the discrete experimental peaks in the 3rd and 4th columns, for the case of the 52 MeV field setting at $\theta_{lab} = 0.5^\circ$.

The calibration procedure is as follows:

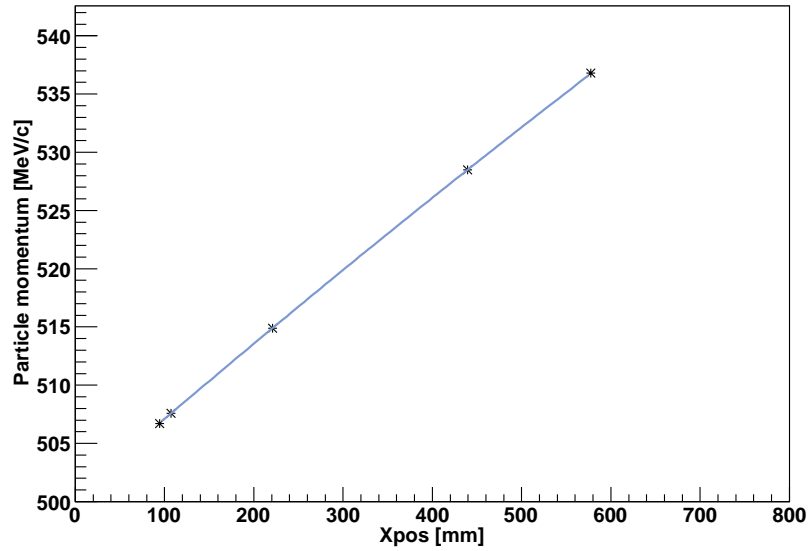


FIG. 4.12: Fit on the calibration points from Table 4.2 to illustrate the approximately linear relationship between particle momentum and focal plane position

1. Using the states already identified, a quadratic fit of momentum to focal plane position is obtained.
2. This fit is used with the relationship between triton energy E_t , momentum P and particle mass m , working in natural units

$$E_t = \sqrt{m^2 + P^2} - m \quad (4.2)$$

to provide values for the triton energy at any position in the focal plane.

3. Triton energy is converted to ^{20}Ne excitation energy E_x using the equation for the two-body reaction:

$$E_x = E_p + m_T - E_t - E_r \quad (4.3)$$

where E_p represents the total energy of the projectile, m_T is the mass of the target nucleus, E_t is the total energy of the ejectile and E_r is the total energy of the residual target nucleus. The residual target nucleus energy is calculated to be [111]

$$E_r = \sqrt{((P_0)^2 + (P_2)^2 - 2.P_0.P_2.\cos(\theta) + (m_3)^2)}. \quad (4.4)$$

Eventually the following quadratic relationship between excitation energy E_x and horizontal focal plane position X_{pos} was obtained:

$$E_x = (3.15464 \times 10^{-7})X_{pos}^2 + (-0.0121708)X_{pos} + 6.9218. \quad (4.5)$$

Calibrations were obtained by employing the same procedure for all the different sets of field setting and angle which were investigated, in each case using a minimum of three states which could be identified with certainty. Thus an energy spectrum such as the one shown in Fig. 4.13, which was plotted with Eq. 4.5, was generated for every set of conditions. Fig. 4.14 shows the differences Δ between the mean values of the states in Fig. 4.13 and the known values of these states from EXFOR [3], thus proving the calibration to be accurate to within 30 keV.

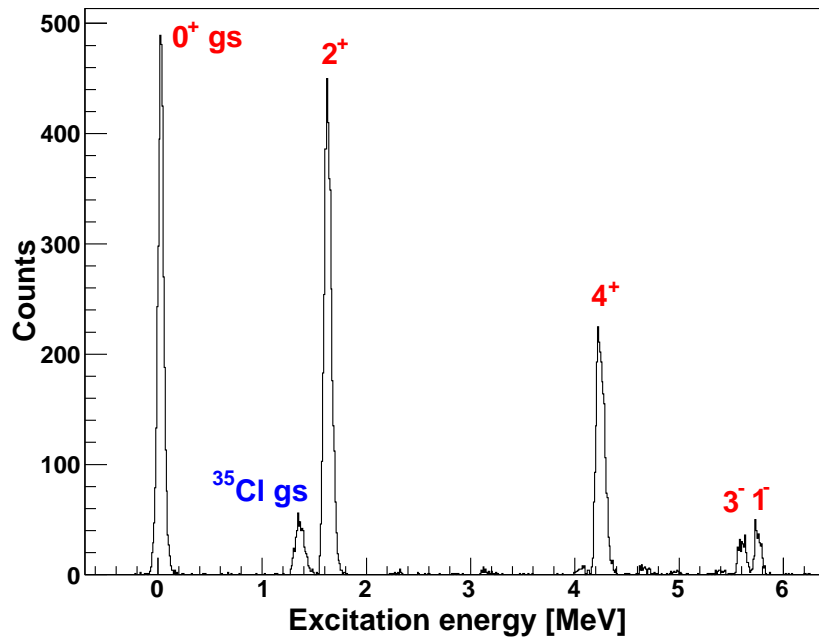


FIG. 4.13: An excitation energy spectrum for the 52 MeV $^{22}\text{Ne}(p,t)^{20}\text{Ne}$ field setting at $\theta_{lab} = 0.5^\circ$

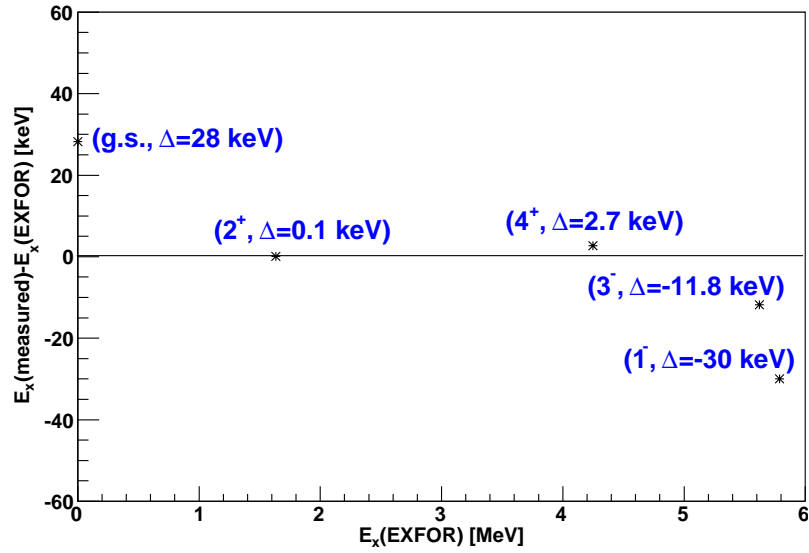


FIG. 4.14: The differences between the known values and the measured mean values from the energy calibration in the present experiment for the states observed with the 52 MeV $^{22}\text{Ne}(p,t)^{20}\text{Ne}$ field setting at $\theta_{lab} = 0.5^\circ$

4.3 Analysis of the 46 MeV and 48 MeV (p,t) data sets

The data at $\theta_{lab} = 0^\circ$ and $\theta_{lab} = 7^\circ$ were obtained with the 46 MeV field setting, while the data at $\theta_{lab} = 16^\circ$ were obtained with the 48 MeV field setting, yielding adequate results to link the data of this field setting to the 52 MeV setting from Section 4.2, as well as to the 42 and 41 MeV settings which are described in Section 4.4. Table 4.3 shows the recorded values of parameters for this step in ^{20}Ne excitation energy. The background data were collected with the parameter-values indicated in Table 4.4. The $^{22}\text{Ne}(p,t)^{20}\text{Ne}$ and background spectra which were measured at this field setting are shown in Fig. 4.15. The excitation energies of the known states in Fig. 4.15 were taken from the EXFOR database, as they were for all spectra or tables to come in this chapter.

θ_{lab} [degrees]	Field setting [MeV]	Weekend	I_p [nA]	Count rate [Hz]	Time [minutes]	Pressure [bar]
-0.5	46	2	5	650	331	1.5
7	46	2	20	200	114	1.3
16	48	1	20	40	52	0.5

TABLE 4.3: The various parameter-values with which the 46/48 MeV (p,t) field setting was investigated.

θ_{lab} [degrees]	Field setting [MeV]	Weekend	I_p [nA]	Count rate [Hz]	Time [minutes]	Target
-0.5	46	2	7.5	410	60	Empty cell
7	46	2	13	120	16	Empty cell
16	48	1	20	40	52	Aramid foil

TABLE 4.4: The parameter-values with which the 46 - 48 MeV (p,t) field setting background data were obtained

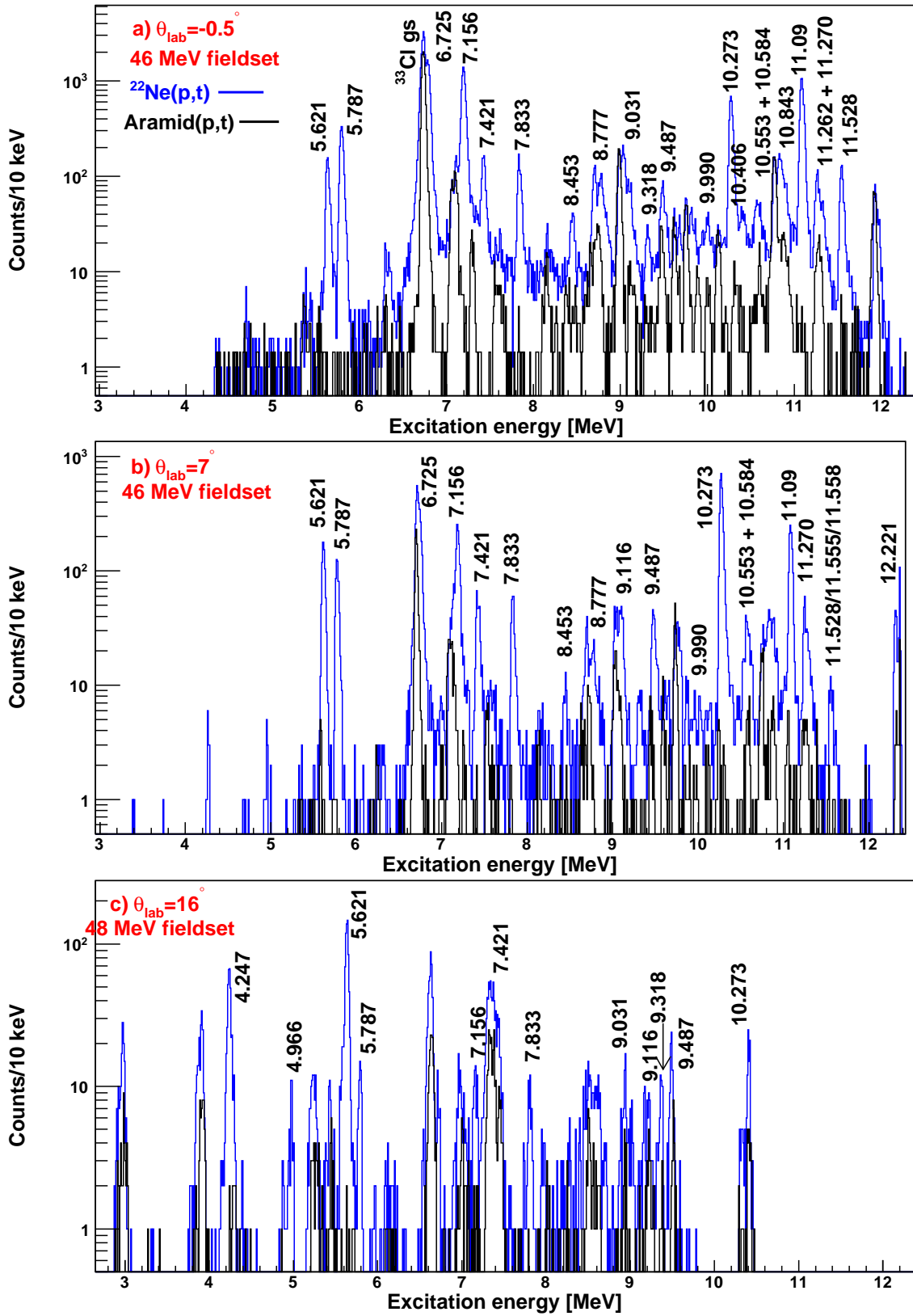


FIG. 4.15: The calibrated excitation energy spectra from the 46 MeV and 48 MeV (p,t) field settings

4.4 Analysis of the 41 MeV and 42 MeV (p,t) data sets

The data at $\theta_{lab} = -0.5^\circ$ were obtained with the 41 MeV field setting over the second weekend, while the data at $\theta_{lab} = 7^\circ$ and $\theta_{lab} = 16^\circ$ were obtained with the 42 MeV field setting during the fourth weekend. Table 4.5 shows the approximate values of the parameters which were employed with the ^{22}Ne gas in the gas cell target at this field setting, while Table 4.6 shows the parameter-values which were employed to measure the background. The $^{22}\text{Ne}(p,t)^{20}\text{Ne}$ and background spectra which were measured at this field setting are shown in Fig. 4.16. These spectra could be linked to the excitation energy spectra in Section 4.3, and were also used to understand the data at the next field setting, which are discussed in Section 4.5.

θ_{lab}	Field setting	Weekend	I_p	Count rate	Time	Pressure
[degrees]	[MeV]		[nA]	[Hz]	[minutes]	[bar]
-0.5	41	2	8	500	394	1.5
7	42	4	22	1200	59	1.35
16	42	4	22	1100	63	1.35

TABLE 4.5: Parameter-values with which the 41/42 MeV (p,t) field setting was investigated

θ_{lab}	Field setting	Weekend	I_p	Count rate	Time	Target
[degrees]	[MeV]		[nA]	[Hz]	[minutes]	
-0.5	41	2	7.5	410	166	Empty cell
7	42	4	19	960	31	Aramid foil
16	42	4	20	1000	30	Aramid foil

TABLE 4.6: Values of parameters for the background data of the 41/42 MeV (p,t) field setting

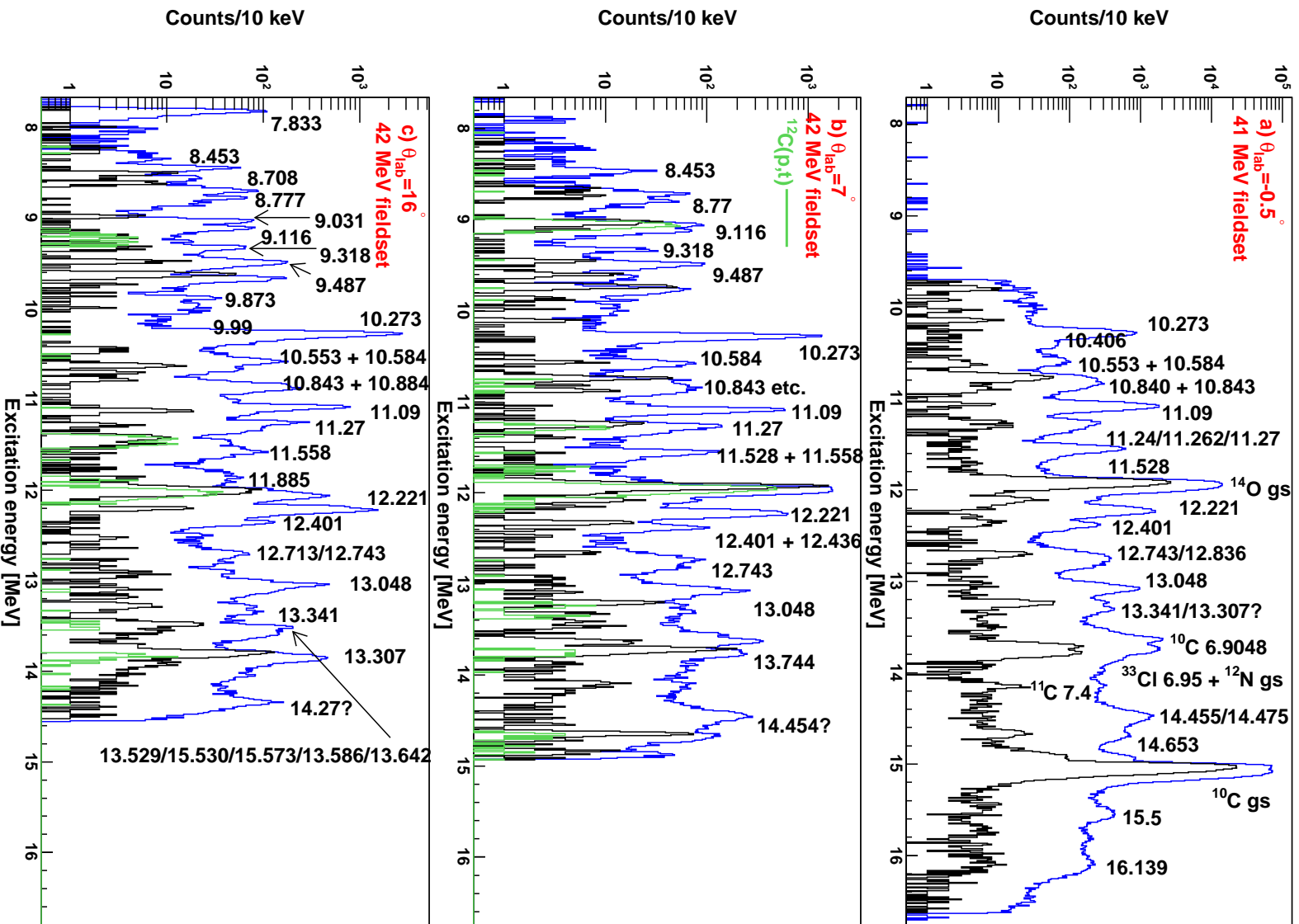


FIG. 4.16: The calibrated excitation energy spectra from the 41 MeV and 42 MeV (p, t) field settings

4.5 Analysis of the 36 MeV and 37 MeV (p,t) data sets

The data at $\theta_{lab} = -1^\circ$ were obtained with the 36 MeV field setting during the second weekend, while the data at $\theta_{lab} = 7^\circ$ and $\theta_{lab} = 16^\circ$ were obtained with the 37 MeV field setting over the fourth weekend. Table 4.7 shows the approximate values of the parameters which were employed with the ^{22}Ne gas in the target cell, while Table 4.8 shows the parameter-values for the background measurements. The deuterons are very prominent in Fig. 4.17, as could be expected from rigidity calculations. Nevertheless, the tritons could be separated from any contaminant particles by setting a software gate within the black rectangle in Fig. 4.17.

θ_{lab}	Field setting	Weekend	I_p	Count rate	Time	Pressure
[degrees]	[MeV]		[nA]	[Hz]	[minutes]	[bar]
-1	36	2	1.5	380	361	1.5
7	37	4	17	1400	60	1.35
16	37	4	17	1100	62	1.35

TABLE 4.7: Parameter-values with which the 36/37 MeV (p,t) field setting was investigated

θ_{lab}	Field setting	Weekend	I_p	Count rate	Time	Target
[degrees]	[MeV]		[nA]	[Hz]	[minutes]	
-1	36	2	1.4	350	127	Empty cell
7	37	4	15	850	37	Aramid foil
16	37	4	20	1100	31	Aramid foil

TABLE 4.8: Values of parameters for the background measurement with the 36/37 MeV (p,t) field setting

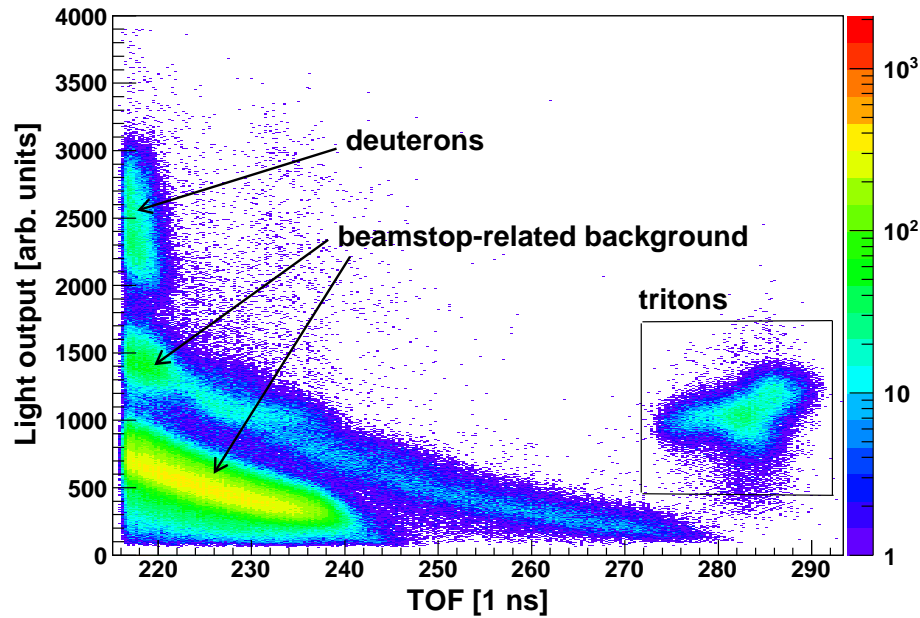


FIG. 4.17: The measured Paddle 1 vs TOF spectrum for the 36 MeV (p,t) field setting at $\theta_{lab} = -1^\circ$. The tritons are indicated by the black rectangle.

The $^{22}\text{Ne}(p,t)^{20}\text{Ne}$ and background spectra which were measured at this field setting are shown in Fig. 4.18. This is the first magnetic field setting which crosses into the excitation energy region beyond the $5\text{-}\alpha$ break-up threshold at $E_x = 19.17$ MeV in ^{20}Ne . This threshold value is indicated by a green line in Fig. 4.18 a). The state at $E_x = 16.73$ MeV, which is seen very clearly in all three spectra in Fig. 4.18, is the highest known state in ^{20}Ne with a confirmed 0^+ character. It is also the second highest known isospin $T = 2$ state in ^{20}Ne . The highest known $T = 2$ state is seen clearly at $E_x = 18.43$ MeV in c). This state coincides with the $E_x = 6.59$ MeV state from ^{14}O in a), and in b) it is obscured by the second peak of the $E_x = 3.3537$ MeV state from ^{10}C . These data were sufficient to provide the link to the next field setting, described in Section 4.6, which reveals the most important energy region of this experiment.

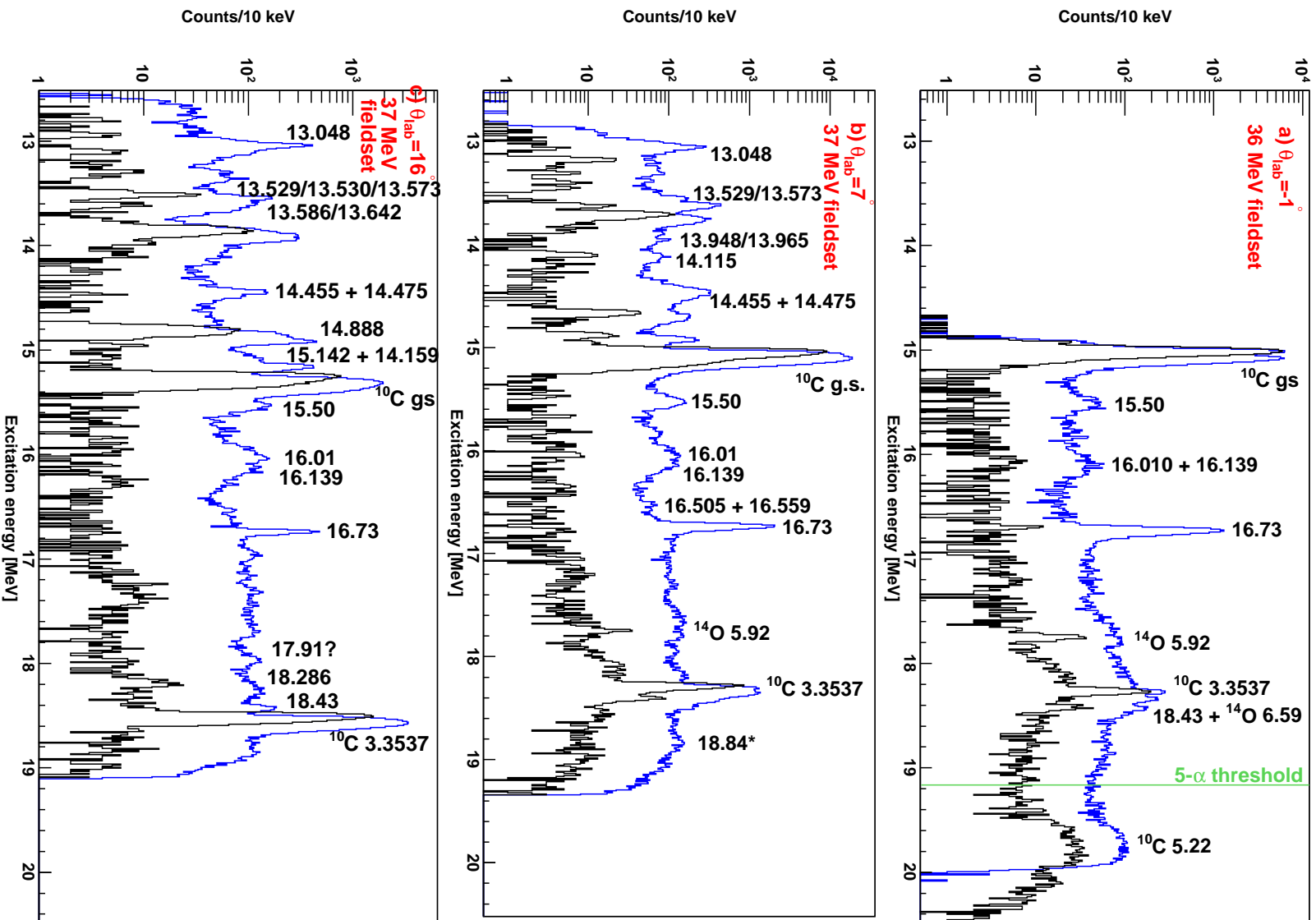


FIG. 4.18: The calibrated excitation energy spectra from the 36 MeV and 37 MeV (p,t) field settings

This experiment experienced the occurrence of contaminant ‘double-peaking’ i.e. two peaks spaced roughly 40 keV apart observed for each state measured in the aramid foils. Fig. 4.19 illustrates this effect for the case of the ground state of ^{10}C , which also displays a visible double-peaked structure in Fig. 4.18 a). This resulted from energy loss by the particles traversing the 1 cm of Ne-gas at pressures close to $P = 1.5$ bar, as illustrated in Fig. 4.20.

Tritons from the first foil reach the focal plane with lower triton momenta due to the greater energy loss of tritons compared to protons in the ^{22}Ne gas. Hence, the peak to the right in the blue spectrum in Fig. 4.19 represents events from the (p,t) reaction in the second carbon foil, while the peak to the left represents events from the first. The peak in the black spectrum occurs at a slightly higher triton momentum than both in the blue spectrum, since the tritons traverse one less foil and no ^{22}Ne gas.

This effect had to be taken into account for background subtraction and calibrations based on the aramid data.

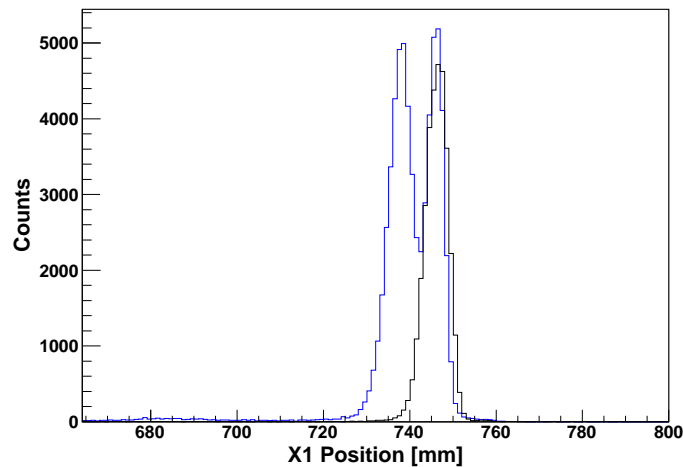


FIG. 4.19: The ground state of ^{10}C , as observed with a single $6\text{-}\mu\text{m}$ -thick aramid foil (black spectrum) and two aramid foils separated by 10 mm of ^{22}Ne gas (blue spectrum). The triton energy increases from left to right.

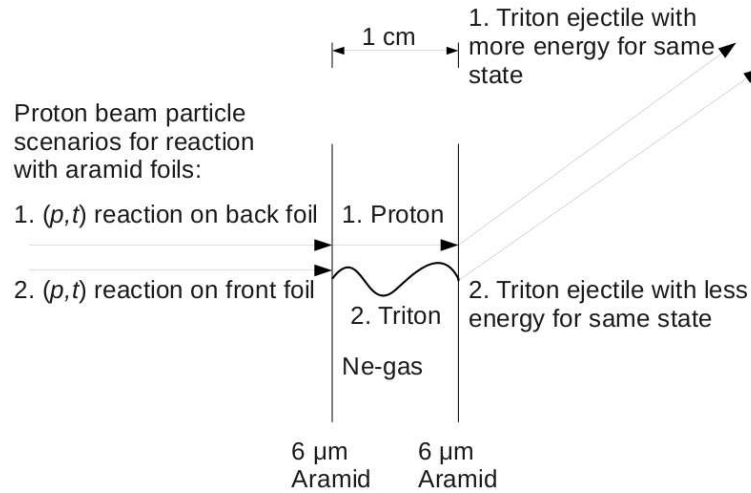


FIG. 4.20: Ejectile triton particles may come from either the 2^{nd} or back aramid foil as in scenario 1, or from the 1^{st} or front foil, as in scenario 2. Tritons from the 2^{nd} foil will lose less energy to the ^{22}Ne gas and therefore have higher triton momenta at the focal plane than tritons from the 1^{st} . Hence, in the blue spectrum in Fig. 4.19, tritons from the 1^{st} foil generate the peak to the left, and tritons from the 2^{nd} foil generate the peak to the right.

4.6 Analysis of the 33.5 MeV (p,t) data set

Investigating the data acquired at this field setting for low-spin states was the main objective of this study, hence it is also the setting with the longest counting times. The data at $\theta_{lab} = -1^\circ$ were obtained during the third weekend, while the data at $\theta_{lab} = 7^\circ$ were obtained during the third and fourth, and the data at $\theta_{lab} = 16^\circ$ and $\theta_{lab} = 27^\circ$ during the fourth weekend. The approximate parameter-values are shown in Table 4.9. Rigidity calculations indicated that tritons and deuterons were both likely to be found in the focal plane. Tritons could be expected to lose far less energy in Paddle 1, hence they were identified with the locus which is lower in energy loss, or paddle light output, shown in Fig. 4.21.

θ_{lab}	Target material	Weekend(s)	I_p	Count rate	Time	Pressure
[degrees]			[nA]	[Hz]	[minutes]	[bar]
-1	^{22}Ne + aramid	3	2.2	900	798	1.4
-1	Empty cell	3	2.3	800	862	
7	^{22}Ne + aramid	3,4	16	1200	307	1.5
7	Empty cell	3,4	15	1000	239	
16	^{22}Ne + aramid	4	13	980	895	1.4
16	Aramid foil	4	14	700	192	
27	^{22}Ne + aramid	4	14	700	579	1.5
27	Aramid foil	4	13	730	230	

TABLE 4.9: Parameter-values with which the target material (^{22}Ne + aramid) and background material were investigated with the 33.5 MeV (p,t) field setting.

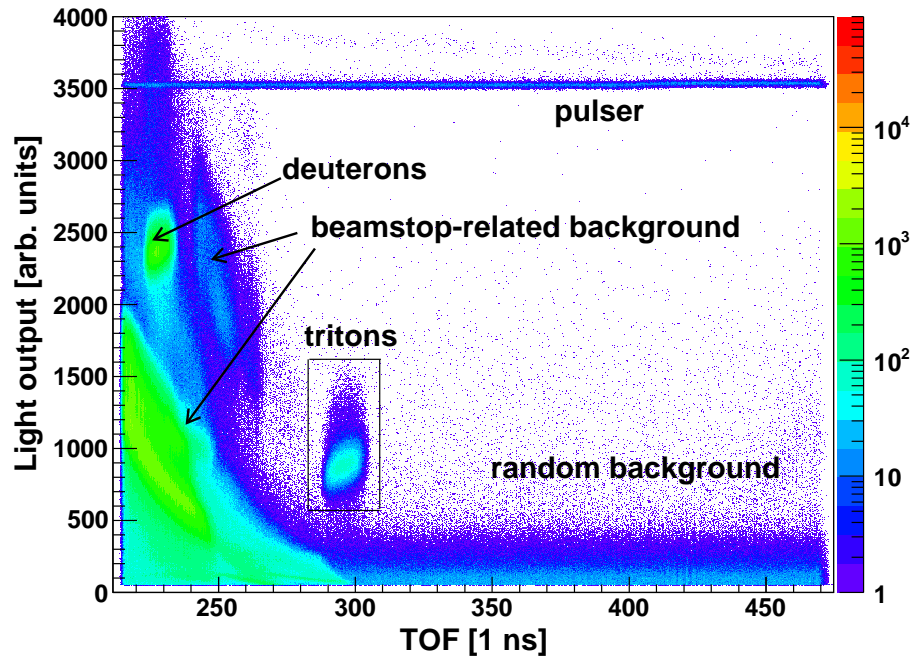


FIG. 4.21: The measured Paddle 1 vs TOF spectrum for the 33.5 MeV (p,t) field setting at $\theta_{lab} = -1^\circ$. The tritons are indicated by the black rectangle.

4.6.1 Mapping of background

Kinematic calculations indicated that carbon, oxygen and nitrogen, along with some of their less abundant isotopes, would interfere in the region of interest. Therefore it was imperative to know where the states from these elements could be expected in the focal plane energy spectra, and also to obtain sufficient data with plain aramid, without any neon gas, to make a sensible background subtraction during the analysis.

A carbon target was used as a first step towards mapping out the states from the aramid foils, and at the beginning of the third weekend the gas cell was also filled with natural oxygen, nitrogen, neon and argon gasses.

Table 4.10 shows the set of reactions that were expected to interfere with the anticipated triton energies of their ground states. Carbon, oxygen and nitrogen were investigated, since the aramid foils contained these elements. Natural ^{20}Ne was tested because it is the most abundant neon isotope and also present in the air, which always leaks into the scattering chamber vacuum. Lastly, the ^{40}Ar gas was also put in the gas cell, since 1% of the air consists of this gas. The less abundant isotopes of all these elements are also included in Table 4.10. The reactions from the chlorine isotopes are also listed, since this element is known to be present in the foils.

Table 4.10 indicates that the most abundant isotope on the aramid foil, namely ^{12}C , will cause significant contamination with discrete states through the ground and first few excited states of ^{10}C in the region of interest ($E_t = 28$ MeV to 35 MeV). This can also be an advantage, since these peaks can aid energy calibration in this region. Peaks from natural oxygen and nitrogen on the foil could also be expected to interfere.

The energy regions between these peaks could be expected to contain a continuum of states originating from other contaminants indicated in Table 4.10 with ground states at higher E_t values, and also from the ^{22}Ne gas. With sufficient background measurements, the background resulting from the aramid foils could be subtracted. However, this still leaves a continuum consisting of broad states of ^{20}Ne . States which are either narrow or strong should stand out from this continuum, especially if they are enhanced and the broad, high spin states are suppressed by the reaction and angle.

The $^{12}\text{C}(p,t)^{10}\text{C}$ spectra from the natural carbon foil in Figs. 4.22 a) and b) were useful as a tool to understand the $^{16}\text{O}(p,t)^{14}\text{O}$ spectra in Figs. 4.22 c) and d), since the ^{10}C ground and first excited states show up very clearly. These states would have triton kinetic energies

Material	Reaction	Q -value [MeV]	Excitation energy [MeV]	Triton energy [MeV]
Neon-22	$^{22}\text{Ne}(p,t)^{20}\text{Ne}$	-8.64	0	50.4
	$^{22}\text{Ne}(p,t)^{20}\text{Ne}$	-8.64	19.2	32.0
Carbon	$^{12}\text{C}(p,t)^{10}\text{C}$	-23.3	0	36.5
	$^{13}\text{C}(p,t)^{11}\text{C}$	-15.2	0	43.9
Oxygen	$^{16}\text{O}(p,t)^{14}\text{O}$	-20.4	0	39.4
	$^{18}\text{O}(p,t)^{16}\text{O}$	-3.7	0	54.3
	$^{17}\text{O}(p,t)^{15}\text{O}$	-11.3	0	47.1
Nitrogen	$^{14}\text{N}(p,t)^{12}\text{N}$	-22.1	0	37.7
	$^{15}\text{N}(p,t)^{13}\text{N}$	-12.9	0	45.4
Neon-20	$^{20}\text{Ne}(p,t)^{18}\text{Ne}$	-20.0	0	39.5
Argon	$^{40}\text{Ar}(p,t)^{38}\text{Ar}$	-7.99	0	51.5
	$^{36}\text{Ar}(p,t)^{34}\text{Ar}$	-19.5	0	40.2
	$^{38}\text{Ar}(p,t)^{36}\text{Ar}$	-12.1	0	47.4
Chlorine	$^{37}\text{Cl}(p,t)^{35}\text{Cl}$	-10.4	0	49.6
	$^{35}\text{Cl}(p,t)^{33}\text{Cl}$	-15.7	0	44.3

TABLE 4.10: Calculated triton ejectile energies for the ground states in the 5th column, from different possible reactions in the 2nd column. The first two rows show where the ground state and 5- α break-up threshold of ^{20}Ne from the $^{22}\text{Ne}(p,t)^{20}\text{Ne}$ reaction could be expected. All calculations were performed for a beam energy of $E_{lab} = 60$ MeV and a $K600$ angle of $\theta_{lab} = 0^\circ$. All Q -values are from Ref. [56].

of $E_t = 36.5$ MeV and $E_t = 33.3$ MeV respectively. After locating the ground and 1st excited states in the 36 MeV (p,t) field setting in Fig. 4.22 b), one could identify the broad peak in Fig. 4.22 a) and c) as the 2nd and 3rd excited states of ^{10}C . This broad peak comes from the carbon foil in a), and from the carbon in the aramid foil in c). These carbon peaks provide triton energy reference points in Figs. 4.22 d) and c). After the oxygen peaks in Fig. 4.22 d) were identified, the ^{14}O states at $E_x = 5.92$ MeV, $E_x = 6.59$ MeV and $E_x = 7.768$ MeV, and the ^{10}C $E_x = 3.3537$ MeV state, were also identified in Fig. 4.22 c), so the last mentioned spectrum could be understood and calibrated.

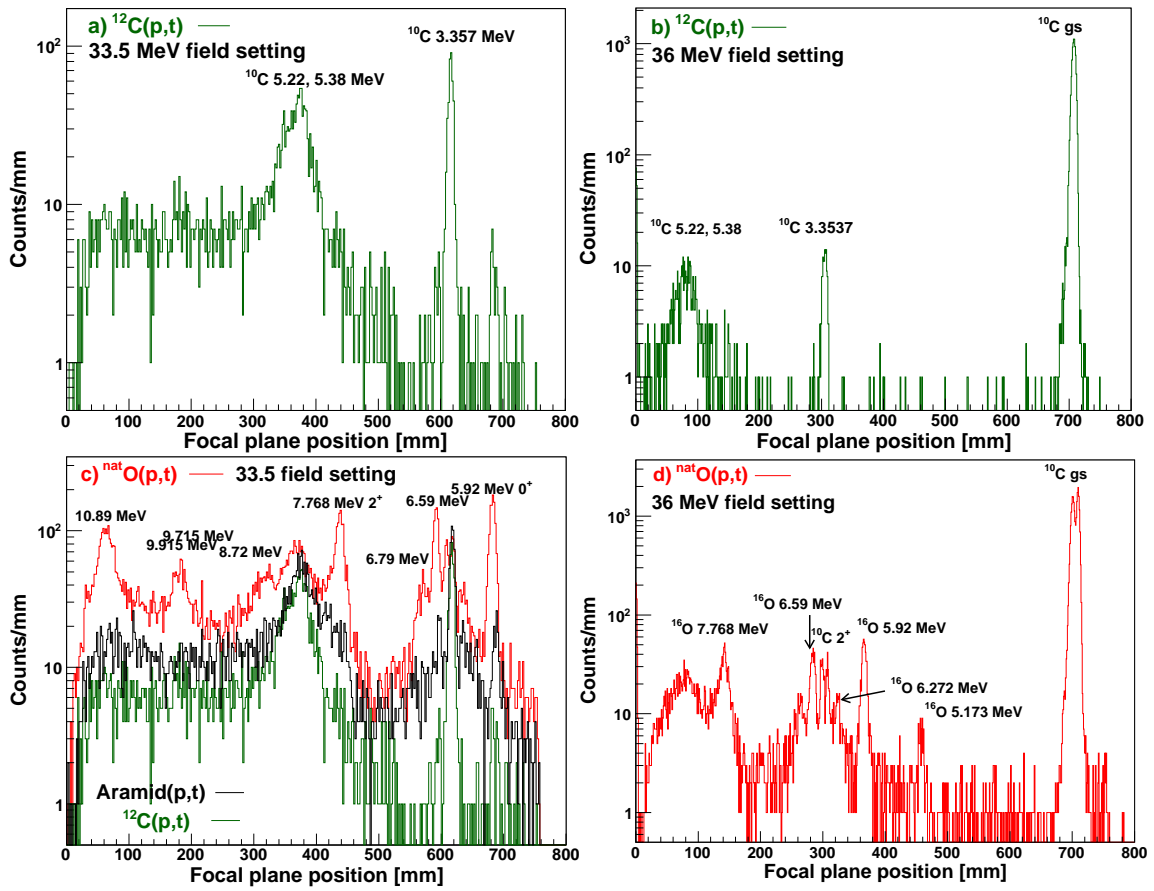


FIG. 4.22: The $^{12}\text{C}(p,t)^{10}\text{C}$ spectra from the carbon foil and $^{16}\text{O}(p,t)^{14}\text{O}$ spectra from the natural oxygen gas at $\theta_{\text{lab}} = -1^\circ$ for the 33.5 MeV and 36 MeV (p,t) field settings

4.6.2 Calibration with oxygen peaks

Oxygen peaks, listed in Table 4.11 and indicated in Fig. 4.23, were used for the energy calibration of the 33.5 MeV (p,t) field setting at $\theta_{lab} = -1^\circ$, since, with the $^{16}\text{O}(p,t)^{14}\text{O}$ reaction from the oxygen gas, the tritons must pass through the same average amount of gas and foil to reach the focal plane, as is the case with the $^{22}\text{Ne}(p,t)^{20}\text{Ne}$ reaction from the ^{22}Ne gas-filled target. Hence, this yields the most accurate calibration possible. According to the EXFOR database [3], the ^{14}O states at $E_x = 10.89$ MeV, $E_x = 9.915$ MeV and $E_x = 6.79$ MeV had never been measured with the (p,t) reaction before this experiment.

^{14}O Excitation energy [MeV]	J^π	Triton energy [MeV]	Position [mm]	Triton momentum [MeV/c]
7.768	0^+	33.65	437.2	436.1
6.59	2^+	33.01	591.6	431.9
5.92	2^+	31.88	682.0	424.4

TABLE 4.11: Known experimental excitation energy values of the energy levels of ^{14}O , taken from the literature [3], matched to the positions of the discrete experimental peaks, for the case of the 33.5 MeV (p,t) field setting at $\theta_{lab} = -1^\circ$

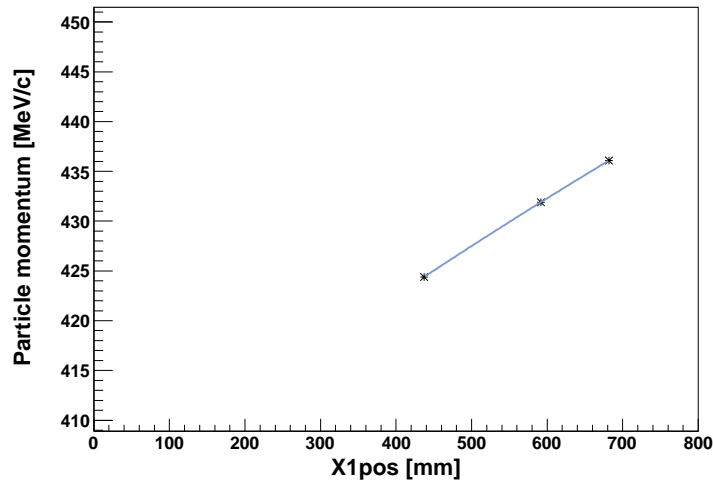


FIG. 4.23: Fit to illustrate the approximately linear relationship between the particle momentum and focal plane position for the states mentioned in Table 4.11.

4.6.3 Spectra from possible contaminants

The black spectrum in Fig. 4.24 a) and b) is from the measurement which was made on the foils prior to any gas being injected into the the gas cells at the beginning of the third weekend. In Fig. 4.24 a) it is evident that the strongest peaks from the aramid correspond to peaks also seen in the carbon spectrum, in green. The weaker peaks in the aramid spectrum seem to correspond to the oxygen spectrum (in red) and the nitrogen spectrum (in purple) in Fig. 4.24 b). This may be expected from the chemical composition of the aramid ($\text{C}_{14}\text{O}_2\text{N}_2\text{Cl}_2\text{H}_8$). No discrete states from the chlorine isotopes are known in this energy range.

Data measured with the ^{22}Ne gas-filled target are shown by the blue spectrum in Fig. 4.24 c). Two strong and narrow peaks between $X_{1\text{pos}} = 100$ mm and $X_{1\text{pos}} = 300$ mm which protrude from the background are seen in this spectrum. Two of the strong peaks in the ^{18}Ne spectrum in pink (at $X_{\text{pos}} = 305$ mm and $X_{\text{pos}} = 540$ mm) resulting from the measurement with the natural neon gas seem to correspond to two of the peaks in the blue spectrum. A comparison of the strengths of these peaks showed that the peaks in the $^{22}\text{Ne}(p,t)^{20}\text{Ne}$ spectrum were unlikely to originate from contaminant $^{20}\text{Ne}(p,t)^{18}\text{Ne}$ peaks.

The argon isotopes have reached their continuum region at this field setting, hence only the carbon peaks and one state from $^{38}\text{Ar}(p,t)^{36}\text{Ar}$ are observed in the orange argon spectrum in Fig. 4.24 c).

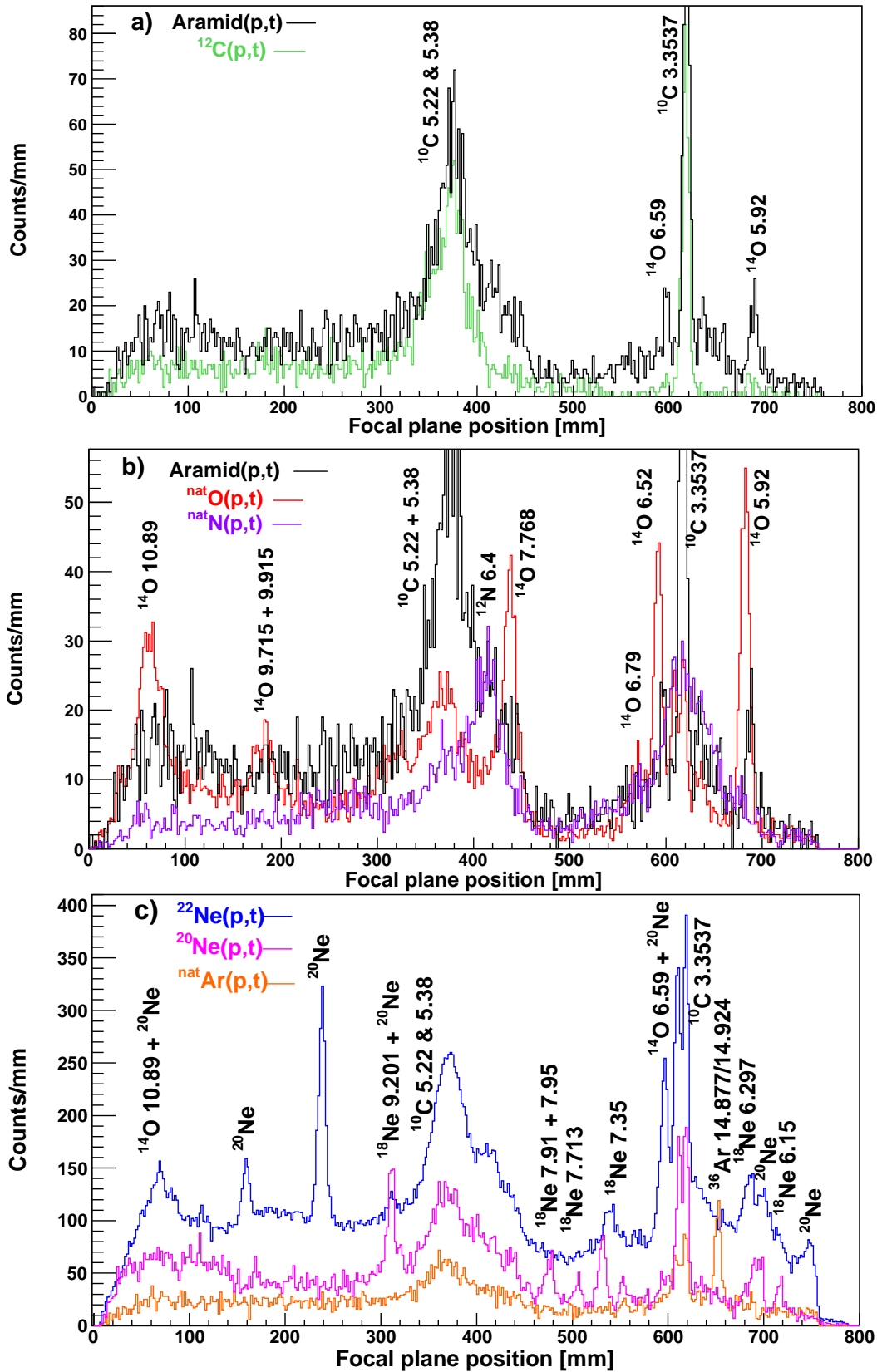


FIG. 4.24: The aramid and carbon data in a), compared to the natural oxygen and nitrogen data in b), and the natural neon, natural argon and ^{22}Ne data in c). All data were taken at $\theta_{\text{lab}} = -1^\circ$.

A number of states in ^{20}Ne which have not been experimentally observed prior to this experiment are seen in the ^{20}Ne excitation energy spectra in Fig. 4.25. Each such state is indicated by an asterisk next to its energy label (in MeV). Most notable are the three strong states at $E_x = 18.84$ MeV, $E_x = 21.16$ MeV and $E_x = 21.80$ MeV in Fig. 4.25, which are also seen at slightly different energies at $\theta_{lab} = 7^\circ$. This change in values probably results from the fact that the $\theta_{lab} = -1^\circ$ data were calibrated with the oxygen gas, while the $\theta_{lab} = 7^\circ$ data were calibrated with states from the aramid foil and the neon gas. Therefore, the values recorded at $\theta_{lab} = -1^\circ$ could be expected to be more accurate.

Upon closer inspection of the data at $\theta_{lab} = -1^\circ$, the state at $E_x = 18.84$ MeV appeared to be an amalgamation of states which could not be resolved in this experiment. Further suggestions of states around $E_x = 17.67$ MeV, $E_x = 20.59$ MeV and $E_x = 22.5$ MeV are discussed in forthcoming sections.

At $\theta_{lab} = 16^\circ$, in Fig. 4.26 a), a strong new state is observed at $E_x = 21.14$ MeV, which corresponds to the $E_x = 21.16$ MeV state measured at $\theta_{lab} = -1^\circ$. Unfortunately, the broad $E_x = 6.58$ MeV state from ^{10}C is centred at a ^{20}Ne energy of $E_x = 21.71$ MeV in this spectrum, and with an effective width of $\text{FWHM} = 406$ keV. This is much broader than the known width of this state ($\Gamma = 190$ keV), but a larger than natural effective width is expected because of the kinematic effect that results in a tilt in the $^{12}\text{C}(p,t)^{10}\text{C}$ lineshape. This broad peak blocks out the area at around $E_x = 21.80$ MeV where another ^{20}Ne state may be anticipated at $\theta_{lab} = 16^\circ$.

At $\theta_{lab} = 27^\circ$ in Fig. 4.26 b), the new state with $E_x = 21.16$ MeV is observed on the high excitation energy shoulder of the 2^{nd} and 3^{rd} excited states of ^{10}C . This may explain the fact that its observed energy ($E_x = 21.10$ MeV) is lower than what was measured at the other angles. The new state which may be expected at $E_x = 21.80$ MeV is not seen because it lies beyond the region of excitation energy which was investigated at this angle. The candidate new state at $E_x = 17.67$ MeV was seen at all four angles.

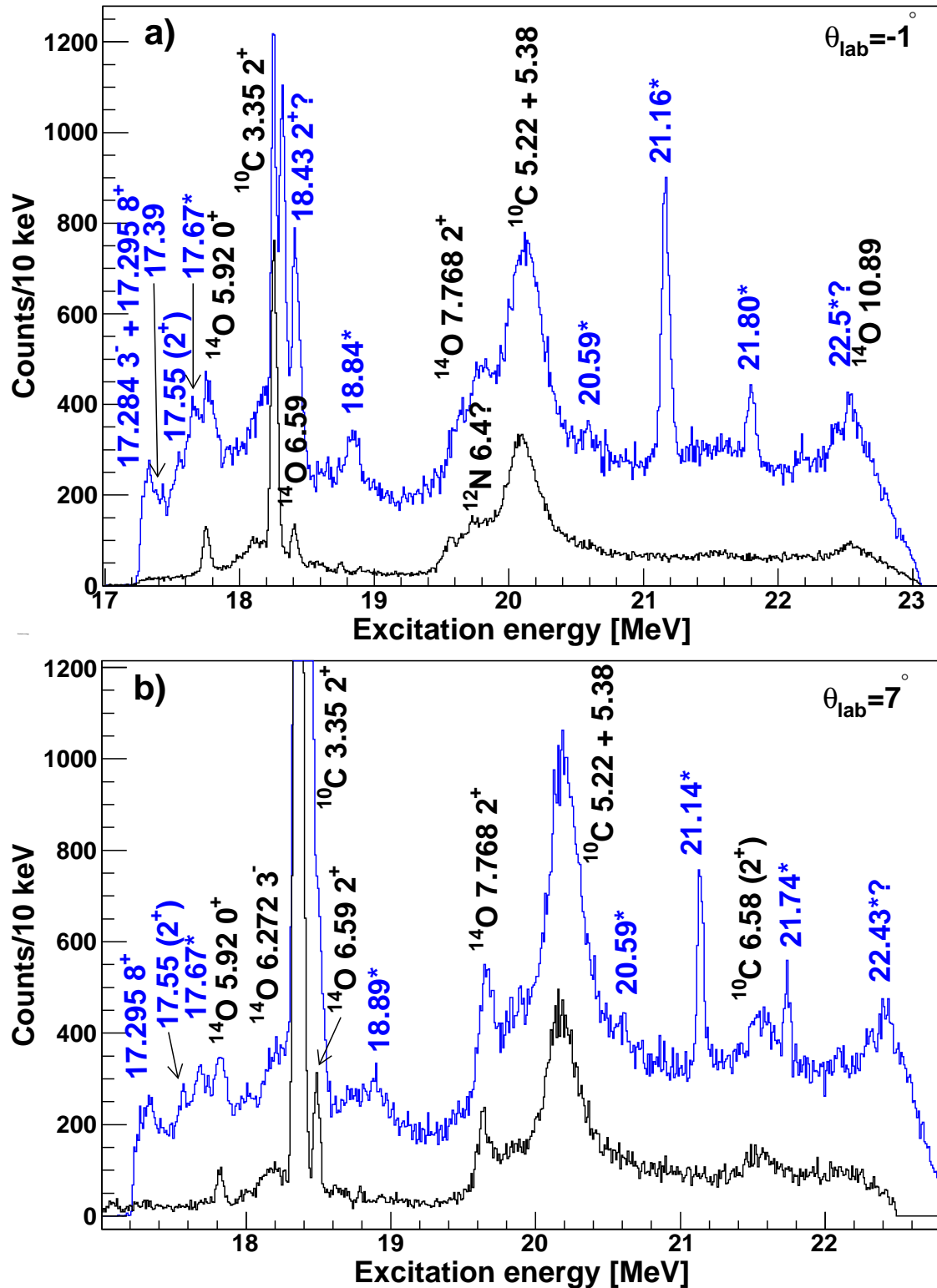


FIG. 4.25: Excitation energy spectra from $^{22}\text{Ne}(p,t)^{20}\text{Ne}$ and $\text{Aramid}(p,t)$ measured at $\theta_{\text{lab}} = -1^\circ$ and $\theta_{\text{lab}} = 7^\circ$ with the 33.5 MeV triton field setting are shown in a) and b) respectively. The energy values of the known states were obtained from the EXFOR database [3].

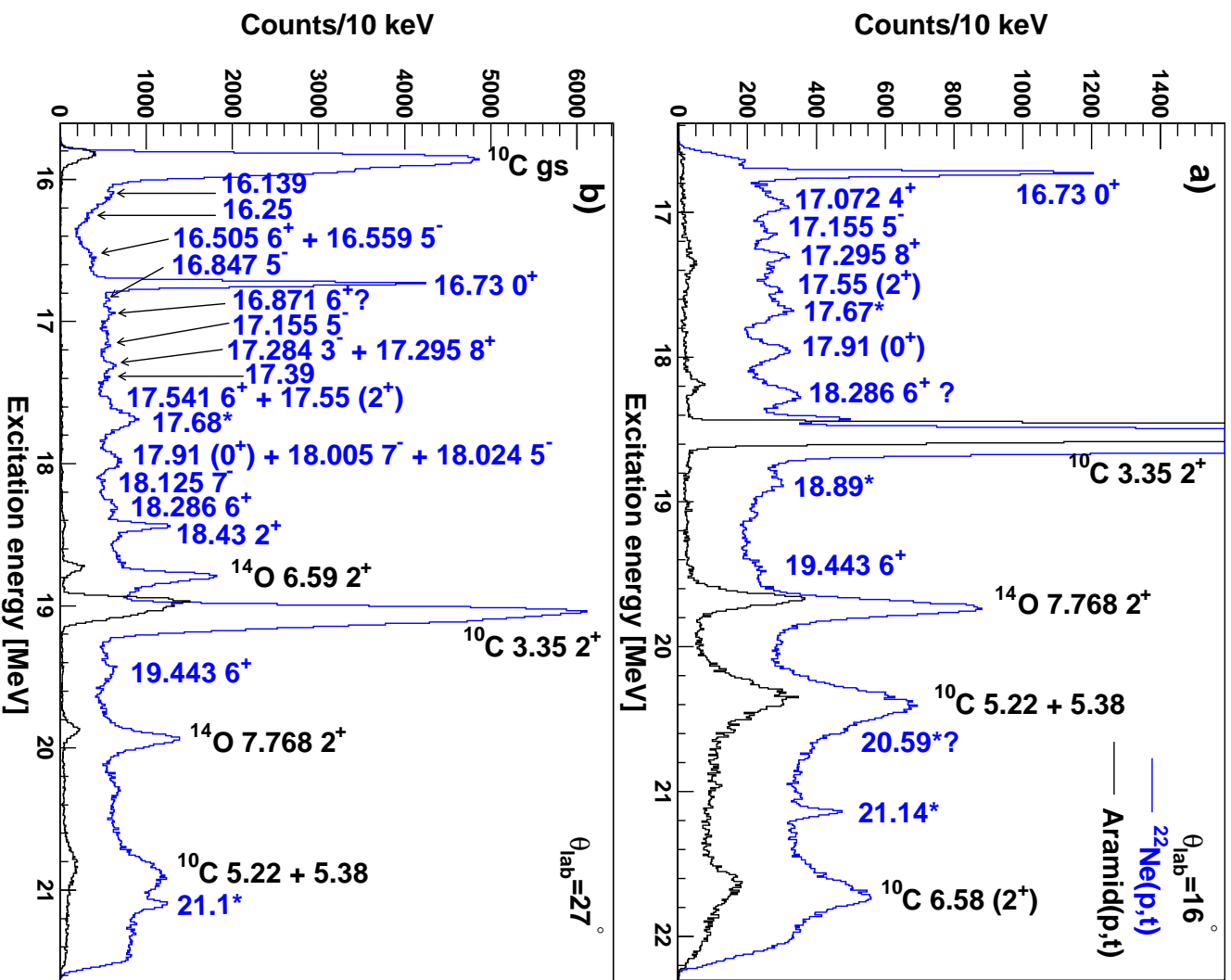


FIG. 4.26: The excitation energy spectrum for the 33.5 MeV (p,t) field setting is shown at $\theta_{\text{lab}} = 16^\circ$ in a), and at $\theta_{\text{lab}} = 27^\circ$ in b).

4.7 Summary of all data sets

Fig. 4.27 shows the values of the different terms which were used for each energy calibration at $\theta_{lab} \cong 0^\circ$. The constant and linear terms display an evident linear relationship to particle momentum. The deviations from the fits in this figure, Δa , Δb and Δc , were used to provide an estimate of the uncertainty in the measured triton momenta ΔP through Eq. 4.6:

$$\Delta P = \Delta a \cdot x^2 + \Delta b \cdot x + \Delta c, \quad (4.6)$$

where x represents the triton momentum of the observed state. The uncertainties in momentum values were then translated to uncertainties in energy values for all the newly observed states in ^{20}Ne at this field setting. Figs. 4.28 and 4.29 show data measured at $\theta_{lab} \cong 0^\circ$ from all the preceding field settings, joined together from $E_x = 0$ MeV to beyond $E_x = 20$ MeV (see Appendix B for the same spectra for larger angles). The data are normalised to the field setting which has the most statistics, which was the $E_t = 33.5$ MeV set in each case. This normalisation does not take into account the different angular ranges which are subtended due to slightly different central angles in Figs. 4.28 and 4.29. The continuity between adjacent field settings serves as further evidence that the energy calibrations may be trusted.

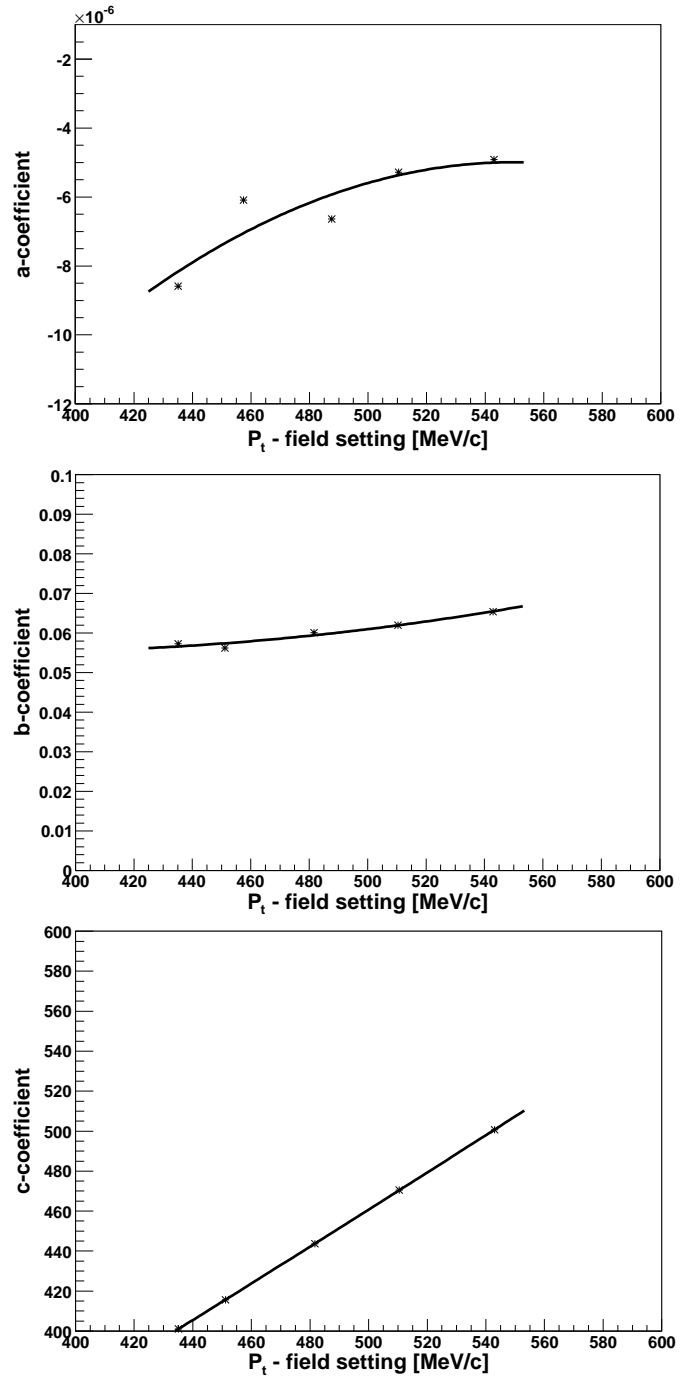


FIG. 4.27: The quadratic, linear and constant terms in the calibration equations are shown respectively from top to bottom for each energy setting at $\theta_{lab} \cong 0^\circ$.

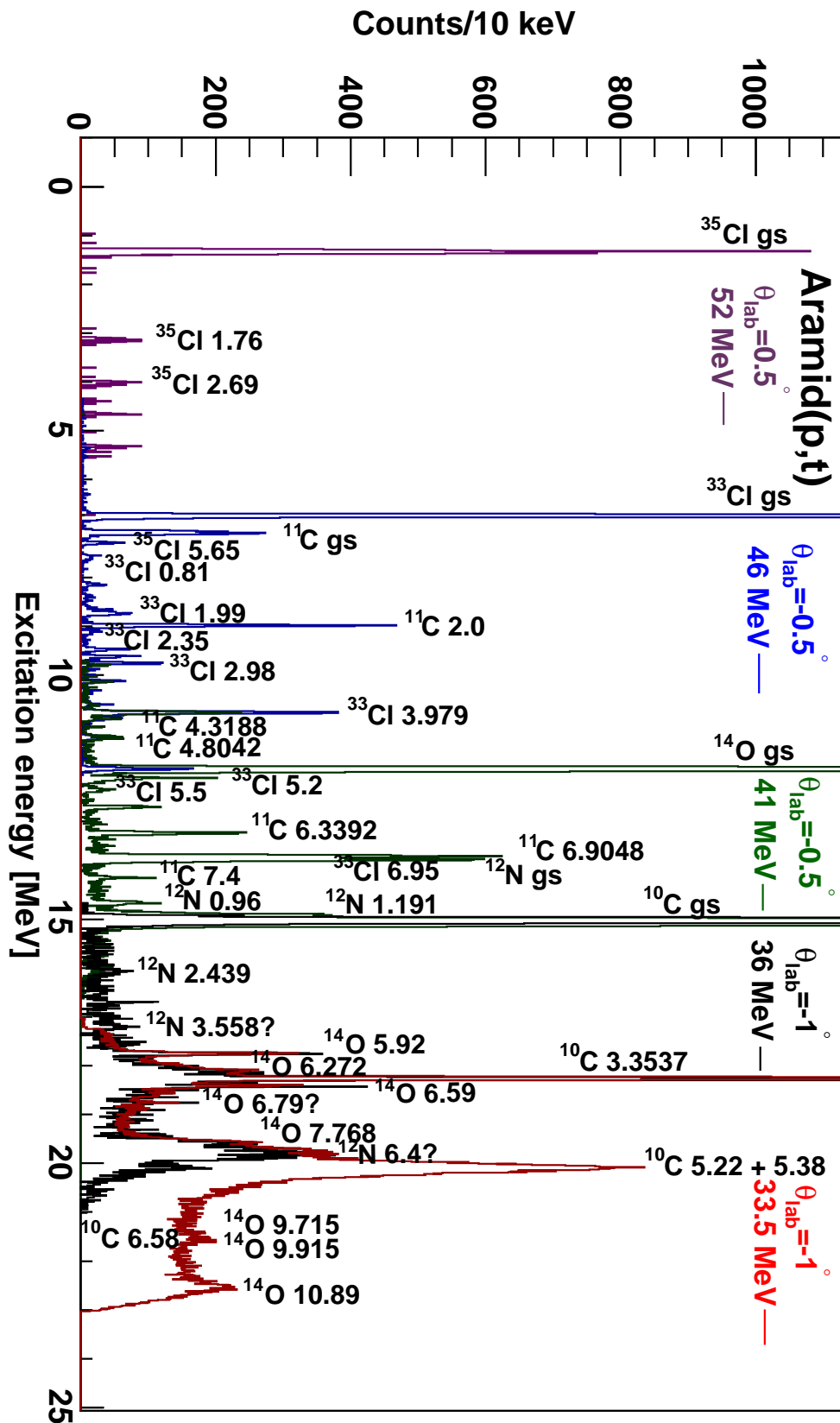


FIG. 4.28: The excitation energy spectrum for all field settings on the aramid foil close to or at $\theta_{lab} = 0^\circ$. The energy values are indicated in MeV, as with all figures in this section.

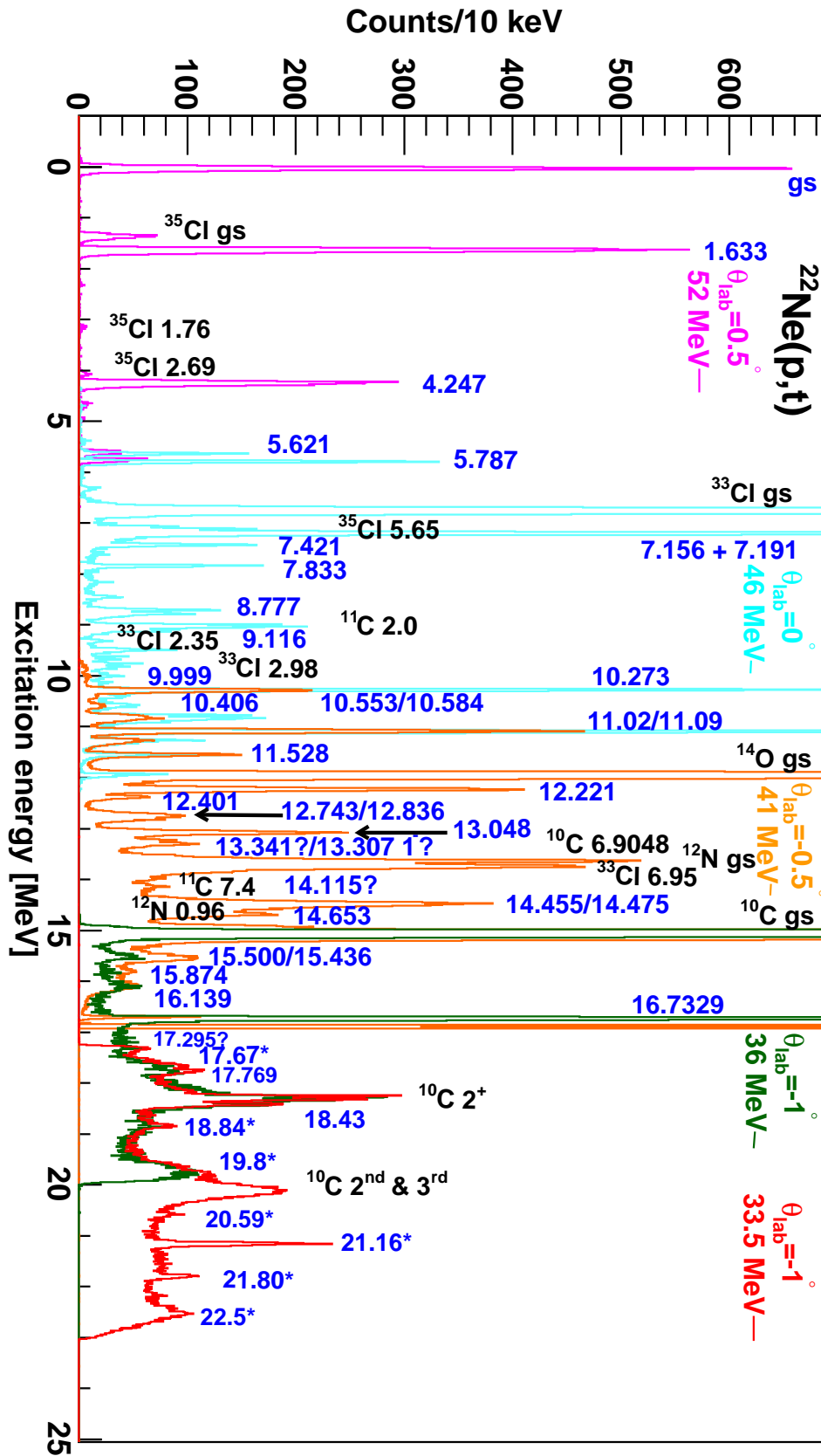


FIG. 4.29: The excitation energy spectrum for all field settings on the ^{22}Ne gas-filled target close to or at $\theta_{lab} = 0^\circ$. States from ^{20}Ne have blue labels and states from the aramid foil have black labels.

4.8 Cross sections

4.8.1 Method of extraction

The double differential cross sections were extracted following:

$$\frac{d^2\sigma}{d\Omega dE} = \frac{N_{cts} \cdot \cos(\theta_{tgt})}{I_f \cdot \rho \cdot D \cdot \varepsilon \cdot \Delta\Omega \cdot \Delta E}, \quad (4.7)$$

The variable N_{cts} in Eq. 4.7 represents the number of events per bin. The resolution of the experiment was low enough to measure peaks which were sufficiently narrow for the Breit-Wigner distribution to be dominated by the Gaussian distribution. Furthermore, these peaks were usually generated by a large number of events. Therefore N_{cts} was determined for each individual peak by performing a Gaussian fit over the peak and integrating the equation for a continuous Gaussian distribution

$$\int C \cdot e^{-\frac{(x-\bar{x})^2}{2\sigma^2}} dx = C \cdot \sigma \cdot \sqrt{2\pi}, \quad (4.8)$$

where $\text{FWHM} = 2.35 \times \sigma$, C represents the amplitude of the function, and \bar{x} is the mean value. Many peaks were situated on a significant background. In these cases it was mostly adequate to perform a 5-parameter fit which included a linear fit to the background and a Gaussian fit to the peak itself. In some cases, when two or more peaks sitting on the background were in close proximity to one another, an 8-, 11- or more parameter fit which included two or more Gaussian fits and a linear fit through the background was necessary. The mean energy values and widths of the measured states were also deduced from these fits. Regarding the other variables in Eq. 4.7,

- θ_{tgt} is the angle between the target and the beam,
- I_f is the incident flux,
- ρ is the number of target nuclei per unit area,
- D represents the electronic dead time correction factor,
- ε is the VDC efficiency,
- $\Delta\Omega$ is the solid angle in msr, and
- ΔE is the energy bin size in MeV.

The incident flux is calculated with the equation:

$$I_f = \frac{CII \cdot R}{e}, \quad (4.9)$$

where

- CII is the current integrator scaler reading,
- R represents the range which was set on the current integrator (in nA), and
- e is the charge of a single proton beam particle (in Coulomb).

The number of target nuclei per unit area is calculated as

$$\rho = \frac{\lambda \cdot N_A}{A}, \quad (4.10)$$

where

- N_A represents the Avogadro constant,
- λ is the target thickness in $\text{mg}\cdot\text{cm}^{-2}$, and
- A is the mass number of the target nucleus.

For a gas target, λ is usually calculated with the following formula:

$$\lambda = \rho_g \cdot d, \quad (4.11)$$

where ρ_g is the gas density, which may be deduced from the gas pressure measurement, and d is the thickness of gas target material that the particles must traverse. During off-line data analysis, the target thickness was calculated more accurately by investigating the double-peaked states from the aramid foils. The energy distance between two of these peaks corresponds to the difference between the mean energy losses of tritons ΔE_t and protons ΔE_p through the gas. The target thickness

$$\lambda = \rho_g \cdot d \propto \Delta E_t - \Delta E_p, \quad (4.12)$$

therefore an appropriate combination of ρ_g and d could be found to reproduce the measured value of $\Delta E_t - \Delta E_p$, using the Lise₊₊ code [112]. The target thickness was then calculated with Eq. 4.11 using these values of ρ_g and d .

Eq. 4.7 was utilised to extract the integrated cross sections for each of the measured ^{20}Ne peaks, which are shown in Tables C.2 and C.1 in Appendix C, and Table 4.14 in Section 4.10.

4.8.2 Background subtraction

In order to make an accurate background subtraction, the effect of the energy loss of particles moving through the ^{22}Ne gas must be taken into account. The energy shift between the foils observed by double-peaks from the aramid could be used for this purpose since it already provides a simulation of this energy loss. The background spectrum may be shifted by this energy difference and plotted again on the same graph, as was done to produce the red spectrum in Fig. 4.30 a). The double-peak created by the ^{10}C first 2^+ state in the gas-filled spectrum in Fig. 4.30 a) illustrates the effect.

The sum of the black and the red background spectra of Fig. 4.30 a) were normalised in total charge to the blue ^{22}Ne gas target spectrum. The two background spectra were then subtracted from the blue spectrum to produce what should be a purely $^{22}\text{Ne}(p,t)^{20}\text{Ne}$ spectrum in Fig. 4.30 b).

The states at $E_x = 18.84$ MeV, $E_x = 20.59$ MeV, $E_x = 21.16$ MeV and $E_x = 21.80$ MeV are all prominent above the background, which presumably consists of a continuum of broad ^{20}Ne states. It is seen that some strength remains in the peak around $E_x = 22.5$ MeV, indicating that this peak may be related to ^{20}Ne . It is located just 0.32 MeV above the value which T. Yamada and P. Schuck predicted for the $5-\alpha$ cluster state [26]. Furthermore it has a large width of $\Gamma = 266$ keV, deduced from the fit displayed in Fig. 4.31, indicating that it is short-lived. This 5-parameter fit takes into account an approximately linear background, and its parameters are kept within the bounds of full angular coverage in the spectrometer focal plane. This state was considered as a tentative candidate for the $5-\alpha$ cluster state of interest.

A heretofore unseen narrow state is also observed at $E_x = 19.8$ MeV, but with very low statistics, making it difficult to discern whether this peak is a real state from ^{20}Ne or merely an artifact of the background subtraction procedure.

As far as the data at $\theta_{lab} = 7^\circ$ is concerned, consider the gas-filled target data represented by the blue spectrum in Fig. 4.32 a). These data were generated during the third weekend, with $E_p = 60.32$ MeV, and the background data, represented by the black and red spectra, during the fourth, with $E_p = 60.01$ MeV. This implies a 0.31 MeV difference in the observed triton energy. Hence the region between $E_x = 22.25$ MeV and $E_x = 22.56$ MeV still has full focal plane coverage in the case of the gas-filled target data, but not in the case of the background data. This region is indicated by the two black lines in Fig. 4.32. Therefore, the background data in Fig. 4.32 are still valid for the region of all the candidate new states, apart from the $5-\alpha$ cluster candidate. This makes a valid background subtraction impossible at $\theta_{lab} = 7^\circ$ for the $5-\alpha$ cluster state candidate, with the 33.5 MeV (p,t) data set.

However, some data were collected at $\theta_{lab} = 7^\circ$ with the 31 MeV (p,t) field setting, which sheds light on an excitation energy region from $E_x = 20.0$ MeV to $E_x = 25.2$ MeV, as shown in Fig. 4.33. These data were obtained with beam currents close to $I_p = 20$ nA during Weekend 2, yielding count rates from 700 to 900 Hz during both the background and the neon gas-filled runs. The gas pressure was about $P = 1.3$ bar throughout and data were acquired for about 100 minutes both with and without the gas. The normalised background data could be subtracted from the neon gas-filled data at this field setting. Some strength is still present for $5-\alpha$ cluster candidate in the subtracted spectrum in Fig. 4.33 b).

However, close inspection of the $\theta_{lab} = 7^\circ$ data in Fig. 4.33 b), and of the $\theta_{lab} = -1^\circ$ data as shown in Fig. 4.31, indicates that this $5-\alpha$ cluster candidate may possibly consist of more than one states, though it is difficult to tell with the low statistics of the 31 MeV (p,t) data set. This would make a $5-\alpha$ cluster state unlikely, as the widths of these separate states would be much narrower than what can be expected for an α -cluster state at an energy of more than 15 MeV above the α -decay threshold, and more than 3 MeV above the $5-\alpha$ -decay threshold. In any case, the cross section of this state could not be reliably extracted at either $\theta_{lab} = -1^\circ$ or $\theta_{lab} = 7^\circ$, and at $\theta_{lab} = 16^\circ$ and $\theta_{lab} = 27^\circ$ it was not measured due to background and the limit of the excitation energy region respectively. Therefore, the spin and parity of this state could not be established.

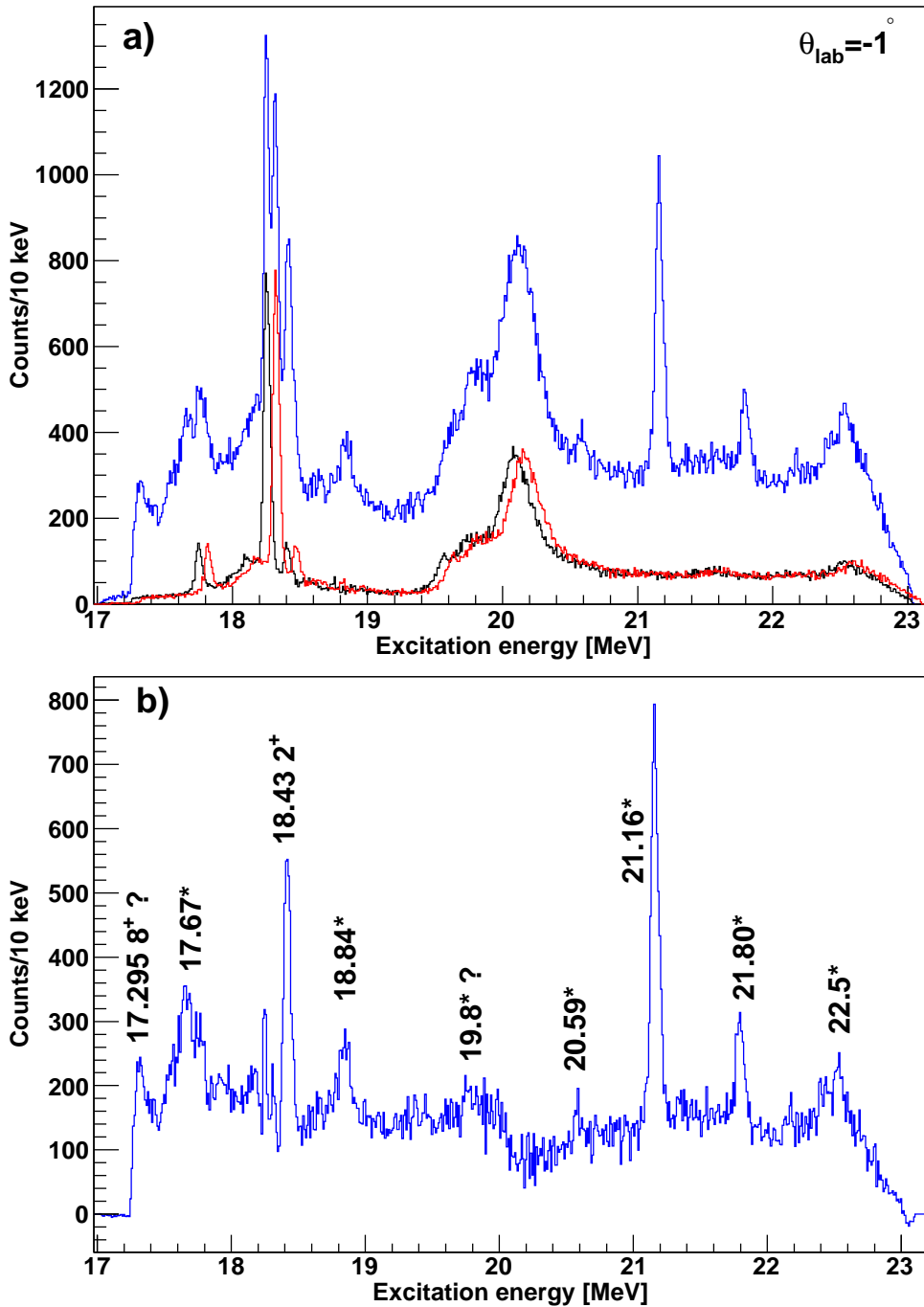


FIG. 4.30: The excitation energy spectrum from the ^{22}Ne gas-filled target for the 33.5 MeV (p,t) field setting at $\theta_{lab} = -1^\circ$ is shown by the blue spectrum in a). The black spectrum in a) shows the spectrum from the single aramid foil, while the red spectrum shows the same spectrum shifted to the right according to the measured energy loss of the tritons through the gas. The spectrum in b) was generated by subtracting the blue spectrum in a) from the red and black background spectra.

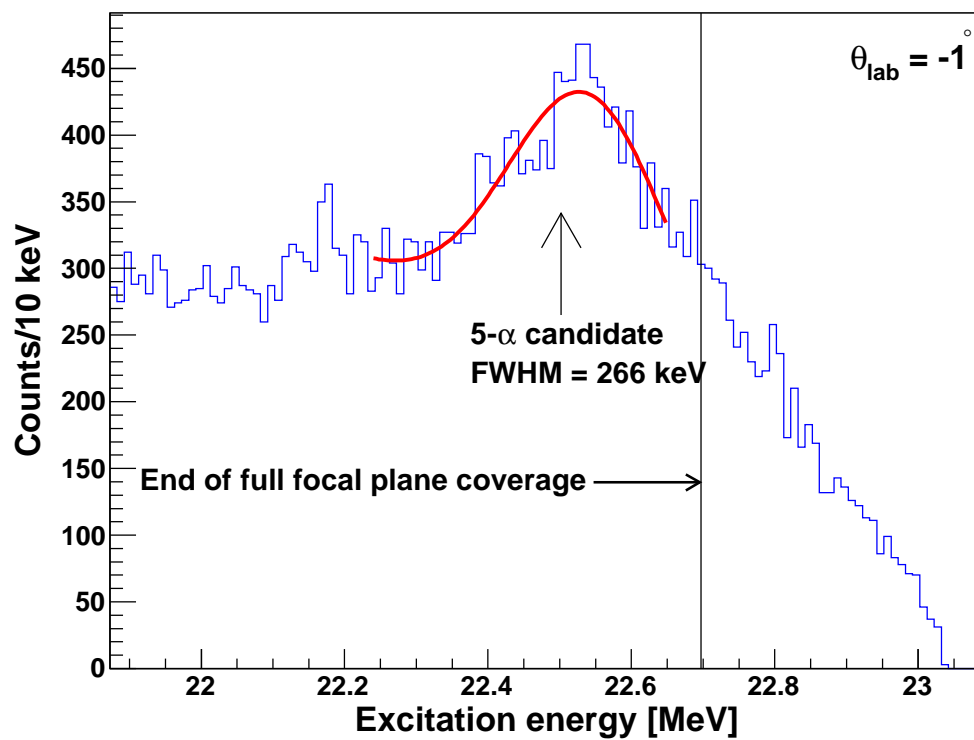


FIG. 4.31: A section of the excitation energy spectrum from the ^{22}Ne gas-filled target for the 33.5 MeV (p,t) field setting at $\theta_{lab} = -1^\circ$, illustrating the fit of the state at $E_x = 22.5$ MeV

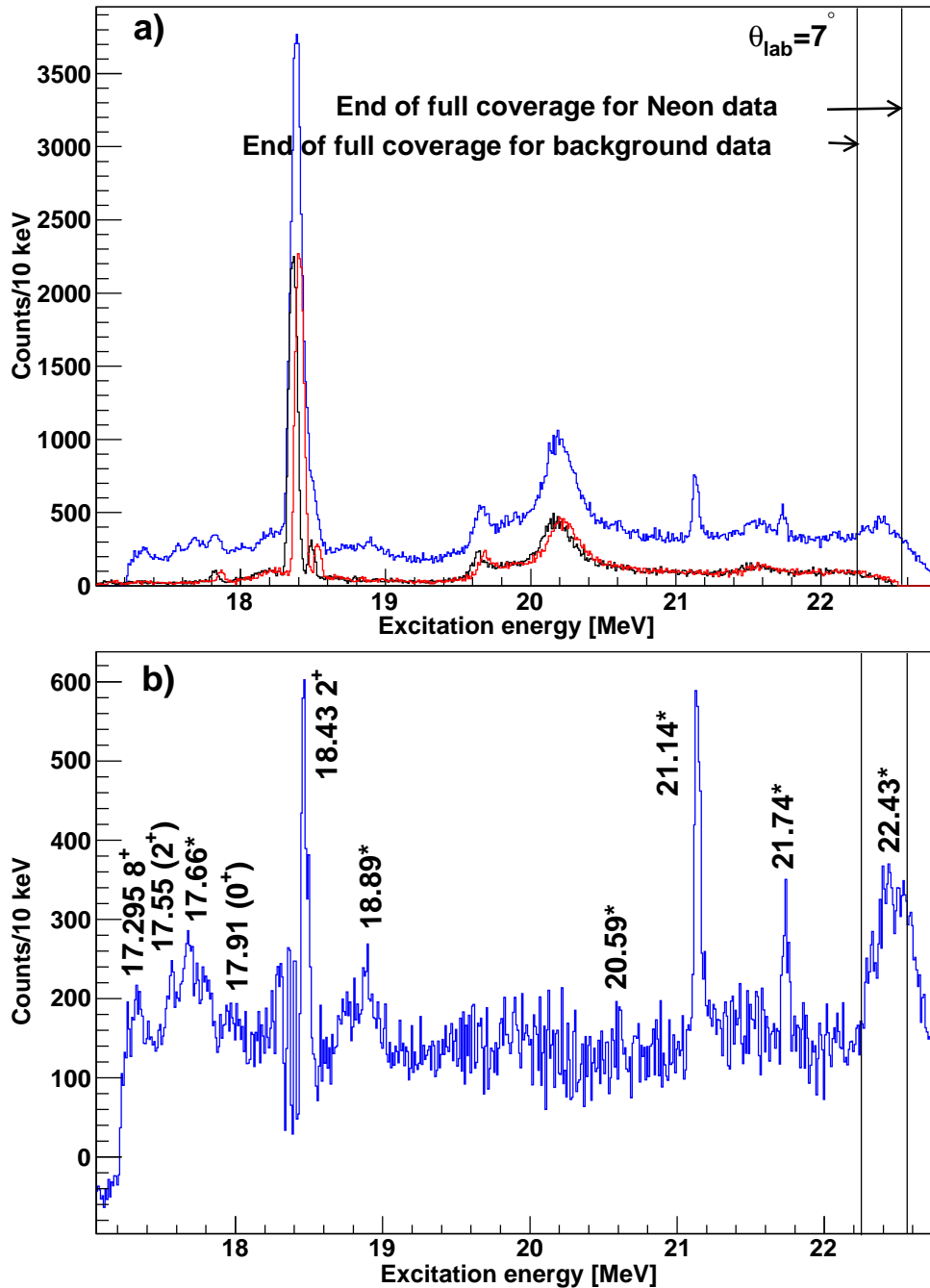


FIG. 4.32: The excitation energy spectrum from the ^{22}Ne gas-filled target for the 33.5 MeV (p,t) field setting at $\theta_{\text{lab}} = 7^\circ$ is shown by the blue spectrum in a). The black spectrum in a) shows the spectrum from the single aramid foil, while the red spectrum shows the same spectrum shifted to the right according to the measured energy loss of the tritons through the gas. The background-subtracted spectrum is shown in b).

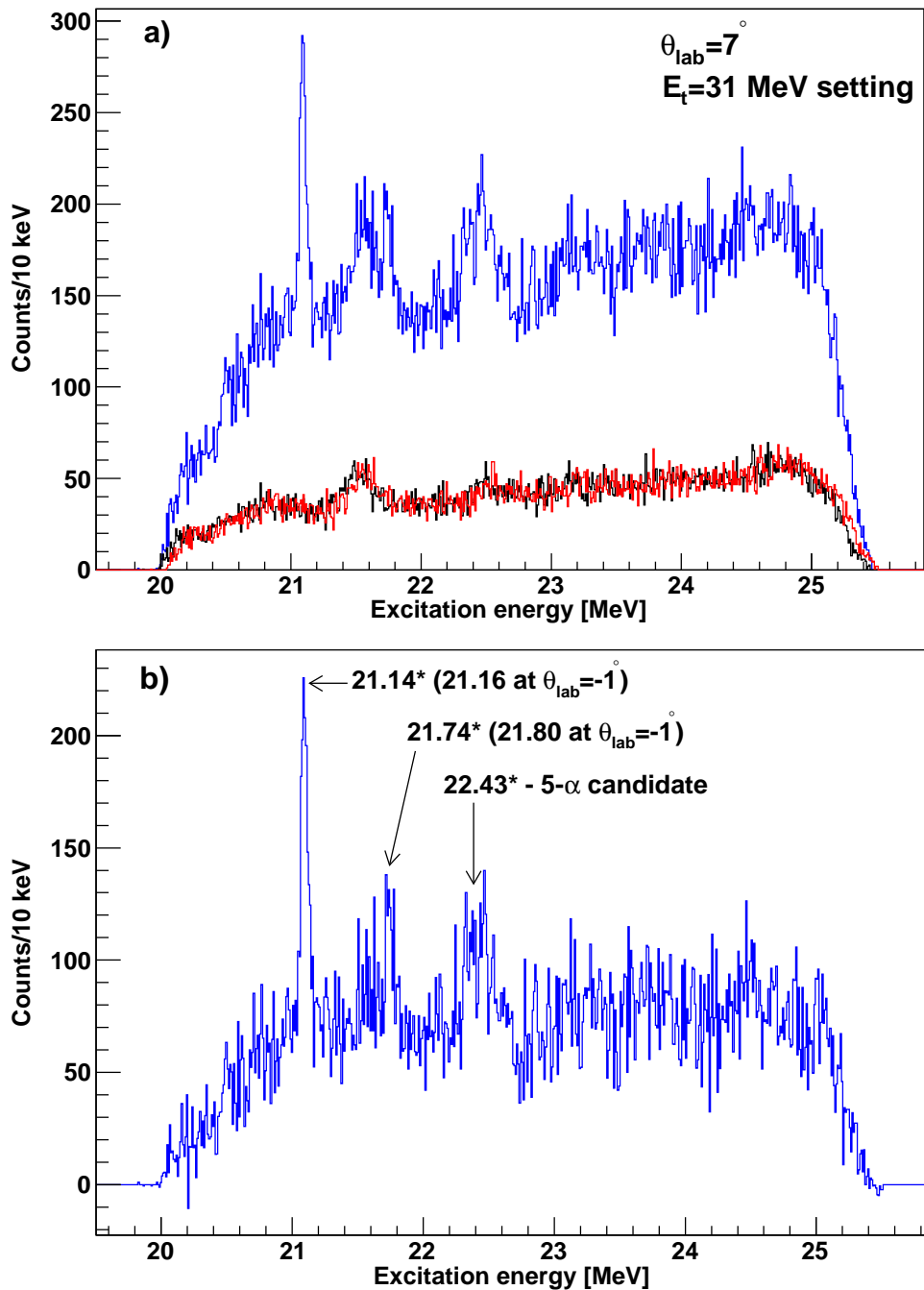


FIG. 4.33: The excitation energy spectrum from the ^{22}Ne gas-filled target for the 31 MeV (p,t) field setting at $\theta_{lab} = 7^\circ$ is shown by the blue spectrum in a). The black spectrum in a) shows the spectrum from the single aramid foil, while the red spectrum shows the same spectrum shifted to the right according to the measured energy loss of the tritons through the gas. The background-subtracted spectrum is shown in b).

The background subtractions at $\theta_{lab} = 16^\circ$ and $\theta_{lab} = 27^\circ$ were complicated by the fact that the thickness of the aramid foil changed significantly during these measurements due to sputtering of the aramid material by the beam. Therefore, the change in carbon composition of the foil, deduced from the RBS data from Section 3.5.3, was taken into account in normalising the background data shown in Fig. 4.34.

It is not clear from Fig. 4.34 b) whether the peaks indicated as candidates for the known $E_x = 18.538$ MeV 8^+ , $E_x = 18.621$ MeV 8^+ and $E_x = 19.731$ MeV 8^+ states in ^{20}Ne are mainly composed of true ^{20}Ne states or of remnants of the $E_x = 3.3537$ MeV 2^+ state from ^{10}C and the $E_x = 7.768$ MeV 2^+ state from ^{14}O . A width of FWHM = 129 keV was measured for the candidate $E_x = 18.538$ MeV state, which is in good correspondence to the known value of the natural width of this state ($\Gamma = 138$ keV [3]). However, for the candidate $E_x = 18.621$ MeV state, a width of FWHM = 95 keV was measured. This is almost a factor of 2 smaller than the known natural width of this state ($\Gamma = 185$ keV [3]). The width of this peak may be influenced by the remnant of the ^{10}C 3.3537 MeV state. For the candidate $E_x = 19.731$ MeV state, a width of approximately FWHM = 185 keV was measured in the background-subtracted data. This is very close to the value of FWHM = 183 keV which was measured for the $E_x = 7.768$ MeV state of ^{14}O without background subtraction. The $E_x = 19.731$ MeV state in ^{20}Ne has a natural width of $\Gamma = 330$ keV, which is almost a factor of 2 more than what was measured for this candidate state.

These findings cast doubts on the validity of the background subtraction for $\theta_{lab} = 16^\circ$ in the regions of prominent contaminant peaks, even though the RBS information from Section 3.5.3 was taken into account. Factors contributing to the inaccuracy of this normalisation may include variations in the original foil thicknesses and the uncertainty in the energy loss calculation. Another factor which must be considered is that the different elements in the aramid foil which contribute to the background (chlorine, oxygen, nitrogen, carbon) would not be sputtered in equal amounts by the beam. If the background data were normalised to the data taken with the foil which held the gas, with regards to any one of these elements, a systematic error would immediately be introduced since the background can no longer be normalised with regards to any of the other 3 elements.

Nevertheless, a peak with FWHM = 245 keV is seen at $E_x = 21.74$ MeV in the background-subtracted $\theta_{lab} = 16^\circ$ spectrum (Fig. 4.34). This is much narrower than

the value of FWHM = 410 keV measured for the $E_x = 6.58$ MeV state in ^{10}C , which is found in this excitation energy region. Therefore, it seems likely that a large part of the strength in this peak comes from the new state in ^{20}Ne , which is seen at $E_x = 21.80$ MeV in the $\theta_{lab} = -1^\circ$ data (Fig. 4.30), and at a similar energy in the $\theta_{lab} = 7^\circ$ data (Fig. 4.32).

The same complications may be anticipated for the data obtained at $\theta_{lab} = 27^\circ$, since these data also experienced high beam currents ($I_p \geq 15$ nA) for an extended period of time (about 16 hours). The background data in Fig. 4.35 were normalised iteratively with the data obtained with the gas-filled target. Some strength from carbon and oxygen peaks seems to have remained in the spectrum. The region around $E_x = 21$ MeV seems to have been cleaned up very well, and the state measured at $E_x = 21.16$ MeV in the $\theta_{lab} = -1^\circ$ data is again seen prominently above the ^{20}Ne continuum in Fig. 4.35 b). Unfortunately, the $E_x = 21.80$ MeV state lies beyond the limit in excitation energy in this case. The state at $E_x = 17.67$ MeV is seen more clearly in the background subtracted spectra, but with some interference from the near-lying 5^- state at $E_x = 17.606$ MeV with $\Gamma = 140$ keV [3].

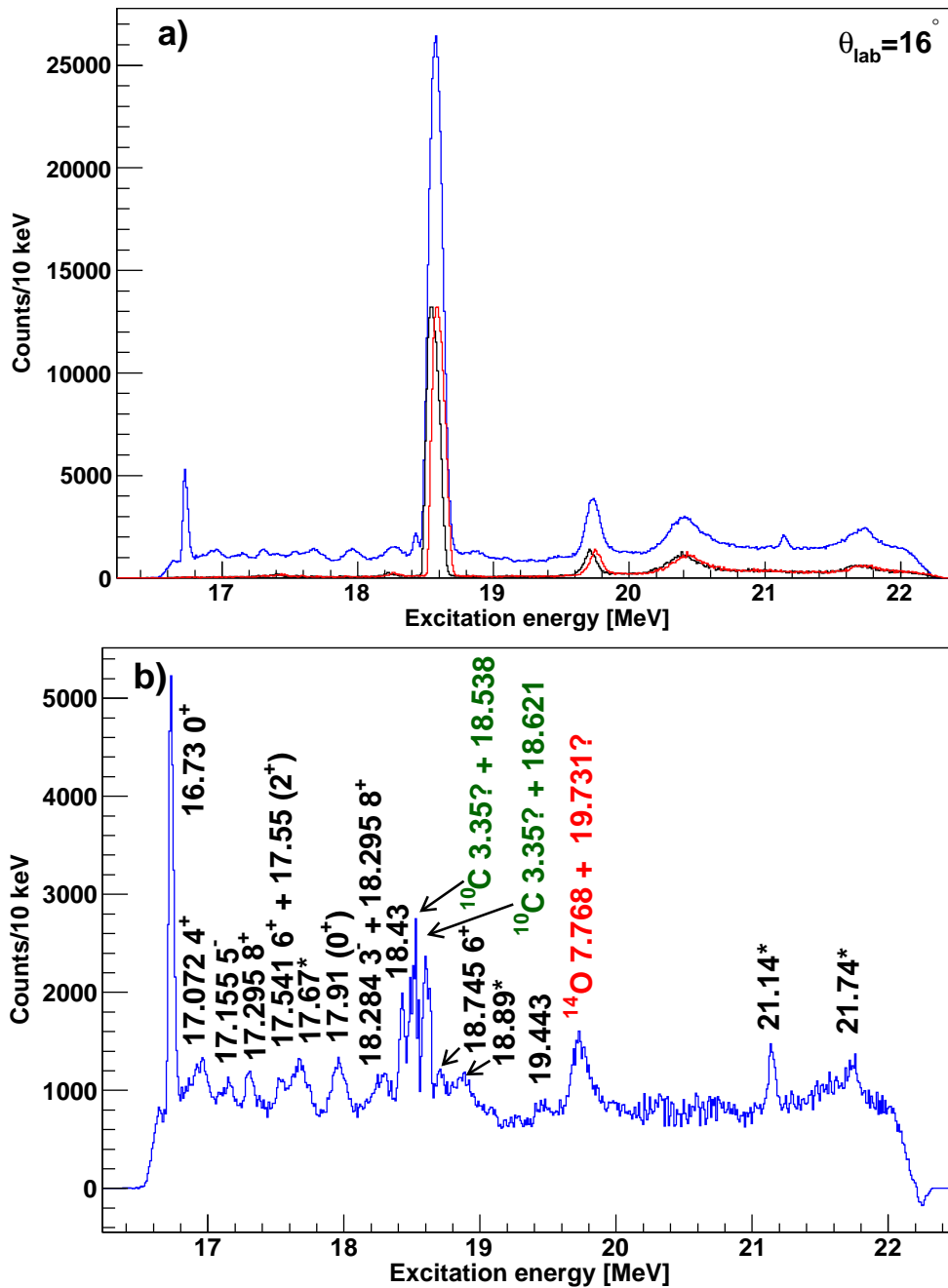


FIG. 4.34: The excitation energy spectrum from the ^{22}Ne gas-filled target for the 33.5 MeV (p,t) field setting at $\theta_{\text{lab}} = 16^\circ$ is shown by the blue spectrum in a). The black spectrum in a) shows the spectrum from the single aramid foil, while the red spectrum shows the same spectrum shifted to the right according to the measured energy loss of the tritons through the gas. The background-subtracted spectrum is shown in b).

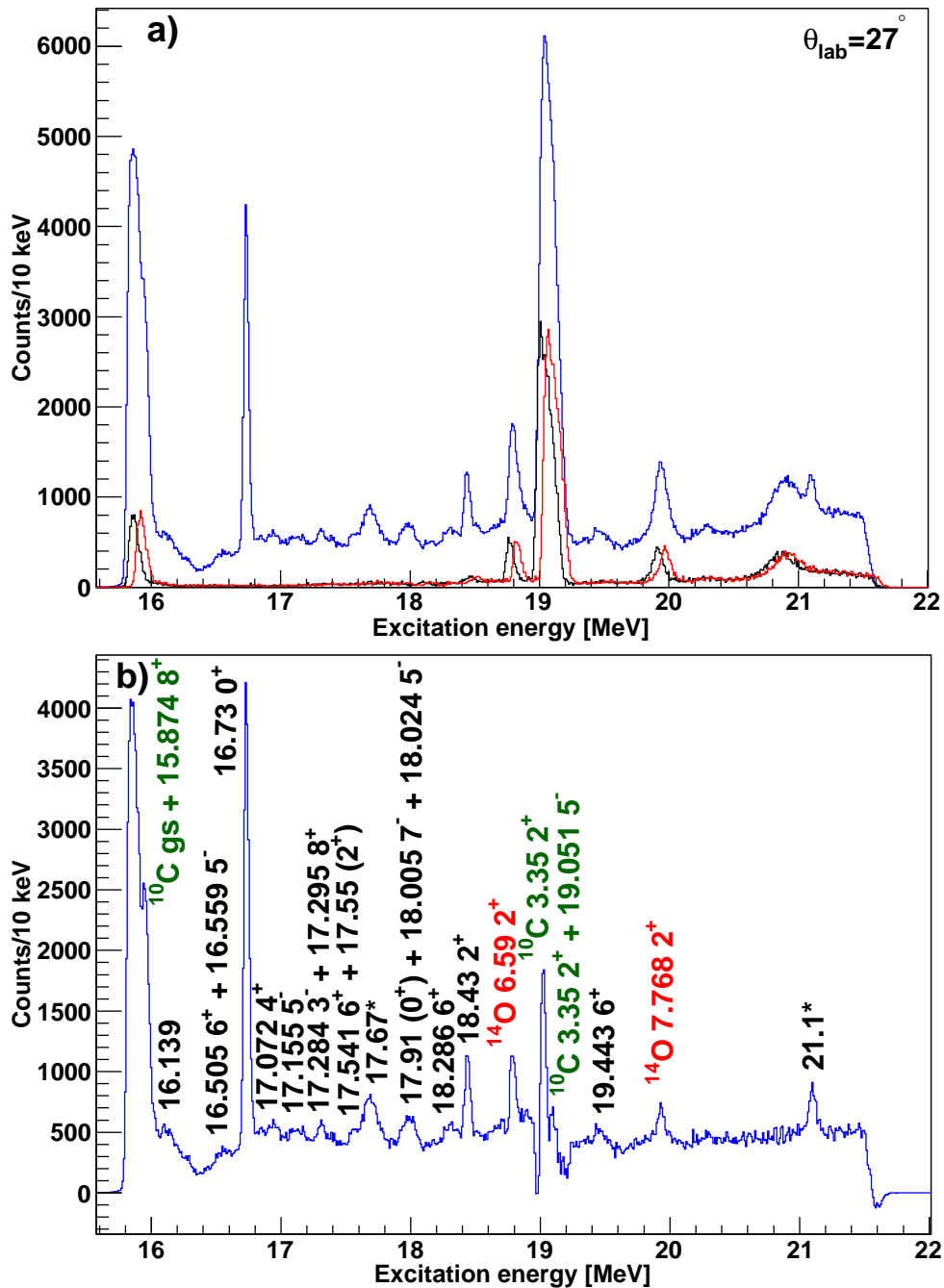


FIG. 4.35: The excitation energy spectrum from the ^{22}Ne gas-filled target for the 33.5 MeV (p,t) field setting at $\theta_{lab} = 27^\circ$ is shown by the blue spectrum in a). The black spectrum in a) shows the spectrum from the single aramid foil, while the red spectrum shows the same spectrum shifted to the right according to the measured energy loss of the tritons through the gas. The background-subtracted spectrum is shown in b).

4.8.3 Errors

The *error propagation formula* was employed to determine the error of variables related to more than one measured quantity in this experiment:

$$\sigma_u^2 = \left(\frac{\delta u}{\delta x}\right)^2 \cdot \delta\sigma_x^2 + \left(\frac{\delta u}{\delta y}\right)^2 \cdot \delta\sigma_y^2 + \left(\frac{\delta u}{\delta z}\right)^2 \cdot \delta\sigma_z^2 + .. \quad (4.13)$$

The variables x , y and z in Eq. 4.13 represent independent measured quantities for which the standard deviations σ_x , σ_y and σ_z are known. The standard deviation of any quantity u which is calculated from these variables is found by solving this equation for σ_u [113].

4.8.3.1 Angular uncertainty

The maximum angular uncertainty of this measurement, owing to the thickness of the gas cell, was calculated to be $\Delta\theta_t = 0.12^\circ$ in Section 3.5.1.2. The factors which normally contribute to the angular uncertainty of measurements with the $K600$ are the uncertainties in the $K600$ angle and in the offsets of the two scintillating viewers which are used for beam optimisation. Together, these factors normally generate an uncertainty of $\Delta\theta_n = 0.06^\circ$ [114]. This makes the total angular uncertainty of the present measurement $\Delta\theta = \sqrt{(\Delta\theta_t)^2 + (\Delta\theta_n)^2} = 0.13^\circ$.

4.8.3.2 Variables which influence cross section

The uncertainty related to the determination of the cross section in Eq. 4.7 is dominated by the systematic error associated with the calculation of the effective thickness of material $\Delta\lambda$. The error in this calculation comes from the error associated with the energy loss calculation performed with the double-peaks from states related to the aramid material. A systematic error of $\pm 23\%$ was estimated for this calculation, by observing the maximum discrepancy in density values which were extracted via the energy loss calculation on two different aramid-related states in the same set of data. Note that this λ value is an average value for a given run, since the real value of the gas pressure P upon which it is dependent is constantly decreasing, and sometimes the gas cell had to be refilled during a run.

To accurately determine the systematic error associated with the calculation of the cross section, σ , of any given peak, one must also consider the errors associated with the $K600$ solid angle ($\Delta\Omega = 0.3\%$ [89]), the integrated current ($\Delta I_f = 0.5\%$ [89]) and the

efficiency ($\Delta\epsilon = 1\%$). However, all these contributions are negligibly small compared to the systematic error resulting from the calculation of the target thickness.

4.8.3.3 Uncertainty in excitation energy

The statistical error in the determination of excitation energy ΔE_{st} for a given experimental peak is given by the FWHM divided by the square root of the number of counts N

$$\Delta E_{st} = \frac{\text{FWHM}}{\sqrt{N}}, \quad (4.14)$$

hence ΔE_{st} can be almost negligible for a large number of counts. The aramid background data introduce another statistical error, as well as a systematic error related to the simulation of energy loss, in the background-subtracted spectra. The systematic uncertainty in the determination of the excitation energy is dominated by the inaccuracy of the energy calibration. This uncertainty is discussed in Section 4.7.

4.9 Observed energy resolution values

Some of the observed energy resolution values are very close to the energy resolution of the measurement, therefore the natural widths of these states were calculated by assuming that:

$$\sigma_{\text{FWHM}} = \sqrt{\sigma_{\Gamma}^2 + \sigma_{\text{Res}}^2}, \quad (4.15)$$

where σ_{Res} is the energy resolution which was extrapolated from the values shown in Table 4.12, σ_{FWHM} is the measured width of the new state shown in Table 4.13, and σ_{Γ} is the natural width. The uncertainty in σ_{Res} was estimated for each state with the maximum deviation from the fit to the energy resolution data points in Figs. 4.36 to 4.39, for the specific angle which was used in each case. The statistical uncertainty was then calculated for σ_{FWHM} and Eq. 4.15 could be solved for the uncertainty in σ_{Γ} , which is also indicated in Table 4.13.

The measured widths and cross sections of the candidate new states indicated in Fig. 4.30 are shown for all four angles in Tables 4.13 and 4.14. Fig. 4.36 shows the linear deterioration of energy resolution with increase in excitation energy at angles near to $\theta_{lab} = 0^\circ$. By observing the rate of this deterioration in the figure, one may infer the resolution values above $E_x = 16.73$ MeV, which is the location of the highest known narrow

($\Gamma \leq 10$ keV) state.

The observed energy resolution values from data at $\theta_{lab} = 7^\circ$ are graphically represented in Fig. 4.37. It is observed that the new state at $E_x = 21.80$ MeV has a smaller observed width than some of the known narrow states at lower excitation energies. This may be attributed to a lower gas pressure during the readings in the $E_x = 18.2\text{-}22.6$ MeV excitation energy region, compared to the data obtained at lower E_x field settings. The data at $\theta_{lab} = 7^\circ$ were obtained at comparatively low gas pressures, and over shorter periods of time than the data from the other other angles, which minimizes contributions to the measured widths from factors such as movement of the beam over long periods. Hence, the resolution values observed at $\theta_{lab} = 7^\circ$ are on average the best out of all the angles. From these data one may already assign maximum natural widths of $\Gamma = 47$ keV and $\Gamma = 41$ keV to the states at $E_x = 21.16$ MeV and $E_x = 21.80$ MeV. The state at $E_x = 20.59$ MeV is closer to the 2^{nd} and 3^{rd} excited states of ^{10}C at $\theta_{lab} = 7^\circ$. This makes it difficult to perform an accurate fit, hence a higher than expected width is observed. The value recorded at $\theta_{lab} = -1^\circ$ was provisionally taken as an upper bound in this case.

The upper bounds of the natural widths of the states at $E_x = 21.16$ MeV and $E_x = 21.80$ MeV were calculated by employing Eq. 4.15 to a fit on the known narrow states in Fig. 4.36. Note that the energy values found at $\theta_{lab} = -1^\circ$ are trusted most, since its method of calibration, which uses peaks from the oxygen gas in the gas cell, can be expected to be the most reliable.

The observed energy resolution values from $\theta_{lab} = 16^\circ$ indicated in Fig. 4.38 remain relatively flat between 40 keV and 50 keV for the known states (probably due to a slightly higher gas pressure during measurements at lower E_x field setting), apart from the states at $E_x = 5.621$ MeV and $E_x = 5.787$ MeV which have a noticeably lower energy resolution. These states were measured with the $E_t = 48$ MeV (p,t) field setting at $\theta_{lab} = 16^\circ$ during the first weekend. During this weekend, a 3 mm-thick target was used as discussed in Section 3.6, instead of the 10-mm-thick target, discussed in Section 3.5, that was used to measure all the other widths in Figs. 4.36 to 4.39. The new state at $E_x = 21.16$ MeV has an unexpectedly high measured width of FWHM = 58 keV. This may be due to another ^{20}Ne peak which is stronger at this larger angle and could not be resolved in this experiment. The energy straggling could also play a role since the tritons must pass through more ^{22}Ne gas material at this larger angle.

At $\theta_{lab} = 27^\circ$ in Fig. 4.39, the energy resolution seems to worsen at a rate of 3.5 keV/MeV as one moves from $E_x = 16.73$ MeV to the new state at $E_x = 21.16$ MeV. This state corresponds to a triton energy of $E_t = 29.3$ MeV at a centre-of-mass angle of $\theta_{cm} = 29^\circ$. The value of FWHM = 59 keV which was measured for this state is in good agreement with the value of FWHM = 54 keV which was calculated in Section 3.5.1 for a state at $E_t = 33$ MeV and $\theta_{lab} = 30^\circ$. This rapid deterioration in energy resolution at $\theta_{lab} = 27^\circ$ may indicate some threshold where the triton energy becomes low enough that the straggling of the tritons increases rapidly. It may also be that the higher excitation energy states in Fig. 4.39, which are both far weaker than the $E_x = 16.73$ MeV state, were more adversely affected by aramid contamination than the $E_x = 16.73$ MeV state. In any case, the measured value is still within the range which was anticipated and which is acceptable for this measurement, as is the case with all the resolution values shown in Tables 4.12 and 4.13.

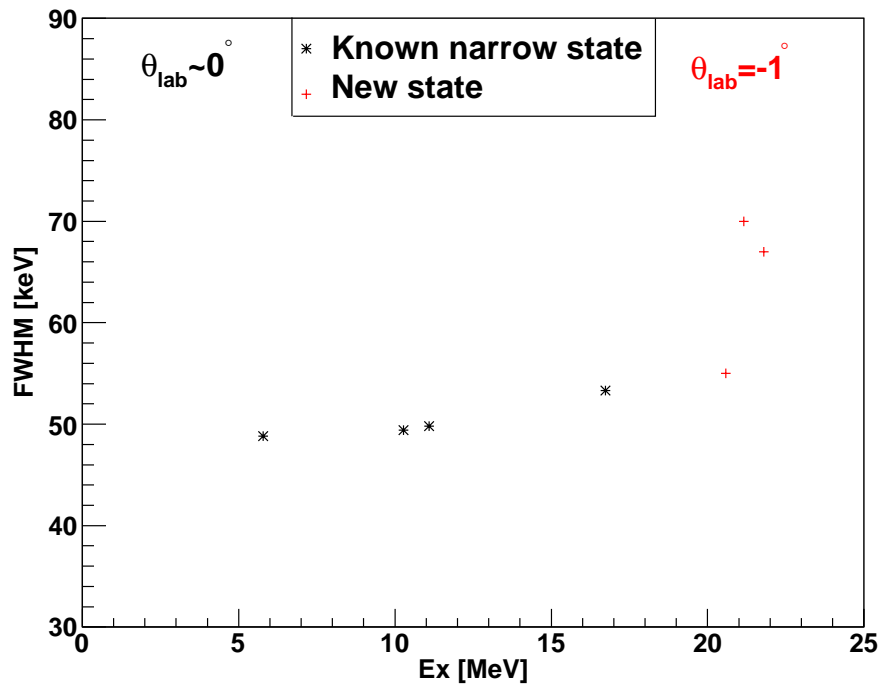


FIG. 4.36: Observed energy resolution values of known narrow ($\Gamma \leq 2$ keV) states in ^{20}Ne , measured close to $\theta_{lab} = 0^\circ$, and candidate new states measured at $\theta_{lab} = -1^\circ$ (highest three in excitation energy)

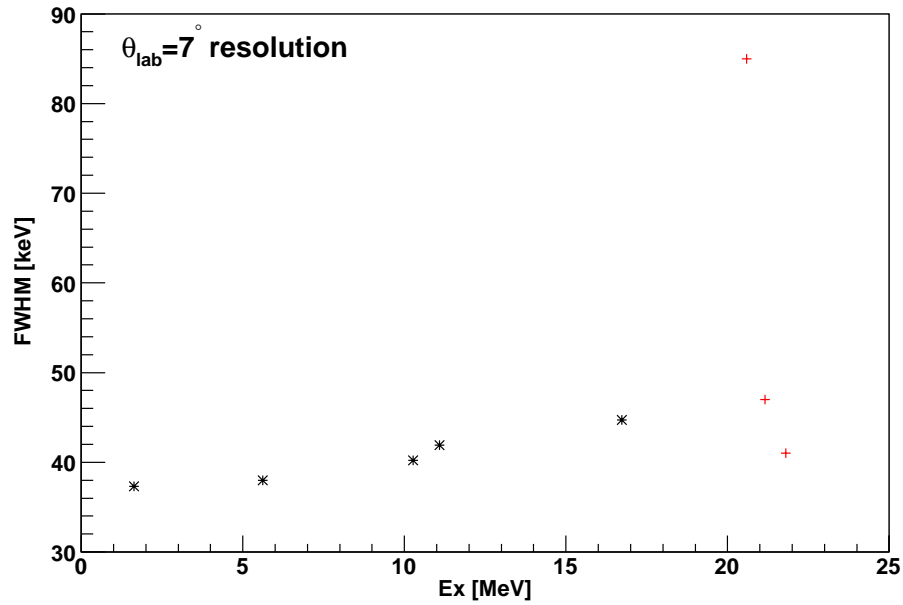


FIG. 4.37: Observed energy resolution values of known narrow ($\Gamma \leq 2$ keV) states in ^{20}Ne and candidate new states measured at $\theta_{\text{lab}} = 7^\circ$ (highest three in excitation energy)

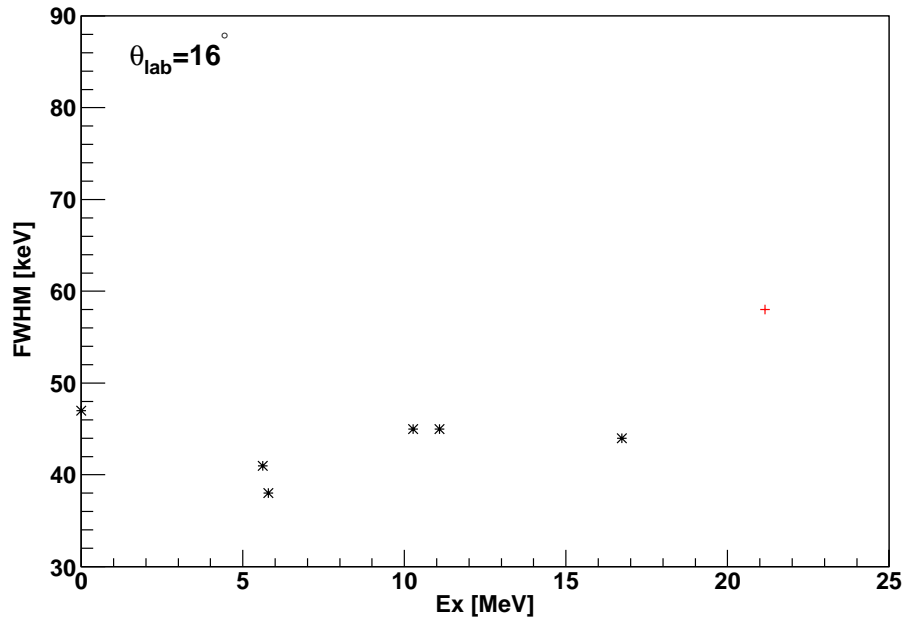


FIG. 4.38: Observed energy resolution values of known narrow ($\Gamma \leq 2$ keV) states in ^{20}Ne and a candidate new state measured at $\theta_{\text{lab}} = 16^\circ$ (highest state in excitation energy). The values at $E_x = 5.621$ MeV and $E_x = 5.787$ MeV were measured with a 3-mm-thick target. All other values were measured with a 10-mm-thick target.

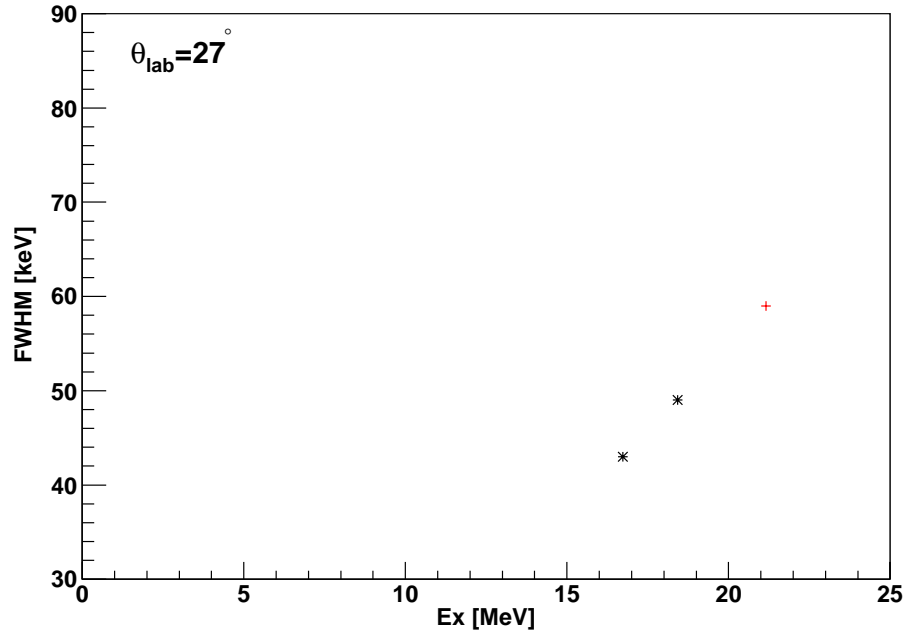


FIG. 4.39: Observed energy resolution values of known narrow ($\Gamma \leq 9$ keV) states in ^{20}Ne and a candidate new state measured at $\theta_{lab} = 27^\circ$ (highest state in E_x)

4.10 Results

Six newly observed states were found at excitation energies of $E_x = (17.67$ MeV, 18.84 MeV, 20.59 MeV, 21.16 MeV, 21.80 MeV, 22.5 MeV). The cross sections of the newly observed states are shown in Table 4.14, while those of all the known states which were measured in ^{20}Ne are shown in Tables C.1 and C.2 in Appendix C. The state at $E_x = 22.5$ MeV was considered as a tentative candidate for the $5\text{-}\alpha$ cluster state, owing to its energy position and its broad width ($\Gamma = 266$ keV). The new states at $E_x = 20.59$ MeV, $E_x = 21.16$ MeV and $E_x = 21.80$ MeV are narrow and high in ^{20}Ne excitation energy. It was presumed that they may be isobaric analogue states with isospin values of $T = 2$. IMME (isobaric multiplet mass equation) and shell-model based calculations were performed to test this hypothesis. These are discussed in Chapter 5. The peak at $E_x = 18.84$ MeV still appears to be a collection of states, with a collective width of $\Gamma = 97$ keV. Cross section values for the $E_x = 17.67$ MeV state could be extracted only at $\theta_{lab} = 16^\circ$ since there was usually too much interference from near-lying states to perform a reliable fit and background subtraction.

The angular distribution plots in Figs. 4.40 and 4.41 were generated from the values in Table 4.14, and Tables C.1 and C.2 in Appendix C. The angular distribution plots of other known states measured in ^{20}Ne are shown in Figs. C.1 to C.4 in Appendix C. The ground and 1.634 MeV excited states of ^{20}Ne do not display the exact trend expected from the DWBA calculations between $\theta_{cm} = 0.5^\circ$ and $\theta_{cm} = 7.7^\circ$ in Fig. 4.40. This could be attributed to interference from the L-shaped beam stop over an angular range which is difficult to establish for these states with the spectrometer settings of $\theta_{lab} = (0.5^\circ, 7^\circ)$ and anticipated triton energy $E_t = 52$ MeV. This makes the cross section values unreliable at this angle for the aforementioned states. The same does not hold for the $E_x = 4.247$ MeV state which received full angular coverage in the focal plane at the same angle and field setting.

The $E_x = 21.16$ MeV state in Fig. 4.41 follows a very similar trend to the $E_x = 16.73$ MeV 0^+ state, which is the nearest 0^+ state for which a reliable angular distribution plot could be generated. This is in good agreement with the DWBA calculation, which predicts a maximum at $\theta_{cm} = 0^\circ$, a minimum at $\theta_{cm} = 20^\circ$, and a second maximum at $\theta_{cm} = 29^\circ$ for these states, assuming that both have a 0^+ character. The narrow width of this state, listed in Table 4.13, is also in accordance with a 0^+ , $T = 2$ state. It is not easy to assign spins and parities to the states observed at $E_x = 20.59$ MeV and $E_x = 21.80$ MeV since their cross sections could only be measured at two angles, but the narrow widths indicate a strong possibility of 0^+ characters, especially for the $E_x = 21.80$ MeV state.

Excitation energy	Width(0°)	Width (7°)	Width (16°)	Width (27°)
[MeV]	[keV]	[keV]	[keV]	[keV]
gs			47	
1.63		37		
5.62		38	41	
5.79	49		38	
10.27	49	40	45	
11.09	50	42	45	
16.73	53	45	44	43
18.43				49

TABLE 4.12: The known energies of previously observed narrow states ($\Gamma \leq 10$ keV) in ^{20}Ne are shown in the 1st column [3], and the widths which were measured for them at each angle for this experiment are shown in the other four columns.

Excitation energy [MeV]	Width(-1°) [keV]	Width (7°) [keV]	Width (16°) [keV]	Width (27°) [keV]	Γ [Natural width] [keV]
17.670(57)		126			114.2(48)
18.840(56)	111	116			97.2(41)
20.590(54)	55	85			≤ 55
21.160(53)	70	47	58	59	≤ 43
21.800(53)	67	41			≤ 38
22.500(52)	266				260.2(52)

TABLE 4.13: The excitation energies measured at $\theta_{lab} = -1^\circ$ and the measured widths for the candidate new states in ^{20}Ne . The 6th column shows the natural width values which were extracted with Eq. 4.15.

State [MeV]	$\sigma (\theta_{lab} = 0^\circ)$ [$\mu\text{b}.\text{sr}^{-1}$]	$\sigma (\theta_{lab} = 7^\circ)$ [$\mu\text{b}.\text{sr}^{-1}$]	$\sigma (\theta_{lab} = 16^\circ)$ [$\mu\text{b}.\text{sr}^{-1}$]	$\sigma (\theta_{lab} = 27^\circ)$ [$\mu\text{b}.\text{sr}^{-1}$]
17.67			1.4(3)	
18.84	12(3)		6.7(15)	
20.59	2.4(5)	6.7(15)		
21.16	38(9)	22(5)	7.2(16)	7.7(17)
21.80	11.0(26)	7.3(16)		

TABLE 4.14: The observed absolute cross sections of all newly observed states in ^{20}Ne

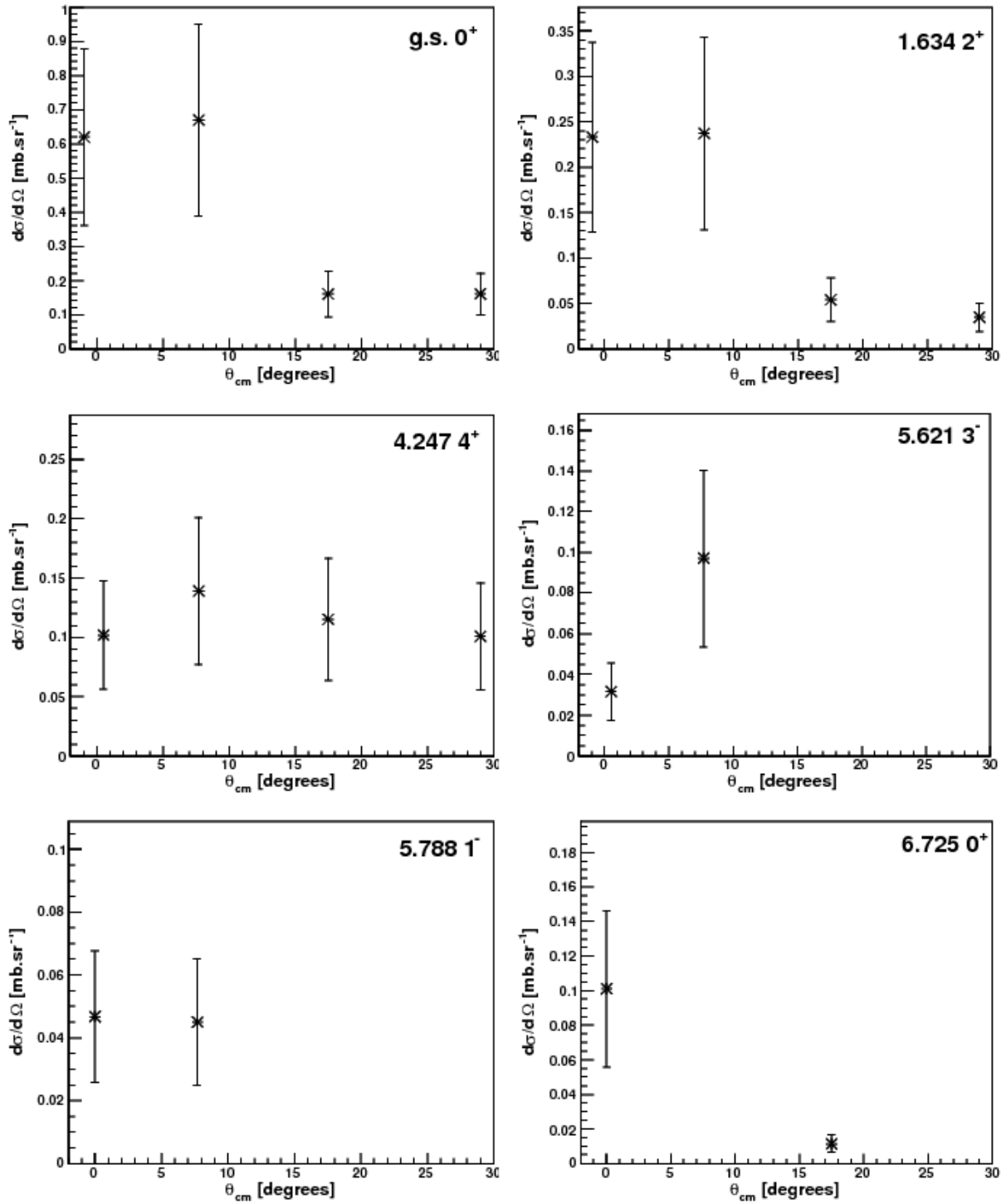


FIG. 4.40: Angular distribution plots for states measured between $E_x = 0$ and $E_x = 7$ MeV. The excitation energy values of the states are indicated in MeV, as they are for all forthcoming angular distribution plots.

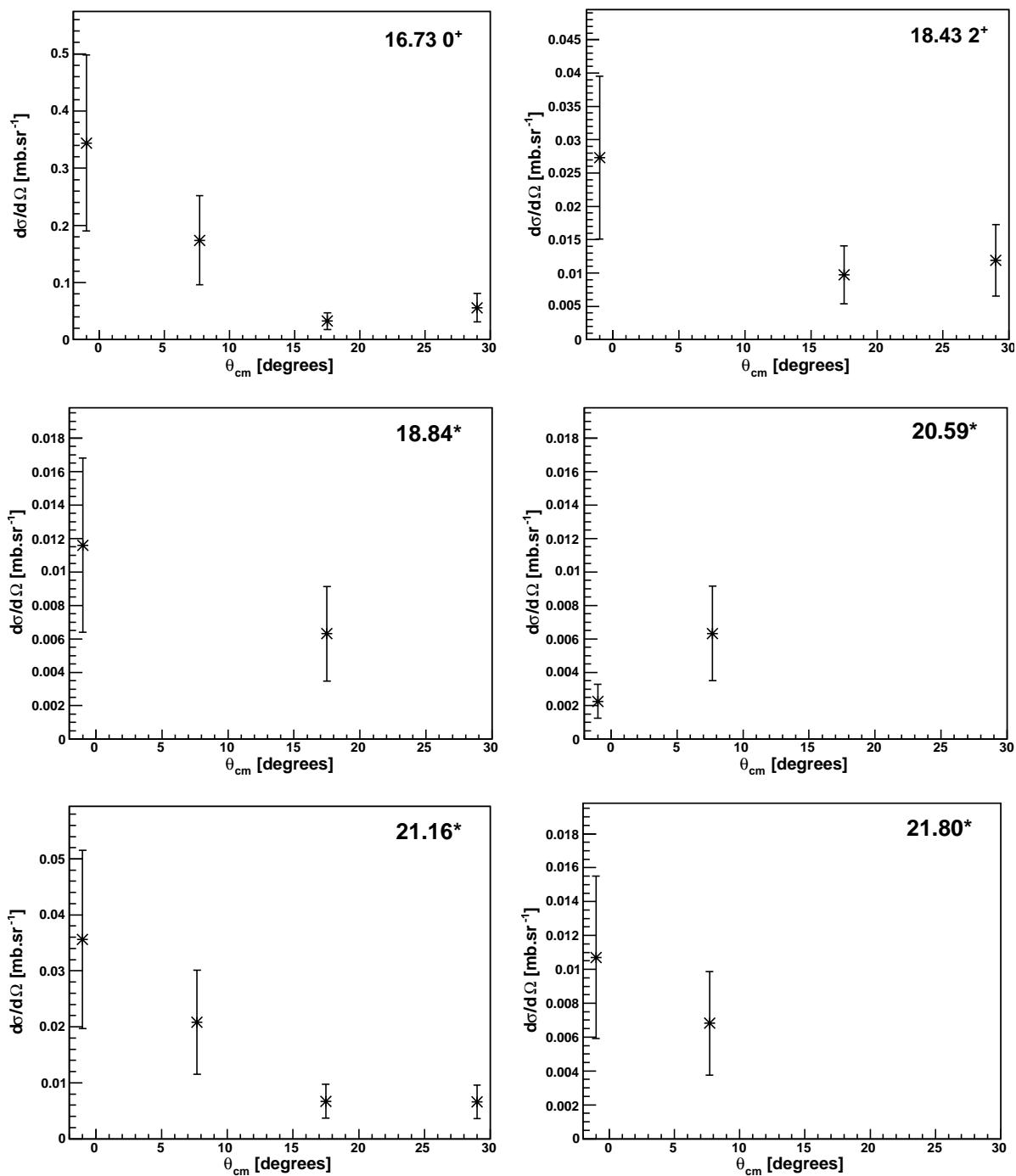


FIG. 4.41: Angular distribution plots for some of the states measured above $E_x = 16$ MeV. Newly observed states are indicated by an asterisk.

CHAPTER 5

Interpretation of the new states

It has long been known that isobaric analogue resonances may occur at high excitation energies in nuclei yet still have relatively narrow widths (Γ close to or within 100 keV), making them distinguishable from a continuous background of states by their isospin quantum number [44]. Hence, it was presumed that the narrow ($\Gamma < 60$ keV) states experimentally observed above $E_x = 20$ MeV in this measurement may be states of this nature. Known states with similar binding energies were identified in the isobaric nucleus ^{20}O , between $E_x = 3$ MeV and $E_x = 6$ MeV.

By implication, these states would have isospin values of $T = 2$, which would explain how they can have such narrow widths despite being more than 3 MeV above the separation energies for both protons ($S_p = 16.9$ MeV) and neutrons ($S_n = 12.8$ MeV) in ^{20}Ne . Consider if one of these states were to undergo proton decay. After the decay, ^{20}Ne becomes ^{19}F with $T_z = 1/2$ and g.s. isospin $T = 1/2$ and a proton with $T_z = -1/2$ and $T = 1/2$. The vector sum of two $T = 1/2$ states may equal only $T = 0$ or $T = 1$, therefore proton decay to the g.s. or any other $T = 1/2$ state in ^{19}F is not allowed. Proton decays are only possible to the $T = 3/2$ states which are located at $E_x = 7.5$ MeV and above in ^{19}F [3]. This makes the effective proton binding energy for $T = 2$ states $S_p = 16.9$ MeV + 7.5 MeV = 24.4 MeV. By following a similar argument for neutron decay to ^{19}Ne , the effective neutron binding energy for $T = 2$ states is $S_n = 20.4$ MeV. These states may also undergo β -decay to isobaric neighbour nuclei and γ -decay to states in ^{20}Ne , but following isospin selection rules.

Among self-conjugate α nuclei lighter than ^{20}Ne , $T = 2$ states are observed with narrow widths ($\Gamma \leq 50$ keV) in ^{16}O at $E_x = 22.721$ MeV and $E_x = 24.522$ MeV, in ^{12}C (with $\Gamma \leq 200$ keV) at $E_x = 27.595$ MeV and $E_x = 29.630$ MeV, and even in ^8Be at $E_x = 27.494$ MeV with $\Gamma = 5.5$ keV. This indicates that a pair of narrow $T = 2$ states is likely to be found above $E_x = 20$ MeV in ^{20}Ne . The highest known $T = 2$ states in ^{24}Mg and ^{28}Si exist at $E_x = 15.436$ MeV and $E_x = 15.227$ MeV respectively [3].

Theoretical calculations were performed with the isobaric multiplet mass equation (IMME) (Section 5.1) and with NuShellX and FRESKO (Section 5.2), to test whether

these states in ^{20}O are related to the observed states in ^{20}Ne .

5.1 IMME calculations

The excitation energy values for states in ^{20}O which were obtained from this calculation, using the measured energy values of the candidate $T = 2$ states in ^{20}Ne , are shown in Table 5.1 [82]. These values are compared to the energy values of known experimental states in ^{20}O in the same table. From the IMME calculations, the ^{20}Ne state at $E_x = 21.16$ MeV seems very likely to be an isobaric analogue (IAS) state of the 4.456 MeV 0^+ state of ^{20}O since the calculated energy value in ^{20}O is within 20 keV of the known experimental value. Furthermore, the angular distribution plots in Fig. 5.1 e) of the 16.73 MeV 0^+ state and Fig. 5.2 a) of the $E_x = 21.16$ MeV state follow a very similar trend, indicating that the $E_x = 21.16$ MeV state must also have a 0^+ spin and parity. The angular distribution plots in Figs. 5.1 and 5.2 were generated from the experimental data, as well as from the coupled reaction channels calculations with FRESCO, which are discussed in Section 5.2.

New ^{20}Ne state [MeV]	Calculated ^{20}O E_x [MeV]	Known ^{20}O state [MeV]	Reference
20.590(54) $2^+/4^+?$	3.86	3.570 4^+	[3]
		3.895	[115]
		4.072 2^+	[3]
		4.353	[115]
21.160(53) 0^+	4.44	4.456 0^+	[3]
21.800(53) $0^+?$	5.06	4.598	[115]
		4.850 4^+	[3]
		4.99 (2^+)	[116]
		5.115	[115]
		5.23 3^+	[116]
		5.304 2^+	[3]
		5.387 0^+	[3]

TABLE 5.1: The ^{20}O excitation energy values in the 2^{nd} column, which were obtained from the IMME calculation employing the new ^{20}Ne states in the 1^{st} column, are compared to the excitation energies of known states of ^{20}O in the 3^{rd} column.

The state at $E_x = 20.59$ MeV does not have a 0^+ spin and parity since its cross section increases as one moves from $\theta_{cm} = 0^\circ$ to $\theta_{cm} = 7.7^\circ$ in Fig. 5.2 a), and could possibly have either a 2^+ or a 4^+ character. This means that it may be associated with either one of the

5. Interpretation of the new states

states at $E_x = 3.570$ MeV 4^+ , $E_x = 3.895$ MeV (which has an unknown spin and parity) and $E_x = 4.072$ MeV 4^+ in ^{20}O .

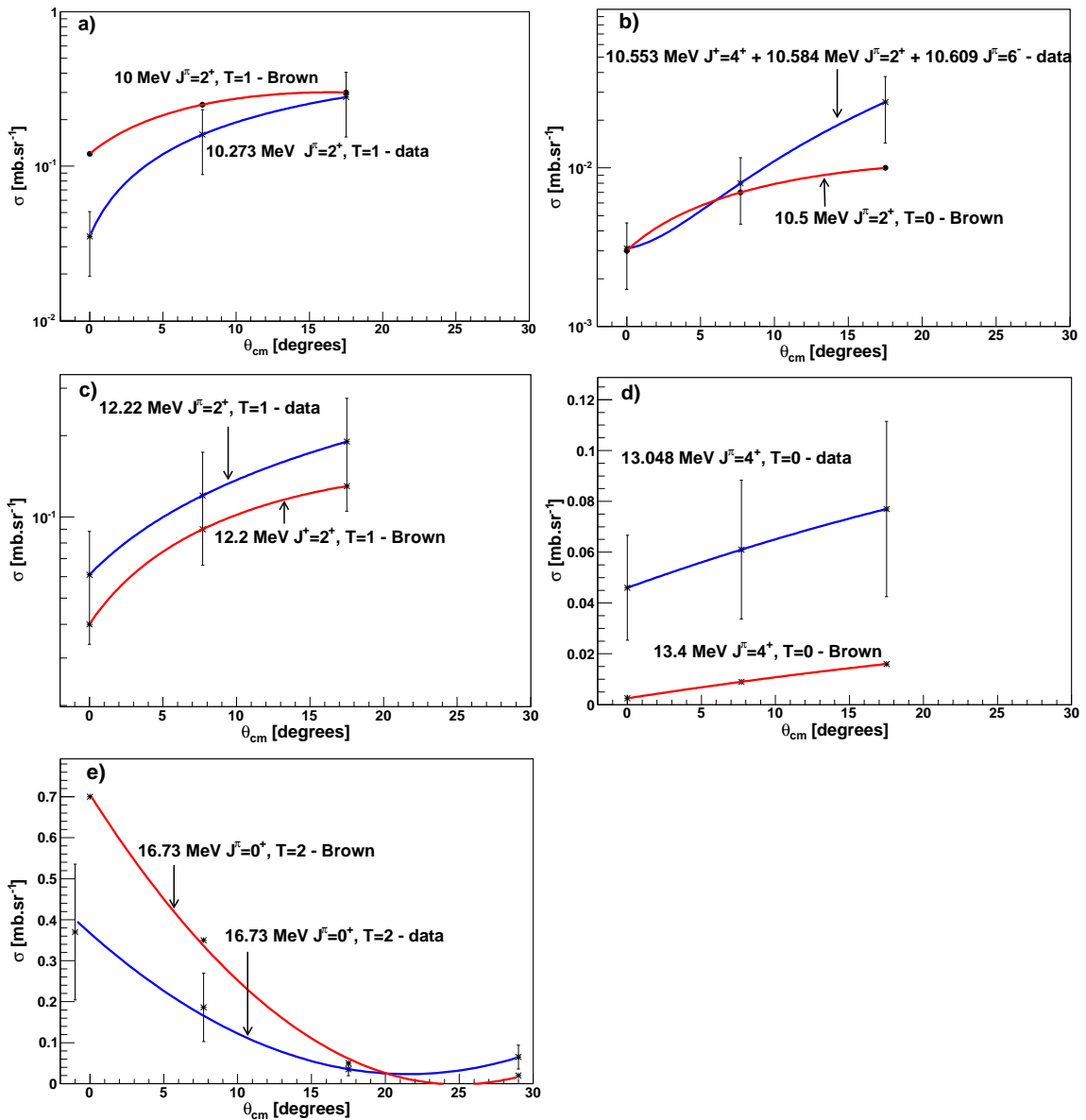


FIG. 5.1: Measured angular distribution plots (fitted with blue lines to guide the eye) are compared to angular distribution plots calculated with NuShellX and FRESKO (fitted with red lines to guide the eye) for states in ^{20}Ne .

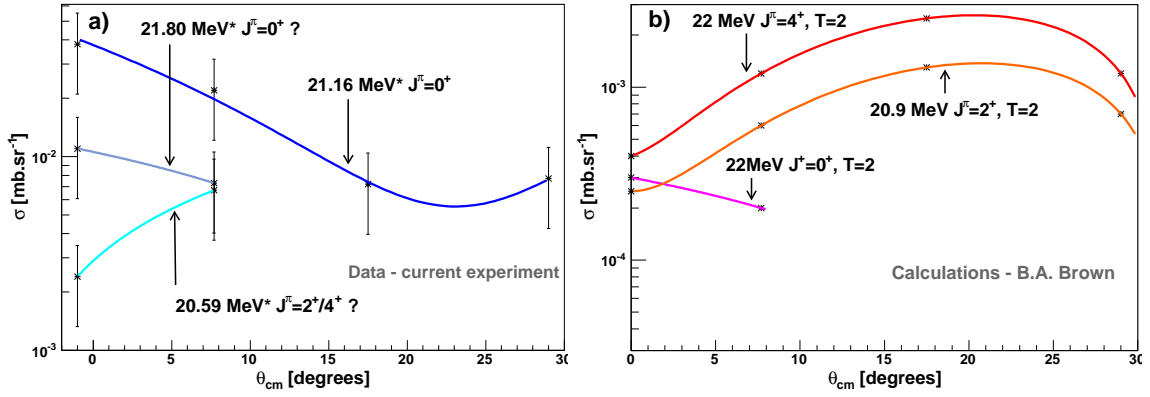


FIG. 5.2: Angular distribution plots of experimentally observed $T = 2$ candidate states are shown in a), and of $T = 2$ states calculated with NuShellX and FRESCO in b) for states in ^{20}Ne . The lines were added to these plots to guide the eye.

Fig. 5.3 shows a comparison between the experimental levels and levels generated by a p - sd shell-model calculation from Ref. [115], which is where the state at $E_x = 3.895$ MeV was reported to be observed. It seems likely, in Fig. 5.3, that one may relate the observed $E_x = 3.568$ MeV 4^+ state to the calculated $E_x = 3.771$ MeV 4^+ state, and the observed $E_x = 4.070$ MeV 2^+ state to the $E_x = 4.174$ MeV 2^+ . This leaves no obvious state in Fig. 5.3 with which the $E_x = 3.895$ MeV may be related, hence no spin and parity can be assigned to this state. The first three known ^{20}O states in Table 5.1 must therefore remain viable candidates for the IAS state of the $E_x = 20.59$ MeV state in ^{20}Ne .

The angular distribution plot of the $E_x = 21.8$ MeV state in Fig. 5.2 a), which could only be determined from $\theta_{cm} = 0^\circ$ to $\theta_{cm} = 7.7^\circ$, does not correspond to either a 2^+ or a 4^+ character, but is consistent with a 0^+ character. This means that it may be related to any of the states at $E_x = 4.598$ MeV, $E_x = 5.115$ MeV and $E_x = 5.387$ MeV. In Fig. 5.3, the state at $E_x = 4.598$ MeV may well be related to one of the $1p$ - $1h$ negative parity states predicted by the p - sd calculation in Ref. [115]. The state at $E_x = 5.115$ MeV is within 80 keV of a predicted pure sd -shell 0^+ state at $E_x = 5.038$ MeV 0^+ . This state may be related to the $E_x = 5.059$ MeV state deduced from an IMME calculation on the $E_x = 21.8$ MeV state from the current measurement, and be reproduced by the $E_x = 5.038$ MeV state from the p - sd shell-model in Ref. [115]. However, since an error of a few hundred keV may typically be associated with both IMME and shell-model calculations, both the state with unknown spin and parity at $E_x = 4.598$ MeV and the $E_x = 5.387$ MeV 0^+ state remain candidates for the IAS state in ^{20}O of the newly observed $E_x = 21.8$ MeV state in ^{20}Ne .

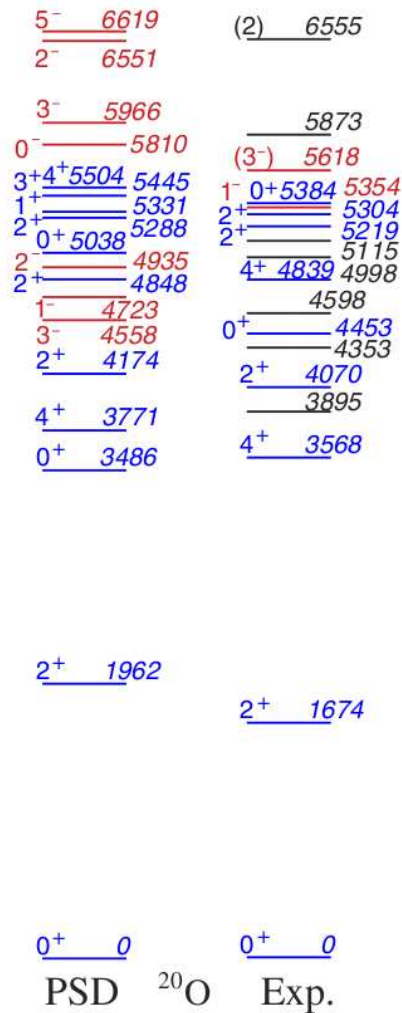


FIG. 5.3: Calculated and experimental states in ^{20}O . Positive parity states have blue labels, negative parity states have red labels. All negative parity states are from $1p$ - $1h$ states, and positive parity states are $0p$ - $0h$ states, apart from 3.486 and 4.848 MeV which are $2p$ - $2h$ states. The states with black labels, as well as the figure itself, are from Ref. [115].

Table 5.2 lists the results obtained with the IMME.C code by following the methodology described in Section 2.4.2.2, for the states in Table 5.1 which remain candidate $T = 2$ analogue states after the discussion thus far. These are compared to the results for the two known $T = 2$ states of ^{20}Ne at $E_x = 16.73$ MeV and $E_x = 18.43$ MeV on the same table. The known $T = 2$ states are both underpredicted by approximately 600 keV. The calculated values in ^{20}Ne for the states of ^{20}O at $E_x = 3.895$ MeV, $E_x = 4.456$ MeV and $E_x = 5.115$ MeV are all within 50 keV of 600 keV below the states measured in this experiment. Hence, from the predictions using the IMME.C code, these three states in ^{20}O

are the most likely candidates for $T = 2$ IAS states of the three newly measured narrow states in ^{20}Ne . From their excitation energy positions, these three states are also the most likely $T = 2$ states from the predictions shown in Table 5.1.

Known ^{20}O state [MeV]	Calculated ^{20}Ne E_x (IMME code) [MeV]	Measured ^{20}Ne state [MeV]	Exp. - theory [MeV]
g.s.	16.13	16.73	0.60
1.674	17.81	18.43	0.62
3.570 4^+	19.70	20.59 $2^+/4^+?$	0.89
3.895	20.03		0.56
4.072 2^+	20.21		0.38
4.456 0^+	20.59	21.16 0^+	0.57
4.598	20.73	21.80 $0^+?$	1.07
5.115	21.25		0.55
5.387 0^+	21.52		0.28

TABLE 5.2: The values of ^{20}Ne excitation energies which were calculated from known states in ^{20}O with the IMME.C code are compared to the excitation energies of candidate $T = 2$ states from the current, and known $T = 2$ states from previous experiments on ^{20}Ne .

5.2 NuShellX and FRESKO calculations

Fig. 5.4 shows the results of calculations for the $^{22}\text{Ne}(p,t)^{20}\text{Ne}$ reaction at $\theta_{cm} = 0^\circ$ with an incoming proton beam energy of $E_p = 65$ MeV, performed by Alex Brown with NuShellX and FRESKO [71]. All 4^+ , 2^+ and 0^+ states in ^{20}Ne from $E_x = 0$ to 25 MeV were included. The same calculations were also performed for $\theta_{lab} = (7^\circ, 16^\circ, 27^\circ)$, and these are included in Appendix D. The results of these calculations may be compared to the cross section values which were extracted for the same states at $\theta_{lab} \cong 0^\circ$ in Fig. 5.5. Cross sections were extracted for states observed at $\theta_{lab} = (7^\circ, 16^\circ, 27^\circ)$, and are also shown in Appendix D. The cross section values extracted for the observed isobaric analogue candidates in ^{20}Ne are shown in Fig. 5.2 a), and the values found from the calculations for three $T = 2$ states above $E_x = 20$ MeV are shown in Fig. 5.2 b). Width values could not be assigned to these states by the calculations, hence none were assigned to the experimental spectra in Fig. 5.5 to aid comparisons with the calculations in Fig. 5.4.

Numerous $T = 0$ and $T = 1$ states are predicted by the calculations between $E_x = 15$ MeV and $E_x = 25$ MeV. Most of these states could not be identified in the data from this measurement. It is presumed that they are much broader than the newly observed states and will therefore form part of the continuous background of states from ^{20}Ne . The lowest known $T = 2$ state in ^{20}Ne , the 16.73 MeV 0^+ state, is seen to be narrow and strong at each angle. The second $T = 2$ state, the 18.43 MeV 2^+ , is seen at only two angles, due to contamination from the aramid gas-target foil.

The measured angular distribution plots of a few of the known states in ^{20}Ne are compared to the angular distribution plots from calculations in Fig. 5.1. The measured and calculated spectra mostly follow similar trends, with the absolute cross section values usually differing by factors between 2 and 10. In the case of the 2^+ state at $E_x = 12.2$ MeV, the measurement and the calculation are almost perfectly matched. The 2^+ state calculated at around $E_x = 10.5$ MeV does not match the trend of the peak measured nearest to this line, since this peak is composed of 4^+ , 2^+ and 6^- states which could not be resolved.

The calculated spectra for $\theta_{lab} = 0^\circ$ and $\theta_{lab} = 7^\circ$ indicate a $T = 2$ state with 0^+ character just above $E_x = 22$ MeV. This state may be related to either the observed 0^+ state at $E_x = 21.16$ MeV, or to the observed state at $E_x = 21.8$ MeV, which may possibly have a 0^+ character. This calculated state is significantly weaker than the observed states

at $E_x = 21.16$ MeV (by a factor of 100) and $E_x = 21.8$ MeV (by a factor of 30).

The calculations also indicate a 4^+ state with $T = 2$ which occurs just above $E_x = 22$ MeV at all four angles, and a 2^+ state at slightly below $E_x = 22$ MeV at $\theta_{lab} = (7^\circ, 16^\circ, 27^\circ)$, but not at $\theta_{lab} = 0^\circ$. Neither of the strong experimentally evidenced states at $E_x = 21.16$ MeV and $E_x = 21.8$ MeV exhibit a 4^+ character, and both are observed near $\theta_{lab} = 0^\circ$, therefore these two calculated 4^+ and 2^+ states cannot be associated with them.

There is a 2^+ state with $T = 2$ from the calculations which occurs at each angle at an excitation energy of slightly below 21 MeV. This state may be related to the ^{20}Ne state which was measured at $E_x = 20.59$ MeV. This would imply that the 20.59 MeV ^{20}Ne state has a 2^+ spin and parity and may therefore be an IAS state to the $E_x = 4.072$ MeV 2^+ state in ^{20}O , rather than to the $E_x = 3.895$ MeV state. The observed state at $E_x = 20.59$ MeV follows a very similar trend to the calculated 2^+ state in its angular distribution plot from $\theta_{cm} = 0^\circ$ to $\theta_{cm} = 7.7^\circ$ in Fig. 5.2, with measured absolute cross section values which are larger than the calculated values by a factor of 5. This state is indicated as a 2^+ state in the experimental spectra in Figs. 5.5 and D.4 (in Appendix D). This leaves one with no measured states which could be associated with the aforementioned 4^+ and 2^+ $T = 2$ states located above and below $E_x = 22$ MeV in the calculations.

In summary, the calculated $T = 2$ state with 0^+ character just above $E_x = 22$ MeV may be associated with the states observed at either $E_x = 21.16$ MeV or $E_x = 21.8$ MeV, and the state observed at $E_x = 20.59$ may correspond to the $T = 2$ state with 2^+ character at an excitation energy slightly below $E_x = 21$ MeV from the calculations. The fact that the calculated 0^+ , $T = 2$ state close to $E_x = 22$ MeV is so much weaker than either of the states measured at $E_x = 21.16$ MeV and $E_x = 21.8$ MeV, indicates that these two states are not sd -shell states, if indeed they are $T = 2$ states. It is possible that they are $2p$ - $2h$, or even $4p$ - $4h$, intruder states, coming from holes in the p -shell. This would explain how they are not reproduced by the sd -shell calculation, while retaining their positive parities.

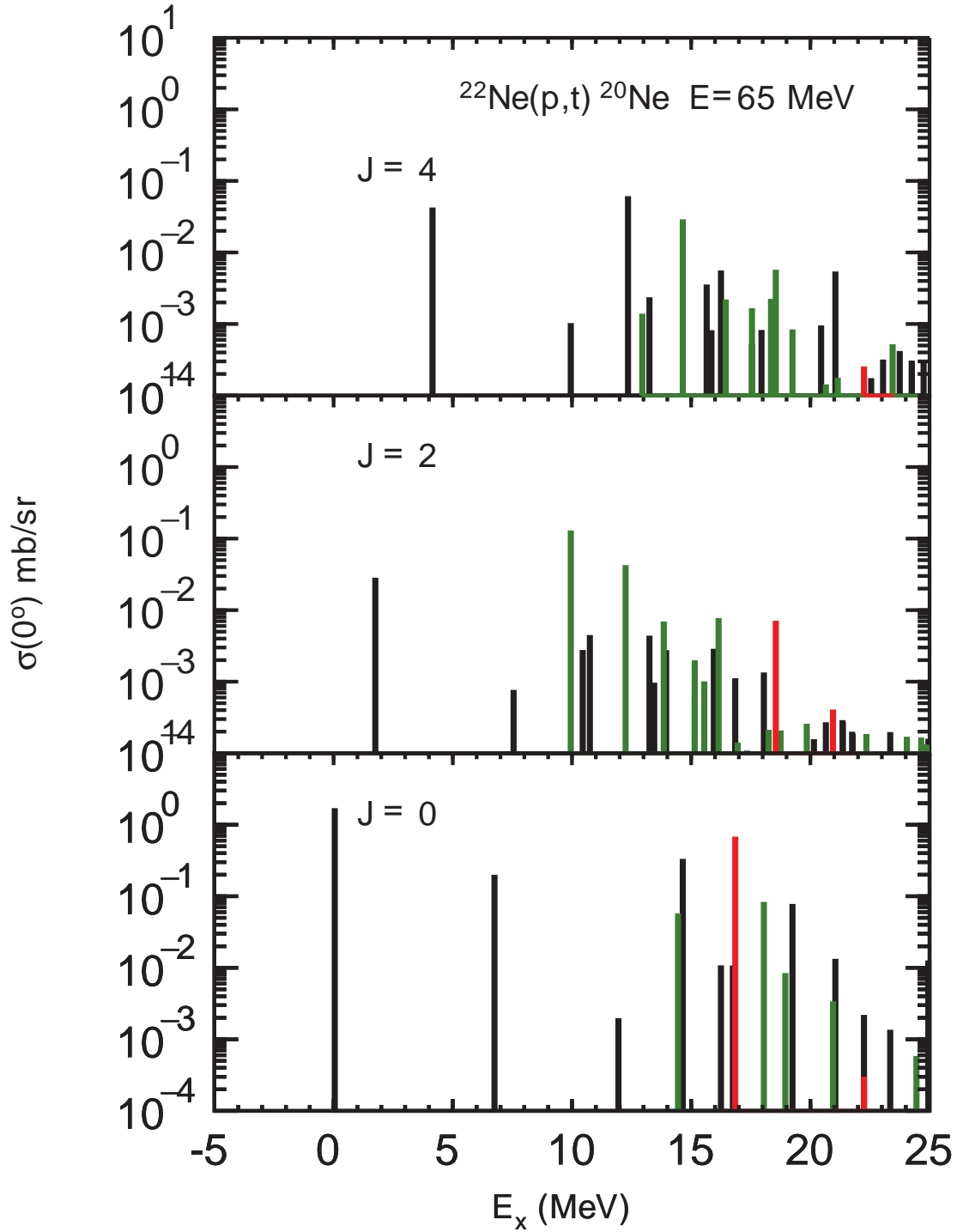


FIG. 5.4: Calculated cross section values of 4^+ , 2^+ and 0^+ states at $\theta_{lab} = 0^\circ$ in ^{20}Ne . The black lines are $T = 0$, green lines are $T = 1$ and the red lines are $T = 2$. This figure is from Ref. [71].

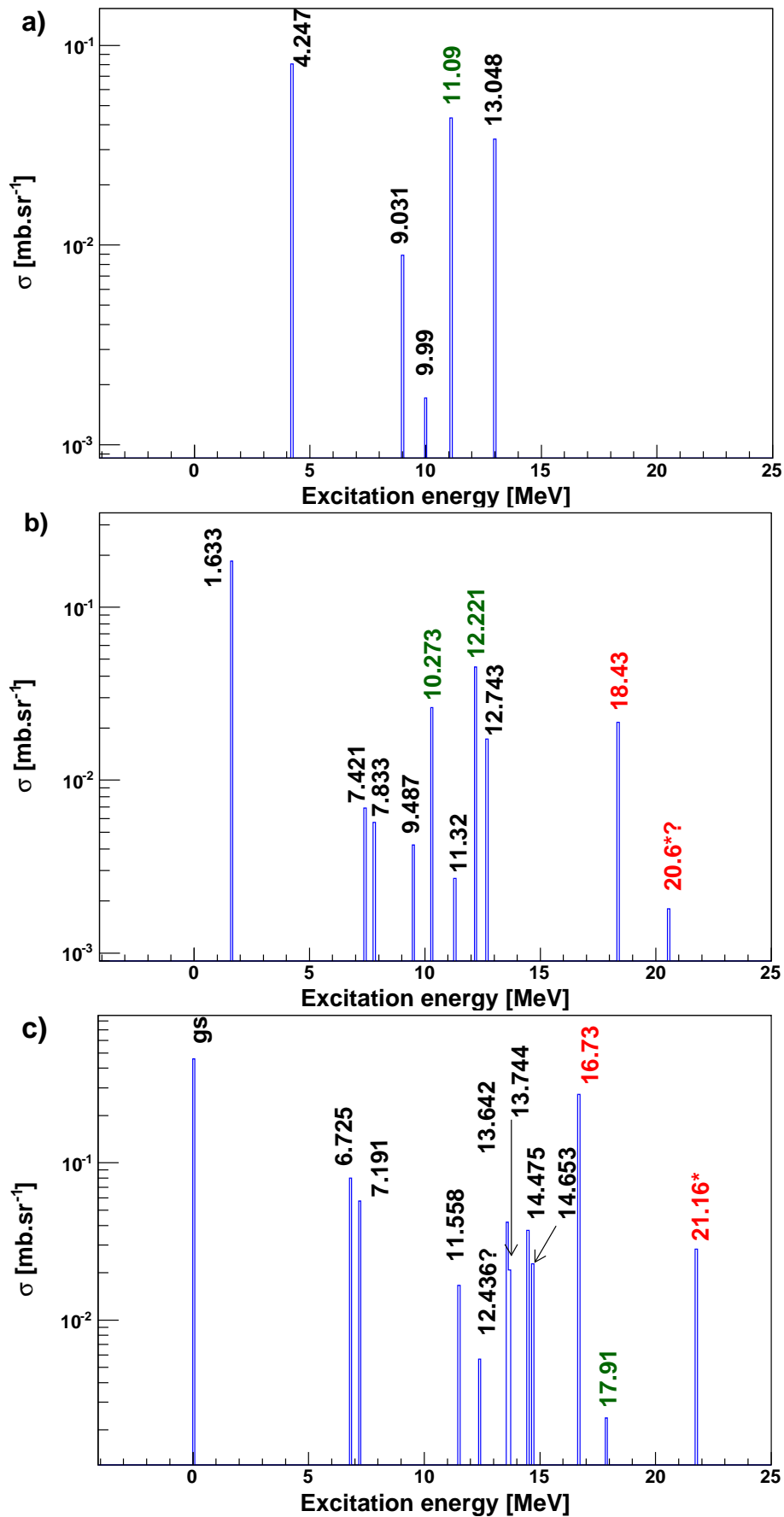


FIG. 5.5: Cross section values extracted from the $\theta_{lab} = 0^\circ$ data for states of spins and parities 4^+ , 2^+ , 0^+ from top to bottom. States with black labels are $T = 0$, green labels are $T = 1$ and red labels are either known $T = 2$ or candidate $T = 2$ states.

Fig. 5.6 shows a comparison between the predicted states from Fig. 5.4, and states of all spins and parities that have been observed near to $\theta_{lab} = 0^\circ$ in the present experiment. Good agreement is seen between experiment and theory from the ground states up to $E_x = 10$ MeV, with most of the measured states which were not predicted being negative parity states. Among the predicted excitation energies above $E_x = 15$ MeV, there are several $T = 0$ and $T = 1$ states, as well as a few $T = 2$ states, which could possibly be associated with the six newly observed states. However, the predicted energy levels become too dense at these energies to associate the new states with specific predicted states. Furthermore, in the case of the newly observed $E_x = 18.84$ MeV state, it is likely that more than one state contributes to the observed peak.

5.3 The 5- α cluster candidate

If the state observed at $E_x = 22.5$ MeV is the 5- α cluster state, then it should not be expected that it would be reproduced by this shell-model calculation. However, as discussed in Chapter 4, this state could possibly be composed of more than one state, which may all have no relation to the 5- α cluster state. If this is true, then these states may be related to states which were generated in close vicinity in excitation energy by the NuShellX calculation.

Comparing to known and candidate multi- α cluster states, the well-known 3- α Hoyle state in ^{12}C is situated 0.38 MeV above the 3- α break-up threshold and has a width of merely $\Gamma = 8.5$ eV [3]. The candidate 4- α cluster state at $E_x = 15.097$ MeV in ^{16}O has a width of $\Gamma = 166$ keV at 0.66 MeV above the 4- α break-up threshold. This state is also 7.9 MeV above the α -decay threshold, 2.97 MeV above the neutron-decay threshold and 0.57 MeV below the proton-decay threshold in ^{16}O . The newly observed state at $E_x = 22.5$ MeV in ^{20}Ne is situated 3.33 MeV above the 5- α break-up threshold, 17.8 MeV above the α -decay threshold, 5.63 MeV above the neutron-decay threshold and 9.66 MeV above the proton-decay threshold [3]. Based on this information, one might anticipate a width of at least a few hundred keV, and possibly much larger than 1 MeV, for a $T = 0$, 5- α cluster state at $E_x = 22.5$ MeV. Hence, the value of $\Gamma = 260$ keV which was observed for the state at $E_x = 22.5$ MeV may possibly be a bit small to signify a 5- α cluster state in any case.

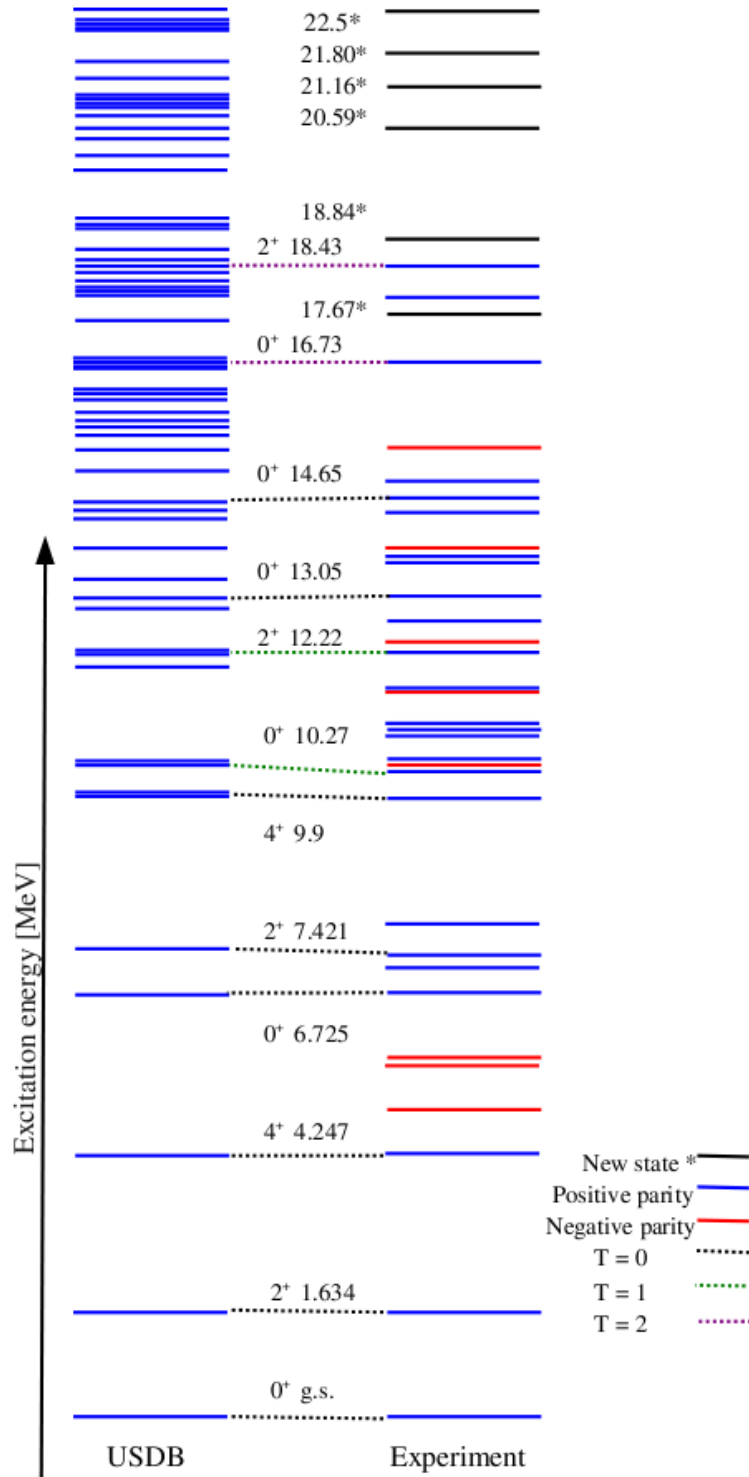


FIG. 5.6: Comparison of calculated (with NuShellX and FRESKO, left) and observed states (right) in ^{20}Ne from the $^{22}\text{Ne}(p,t)^{20}\text{Ne}$ reaction. Calculations were performed at $\theta_{cm} = 0^\circ$, and measurements were performed at $\theta_{lab} = -1^\circ$.

CHAPTER 6

Conclusion and future prospects

6.1 Conclusion

A measurement was performed with the *K600* magnetic spectrometer using the $^{22}\text{Ne}(p,t)^{20}\text{Ne}$ reaction to attempt to identify low-spin states, which would possibly include the 5- α ‘Hoyle analogue’ cluster state, in a high excitation energy range of ^{20}Ne at four different spectrometer angles. A 10-mm-thick ^{22}Ne gas target, which employed aramid foils with a thickness close to 6 μm as target windows, was used for almost all the measurements, with observed resolution values close to $\text{FWHM} = 60 \text{ keV}$ at $\theta_{lab} = 27^\circ$ with a gas pressure approaching $P = 1.5 \text{ bar}$.

A tentative candidate for the 5- α cluster state was observed with a width of $\Gamma = 260 \text{ keV}$ at $E_x = 22.5 \text{ MeV}$, but this could not be confirmed due to interference of carbon and oxygen contaminants on the aramid foils at $\theta_{lab} = -1^\circ$ and $\theta_{lab} = 7^\circ$, and the limited energy ranges at $\theta_{lab} = 16^\circ$ and $\theta_{lab} = 27^\circ$. Data obtained at $\theta_{lab} = 7^\circ$ indicate that this peak may be composed of more than one state in ^{20}Ne . If it were to be two unresolved states then the individual widths of these states would be too narrow to be associated with the 5- α cluster state, for which a width of at least a few hundred keV may be anticipated.

New narrow states ($\Gamma < 60 \text{ keV}$) were observed at $E_x = 20.590(54) \text{ MeV}$, $E_x = 21.160(53) \text{ MeV}$ and $E_x = 21.800(53) \text{ MeV}$ in ^{20}Ne . The state at $E_x = 21.16 \text{ MeV}$ appears to have a 0^+ character and IMME calculations in Section 5.1 indicate that it may be an IAS state of the $E_x = 4.456 \text{ MeV}$ 0^+ state in ^{20}O .

It is difficult to draw conclusions from the NuShellX and Fresco calculations in Section 5.2, since the cross sections generated by these calculations differ by a factor of up to almost 100 from the experimental values for the candidate $T = 2$ states. In addition, the calculations indicate only one $T = 2$ state for which the absolute cross section decreases from $\theta_{cm} = 0^\circ$ to $\theta_{cm} = 7.7^\circ$, while the measured data indicate two.

Nevertheless, these calculations indicate that the $E_x = 20.59 \text{ MeV}$ state is more likely to be related to the $E_x = 4.072 \text{ MeV}$ 2^+ in ^{20}O , shown in Tables 5.1 and 5.2, if it is indeed a $T = 2$ state. The $E_x = 21.80 \text{ MeV}$ state is probably related to either the $E_x = 5.115 \text{ MeV}$ state with unknown spin and parity, or to the $E_x = 5.387 \text{ MeV}$ 0^+ state in ^{20}O , if it is a

$T = 2$ state.

There is an indication of another state in ^{20}Ne at $E_x = 17.670(57)$ MeV, and of a collection of states, with a total width of approximately $\Gamma = 100$ keV, which could not be resolved at $E_x = 18.840(56)$ MeV. Numerous $T = 0$ and $T = 1$ states, which may be related to some of the newly observed states mentioned here, were generated within the sd -shell of ^{20}Ne by the NuShellX code [71].

6.2 Future prospects

A coincident measurement with cleaner background conditions will be necessary to identify the $5\text{-}\alpha$ cluster state and to ascertain the nature of some of the newly observed states from this experiment. The $5\text{-}\alpha$ cluster candidate at $E_x = 22.5$ MeV needs to be investigated specifically to determine whether it is composed of one or more states, and whether it has an α -cluster character.

The cryogenic target development described in Section 3.6 may be continued, either to create a target with a better resolution by compressing the gas in a target with a smaller absolute thickness, or to make a target which can contain a larger areal density of material with a similar absolute thickness to improve the ratio of gas cell-related statistics to target foil-related statistics. This can be done up to some limit, however, where the effective thickness of material may excessively affect the resolution.

Another way to improve the resolution with the gas cell would be to increase the beam energy. At high enough beam energies (E_{beam} close to 200 MeV) the energy loss through the foils would be low enough for no double-peaking to be observed from foil-related peaks, even with an α -particle beam. The main disadvantage related to an increased beam energy is that the cross section values decrease substantially.

Nevertheless, the $^{20}\text{Ne}(\alpha, \alpha')^{20}\text{Ne}$ and $^{16}\text{O}(\alpha, \alpha')^{16}\text{O}$ reactions, which would give the best selectivity for the 0^+ multi- α cluster states, may be employed. The $^{22}\text{Ne}(\alpha, \alpha')^{22}\text{Ne}$ and $^{21}\text{Ne}(\alpha, \alpha')^{21}\text{Ne}$ reactions may also be investigated. Some of the bands in these nuclei may be interpreted as having $^{16}\text{O} + \alpha$ molecular structures with covalent valence neutrons [38, 117].

In order to conclusively identify a state with the $5\text{-}\alpha$ cluster character, it will be necessary to measure its α -decay. One possibility is to use an array of silicon semi-conductor detectors in the scattering chamber to observe the α -decay in coincidence with the spec-

trometer focal plane measurement of tritons, α -particles or any other ejectile. This may not be effective, however, since the α particles from the gas might fail to penetrate the gas target foils.

To avoid this problem, the ‘Actar’ or ‘active target’, where the gas target is designed to be a position-sensitive drift-chamber detector, is being designed. This target would have an electric field applied over it so that the drift times of electrons towards its signal wires may be used to track the particles which decay from the residual nucleus, in the same way that the VDCs of the *K600* track ejectile particles. A Si layer may also be included to aid the measurement of α -decay. The Actar measurements may be recorded in coincidence with the high energy resolution measurements recorded by the *K600*’s VDCs to provide information about the decay modes of excited states in nuclei, using either solid or gas targets [118]. A similar detector was designed and built for nuclear astrophysics by TRIUMF (Tri-University Meson Facility) and the University of York [119].

The *Hagar* NaI γ -detector at iThemba LABS, shown in Fig. 6.1, would be ideal as an ancillary detector to identify $T = 2$ states in $T_z = 0$ nuclei, because it provides fast counting over a large volume and it can measure large γ -energies [120, 121], which may be expected from γ -decays from the $T = 2$ states to the nearest $T = 1$ states in such nuclei.



FIG. 6.1: The *Hagar* NaI detector for large-volume γ -ray detection

Another way to test whether the newly observed states at $E_x = 20.59$ MeV, $E_x = 21.16$ MeV and $E_x = 21.80$ MeV are isobaric analogue states would be to employ the $^{22}\text{Ne}(p, ^3\text{He})^{20}\text{F}$ reaction in the manner of Ref. [45] in the appropriate energy range in ^{20}F and to compare that with the $^{22}\text{Ne}(p, t)^{20}\text{Ne}$ data from this measurement. Peaks with similar widths at similar energy positions (within a few hundred keV) and with the same spins and parities in both nuclei would be indicative of IAS states.

There are several examples of (p, t) and $(p, ^3\text{He})$ reactions having been used to identify IAS states in isobaric nuclei in the past [45, 54, 122], and there are a number of possibilities for this to be done in the future. These reactions provide the advantage that the magnetic fields of the spectrometer can be adjusted to each separate particle species of interest, while maintaining the same beam and target.

The calculated cross section ratios in Table 6.1 were obtained by employing DWBA to two-nucleon reactions, for which $T_f = T_i + 1$ where T_f denotes the isospin of the residual nucleus and T_i is that of the target. The final results are valid for sd -shell states in the final nucleus. In Fig. 6.2, the 16.73 MeV 0^+ , $T = 2$ state in ^{20}Ne is populated, but not nearly as strongly as in the present measurement, and its $T = 2$ analogue in ^{20}F , at $E_x = 6.519$ MeV, is populated with a strength which corresponds well to the prediction for ^{22}Ne as the target nucleus in Table 6.1 [123].

Final states J^π, T_f	Allowed L -value(s)	Target nucleus	Cross section ratio - experimental	Cross section ratio - calculated
$0^+, 1$	0	^{16}O	2.19 ± 0.22	1.88
$0^+, 1$	0	^{36}Ar	1.92 ± 0.19	1.80
$2^+, 1$	2	^{36}Ar	1.54 ± 0.20	1.78
$5/2^+, 3/2$	0, 2	^{21}Ne	1.05 ± 0.10	0.93
$5/2^+, 3/2$	0, 2, 4	^{25}Mg	0.85 ± 0.09	0.92
$5/2^+, 3/2$	0, 2, 4	^{27}Al	0.89 ± 0.09	0.90
$5/2^+, 3/2$	2	^{31}P	0.71 ± 0.11	0.88
$0^+, 2$	0	^{22}Ne	0.70 ± 0.09	0.62
$0^+, 2$	0	^{26}Mg	0.61 ± 0.06	0.61
$0^+, 2$	0	^{30}Si	0.54 ± 0.10	0.60

TABLE 6.1: Calculated and experimental relative cross sections $\frac{d\sigma(p, t)/d\Omega}{d\sigma(p, ^3\text{He})/d\Omega}$ for states with $T_f = T_i + 1$. Note that $d\sigma(p, ^3\text{He})/d\Omega$ is stronger than $d\sigma(p, t)/d\Omega$ when ^{22}Ne is the target nucleus, according to both the calculated and experimental values [123].

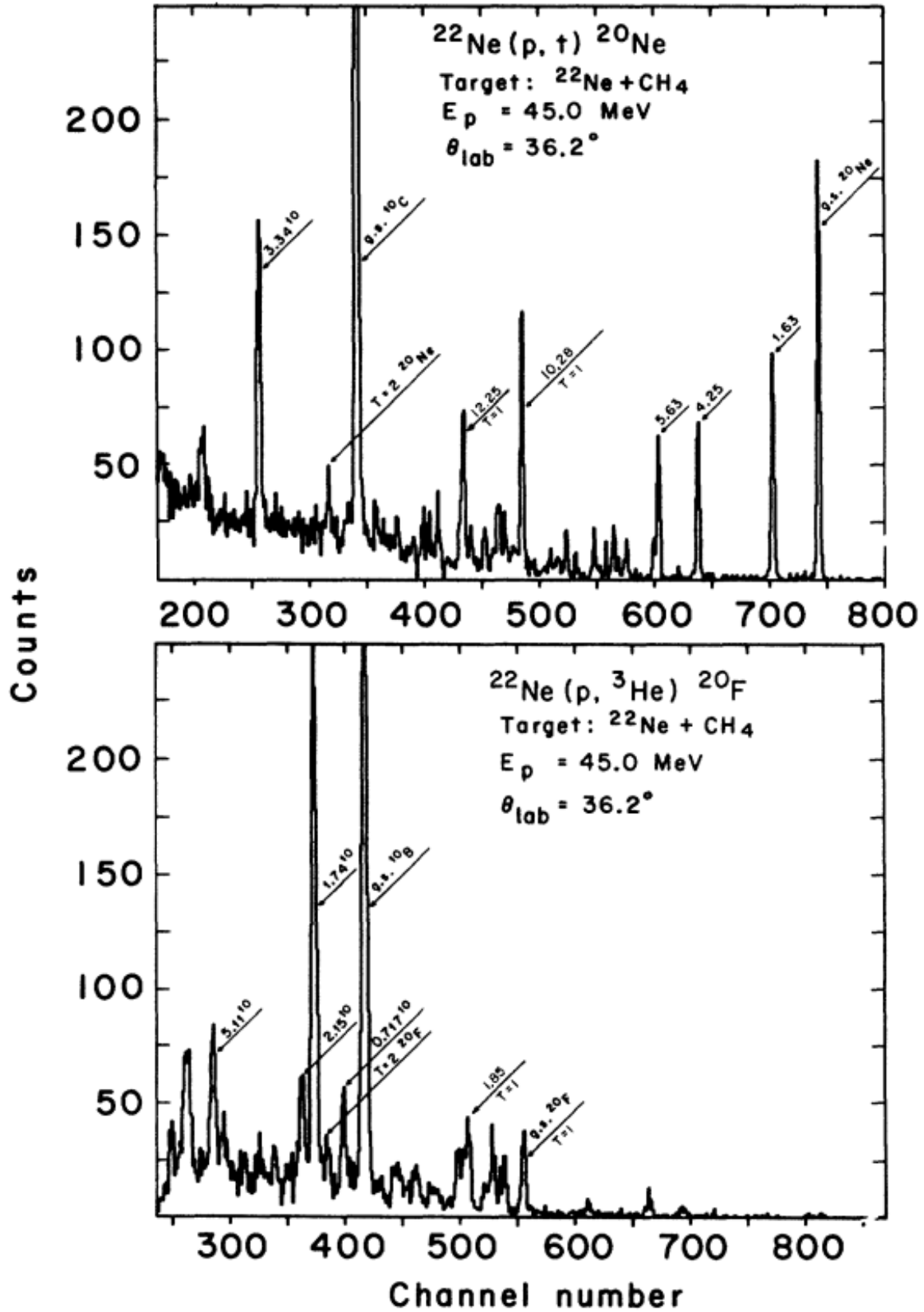


FIG. 6.2: Energy spectra measured with the (p,t) and $(p,^3\text{He})$ reactions using the same ^{22}Ne gas target, beam and angle

The angle of the measurement in Ref. [123] ($\theta_{lab} = 36.2^\circ$) was probably detrimental to the measurement of 0^+ , $T = 2$ analogue states in ^{20}Ne and ^{20}F . At small angles with the magnetic spectrometer, these states should be strongly populated, as was the case with the $E_x = 16.73$ MeV state in the present measurement.

If the states measured at $E_x = 20.59$ MeV, $E_x = 21.16$ MeV and $E_x = 21.80$ MeV with the $^{22}\text{Ne}(p,t)^{20}\text{Ne}$ reaction are of isospin $T = 2$, then their analogues should be populated by the $^{22}\text{Ne}(p,^3\text{He})^{20}\text{F}$ reaction with relative strengths corresponding to the inverse of the ratio in Table 6.1. The next $T = 1$ level in this nucleus is situated at $E_x = 12.221$ MeV, which means that γ -decays with energies exceeding 8 MeV may be anticipated, following isospin selection rules. A NaI detector would be ideal for identifying such decays.

If the lower two of these states are related to the $E_x = 4.072$ MeV and $E_x = 4.456$ MeV states in ^{20}O , then Coulomb shift calculations predict $T = 2$ states at $E_x = 10.470$ MeV and $E_x = 10.827$ MeV in ^{20}F [48]. Another $T = 2$ state, related to the $E_x = 21.80$ MeV state in ^{20}Ne , could then be expected at about 600 keV above this hypothetical $E_x = 10.827$ MeV state. Table 6.2 shows the states which are known in this region of ^{20}F , according to the EXFOR data base [3].

E_x [MeV]	Reaction	J^π	Γ [keV]
10.228	AB	$0^-, 1$	200
10.480	B		10
10.641	AB	1,2	70
10.807	AB	$0^-, 1$	310
10.990	A		190
11.045	A		30
11.130	A		≤ 25
11.244	A		≤ 25
11.287	A		
11.490	B		

TABLE 6.2: Known states in the region of ^{20}F where $T = 2$ states may be anticipated. A denotes the reactions $^{16}\text{O}(\alpha, \alpha')$ and $^{16}\text{O}(\alpha, 2\alpha')$, and B denotes $^{16}\text{O}(^6\text{Li}, d)$ [3].

The isospins of the states in Table 6.2 are unknown, and little is known about their γ -decay strength, spin and parities. A few of these states are potential candidates for $T = 2$ states owing to their narrow widths, e.g. at $E_x = 10.480$ MeV, $E_x = 10.641$ MeV. Measurement of relative strengths corresponding to the values in Table 6.1, along with the anticipated

γ -decays in ^{20}Ne and ^{20}F , would serve as conclusive evidence of IAS states.

This type of measurement could be expanded to a number of other nuclei in the same mass region ($A = 8 - 50$), as was done in Ref. [124], for instance. The iThemba LABS cyclotron and magnetic spectrometer provide higher beam energies and lower experimental resolutions than the aforementioned examples of such investigations, which were mostly performed during the 1960s or 70s. This makes the generation of more detailed data at higher excitation energies a possibility. In addition, the zero degree mode of the spectrometer provides the best selectivity for the $T = 2$, $J^\pi = 0^+$ states.

One interesting possibility would be the use of a ^{24}Mg target to study ^{22}Mg and ^{22}Na . This could be combined with a $^{22}\text{Ne}(\alpha, \alpha')^{22}\text{Ne}$ experiment to study the isobaric analogues in $A = 22$ nuclei. Other examples of possible targets include ^{11}B , ^{12}C , ^{16}O , ^{28}Si , etc. Fig. 6.3 shows an example where the two lowest $T = 2$ states in ^{12}C , and their analogues in ^{12}B , were measured with this technique [125].

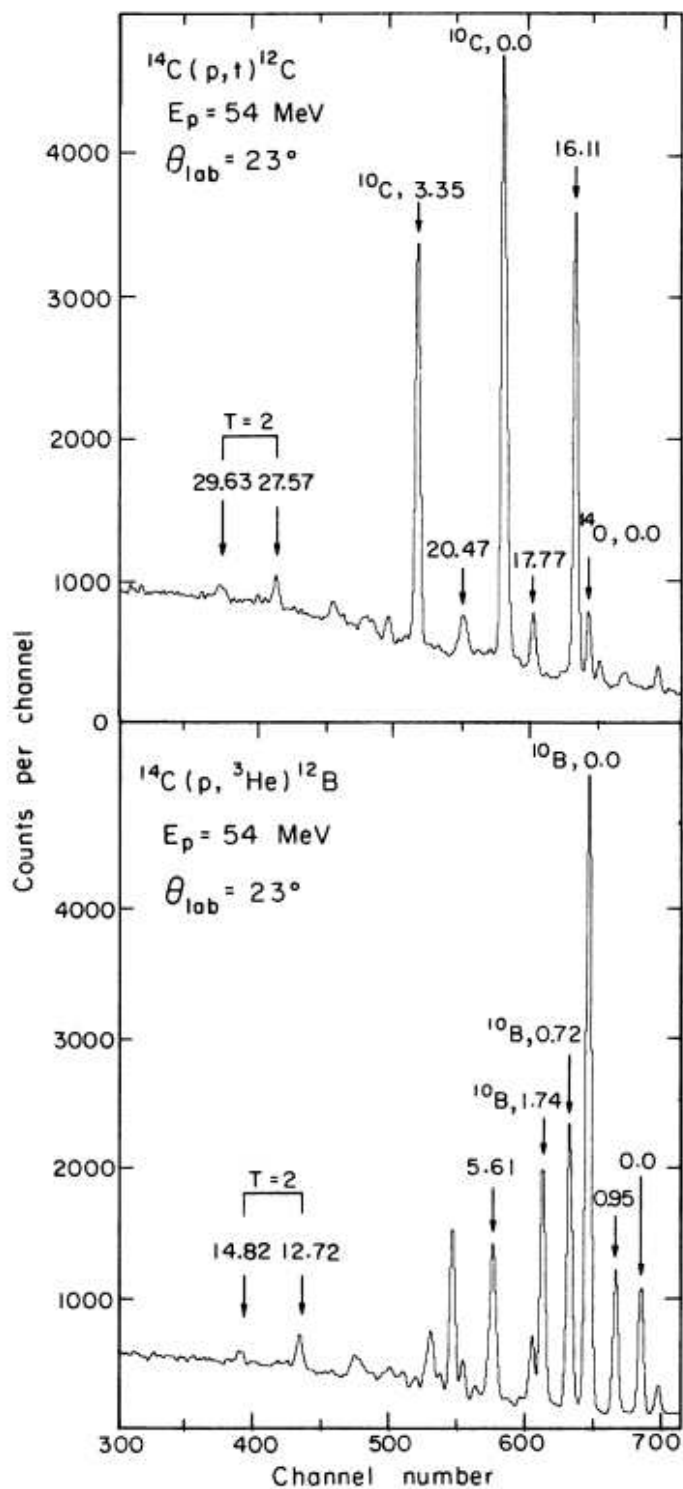


FIG. 6.3: Energy spectra measured with the (p,t) and $(p,^3\text{He})$ reactions on a ^{14}C target [125]

APPENDIX A

The IMME.C code

The IMME.C code, described in Section 2.4.2.2, is displayed here. This code was written with C++ programming language in ROOT version 5 [83]. It is based on the formalism of Ref. [84], and the equations refer to Section 2.4.2.2. The first seven lines of this code have been filled in for the calculation of the ground state mass of ^{20}Ne .

```
// IMME calculation for mass of  $^{20}\text{Ne}$ 
Int_t n=5;          // number of nuclei used
Float_t ME[n] = 67.133,37.56,21.77,3.969,-0.0174; // mass excess values from EXFOR
database [3]
Float_t Z[n] = 5,6,7,8,9;          // Z
Float_t Tz[n] = -5,-4,-3,-2,-1;    // Tz = (Z-N)/2
double T = 5.0;                    //Max Tz value
double Tf = 0.0;                   //Final isospin - nucleus investigated
double A = 20.0;                   //Mass of nucleus
//Enter all fields above, and then let the code work.
//-----//
Float_t Mo[n];
for(int i = 0; i <= n ; i++)
Mo[i] = A*931.494+ME[i];

double Ec1 = (1.1267e-15*pow(A,2.0/3.0))/(5.0*1.2e-15); // Eq. 2.24
double Ec2 = (1.1267e-15)/(5.0*1.2e-15*pow(A,2.0/3.0)); // Eq. 2.25
double b = 0.782354-Ec1; //Eq. 2.22
cout <<b<<endl;
double c = 3.0*Ec2; //Eq. 2.23
cout <<c<<endl;
Float_t Ec0[n];
for(int i = 0; i < n ; i++)
```

A. The IMME.C code

```

Ec0[i] = Mo[i+1]-Mo[i]+T*(T+1)*Ec2-b*Tz[i]-c*pow(Tz[i],2);    //Eq. 2.19

TCanvas *K1 = new TCanvas("CobusC",0);    //draw canvas
K1->Divide(1,1);
K1->cd(1);    //make pad 1 active:
TGraph *g2 = new TGraph(n-1,Z,Ec0);
TH2F *h02 = new TH2F("h01", "Ec0 vs Z",20,0,20,200,-100,100);    //set range
h02->Draw();
g2->Draw("same");
cout <<Ec0[n-2]<<endl;
cout <<Ec0[0]<<endl;
cout <<Z[n-2]<<endl;
cout <<Z[0]<<endl;
double slope=(Ec0[n-2]-Ec0[0])/(Z[n-2]-Z[0]); //calculate slope
cout <<slope<<endl;
double Eczero=Ec0[n-2]+slope;    //find Ec0 for nucleus being investigated
cout<<Eczero<<endl;
double a=ME[n-1]+Eczero-Tf*(Tf+1)*Ec2; //Eq. 2.21
cout <<a<<endl;
double M=a+b*Tf+c*pow(Tf,2.0);    //Eq. 2.20 (IMME)
cout <<M<<endl;

```

APPENDIX B

Data sets over full energy range

Excitation energy spectra measured at every magnetic field setting which was investigated over an excitation energy range from $E_x = 0 - 25$ MeV are shown for $\theta_{lab} = (7^\circ, 16^\circ, 27^\circ)$ in Figs. B.1, B.2 and B.3 respectively. The excitation energy spectrum measured at angles near $\theta_{lab} = 0^\circ$ is displayed in Fig. 4.29 in Chapter 4. Note that, for $\theta_{lab} = 27^\circ$, data were obtained only with the $E_t = 52$ MeV and $E_t = 33.5$ MeV settings due to experimental time constraints. The data acquired with these settings represent the lowest and highest excitation energy ranges which were investigated. This explains the gap in excitation energies from $E_x = 5$ MeV to $E_x = 15.7$ MeV in Fig. B.3. The states are labelled by their excitation energy values in MeV in all figures in this section.

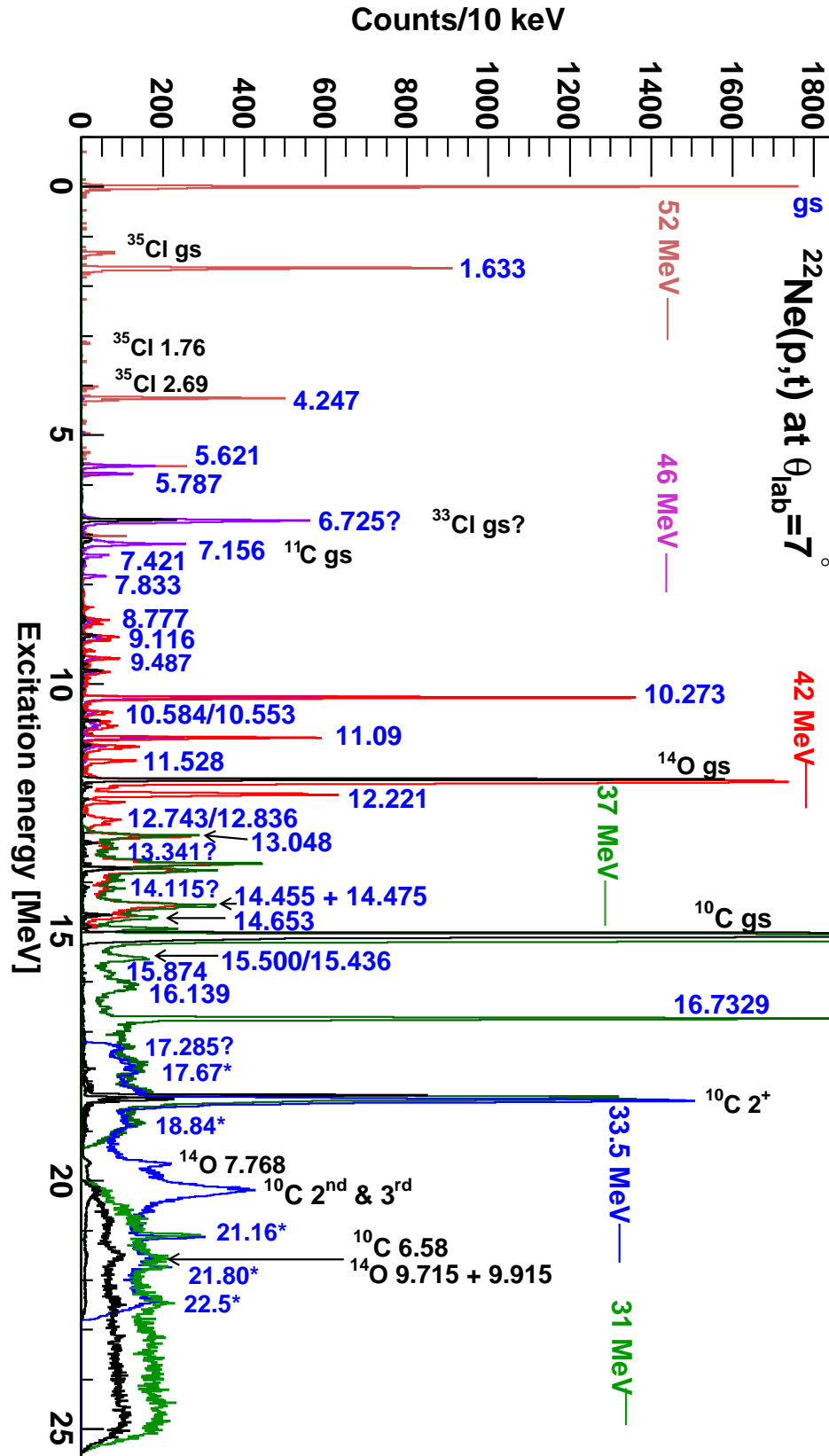


FIG. B.1: The excitation energy spectrum for all field settings on the ^{22}Ne gas-filled target at $\theta_{\text{lab}} = 7^\circ$. States from ^{20}Ne have blue labels and states from the aramid foil have black labels, as with all figures to come in this section.

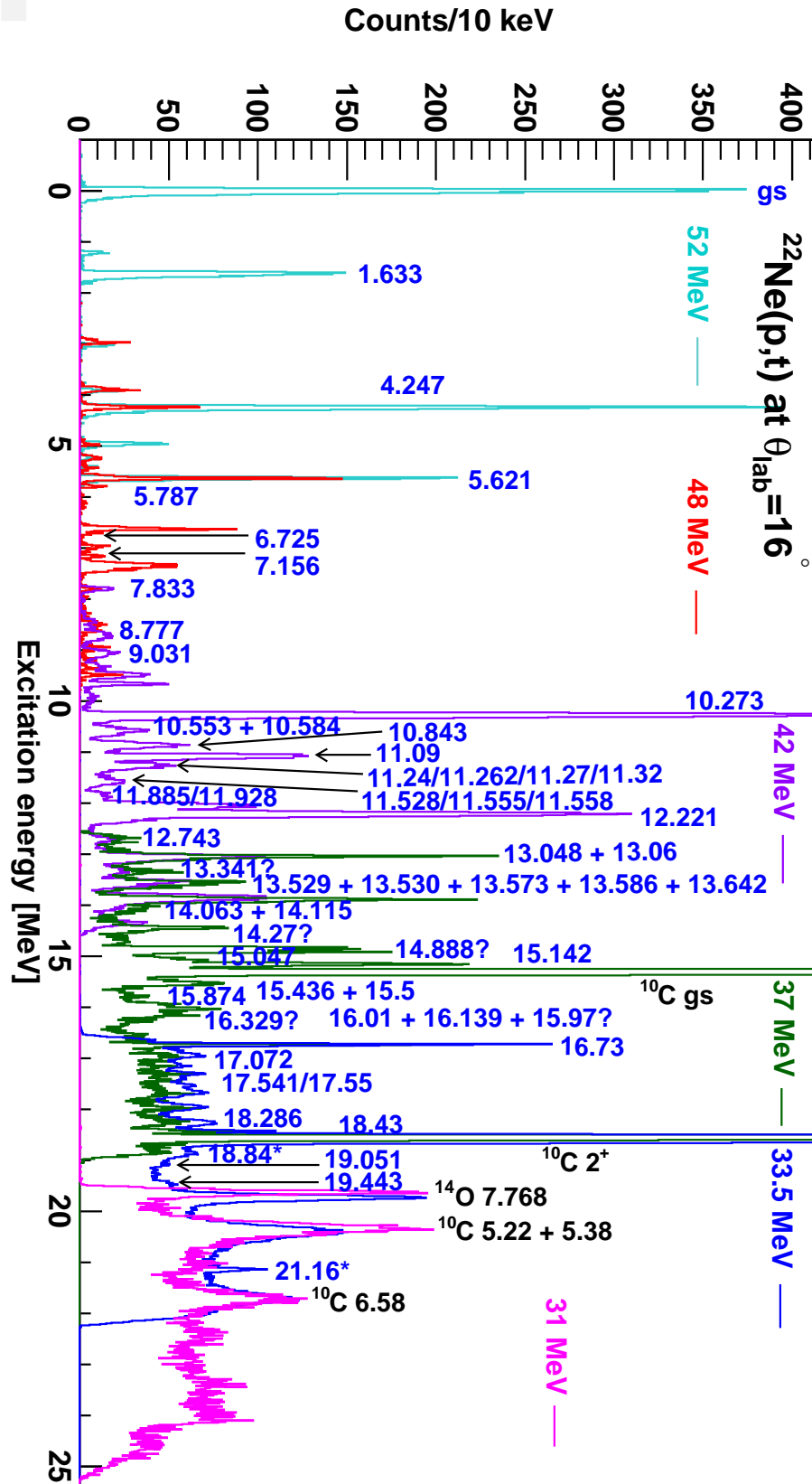


FIG. B.2: The excitation energy spectrum for all field settings on the ^{22}Ne gas-filled target at $\theta_{lab} = 16^\circ$

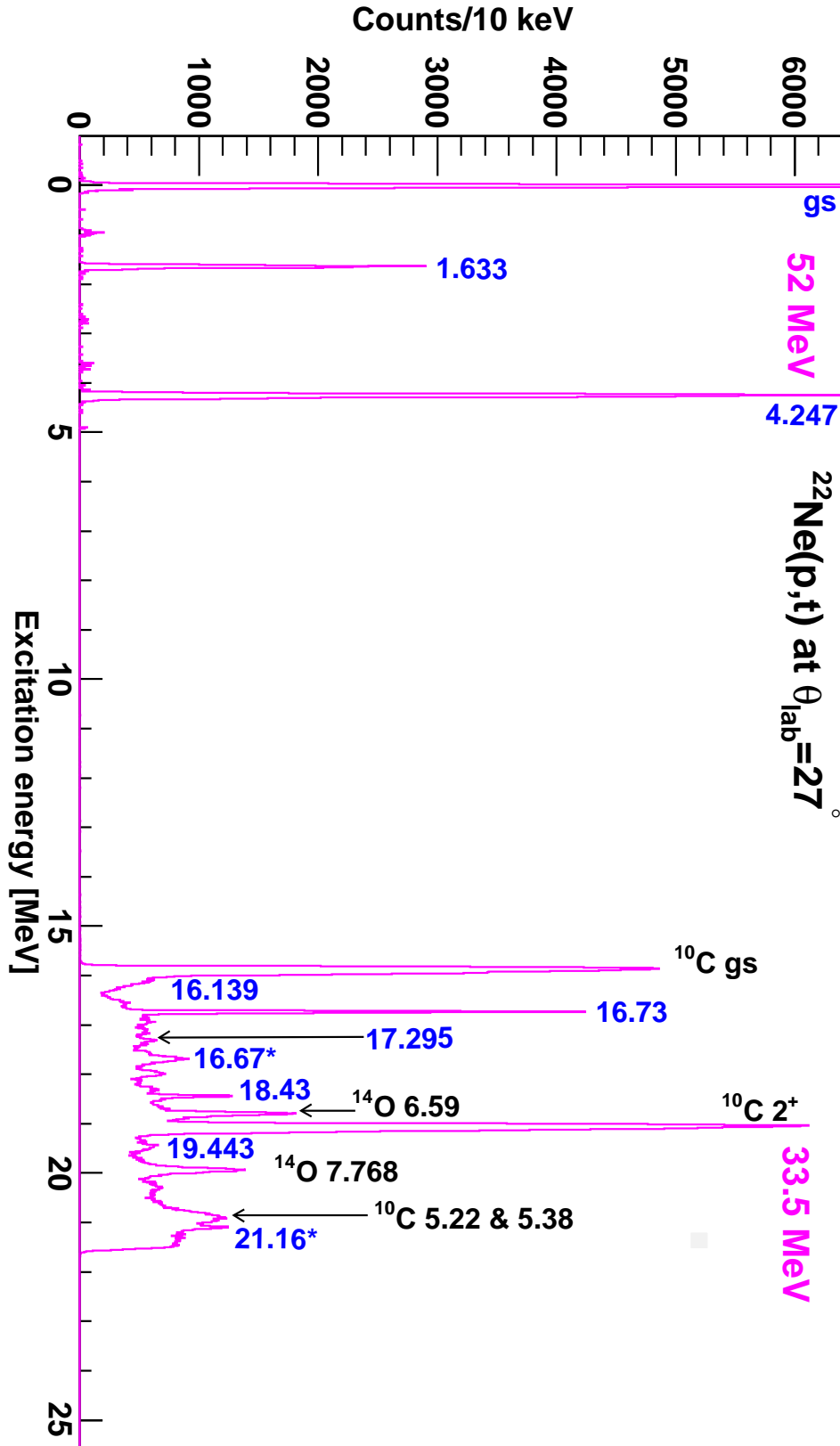


FIG. B.3: The excitation energy spectrum for all field settings on the ^{22}Ne gas-filled target at $\theta_{\text{lab}} = 27^\circ$

APPENDIX C

Absolute cross sections of known states

The integrated cross sections which were measured for the known states in ^{20}Ne are shown in Tables C.1 and C.2. The angular distribution plots of all the known states in ^{20}Ne which were not shown in Chapter 4 are shown in Figs. C.1 to C.4.

State [MeV]	$\sigma (\theta_{lab} = 0^\circ)$ [$\mu\text{b}.\text{sr}^{-1}$]	$\sigma (\theta_{lab} = 7^\circ)$ [$\mu\text{b}.\text{sr}^{-1}$]	$\sigma (\theta_{lab} = 16^\circ)$ [$\mu\text{b}.\text{sr}^{-1}$]	$\sigma (\theta_{lab} = 27^\circ)$ [$\mu\text{b}.\text{sr}^{-1}$]
5.621 3^-	34(7)	104(23)		
5.788 1^-	50(11)	48(11)		
9.873 3^-			3.3(7)	
10.406	5.8(13)		3.3(8)	
10.84, 10.843, 10.884	16.0(35)	49(11)	45(10)	
11.528, 11.555, 11.558	22(5)	21(5)	19(4)	
12.401 3^- , 12.436 0^+	7.6(17)	12.0(27)	12.0(26)	
13.827, 13.866	3.2(7)		2.7(6)	
14.370			23(5)	
15.436, 15.500	16.0(36)			
17.155			3.2(7)	
17.284			4.6(10)	2.7(6)
18.286				4.1(9)
20.296 7^-				5.0(11)

TABLE C.1: The observed absolute cross sections of all known negative parity states, or of peaks consisting at least partly of negative parity states, in ^{20}Ne [3]

State [MeV]	$\sigma (\theta_{lab} = 0^\circ)$ [$\mu\text{b}\cdot\text{sr}^{-1}$]	$\sigma (\theta_{lab} = 7^\circ)$ [$\mu\text{b}\cdot\text{sr}^{-1}$]	$\sigma (\theta_{lab} = 16^\circ)$ [$\mu\text{b}\cdot\text{sr}^{-1}$]	$\sigma (\theta_{lab} = 27^\circ)$ [$\mu\text{b}\cdot\text{sr}^{-1}$]
g.s. 0^+	620(140)	670(150)	160(36)	160(35)
1.634 2^+	250(56)	250(57)	58(13)	40(9)
4.428 4^+	110(24)	150(33)	120(27)	120(26)
6.725 0^+	110(24)		12.0(25)	
7.191 0^+	77(17)	27(6)	24(5)	
7.421 2^+	93(21)	21(5)		
7.833 2^+	7.7(17)	19(4)	18(4)	
9.031 4^+	12.0(27)		9(2)	
9.487 2^+	5.7(13)	17(4)	66(15)	
9.9 4^+	2.3(5)			
10.273 2^+	35(8)	160(36)	280(63)	
10.553 4^+ , 10.584 2^+	3.1(7)	8(2)	26.0(58)	
11.02 4^+	0.4(1)		1.2(3)	
11.09 4^+	58(13)	77(17)	81(18)	
11.32 0^+		5.8(13)		
12.221 2^+	61(14)	120(26)	190(41)	
12.743 (2^+)	23(5)	15.0(34)		
13.048 4^+	46(10)	61(14)	77(17)	
13.642 0^+	57(13)	42(9)		
13.744 0^+	28(6)	59(13)		
14.063 2^+ , 14.115 2^+		18(4)		
14.455 ($0^+, 2^+$), 14.475	50(11)	52(11)	18(4)	
14.653 0^+	24.0(69)			
14.839 (4^+), 14.888 2^+	11.0(25)	16.0(35)	39.0(87)	
16.73 0^+	370(82)	186(42)	35(8)	65(15)
17.541, 17.55 (2^+)			11(2)	
17.91 (2^+)	3.2(7)		14(3)	13(3)
18.43 2^+	29(7)		10(2)	14(3)
19.443 6^+				20(4)

TABLE C.2: The observed absolute cross sections of all known positive parity states in ^{20}Ne [3] which were observed in the present measurement

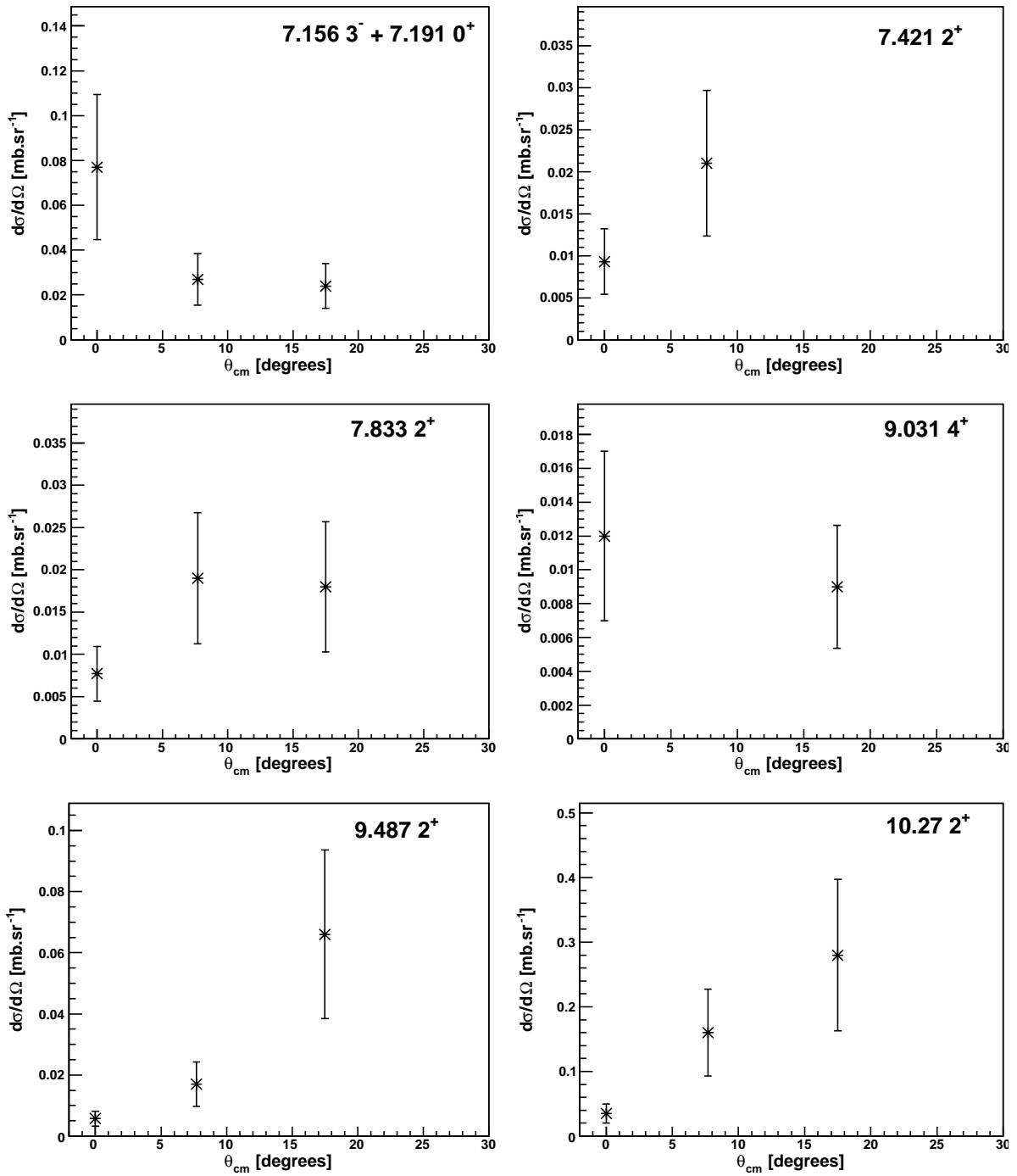


FIG. C.1: Angular distribution plots for states measured between $E_x = 7$ and $E_x = 10.3$ MeV. The states are labelled by their known excitation energy values in MeV, as with all figures to come in this section.

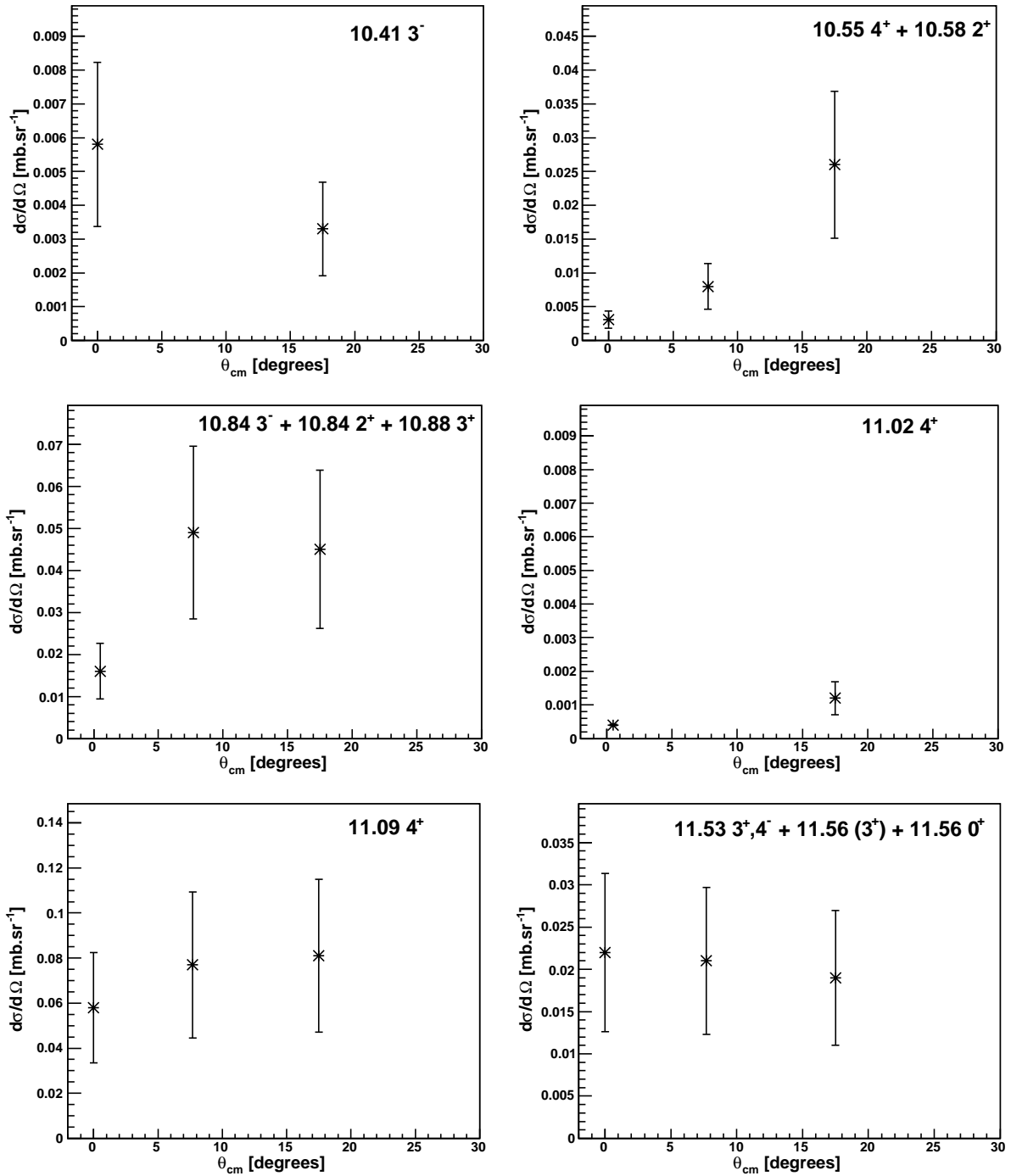


FIG. C.2: Angular distribution plots for states measured between $E_x = 10.3$ and $E_x = 12$ MeV

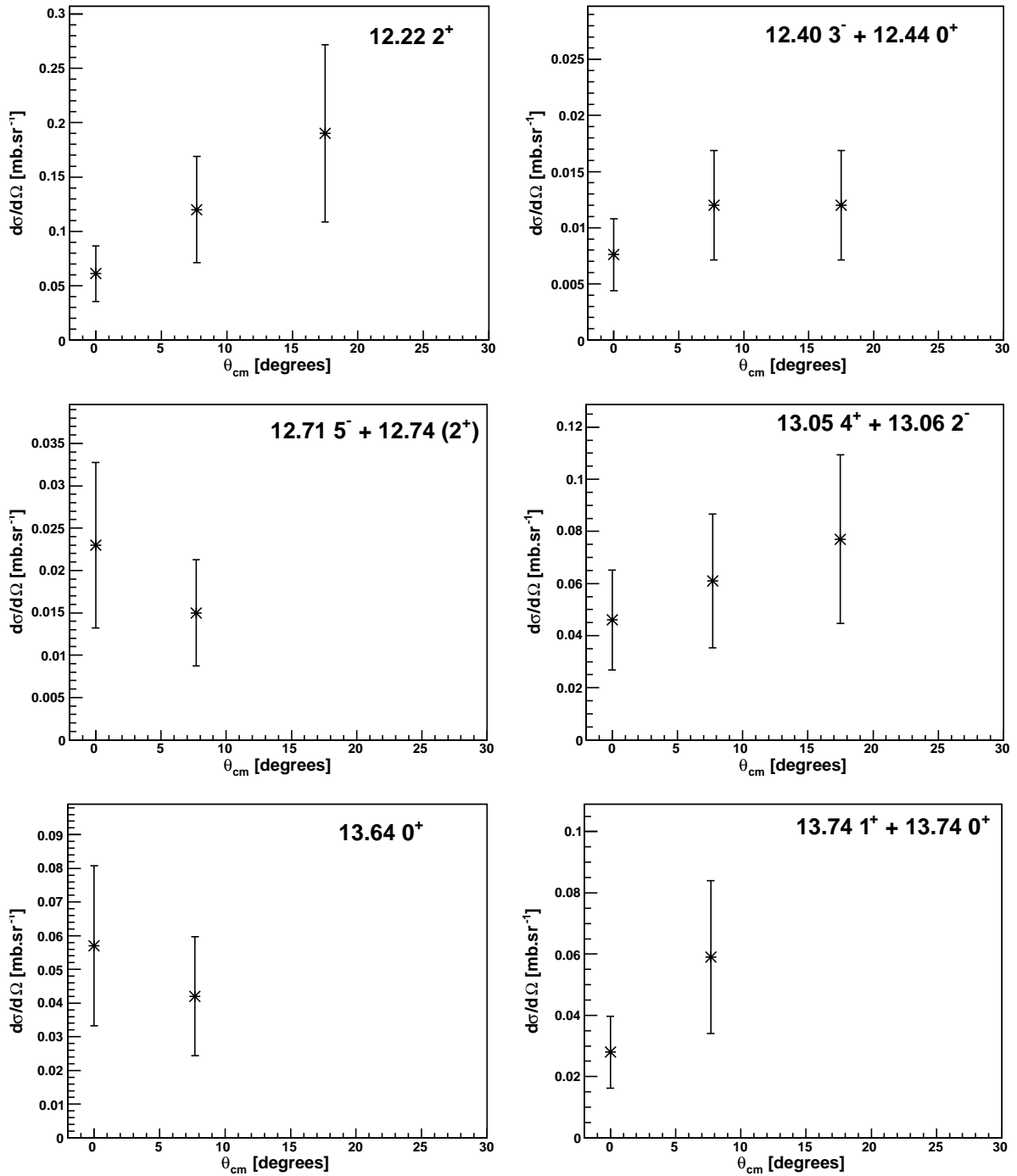


FIG. C.3: Angular distribution plots for states measured between $E_x = 12$ and $E_x = 13.8$ MeV

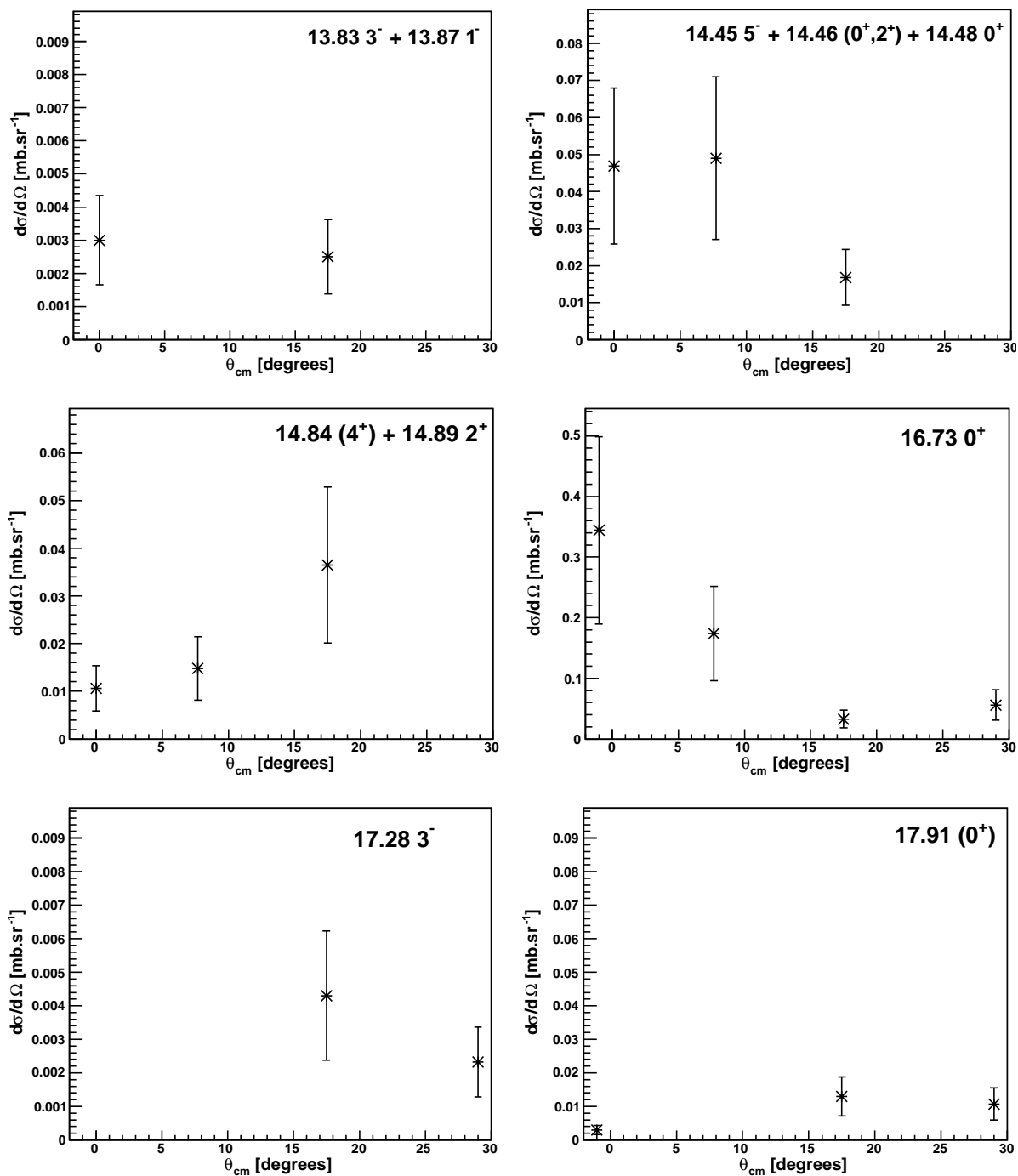


FIG. C.4: Angular distribution plots for states measured between $E_x = 13.8$ and $E_x = 18$ MeV

APPENDIX D

Results from NuShellX and FRESCO at non-zero angles

Figs. D.1, D.2 and D.3 show the results of calculations performed by Alex Brown for 4^+ , 2^+ and 0^+ states from the $^{22}\text{Ne}(p,t)^{20}\text{Ne}$ reaction using NuShellX [126] and FRESCO [59] at $\theta_{lab} = (7^\circ, 16^\circ, 27^\circ)$, with $E_p = 65$ MeV.

The results of these calculations may be compared to the cross section values which were extracted from the data obtained in the present measurement for the same states at the same respective angles in Figs. D.4, D.5 and D.6.

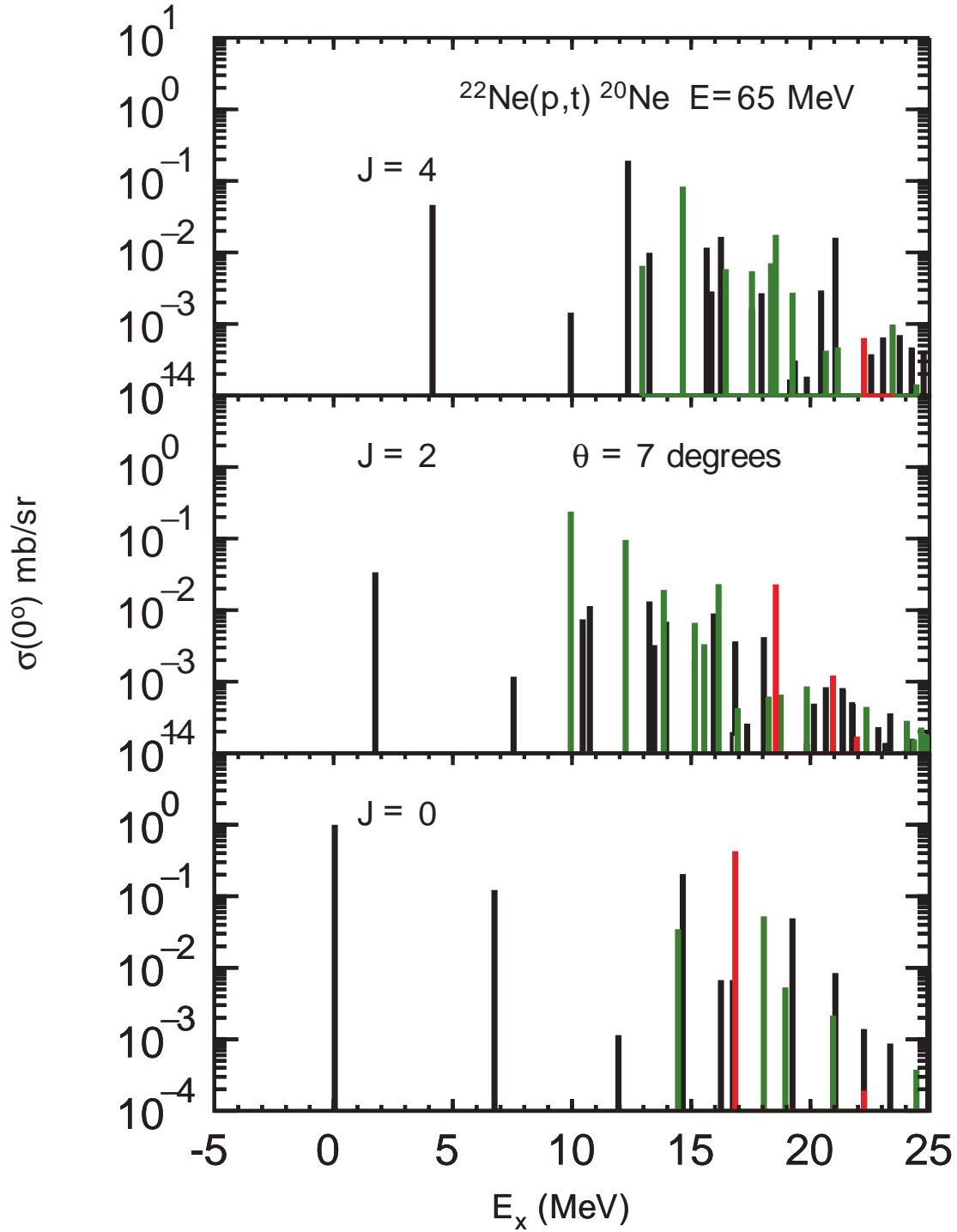


FIG. D.1: Calculated cross section values of 4^+ , 2^+ and 0^+ states at $\theta_{lab} = 7^\circ$ in ^{20}Ne . The black lines are $T = 0$, the green lines are $T = 1$ and the red lines are $T = 2$ states, as they are in all figures to come in this section.

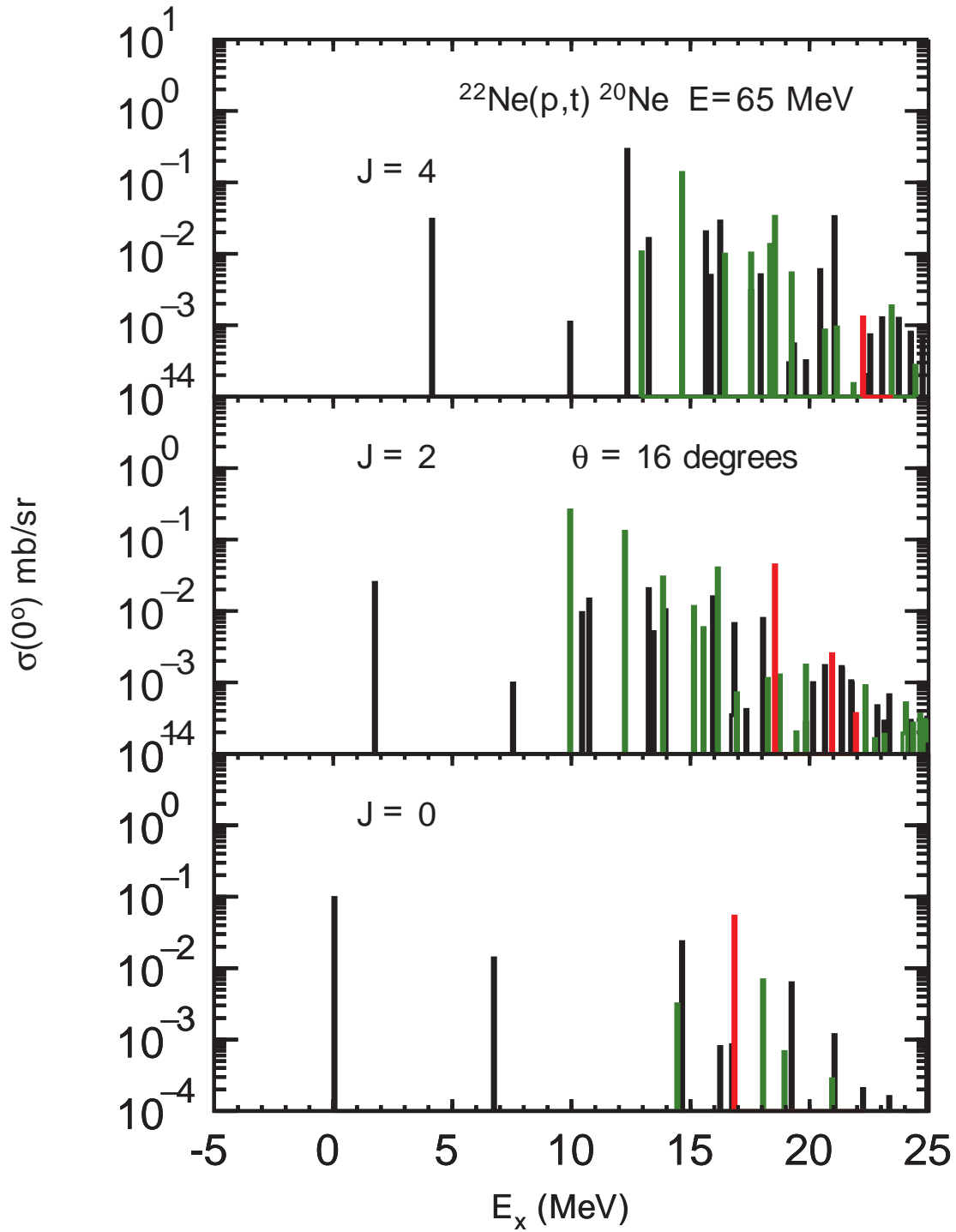


FIG. D.2: Calculated cross section values of 4^+ , 2^+ and 0^+ states at $\theta_{lab} = 16^\circ$ in ^{20}Ne

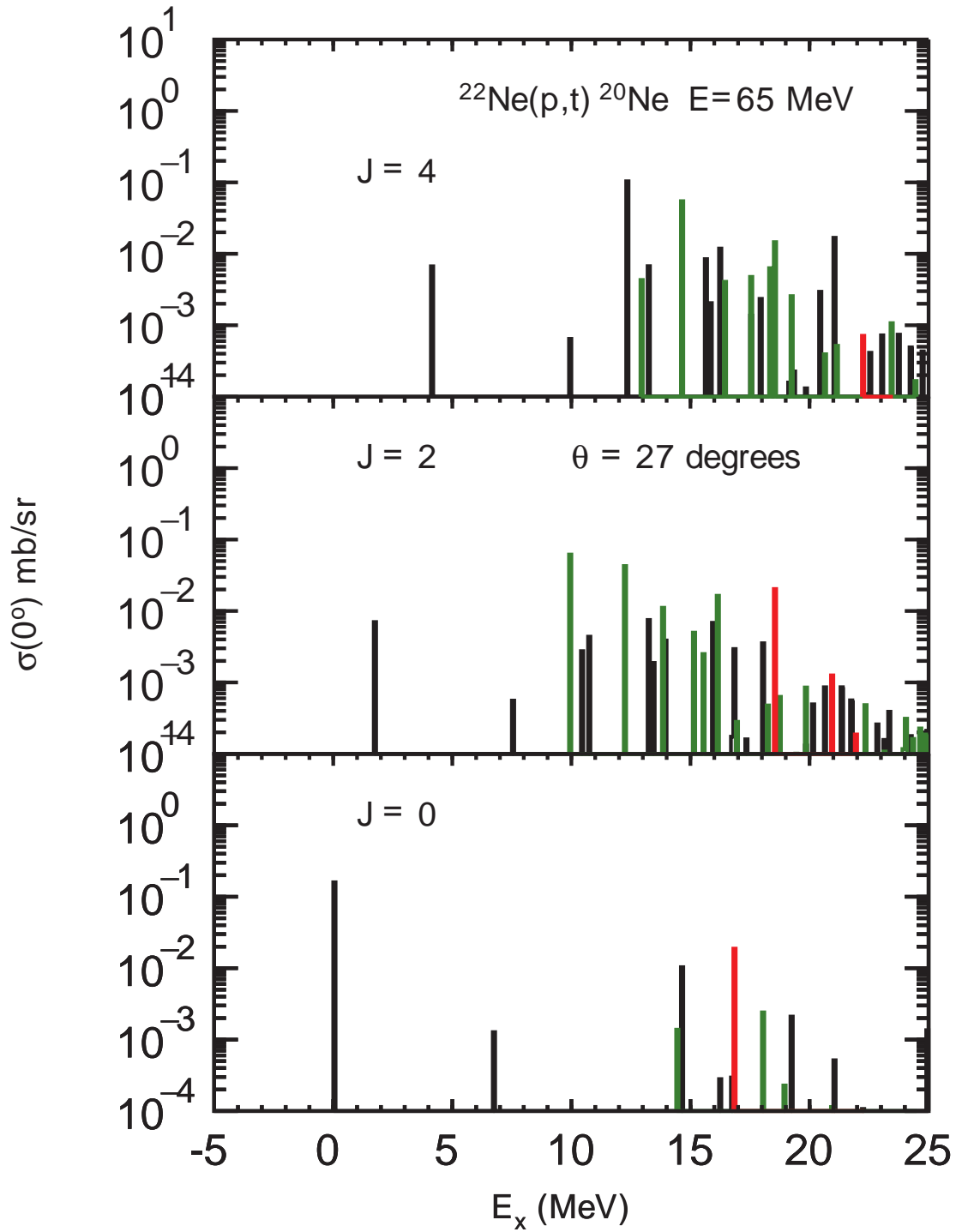


FIG. D.3: Calculated cross section values of 4^+ , 2^+ and 0^+ states at $\theta_{lab} = 27^\circ$ in ^{20}Ne

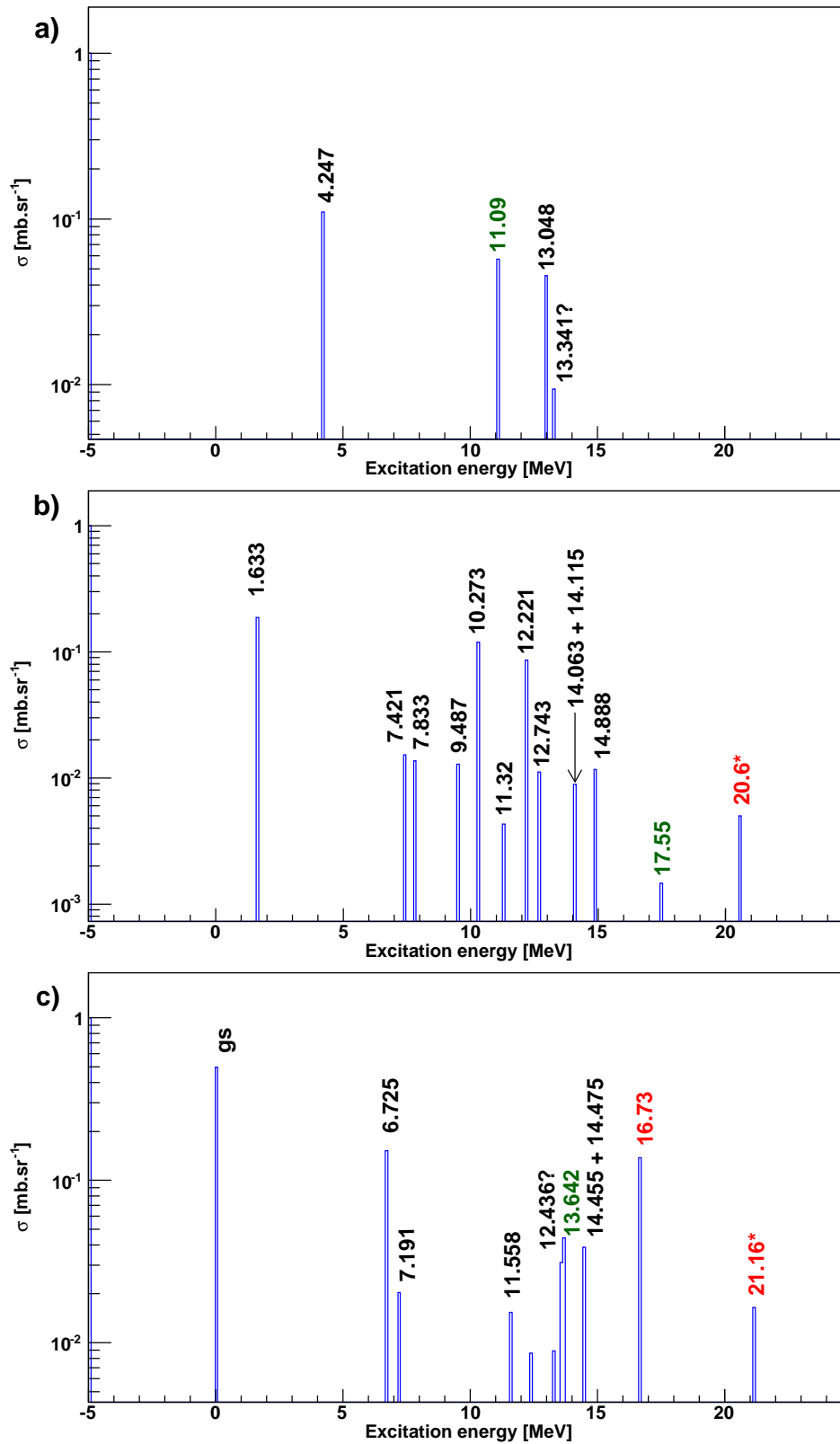


FIG. D.4: Cross section values extracted from the $\theta_{lab} = 7^\circ$ data for states of spins and parities 4^+ , 2^+ and 0^+ from top to bottom. States with black labels have $T = 0$, green labels have $T = 1$ and red labels have $T = 2$, and this is the case in all spectra to come.

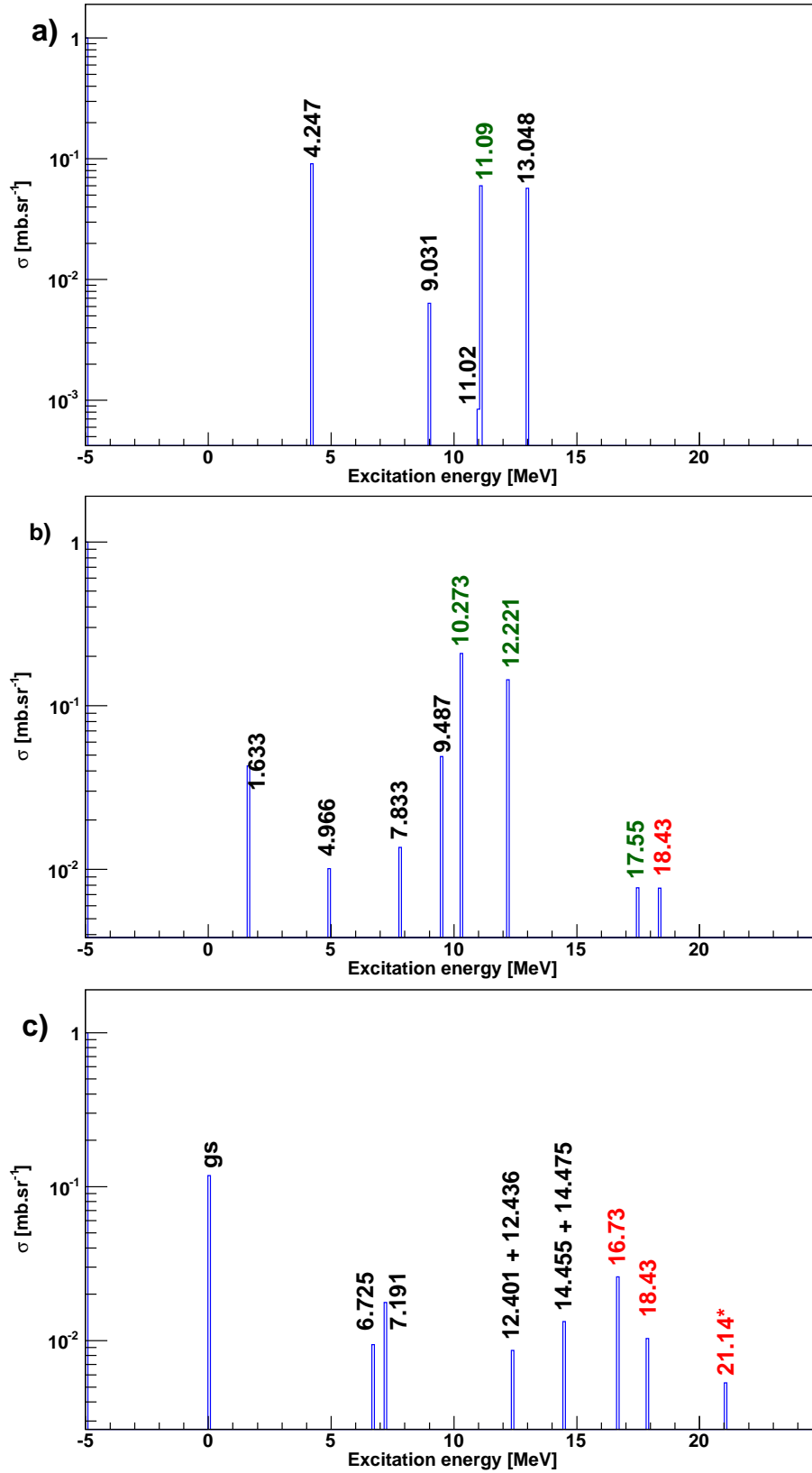


FIG. D.5: Cross section values extracted from the $\theta_{lab} = 16^\circ$ data for states of spins and parities 4^+ , 2^+ and 0^+ from top to bottom

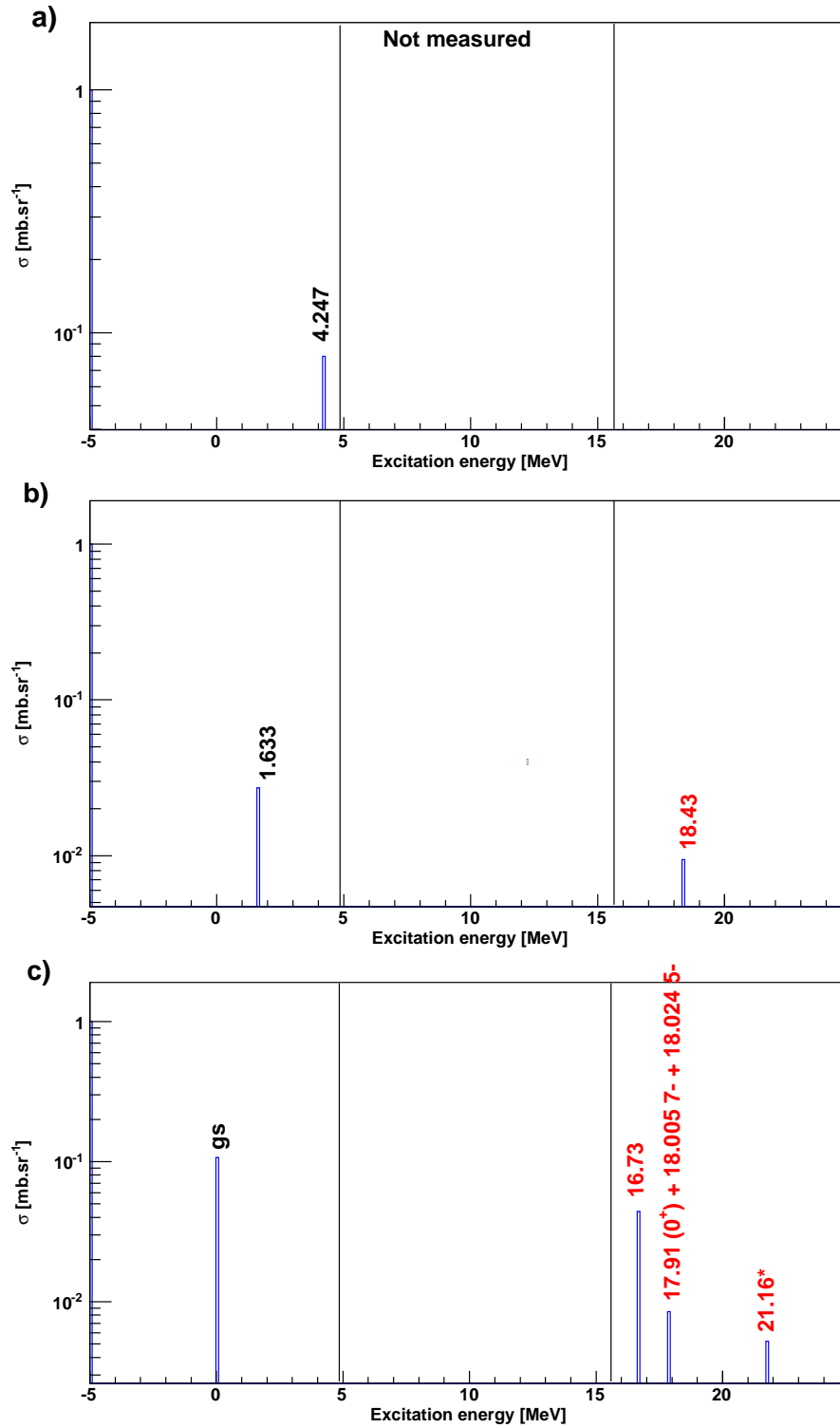


FIG. D.6: Cross section values extracted from the $\theta_{lab} = 27^\circ$ data for states of spin and parities 4^+ , 2^+ and 0^+ from top to bottom

APPENDIX

Bibliography

- [1] O. Hahn, in *Nieuwe atomen*, edited by W. Gaade (Elsevier Publishing Company Inc., New York, 1950).
- [2] L. R. Hafstad and E. Teller, *Phys. Rev.* **54**, 681 (1938).
- [3] Experimental Nuclear Reaction Data Library (*EXFOR*), *IAEA Nuclear Data Section*. See: <http://www-nds.iaea.org/exfor/> or, for the *NNDC* at Brookhaven National Laboratory, the mirror site is <http://www.nndc.bnl.gov/exfor/>. Data from [78].
- [4] F. Hoyle, *The Astrophysical Journal: Supplement Series* **1**, 12 (1954).
- [5] C. W. Cook, W. A. Fowler, C. C. Lauritsen, and T. Lauritsen, *Phys. Rev.* **107**, 508 (1957).
- [6] E. Uegaki, S. Okabe, Y. Abe, and H. Tanaka, *Prog. Theor. Phys.* **57**, 1262 (1977).
- [7] E. Uegaki, S. Okabe, Y. Abe, and H. Tanaka, *Prog. Theor. Phys.* **62**, 1621 (1979).
- [8] Y. Kanada-En'yo, *Phys. Rev. Lett.* **81**, 5291 (1998).
- [9] P. Descouvemont, *Nucl. Phys. A* **709**, 275 (2002).
- [10] T. Neff and H. Feldmeier, *Nucl. Phys. A* **738**, 357 (2004).
- [11] Y. Kanada-En'yo, *Prog. Theor. Phys.* **117**, 655 (2007).
- [12] Y. Funaki *et al.*, *Phys. Rev. C* **80**, 064326 (2009).
- [13] S. Ohkubo and Y. Hirabayashi, *Phys. Lett. B* **684**, 127 (2010).
- [14] B. Buck, A. C. Merchant, and S. M. Perez, *Phys. Rev. C* **87**, 024304 (2013).
- [15] M. Chernykh *et al.*, *Phys. Rev. Lett.* **98**, 032501 (2007).
- [16] E. Epelbaum *et al.*, *Phys. Rev. Lett.* **109**, 252501 (2012).

Bibliography

- [17] E. Epelbaum *et al.*, Eur. Phys. J. A **49**, 82 (2013).
- [18] K. Ikeda, N. Takigawa, and H. Horiuchi, Suppl. Prog. Theor. Phys. **Extra Number**, 464 (1968).
- [19] C. Angulo *et al.*, Nuclear Physics A **656**, 3 (1999).
- [20] H. O. U. Fynbo *et al.*, Letters to Nature **433**, 136 (2005).
- [21] C. A. Diget *et al.*, Influences on the triple alpha process beyond the Hoyle state, Proceedings of Science: International Symposium on Nuclear Astrophysics - Nuclei in the Cosmos - IX:PoS (NIC-IX) 025, 2006.
- [22] R. B. Wiringa, S. C. Pieper, J. Carlson, and V. R. Pandharipande, Phys. Rev. C **62**, 014001 (2000).
- [23] S. Karataglidis, P. J. Dortmans, K. Amos, and R. de Swiniarski, Phys. Rev. C **52**, 861 (1995).
- [24] A. Tohsaki, H. Horiuchi, P. Schuck, and G. Röpke, Phys. Rev. Lett. **87**, 192501 (2001).
- [25] Y. Funaki *et al.*, Phys. Rev. C **67**, 051306(R) (2003).
- [26] T. Yamada and P. Schuck, Phys. Rev. C **69**, 024309 (2004).
- [27] P. Schuck *et al.*, Nucl. Phys. A **738**, 94 (2004).
- [28] S. Ohkubo and Y. Hirabayashi, Phys. Rev. C **70**, 041602(R) (2004).
- [29] Y. Funaki *et al.*, Nuclear Physics News **17**, 11 (2007).
- [30] T. Ichikawa *et al.*, Phys. Rev. C **83**, 061301(R) (2011).
- [31] Y. Funaki *et al.*, J. Phys.: Conf. Ser. **436**, 012004 (2013).
- [32] A. A. Ogloblin, S. A. Goncharov, T. L. Belyaeva, and A. S. Demyanova, Physics of Atomic Nuclei **69**, 1149 (2006).
- [33] N. T. Zinner and A. S. Jensen, Phys. Rev. C **78**, 041306(R) (2008).

Bibliography

- [34] Y. Funaki *et al.*, Phys. Rev. C **82**, 024312 (2010).
- [35] E. M. Burbidge, G. R. Burbidge, W. A. Fowler, and F. Hoyle, Rev. Mod. Phys. **29**, 547 (1957).
- [36] J. B. McGrory and B. H. Wildenthal, Phys. Rev. C **7**, 974 (1973).
- [37] H. C. Lee and R. Y. Cusson, Phys. Rev. Lett. **29**, 1525 (1972).
- [38] H. Horiuchi, K. Ikeda, and K. Kato, Prog. Theor. Phys. Supplement No. 192 p. 1-238 (2012).
- [39] J. P. Ebran, E. Khan, T. Niksic, and D. Vretenar, Letters to Nature **487**, 341 (2012).
- [40] M. M. Hindi, J. H. Thomas, D. C. Radford, and P. D. Parker, Phys. Rev. C **27**, 2902 (1983).
- [41] J. D. MacArthur, H. C. Evans, J. R. Leslie, and H.-B. Mak, Phys. Rev. C **22**, 356 (1980).
- [42] H. Horiuchi and K. Ikeda, Prog. Theor. Phys. **40**, 277 (1968).
- [43] Y. Fujiwara, H. Horiuchi, and R. Tamagaki, Prog. Theor. Phys. **61**, 1629 (1979).
- [44] G. R. Satchler, *Introduction to Nuclear Reactions* (Macmillan Education Ltd., Houndmills, Basingstoke, Hampshire RG21 2XS and London, 1990).
- [45] J. Cerny, R. H. Pehl, and G. T. Garvey, Phys. Lett. **12**, 234 (1964).
- [46] W. N. Catford, E. F. Garman, and L. K. Fifield, Nucl. Phys. A **417**, 77 (1984).
- [47] R. L. McGrath *et al.*, Phys. Rev. C **1**, 184 (1970).
- [48] R. J. De Meijer, H. F. J. Van Royen, and P. J. Brussaard, Nucl. Phys. A **164**, 11 (1971).
- [49] S. R. Leshner *et al.*, Phys. Rev. C **66**, 051305(R) (2002).
- [50] D. Bucurescu *et al.*, Phys. Rev. C **73**, 064309 (2006).

Bibliography

- [51] A. Matic *et al.*, Phys. Rev. C **80**, 055804 (2009).
- [52] S. Pascu *et al.*, Phys. Rev. C **79**, 064323 (2009).
- [53] A. Matic *et al.*, Phys. Rev. C **82**, 025807 (2010).
- [54] G. T. Garvey, J. Cerny, and R. H. Pehl, Phys. Rev. Lett. **12**, 726 (1964).
- [55] D. N. Mihailidis, N. M. Hintz, A. Sethi, and E. J. Stephenson, Phys. Rev. C **64**, 054608 (2001).
- [56] National Nuclear Data Centre, Brookhaven National Laboratory, Q-value calculator, Web programming by B. Pritychenko and A. Sonzogni, Data from Ref. [127].
- [57] G. R. Satchler, *Direct Nuclear Reactions* (Oxford University Press, Walton Street, Oxford OX2 6DP, 1983).
- [58] P. D. Kunz, Zero Range Distorted Wave Born Approximation, <http://spot.colorado.edu/~kunz/DWBA.html>, 2013.
- [59] The FRESCO website, www.fresco.org.uk, (2006).
- [60] W. D. M. Rae, NuShellX for Windows and Linux, <http://knollhouse.org>.
- [61] J. Jänecke, Phys. Rev. **147**, 735 (1966).
- [62] I. J. Thompson, Computer Physics Reports **7**, 167 (1988).
- [63] K. S. Krane, *Introductory Nuclear Physics* (John Wiley and Sons, 111 River Street, Hoboken, USA, 1988).
- [64] F. D. Becchetti and G. W. Greenlees, Phys. Rev. **182**, 1190 (1969).
- [65] D. K. Olsen, T. Udagawa, T. Tamura, and R. E. Brown, Phys. Rev. C **8**, 609 (1973).
- [66] C. King, M. Shahabuddin, and B. Wildenthal, Nucl. Phys. A **270**, 399 (1976).
- [67] T. Tamura, Rev. Mod. Phys. **37**, 679 (1965).

Bibliography

- [68] A. Signoracci, Ph.D. thesis, Michigan State University, (2011),
<http://www.nsl.msui.edu/ourlab/publications/type/Theses/2011>.
- [69] B. A. Brown and W. A. Richter, *Phys. Rev. C* **74**, 034315 (2006).
- [70] NuShellX@MSU, <http://www.nsl.msui.edu/~brown/resources/resources.html>.
- [71] B. A. Brown, Private communication.
- [72] S. M. Blinder, Wolfram Demonstrations Project: Magic Numbers in the Nuclear Shell Model,
<http://demonstrations.wolfram.com/MagicNumbersInTheNuclearShellModel/>,
(2009).
- [73] D. D. Warner, M. A. Bentley, and P. van Isacker, *Nature Physics* **2**, 311 (2006).
- [74] W. Heisenberg, *Z. Phys.* **77**, 1 (1932).
- [75] J. P. Elliot, in *Chapter 3 in Isospin in Nuclear Physics*, edited by D. H. Wilkinson (North-Holland, Amsterdam, 1969).
- [76] Y. H. Lam, N. A. Smirnova, and E. Caurier, *Phys. Rev. C* **87**, 054304 (2013).
- [77] W. E. Ormand, *Acta Physica Polonica B* **29**, 1 (1998).
- [78] D. R. Tilley *et al.*, *Nucl. Phys. A* **636**, 249 (1998).
- [79] M. S. Antony, J. Britz, J. B. Bueb, and A. Pape, *At. Data Nucl. Data Tables* **33**, 447 (1985).
- [80] E. P. Wigner, Proc. 1st Robert A. Welch Foundation Conf. Chem. Res., Houston, Texas, (1957).
- [81] J. A. Swartz, Master's thesis, Stellenbosch University, (2010),
<http://hdl.handle.net/10019.1/4297>.
- [82] W. A. Richter, Private communication.
- [83] ROOT Version 5.19/03 (2008), <http://root.cern.ch>.
- [84] J. Britz, A. Pape, and M. S. Antony, *At. Data Nucl. Data Tables* **69**, 125 (1998).

Bibliography

- [85] The iThemba LABS website, <http://www.tlabs.ac.za>, (2013).
- [86] R. Neveling *et al.*, Nucl. Instr. Meth. A **654**, 29 (2011).
- [87] M. Fujiwara *et al.*, Nucl. Instr. Meth. A **422**, 484 (1999).
- [88] W. Bertozzi *et al.*, Nucl. Instr. Meth. A **141**, 457 (1977).
- [89] R. Neveling, Ph.D. thesis, Stellenbosch University, (2001), <http://hdl.handle.net/10019.1/52370>.
- [90] R. Neveling, F. D. Smit, H. Fujita, and R. T. Newman, Guide to the K600 Magnetic Spectrometer, unpublished, (2011).
- [91] Saint Gobain Crystals, <http://www.detectors.saint-gobain.com>, (2009).
- [92] G. F. Knoll, *Radiation Detection and Measurement, 3rd Edition* (John Wiley and Sons, Hoboken, USA, 2000).
- [93] B. Mouginot *et al.*, Phys. Rev. C **83**, 037302 (2011).
- [94] B. L. Cohen, Rev. Sci. Instr. **30**, 415 (1959).
- [95] H. G. Blosser *et al.*, Nucl. Instr. Meth. **91**, 61 (1971).
- [96] H. Fujita, Nucl. Instr. Meth. A **484**, 17 (2002).
- [97] H. Matsubara *et al.*, Nucl. Instr. Meth. A **678**, 122 (2012).
- [98] S. O'Brien *et al.*, High precision (p,t) measurements to study the (α,p) process, iThemba LABS Annual Report, 2010.
- [99] G. P. A. Berg *et al.*, J. Phys.: Conf. Ser. **387**, 012003 (2012).
- [100] P. Papka and C. Beck, in *Lecture Notes in Physics 818: Clusters in Nuclei*, edited by C. Beck (Springer-Verlag, Berlin Heidelberg, 2011).
- [101] Toray Group, www.toray.com, (2013).
- [102] A. Tamii, Private communication.
- [103] C. A. Pineda-Vargas and C. Mtshali, Private communication.

. Bibliography

- [104] E. F. Garman and E. W. Grime, *Progress in Biophysics and Molecular Biology* **89**, 173 (2005).
- [105] C. G. Ryan, M. Jensen, B. E. Etschmann, and D. R. Cousens, GeoPIXE@Quantitative PIXE/SXRF Trace Element Imaging and Analysis, CSIRO Earth Science and Resource Engineering c/o CSIRO Material Science and Engineering, Clayton VIC 3168, Australia.
- [106] C. G. Ryan, *Nucl. Instr. Meth. B* **181**, 170 (2001).
- [107] Extorr Residual Gas Analyzers, www.extorr.com, (2013).
- [108] Chemgas, <http://www.chemgas.com>, france (2013).
- [109] The Midas Data Acquisition System, Paul Sherrer Institute, Switzerland, <http://midas.psi.ch>, (2013).
- [110] K. G. Fissum *et al.*, *Nucl. Instr. Meth. A* **474**, 108 (2001).
- [111] C. Wheldon, Derivation for two-body kinematics, unpublished, (2012).
- [112] The GANIL website, <http://www.ganil-spiral2.eu/>, (2006).
- [113] G. F. Knoll, *Radiation Detection and Measurement* (John Wiley and Sons, USA, 1979).
- [114] J. J. Van Zyl, Ph.D. thesis, Stellenbosch University, (2012), <http://hdl.handle.net/10019.1/71798>.
- [115] M. Wiedeking *et al.*, *Phys. Rev. Lett.* **94**, 132501 (2005).
- [116] C. R. Hoffman *et al.*, *Phys. Rev. C* **85**, 054318 (2012).
- [117] W. von Oertzen, *Eur. Phys. J. A* **11**, 403 (2001).
- [118] P. Papka, Development of an active target from stable to rare-ion beams - RIB Workshop 2011 at iThemba LABS (<http://www.tlabs.ac.za/rib.htm>), 2013.
- [119] A. M. Laird *et al.*, *Nucl. Instr. Meth. A* **573**, 306 (2007).
- [120] A. Zucchiatti, Ph.D. thesis, University of Witwatersrand, (1988), unpublished.

. Bibliography

- [121] D. Steyn, Ph.D. thesis, University of Cape Town, (1990), unpublished.
- [122] B. Vignon, J. F. Bruandet, and N. Longequeue, Nucl. Phys. A **162**, 82 (1971).
- [123] J. C. Hardy, H. Brunnader, and J. Cerny, Phys. Rev. Lett. **22**, 1439 (1969).
- [124] J. C. Hardy, H. Brunnader, J. Cerny, and J. Jänecke, Phys. Rev. **183**, 854 (1969).
- [125] D. Ashery *et al.*, Phys. Rev. C **13**, 1345 (1976).
- [126] William Rae NuShellX website, <http://www.garsington.eclipse.co.uk/>, (2008).
- [127] G. Audi *et al.*, Nucl. Phys. A **729**, 3, 129, 337 (2003).